Dean, Cameron (2019) *Time dependent studies of B->h+h'- decays and research and operation for the VELO project at LHCb.* PhD thesis.

https://theses.gla.ac.uk/40969/

Time Dependent Studies of B→$h^+h'^-$ Decays and Research and Operation for the VELO Project at LHCb

Cameron Dean

1st Supervisor: Prof. Lars Eklund

2nd Supervisor: Prof. Paul Soler

Submitted in fulfilment of the requirements for the degree of

Doctor of Philosophy

Particle Physics Experiment

School of Physics and Astronomy

January 2019

UNIVERSITY OF GLASGOW

Abstract

College of Science and Engineering
School of Physics and Astronomy

Submitted in fulfilment of the requirements for the degree of
Doctor of Philosophy

Time Dependent Studies of B→$h^+h'^-$ Decays and Research and Operation for the VELO Project at LHCb

by Cameron Dean

The family of B→ $h^+h'^-$ decays, where h refers to protons, pions or kaons, are of great interest to the particle physics community. Two such decays, $B_s^0 \to K^+K^-$ and $B^0 \to \pi^+\pi^-$, are related by U-spin symmetry with their tree levels decays suppressed, resulting in equal contributions from their loop level decays. Hence they are a good place to search for physics beyond the Standard Model.

This thesis discusses two separate studies of this class of decay. One study measures the effective lifetimes of the decays $B^0 \to \pi^+\pi^-$, $B^0 \to K^+\pi^-$, $B_s^0 \to \pi^+K^-$, $B_s^0 \to K^+K^-$, $\Lambda_b^0 \to pK^-$ and $\Lambda_b^0 \to p\pi^-$ at 7 and 8 TeV which corresponds to an integrated luminosity of 1 fb^{-1} and 2 fb^{-1} respectively. The effective lifetime of $B_s^0 \to K^+K^-$ can be used to constrain the value of the CP observable $\mathcal{A}_{KK}^{\Delta\Gamma}$.

The other analysis discusses time-dependent measurements of CP violation in $\mathrm{B}^0 \rightarrow \pi^+\pi^-$ and $\mathrm{B}^0_\mathrm{s} \rightarrow \mathrm{K}^+\mathrm{K}^-$ decays at 13 TeV which corresponds to an integrated luminosity of $2\,\mathrm{fb}^{-1}$. These decays can be used to place constraints on the Unitarity Triangle angles β and γ to test for deviations from inclusive measurements of these angles. The analysis at 13 TeV measured the CP observables for $\mathrm{B}^0 \rightarrow \pi^+\pi^-$ and $\mathrm{B}^0_\mathrm{s} \rightarrow \mathrm{K}^+\mathrm{K}^-$ to be

$$\begin{aligned} C_{\pi\pi} &= -0.237 \pm 0.036(\text{stat.}) \pm 0.018(\text{syst.}) \\ S_{\pi\pi} &= -0.653 \pm 0.043(\text{stat.}) \pm 0.016(\text{syst.}) \\ C_{\mathrm{KK}} &= 0.121 \pm 0.042(\text{stat.}) \pm 0.021(\text{syst.}) \\ S_{\mathrm{KK}} &= 0.138 \pm 0.041(\text{stat.}) \pm 0.012(\text{syst.}) \end{aligned}$$

For $\mathrm{B}^0 \rightarrow \pi^+\pi^-$, the correlation between $S_{\pi\pi}$ and $C_{\pi\pi}$ was measured to be -0.15 while, for $\mathrm{B}^0_\mathrm{s} \rightarrow \mathrm{K}^+\mathrm{K}^-$, the correlation was measured to be -0.012 between S_{KK} and C_{KK}. These results are the most precise from a single experiment to date.

The LHCb detector has performed exceptionally since the start of data taking at the LHC with many important results reported. To ensure the optimal performance it is important to inspect and validate different subdetectors throughout the life of the experiment. The Vertex Locator (VELO) detector surrounds the interaction point of the proton collisions and is the first detector the collision products traverse. To ensure a good signal quality, the silicon strips must be fully depleted. As the detector ages the effective depletion voltage increases so the high voltage system must be qualified to ensure it can cope. Tests of this subsystem were devised to study the high voltage supply at different stages of the system where it was found that the VELO is performing to expectations and that LHCb can meet its physics goals for the foreseen lifetime of the current detector until its replacement by the upgraded LHCb. To ensure that this performance will continue until its end of use, monitoring software was developed and deployed for use by on-call experts to observe the evolution of the leakage currents within the detector.

With the current design of LHCb, it would become prohibitively long to the statistical uncertainties on the physics channels of interest to the collaboration and the current trigger scheme would become saturated in the high-luminosity LHC environment. At the end of Run II of the LHC in 2018, the LHCb collaboration will begin the implementation of an upgraded detector. The current VELO will be removed and replaced with a new design which will improve the physics reach of the collaboration beyond the current limitations.

To this end, studies of the electrical characterisation of high speed transmission lines have been performed on several prototypes to produce the best possible final detector. The signal transmission properties and impedances have been measured and used to define the designs of several components that will be inserted in the final detector. Further to these tests, the bit-error rates, jitter and the effect of bending of the high speed flex cables have been studied with all the properties found to be within the desired constraints. With this knowledge, the design of the VELO is moving to its final stages and should ensure the production of a detector capable of producing the quality of physics expected of the LHCb collaboration within the time frame set out by the upgrade team.

Acknowledgements

It would not be possible to complete a thesis without the help and assistance of many people, both professionally and personally. There are many people I would like to thank for the time and effort they put in to helping me throughout my Ph.D.

Firstly, I would like to give my sincerest thanks to my supervisors Lars Eklund and Paul Soler, not only for allowing me to pursue this thesis in the first place but for putting up with my numerous questions and stumbles along the way. This thesis is as much a show of their teachings as it is the work presented. I would also like to express a huge thank you to Michael Alexander for all the help he has given me. Without his assistance and the time he devoted to these analysis they would never be completed. He has always been there to talk to about any problems I had. I also want to thank Stephen Ogilvy. When I started my Ph.D. he was at the same stage that I am now but took the time to help a new student find his feet.

To my friends and colleagues in Italy, Stefano, Davide and Marta, who I worked closely with on the analysis of CP violation at 13 TeV. They have been fantastic and always willing to sit and discuss various aspects of these decays. The friendly competition between our groups has certainly lead to a very fruitful partnership that I hope we can continue.

The operation of a detector such as LHCb takes the combined effort of many. To Kazu, Kurt, Karol and Sasha I would like to thank them for all their help in making sure I didn't break LHCb though I'm sure I must have come close a few times when they weren't watching me. To Sneha and Manuel who helped me with the work for the VELO upgrade. Without Sneha's excellent designs and Manuel's exhaustive knowledge of electronics, the detector wouldn't be where it is. To Paula who is leading the VELO group to the completion of the upgrade project, I'm sure she is exhausted trying to organise all the different areas of the project while simultaneously conducting her own research. The project is progressing extremely well and I'm sure she will steer it to the production of a vertex detector that will be the envy of other particle physics experiments.

A Ph.D. student's time can't all be spent on research and I've made many great friends along the way who have kept me grounded. Sarah Karodia and I worked together on the $\mathrm{B} \rightarrow h^+ h'^-$ analyses and we would cheer each other up when we got frustrated about the state of our work. Without that, I don't know if I could have made it this far. I would like also thank all the other past Ph.D. students at the Glasgow group; Daniel, John and Iain. To all the later students; Murdo, George, Lauren and Dana, you're all doing amazing work. Keep going, you'll be finished soon. To all the friends I made at Glasgow and CERN, thank you for all the fun nights unwinding and joking around. For some of you, there's only a year left so my advice is to keep your head down, you're almost done.

My family have always been very important to me. I would like to extend my greatest thanks to my parents and to Alexis who stood by me through everything and kept my spirits up throughout my Ph.D. When I injured myself skiing in Geneva they dropped everything and came to look after me, I don't think they could ever know how much this meant and I am forever grateful for them.

Finally, to my grandfather, Jim, who was the first scientist I ever knew. He nurtured my love of science from a young age and I know I would never have made it to this point without him. He sadly wasn't able to see the end of my Ph.D. This thesis is dedicated to his memory.

Declaration of Authorship

The results presented in this thesis are the product of my own work. Appropriate references are provided when results of third parties are mentioned. The research presented here was not submitted for another degree in any other department or university.

Cameron T. Dean

Contents

I Modern Particle Physics and the LHC 1

Part I

Modern Particle Physics and the LHC

Chapter 1

Introduction

The decision on how to start a thesis can be a difficult thing. On the one hand you want to begin with a snappy, flashy sentence to attract the reader while on the other you have just spent many years of your life learning to let the work tell the story, to not embellish or sensationalise. A bad scientist will try to "wow" you without letting you learn something new. Even worse is the scientist who tries to demand that you accept what they have found. A good scientist is someone who will try to explain to you what they have observed. They will critically take the ideas of philosophy such as Popper's falsification [1] or Kuhn's paradigms [2] and use these as a base to understand how to observe the world. It is hoped that the aim of this thesis is not to wow the reader with empty words or force them to accept what lies within but to explain what was observed.

Particle physics has evolved immensely since the discovery of the electron in the late 19th century [3], from individual scientists using pen and paper with small pieces of equipment to massive international collaborations using algorithms to study huge quantities of data produced with the largest and most complex machines ever created. Advances in the field have built steadily over the years, the work of subsequent generations have been made possible by "standing on the shoulders of giants", a quote that feels surprisingly apt in modern particle physics. The dominance of large collaborations could be attributed to the November Revolution in the 70's [4, 5] with these collaborations now being the norm in the experimental field with the number of authors on papers reaching in the thousands.

The crowning achievement of particle physics is the Standard Model (SM) which describes the interaction of fundamental particles. Its predictive power has been immense, culminating in the discovery of the Higgs boson after 60 years [6, 7], but there have also been some problems that it has not been able to explain such as Dark Matter [8], neutrino masses [9] and, most importantly for this thesis, the baryon/photon ratio of the universe, η [10].

Studies of the isotropy of the Cosmic Microwave Background [11] have given much credibility to the theory that the universe began with the Big Bang [12] but one of the drawbacks of the theory is that the creation of matter and antimatter in equal quantities should have resulted in their complete annihilation, leaving nothing but radiation. To explain the apparent asymmetry requires a fundamental difference in the behaviour of particles and their antiparticle. In the 1960's, Sakharov proposed three rules that must be fulfilled to explain this asymmetry, known as the Sakharov conditions. They are [13]

1. Baryon Number Violation,
2. Charge (C) and Charge-Parity (CP) Violation,
3. For these above conditions to occur outside thermal equilibrium.

The third condition is satisfied as long as the time to reach thermal equilibrium, τ_{T}, is greater than the time for electroweak symmetry breaking to occur, τ_{H}, [14]. In reality this means that baryogenesis occured during the time of the Big Bang. Studies of this process requires labs that can reach very high energies such as that produced at the Large Hadron Collider (LHC) at CERN. An added benefit of labs instead of studying cosmic rays (which can be of higher energy) is that the energy is controlled which reduces the systematic errors of measurements made.

So far, CP Violation has been confirmed in three neutral meson systems; K^0 [15], B^0 [16, 17] and $\mathrm{B}^0_{\mathrm{s}}$ [18]. As measured by the Wilkinson Microwave Anisotropy Probe (WMAP) the baryon/photon ratio is

$$\eta = \frac{n_m - n_{\bar{\mathrm{m}}}}{n_\gamma} \approx \frac{n_m}{n_\gamma} = (6.079 \pm 0.090) \times 10^{-10} \tag{1.1}$$

where $n_{\mathrm{m}/\bar{\mathrm{m}}}$ is the [anti]matter density and n_γ is the photon density [19]. As matter/antimatter annihilation typically produces photons this means that to explain the asymmetry present in the observable universe, for approximately every 10^9 antiparticles produced, $10^9 + 1$ particles must have been produced during the Big

Bang. The CP violation predicted by the Standard Model is insufficient in meeting this requirement, with the baryon/photon ratio predicted to be 10^{-20} [20]. The disagreement between these numbers leads to the possibility of new mechanisms to explain the asymmetry collectively known as Physics Beyond the Standard Model (BSM Physics).

The Large Hadron Collider beauty (LHCb) experiment is a dedicated heavy flavour physics experiment which performs studies of particles containing beauty and charm quarks [21]. One of its primary goals is to make precise measurements of these decays, searching for signs of CP violation in an attempt to understand the matter-antimatter asymmetry in the observable universe.

1.1 Overview of the Research Undertaken

This thesis covers several topics related to both particle physics and detector development. Due to the collaborative nature of modern particle physics, the work presented here could not have been achieved without the assistance and hard work of many others. Their contributions are clearly stated where applicable as is the work that was produced as their own with the candidate only assisting in the conclusions they reached.

The thesis is structured as follows. Chapter 2 discusses the theoretical background knowledge required to analyse and understand the physics behind the measurements made within Part III of the thesis. The chapter was compiled from the relevant papers, textbooks and lecture series studied by the candidate. Appendices A and B act as supplementary information to this chapter and were compiled in the same manner as the chapter. Chapter 3 presents the design and performance of the LHC and the LHCb detector which were used to collect the data analysed. This chapter was also compiled from the relevant papers, textbooks and lecture series studied by the candidate.

Part II is devoted to detector studies performed for the LHCb collaboration. Chapter 4 is dedicated to an in depth discussion of the high voltage system of the current VELO at LHCb and the work undertaken by the candidate to ensure it operated with the required performance for the second data taking period of the LHC (known as Run II). This work was undertaken with the coordination of several others throughout the period of the candidate's studies. The software project used to monitor the VELO was led by Doctor Marco Gersabeck with assistance from the candidate in specified areas while the watchdog mentioned at the end of the chapter was implemented by Doctor Manuel Schiller.

Chapter 5 details the design and performance of the VELO upgrade project with a specific emphasis on the electrical system that will be used as this will be produced by the Glasgow LHCb group. The designs of the electronics were not made by the candidate, however a brief study on comparing the physics performance between the current and upgraded VELO for $\mathrm{B} \to h^+h'^-$ decays was performed by the candidate. The initial presentation of the VELO upgrade originally appeared in a conference proceedings [22] and underwent changes to fit within the structure of the thesis.

Part III is devoted to the analysis of $\mathrm{B} \to h^+h'^-$ decays at LHCb. Chapter 7 discusses the lifetime analysis of six different channels at a centre of mass energy ($\sqrt{s}$) of 7 and 8 TeV. This analysis was undertaken during the initial period of the candidate's study where they assisted another Ph.D. candidate, Sarah Karodia, of which this analysis formed the main theme of their thesis. As such, the final results were conducted by Sarah Karodia and are briefly quoted in this thesis only to give completeness to the chapter. The candidates specific contributions to this chapter were in the determination of the particle identification requirements and the initial studies of the invariant mass spectrum from Λ_b^0 decays. Sarah Karodia developed the multivariate analysis techniques to reduce the combinatorial background contaminations, the invariant mass modelling of the other decay modes, the final fit to extracted the effective lifetimes and the systematic studies. The decay time acceptance corrections were performed by Doctor Vladimir Gligorov. The fitting software used was developed by a team from LHCb while the specific fitter used in the analysis was developed by Doctor Michael Alexander.

Chapter 8 is devoted to the analysis of CP violation in $\mathrm{B}_\mathrm{s}^0 \to \mathrm{K}^+\mathrm{K}^-$ and $\mathrm{B}^0 \to \pi^+\pi^-$ decays at $\sqrt{s} = 13\,\mathrm{TeV}$ of which a significant portion was conducted by the candidate and comprises the main topic of this thesis. Several of the techniques used for the previous analysis of $\mathrm{B} \to h^+h'^-$ decays were performed for this analysis, with alterations added to improve upon the previous methods. The fitter used in the analysis was the same as the one used in the Run I analysis, however the probability density functions (PDFs) used to describe both the mass of the signal candidates and their lifetime distributions used to measured the CP observables were developed by the candidate. The PDF used to describe the lifetime distribution is given in Appendix E. The sample of $\mathrm{B_s^0} \to \mathrm{D_s^-}\pi^+$ decays used to calibrate the $\mathrm{B_s^0} \to \mathrm{K^+K^-}$ sample was obtained as a general LHCb sample and was not produced by the candidate.

The thesis concludes with Chapter 9 which summarises the results from all the previous chapters.

Chapter 2

Theoretical Motivation

2.1 The Standard Model

The Standard Model (SM) is undoubtedly one of the crowning achievements of the last hundred years, it has been able to predict the three generations of fermions and given a mechanism whereby particles gain mass to name but a few of it's numerous achievements. Within the SM there are twelve fundamental fermions, four fundamental spin-one bosons and one spin-zero boson. Each of the fermions has a corresponding antiparticle. The fundamental particles and their properties are listed in Table 2.1.

The fermions can be split into two families, the leptons and quarks, and three generations. The first family, the leptons, consist of the electron, muon and tau (of increasing generation) which are massive charged particles and the electron neutrino, muon neutrino and tau neutrino which have no charge and are predicted to be massless within the SM. However, the observation of neutrino oscillations reveals that this can't be the case [23, 24]. The charged leptons can feel the electromagnetic force while all leptons can feel the weak force.

Like the leptons, the quarks have three generations. The quarks can be split into up-like quarks which are the up, charm and top quarks with electric charge of $+2e/3$ and the down-like quarks which are the down, strange and bottom/beauty quarks with electric charge of $-1e/3$. Unlike the leptons, the quarks have colour charge which allows them to feel the strong force. Due to colour confinement [25],

Particle	Symbol	Type	Mass	Spin	Electric Charge
Up	u	Quark	$2.2^{+0.6}_{-0.4}$ MeV	1/2	2/3
Charm	c	Quark	1.27 ± 0.03 GeV	1/2	2/3
Top	t	Quark	173.21 ± 0.87 GeV[1]	1/2	2/3
Down	d	Quark	$4.7^{+0.5}_{-0.4}$ MeV	1/2	-1/3
Strange	s	Quark	96^{+8}_{-4} MeV	1/2	-1/3
Bottom	b	Quark	$4.18^{+0.04}_{-0.03}$, GeV[2]	1/2	-1/3
Electron	e	Lepton	511 keV	1/2	-1
Electron Neutrino	ν_e	Lepton	$<$ 2 eV	1/2	0
Muon	μ	Lepton	105.66 MeV	1/2	-1
Muon Neutrino	ν_μ	Lepton	$<$ 190 keV	1/2	0
Tau	τ	Lepton	1776.86 ± 0.12 MeV	1/2	-1
Tau Neutrino	ν_τ	Lepton	$<$ 18.2 MeV	1/2	0
Photon	γ	Gauge Boson	0	1	0
W-boson	$W^\pm$	Gauge Boson	80.385 ± 0.015 GeV	1	0
Z-boson	Z^0	Gauge Boson	91.188 ± 0.002 GeV	1	0
Gluon	g	Gauge Boson	0	1	0
Higgs	H	Scalar Boson	125.09 ± 0.24 GeV	0	0

Table 2.1: The particles that make up the Standard Model [36].

observed particles are required to be colour neutral which results in the commonly observed states of matter consisting of either quark-antiquark pairs (known as mesons with integer spin) or three quarks/antiquarks (known as baryons/antibaryons with half-integer spin). Larger quark contents are theoretically possible [26, 27] with recent observations of resonances believed to be from tetraquarks [28, 29] and pentaquarks [30]. Angular analyses can determine the total angular momentum and parity of the states, excluding them from being known resonances. While the resonance structure and large production cross-sections tend to favour tetraquark and pentaquark models over molecular models [31] there is still a debate as to what the exact structure of these states truly are [32–35].

At current energy scales, there are four fundamental forces; the electromagnetic, weak, strong and gravitational. The strength of the gravitational force is of the order 10^{-34} less powerful than the other three forces and thus is neglected for the purposes of the work carried out at LHCb [37]. The other three forces are mediated by spin-one gauge bosons (gravity may be mediated by a spin-2 boson known as the graviton, recent observations of gravitational waves by the LIGO collaboration neither proves or disproves this statement [38]). The electromagnetic force satisfies U(1) symmetry and is mediated by the familiar photon while the

---

[1] From direct measurements

[2] In the $\overline{\text{MS}}$ scheme

strong force satisfies SU(3) symmetry and is mediated by eight coloured gluons. The potential of the strong force acts differently to other known forces whereby it increases with increasing separation between the bodies, this can result in pair production and hadronisation if the energy is great enough.

The final force is the weak force and is mediated by three particles; the charged $W^{\pm}$ bosons [39, 40] and the neutral Z^0 boson [41, 42]. These bosons are massive which limits the weak forces range even though its fine structure constant is almost five times greater than that of the electromagnetic force ($\alpha_W = 1/30$ while $\alpha_{EM} = 1/137$ [43]). In the context of b-decays where the momentum transfer, q, is of the order of a few GeV, the propagator, which is proportional to $1/|q^2 - M_W^2|$, is dominated by the mass of the weak boson.

During the 1920's attempts were made to reconcile quantum mechanics with special relativity. The Schödinger equation is first order in time but second order in space which immediately reveals its incompatibility with special relativity. An initial attempt at rectifying this was the formulation of the Klein-Gordon equation which is second-order in both space and time but this was found to describe spin-zero particles, thus it had limited applicability. Paul Dirac postulated the existence of an equation of motion that was first order in both space and time that was consistent with special relativity. The solutions of this equation gave negative energy solutions which troubled physicists at the time as it implied the existence of complimentary particles. Dirac once tried to explain the discrepancy away by claiming that the complimentary particle to the negatively charged electron was the positively charged proton, which is impossible due to the mass difference of a factor of 2000 (it is unknown whether Dirac suggested this as a joke or not). The negative energy solutions are now known to describe antimatter, a full treatment of why this is the case can be found in Appendix A.

The Lagrangian form of the Dirac Equation using Feynman slash notation takes the form

$$\mathcal{L} = i\bar{\psi}\partial\!\!\!/\psi \; - \; m\bar{\psi}\psi \tag{2.1}$$

where $\partial\!\!\!/ = \gamma^{\mu}\partial_{\mu}$, γ^{μ} are the Dirac spinors and ∂_{μ} is the four derivative. The Dirac equation is naturally Lorentz invariant.

We can propose transformations to the quantum states, ψ, that reverse their charge or parity. The construction of the charge conjugate and parity operators are given in Appendix A but are given here for reference as

$$\mathrm{C}\psi = \mathrm{i}\gamma^2\psi^\star \qquad \mathrm{P} = \gamma^0$$

If we apply the charge conjugate or parity operators Equation 2.1 remains unchanged thus it was historically believed that charge, parity and hence their combination, CP, were conserved in the Standard Model. The Dirac equation is a good description of the electromagnetic force and CP is seen to be conserved there, it is also believed to be conserved in the strong force but models violating this are out of the scope of this thesis. It was discovered that CP is maximally violated in the weak sector. The next section discusses this in more detail.

We state the CP operator to be

$$\mathrm{CP}\psi = i\gamma^2\gamma^0\psi^\star \tag{2.2}$$

and define both a spin-half-up particle, u_1, and spin-half-down antiparticle, v_2, (the formal derivation of these states can be found in Appendix A) with energy, E, and momentum, $\mathbf{p} = (p_1, p_2, p_3)$

$$u_1 = N_u \begin{pmatrix} 1 \\ 0 \\ \frac{p_3}{E+m} \\ \frac{p_1+ip_2}{E+m} \end{pmatrix} \tag{2.3}$$

$$v_2 = N_v \begin{pmatrix} \frac{p_1 - ip_2}{E - m} \\ \frac{-p_3}{E - m} \\ 0 \\ 1 \end{pmatrix} \tag{2.4}$$

The application of the charge conjugate operator on the states changes a particle to its antiparticle (and vice-versa)

$$\mathrm{C}^\dagger u_1 \mathrm{C} = \eta_c v_2 \qquad \mathrm{C}^\dagger v_2 \mathrm{C} = \eta_c u_1 \tag{2.5}$$

where $\eta_c = (-1)^{L+S}$ and where L and S are the angular momentum and spin respectively. If we apply it to the four-current[3], A^μ, associated with a state we

---

[3] The four-dimensional equivalent to the electric current density

find that its sign reverses

$$\mathrm{C}^{\dagger}A^{\mu}\mathrm{C} = -A^{\mu}. \tag{2.6}$$

If we apply the Parity operator to the two states, we see that particles and antiparticles both have different transformations

$$\mathrm{P}^{\dagger}u_1(p_\mu)\mathrm{P} = \eta_P u_1(-p_\mu) \qquad \mathrm{P}^{\dagger}v_2(p_\mu)\mathrm{P} = -\eta_P v_2(-p_\mu) \tag{2.7}$$

where $\eta_P = (-1)^{L+1}$. Applying the CP operator to u_1 gives

$$\begin{aligned}
\mathrm{CP}u_1 &= i\begin{pmatrix} 0 & 0 & 0 & -i \\ 0 & 0 & i & 0 \\ 0 & -i & 0 & 0 \\ i & 0 & 0 & 0 \end{pmatrix}\begin{pmatrix} 1 & 0 & 0 & 0 \\ 0 & 1 & 0 & 0 \\ 0 & 0 & -1 & 0 \\ 0 & 0 & 0 & -1 \end{pmatrix}\begin{pmatrix} 1 \\ 0 \\ \frac{p_3}{E+m} \\ \frac{p_1+ip_2}{E+m} \end{pmatrix} e^{i(p^\mu x_\mu)} && (2.8) \\
\mathrm{CP}u_1 &= \begin{pmatrix} \frac{-(p_1 - ip_2)}{E - m} \\ \frac{p_3}{E - m} \\ 0 \\ 1 \end{pmatrix} e^{-i(p^\mu x_\mu)} && (2.9) \\
\mathrm{CP}u_1 &= -v_2 && (2.10)
\end{aligned}$$

It can be seen that the CP operator changes a spin-[up/down] particle to a spin-[down/up] antiparticle and vice-versa.

2.2 The Weak Sector

As previously mentioned, decays that involve the strong or electromagnetic force are CP conserving while those involving the weak force can be CP violating. In the introduction it was mentioned that CP violation is a requirement to explain baryogenesis, thus a more detailed discussion of CP violation and the weak force is required. All of the fundamental fermions of the Standard Model can experience the weak force but this thesis will exclusively concentrate on the weak force as it applies to quarks.

It was previously stated that the weak force is mediated by the massive $\mathrm{W}^{\pm}$ and Z^{0} bosons, the former of which are charged thus these decays can involve a change in charge (though the overall charge of the decay still obeys charge conservation) with down-like quarks, with a charge of $-1e/3$, transitioning to up-like quarks, with a charge of $+2e/3$, and vice-versa. These changes are not limited to transitions between quarks of one generation, but can occur between all three. Furthermore, weak interactions can also be found in transitions amongst lepton generations, involving charged leptons and neutrinos. In terms of the weak force, the flavour eigenstates exist as a linear superposition of their weak eigenstates with the combinations each having their own coupling strengths. The couplings are shown using the Cabibbo-Kobayashi-Maskawa matrix in Equation 2.12

$$\begin{pmatrix} d_{\text{mass}} \\ s_{\text{mass}} \\ b_{\text{mass}} \end{pmatrix} = V_{\text{CKM}} \begin{pmatrix} d_{\text{weak}} \\ s_{\text{weak}} \\ b_{\text{weak}} \end{pmatrix} \tag{2.11}$$

where V$_{\text{CKM}}$ is [44]

$$\begin{pmatrix} |V_{ud}| & |V_{us}| & |V_{ub}| \\ |V_{cd}| & |V_{cs}| & |V_{cb}| \\ |V_{td}| & |V_{ts}| & |V_{tb}| \end{pmatrix} = \begin{pmatrix} 0.974334\,^{+0.000064}_{-0.000068} & 0.22508\,^{+0.00030}_{-0.00028} & 0.003715\,^{+0.000060}_{-0.000060} \\ 0.22494\,^{+0.00029}_{-0.00028} & 0.973471\,^{+0.000067}_{-0.000067} & 0.04181\,^{+0.00028}_{-0.00060} \\ 0.008575\,^{+0.000076}_{-0.000098} & 0.04108\,^{+0.00030}_{-0.00057} & 0.999119\,^{+0.000024}_{-0.000012} \end{pmatrix} \tag{2.12}$$

Due to requirements of a quantum field that the sum of all probabilities is one, the CKM matrix is a unitary matrix [45] and within the Standard Model satisfies

$$\sum_j V_{ij} V^*_{jk} = \delta_{ik}, \tag{2.13}$$

where δ_{ik} is the Krönecker delta. Deviations from unity would thus imply the presence of channels outside of SM theory [46]. Equation 2.12 shows that couplings are typically contained within their own generation but it is possible to see transitions between the generations. A similar matrix exists within the neutrino sector, the PMNS matrix [47, 48], however it is out of the scope of this thesis and is not discussed further here. The CKM matrix can be parametrised in a number of ways. We previously stated that the flavour eigenstates exist as a superposition of the three weak states thus it is natural to try and construct the CKM matrix from a set of three rotation matrices which was achieved by Chau and Keung [49]

$$\begin{pmatrix} 1 & 0 & 0 \\ 0 & c_{23} & s_{23} \\ 0 & -s_{23} & c_{23} \end{pmatrix} \begin{pmatrix} c_{13} & 0 & s_{13}e^{-i\delta_{13}} \\ 0 & 1 & 0 \\ -s_{13}e^{i\delta_{13}} & 0 & c_{13} \end{pmatrix} \begin{pmatrix} c_{12} & s_{12} & 0 \\ -s_{12} & c_{12} & 0 \\ 0 & 0 & 1 \end{pmatrix}$$
$$= \begin{pmatrix} c_{12}c_{13} & s_{12}c_{13} & s_{13}e^{-i\delta_{13}} \\ -s_{12}c_{23} - c_{12}s_{23}s_{13}e^{i\delta_{13}} & c_{12}c_{23} - s_{12}s_{23}s_{13}e^{i\delta_{13}} & s_{23}c_{13} \\ s_{12}s_{23} - c_{12}c_{23}s_{13}e^{i\delta_{13}} & -c_{12}s_{23} - s_{12}c_{23}s_{13}e^{i\delta_{13}} & c_{23}c_{13} \end{pmatrix} \tag{2.14}$$

where $s_{ij} = \sin\theta_{ij}$ and $c_{ij} = \cos\theta_{ij}$. This formalism fully describes the CKM matrix and it can be seen that it contains a complex phase which, as long as its value is not 0 or $\pi/2$, can allow CP violation by introducing differences between some CKM elements and their complex conjugates (which describe the coupling of anti-quark states).

We can expand Equation 2.14 in terms of V_{us} which we call λ and set $c_{13} = c_{23} = 1$ then noting that $\cos\theta_{12} = \sqrt{1 - \sin^2\theta_{12}} \approx 1 - \lambda^2/2$. We can get V_{cb} in terms of λ as $V_{cb} = A\lambda^2$ where $A \approx 4/5$ and introducing a complex term of $s_{13}e^{i\delta} = A\lambda^3(\rho - i\eta)$ to account for the phase which allows us to arrive at the Wolfenstein parametrisation of the CKM matrix [50]

$$V_{\mathrm{CKM}} = \begin{pmatrix} 1-\lambda^2/2 & \lambda & A\lambda^3(\rho - i\eta) \\ -\lambda & 1-\lambda^2/2 & A\lambda^2 \\ A\lambda^3(1-\rho-i\eta) & -A\lambda^2 & 1 \end{pmatrix} + O(\lambda^4). \tag{2.15}$$

As λ is well known [44], we can deduce ρ and η by projecting in the complex plane, which leads to the Unitarity Triangles. The sides of the triangles are given by the modulus of different CKM element combinations, thus measuring different types of particle decays gives you access to different unitarity triangles due to the coupling strengths between different quarks in weak decays.

The unitarity triangles of interest to this thesis are given in Figure 2.1 and their relationship with the CKM elements being

$$\overline{\rho} = \rho\left(1 - \frac{\lambda^2}{2}\right) \tag{2.16}$$

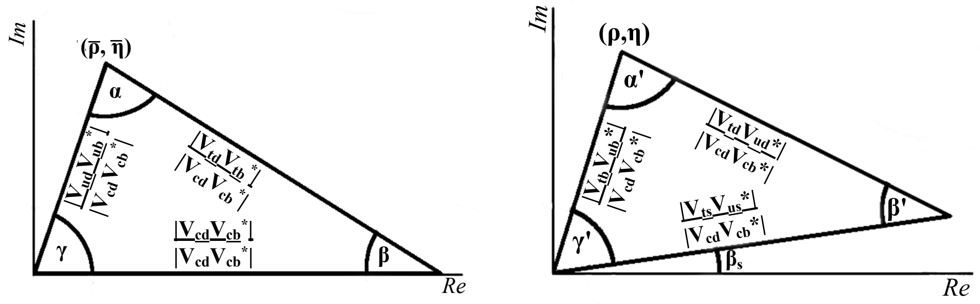

FIGURE 2.1: The unitarity triangles of interest to the research undertaken.

$$\bar{\eta} = \eta\left(1 - \frac{\lambda^2}{2}\right) \tag{2.17}$$

$$\bar{\rho} + i\bar{\eta} = \frac{|V_{ud}V_{ub}^*|}{|V_{cd}V_{cb}^*|}e^{i\gamma} \tag{2.18}$$

$$1 - \bar{\rho} + i\bar{\eta} = \frac{|V_{td}V_{tb}^*|}{|V_{cd}V_{cb}^*|}e^{i\beta} \tag{2.19}$$

$$\rho + i\eta = \frac{|V_{tb}V_{ub}^*|}{|V_{cd}V_{cb}^*|}e^{i(\gamma\prime+\beta_s)}. \tag{2.20}$$

Current bounds on the unitarity triangle constructed from B^0 decays from various experiments can be seen in Figure 2.2.

2.3 CP Violation in Neutral Mesons

It has been shown that CP transformations change particles to antiparticles and vice versa. It is also possible for particles to oscillate between their CP eigenstates under certain circumstances with a measurable effect. This is possible with neutral mesons where the flavour of the quark constituents is different (i.e kaons). This is achieved via weak currents by the exchange of a $W^{\pm}$ and an up[down]-type quark for a down[up]-type quark. These are known as box diagrams with the two diagrams responsible for B^0 and B_s^0 oscillations given in Figure 2.3. These oscillations were first observed in neutral kaons [51] and have subsequently been observed in B^0 [52], B_s^0 [53] and D^0 [54] mesons. If the decay rates of the particle and its CP conjugate state are seen to be different then this would be a clear indication of a CP asymmetry. The aim now is to construct a model where these

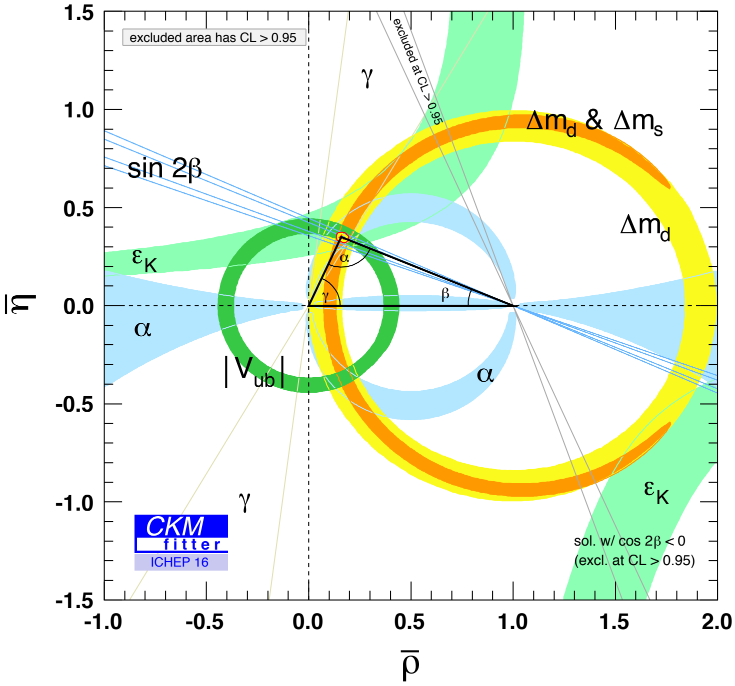

FIGURE 2.2: Current experimental bounds on the main unitarity triangle [44]

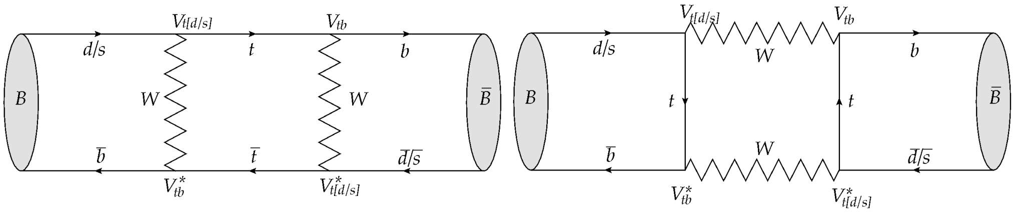

FIGURE 2.3: The two box diagrams for B^0 and B^0_s oscillations. The values of the CKM elements reveal that the dominant contribution comes from top quarks, although contributions from up and charm quarks are also possible.

rates show a fundamental difference that can be measured. A more complete description of this section is given in Appendix B.

If we take particles that have weak eigenstates, $|P^0\rangle$ and $|\bar{P}^0\rangle$, and massive eigenstates, $|P_1\rangle$ and $|P_2\rangle$, then we can create a linear superposition of states as

$$|P_1\rangle = p|P^0\rangle + q|\bar{P}^0\rangle \tag{2.21}$$

and

$$|P_2\rangle = p|P^0\rangle \ - \ q|\bar{P}^0\rangle \tag{2.22}$$

where $p = |p|e^{i\phi_p}$ is the weak amplitude of particle $|P^0\rangle$ and $q = |q|e^{i\phi_q}$ is the weak amplitude of antiparticle $|\bar{P}^0\rangle$ which satisfy $|p|^2 + |q|^2 = 1$. The time evolution of the weak states are thus

$$|P^0(t)\rangle = \frac{1}{2p}\left(|P_1(t)\rangle + |P_2(t)\rangle\right) \tag{2.23}$$

$$|\bar{P}^0(t)\rangle = \frac{1}{2q}\left(|P_1(t)\rangle - |P_2(t)\rangle\right) \tag{2.24}$$

For a two state system, the Hamiltonian, $\mathcal{H}$, can be expressed as

$$\mathcal{H} = \begin{pmatrix} m_{11} - \frac{i}{2}\Gamma_{11} & m_{12} - \frac{i}{2}\Gamma_{12} \\ m_{21} - \frac{i}{2}\Gamma_{21} & m_{22} - \frac{i}{2}\Gamma_{22} \end{pmatrix}. \tag{2.25}$$

We note that $m_{11} = m_{22}$, $m_{12} = m_{21}^*$, $\Gamma_{11} = \Gamma_{22}$ and $\Gamma_{12} = \Gamma_{21}^*$ due to conservation of the CPT symmetry, required for Lorentz invariance. If the off-diagonal elements are zero then the states are fully independent from each other but if these elements are non-zero then the two states exist in a superposition as seen by the box diagrams in Figure 2.3. We can use Equation 2.25 to derive the time evolution of the massive states which can in turn give us expressions for the particle states

$$|P^0(t)\rangle = \frac{1}{2p}\left(e^{-i(m_1 - \frac{i}{2}\Gamma_1)t}(p|P^0\rangle + q|\bar{P}^0\rangle) + e^{-i(m_2 - \frac{i}{2}\Gamma_2)t}(p|P^0\rangle - q|\bar{P}^0\rangle)\right) \tag{2.26}$$

$$|\bar{P}^0(t)\rangle = \frac{1}{2q}\left(e^{-i(m_1 - \frac{i}{2}\Gamma_1)t}(p|P^0\rangle + q|\bar{P}^0\rangle) - e^{-i(m_2 - \frac{i}{2}\Gamma_2)t}(p|P^0\rangle - q|\bar{P}^0\rangle)\right) \tag{2.27}$$

where

$$m_1 - \frac{i}{2}\Gamma_1 = m_{11} - \frac{i}{2}\Gamma_{11} + \frac{q}{p}(m_{12} - \frac{i}{2}\Gamma_{12}), \tag{2.28}$$

$$m_2 - \frac{i}{2}\Gamma_2 = m_{11} - \frac{i}{2}\Gamma_{11} - \frac{q}{p}(m_{12} - \frac{i}{2}\Gamma_{12}). \tag{2.29}$$

This can also be written as

$$|P^0(t)\rangle = f_+(t)|P^0\rangle + \frac{q}{p}f_-(t)|\bar{P}^0\rangle \tag{2.30}$$

$$|\bar{P}^0(t)\rangle = \frac{p}{q}f_-(t)|P^0\rangle + f_+(t)|\bar{P}^0\rangle \tag{2.31}$$

where

$$f_\pm(t) = \frac{1}{2}\left(e^{-i(m_1 - \frac{i}{2}\Gamma_1)t} \pm e^{-i(m_2 - \frac{i}{2}\Gamma_2)t}\right). \tag{2.32}$$

The decay rate is given as the probability of a particle to decay to a final state, in this case a state which is accessible from both $|P^0(t)\rangle$ and $|\bar{P}^0(t)\rangle$. Thus the decay rate, Γ_f, to a final state, $\langle f|$, given an initial state, $|P^0(t)\rangle$, is

$$\Gamma_f = |\langle f|\mathcal{H}|P^0(t)\rangle|^2 \tag{2.33}$$

with a corresponding decay rate, $\bar{\Gamma}_f$, from the state, $|\bar{P}^0(t)\rangle$

$$\bar{\Gamma}_f = |\langle f|\mathcal{H}|\bar{P}^0(t)\rangle|^2 \tag{2.34}$$

If we define the decay amplitudes, A_f and $\bar{A}_f$, as

$$A_f = \langle f|\mathcal{H}|P^0\rangle \tag{2.35}$$

$$\bar{A}_f = \langle f|\mathcal{H}|\bar{P}^0\rangle \tag{2.36}$$

then using the previous terms we can find expressions for the two decay rates

$$\Gamma_f = e^{-\Gamma t}\left[\cosh\left(\frac{\Delta\Gamma}{2}t\right) + \mathcal{A}_f^{\Delta\Gamma}\sinh\left(\frac{\Delta\Gamma}{2}t\right) + C_f\cos(\Delta m t) - S_f\sin(\Delta m t)\right] \tag{2.37}$$

$$\bar{\Gamma}_f = e^{-\Gamma t}\left[\cosh\left(\frac{\Delta\Gamma}{2}t\right) + \mathcal{A}_f^{\Delta\Gamma}\sinh\left(\frac{\Delta\Gamma}{2}t\right) - C_f\cos(\Delta m t) + S_f\sin(\Delta m t)\right] \tag{2.38}$$

where the mass difference between the eigenstates is $\Delta m = m_2 - m_1$ and the decay width difference is $\Delta\Gamma = \Gamma_2 - \Gamma_1$. If Δm and $\Delta\Gamma$ are non zero then this results in different masses and lifetimes for the two flavour eigenstates where Equation 2.21 describes the heavy mass eigenstate and Equation 2.22 describes the light mass eigenstate. The CP observables C_f, S_f and $\mathcal{A}_f^{\Delta\Gamma}$ are

$$C_f = \frac{1-|\lambda|^2}{(1+|\lambda|^2)} = \frac{1-\left(\left|\frac{q}{p}\right|\left|\frac{\bar{A}_f}{A_f}\right|\right)^2}{1+\left(\left|\frac{q}{p}\right|\left|\frac{\bar{A}_f}{A_f}\right|\right)^2}, \tag{2.39}$$

$$S_f = \frac{2\mathrm{Im}(\lambda)}{(1+|\lambda|^2)} = \frac{2\left|\frac{q}{p}\right|\left|\frac{\bar{A}_f}{A_f}\right|\sin(\phi_{\frac{q}{p}} + \phi_{\bar{A}_f} - \phi_{A_f})}{1+\left(\left|\frac{q}{p}\right|\left|\frac{\bar{A}_f}{A_f}\right|\right)^2}, \tag{2.40}$$

$$\mathcal{A}_f^{\Delta\Gamma} = \frac{-2\mathrm{Re}(\lambda)}{(1+|\lambda|^2)} = \frac{-2\left|\frac{q}{p}\right|\left|\frac{\bar{A}_f}{A_f}\right|\cos(\phi_{\frac{q}{p}} + \phi_{\bar{A}_f} - \phi_{A_f})}{1+\left(\left|\frac{q}{p}\right|\left|\frac{\bar{A}_f}{A_f}\right|\right)^2}, \tag{2.41}$$

and

$$\lambda = \frac{q}{p}\frac{\bar{A}_f}{A_f} = \left|\frac{q}{p}\right|\left|\frac{\bar{A}_f}{A_f}\right| e^{i(\phi_{\frac{q}{p}} + \phi_{\bar{A}_f} \; - \; \phi_{A_f})}. \tag{2.42}$$

The λ described above is the eigenvalue and not the same λ that was used in the Wolfenstein parametrisation. $\phi_{\frac{q}{p}}$ is defined as the phase difference between the weak amplitudes. We can define the asymmetry A^{CP}, between Γ_f and $\bar{\Gamma}_f$ as

$$A^{\mathrm{CP}} = \frac{\Gamma_f - \bar{\Gamma}_f}{\Gamma_f + \bar{\Gamma}_f} = \frac{S_f \sin(\Delta m t) \; - \; C_f \cos(\Delta m t)}{\cosh\left(\frac{\Delta\Gamma}{2}t\right) + \mathcal{A}_f^{\Delta\Gamma} \sinh\left(\frac{\Delta\Gamma}{2}t\right)} \tag{2.43}$$

It can be seen that the decay rates of the matter and antimatter states will be different if either C_f or S_f are non zero and CP is violated. It should also be noted that the measurable CP parameters have the property

$$|C_f|^2 + |S_f|^2 + |\mathcal{A}_f^{\Delta\Gamma}|^2 = 1 \tag{2.44}$$

There are three types of CP violation which can arise. One type is CP violation from the decay where a particle decays to a final state with a different CP quantum number and is described in C_f where there is no phase term. This is also commonly expressed as a difference in the decay amplitudes

$$\left|\frac{A_f}{\bar{A}_f}\right| \neq 1. \tag{2.45}$$

The second type is CP violation in the mixing of the two meson states when there is a difference in the mixing amplitudes between $|P^0\rangle$ and $|\bar{P}^0\rangle$.

$$\left|\frac{q}{p}\right| \neq 1. \tag{2.46}$$

The third type arises from quantum interference between the decay and mixing when $\mathrm{Im}(\lambda) \neq 0$ and is given by S_f and $\mathcal{A}_f^{\Delta\Gamma}$ which have an associated phase term.

Further to this, it is also possible to derive an expression for the time-integrated CP asymmetry, $A_{\mathrm{int}}^{\mathrm{CP}}$, using Equations 2.37 and 2.38. The integral of a generic exponential with a generic cosine function can be solved using integration by parts twice:

$$\int e^{ax}\cos(bx)dx = \frac{e^{ax}}{a}\cos(bx) + \int \frac{b}{a}e^{ax}\sin(bx)dx, \tag{2.47}$$

$$\int e^{ax}\cos(bx)dx = \frac{e^{ax}}{a}\cos(bx) + \frac{b}{a}\left[e^{ax}\sin(bx) \; - \; \int \frac{b}{a}e^{ax}\cos(bx)dx\right], \tag{2.48}$$

$$\int e^{ax}\cos(bx)dx = \frac{e^{ax}\left[a\cos(bx) + b\sin(bx)\right]}{a^2+b^2}. \tag{2.49}$$

As particle decays must be real and positive, Equation 2.49 can be solved between 0 and infinity to give

$$\int_0^\infty e^{ax}\cos(bx)dx = \frac{-a}{a^2+b^2}. \tag{2.50}$$

The same treatment can be applied to the other functions in Equations 2.37 and 2.38:

$$\begin{aligned}
\int_0^\infty e^{ax}\sin(bx)dx &= \left[\frac{e^{ax}\left[a\sin(bx) - b\cos(bx)\right]}{a^2+b^2}\right]_0^\infty = \frac{b}{a^2+b^2}, && (2.51)\\
\int_0^\infty e^{ax}\cosh(bx)dx &= \left[\frac{e^{ax}\left[a\cosh(bx) - b\sinh(bx)\right]}{a^2-b^2}\right]_0^\infty = \frac{-a}{a^2-b^2}, && (2.52)\\
\int_0^\infty e^{ax}\sinh(bx)dx &= \left[\frac{e^{ax}\left[a\sinh(bx) - b\cosh(bx)\right]}{a^2-b^2}\right]_0^\infty = \frac{b}{a^2-b^2}. && (2.53)
\end{aligned}$$

These solutions can then be combined appropriately to give an expression for $A_{\text{int}}^{\text{CP}}$:

$$\int_0^\infty \Gamma(t;q)dt = \left(\frac{\mathcal{A}_f^{\Delta\Gamma}\Delta\Gamma}{2} + \frac{1}{\tau}\right)\left(\frac{\tau^2}{1 - \left(\frac{\Delta\Gamma\tau}{2}\right)^2}\right) + q\left(\frac{C_f}{\tau} - S_f\Delta m\right)\left(\frac{\tau^2}{1-(\Delta m\tau)^2}\right) \tag{2.54}$$

where q takes the value of $+1$ for B mesons and -1 for $\bar{\text{B}}$ mesons. The time-integrated CP asymmetry is then given by

$$A_{\text{int}}^{\text{CP}} = \frac{\left(S_f\Delta m - \frac{C_f}{\tau}\right)\left(\frac{\tau^2}{1-(\Delta m\tau)^2}\right)}{\left(\frac{\mathcal{A}_f^{\Delta\Gamma}\Delta\Gamma}{2} + \frac{1}{\tau}\right)\left(\frac{\tau^2}{1-\left(\frac{\Delta\Gamma\tau}{2}\right)^2}\right)} \tag{2.55}$$

2.4 CP Violation in $B^0 \to \pi^+\pi^-$ and $B_s^0 \to K^+K^-$ Decays

A general picture has been painted for how matter and antimatter arise naturally within the Standard Model, how the weak sector can allow particles to change their flavour and how CP violation can arise in a multitude of ways within the decays of neutral mesons. It is now possible to combine these ideas to search for CP violation both within and beyond the Standard Model using two decay channels, $\text{B}^0 \to \pi^+\pi^-$ and $\text{B}_\text{s}^0 \to \text{K}^+\text{K}^-$.

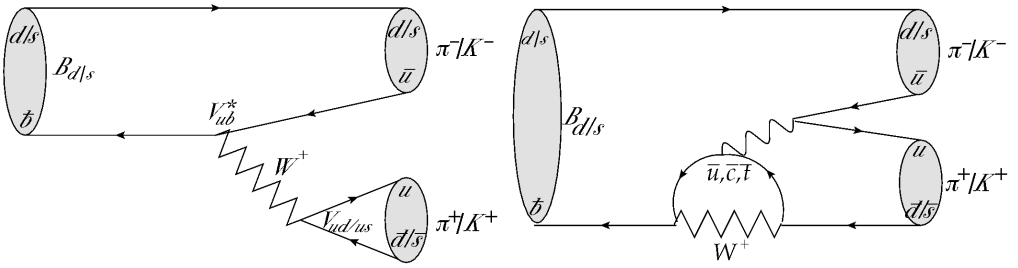

FIGURE 2.4: Examples of the main contributing Feynman diagrams for the decays under study. Left - A tree level decay. Right - A loop level decay.

The B^0 meson consists of a coupled anti-b quark and down quark with a mass of $5279.62 \pm 0.15\,\mathrm{MeV}$ while the B^0_s meson is similar but the down quark is swapped with a strange quark, arising in a mass of $5366.82 \pm 0.22\,\mathrm{MeV}$. Both these particles are able to oscillate due to a mass difference between their heavy and light eigenstates with the B^0 system having a difference of $\Delta m_\mathrm{d} = 0.5096 \pm 0.0036\,\mathrm{ps}^{-1}$ [55][4] and the B^0_s system having a difference of $\Delta m_\mathrm{s} = 17.757 \pm 0.0021\,\mathrm{ps}^{-1}$ [56][5]. The B^0 has no measurable decay width difference, $\Delta\Gamma$ which markedly simplifies the expressions for the decay rate and asymmetry resulting in decays from B^0 mesons while B^0_s mesons have $\Delta\Gamma = 0.088 \pm 0.007\,\mathrm{ps}^{-1}$ [36].

There are two main decay mechanisms for $\mathrm{B}^0 \to \pi^+\pi^-$ and $\mathrm{B}^0_\mathrm{s} \to \mathrm{K}^+\mathrm{K}^-$, tree level decays and loop level decays. The loop level decays contribute in equal amounts as the tree level decays due to the small value of $|V_\mathrm{ub}|$. Examples of a tree and loop level decay for the two channels are given in Figure 2.4. The large loop contribution is important as sources of new physics can appear in loop level decays which would be inaccessible via direct production methods. With the loop decays contributing with equal magnitude to the tree decays then $\mathrm{B}^0 \to \pi^+\pi^-$ and $\mathrm{B}^0_\mathrm{s} \to \mathrm{K}^+\mathrm{K}^-$ decays are good sites to search for new physics contributions.

It has previously been shown that the decay rates are obtained from the decay probabilities (Equations 2.33 and 2.34). These decay probabilities can be calculated from the matrix elements of the decay where the current transferred, j^μ_{ij}, in weak hadronic decays is given by

$$j^\mu_{ij} = -i\frac{g_W}{\sqrt{2}} V_{ij} \bar{q}_i \frac{1}{2}(1 - \gamma^5) q_j \tag{2.56}$$

---

[4] This is one full oscillation every 12.41 ± 0.05 (stat.) $\pm\, 0.02$ (syst.) ps

[5] This is one full oscillation every 353.6 ± 0.5 (stat.) $\pm\, 0.1$ (syst.) fs

where q_k is the quark flavour. There is also a corresponding complex conjugate current to account for decays involving oppositely charged W bosons. Thus, weak decays occur in proportion to the product of the CKM elements involved. Equations 2.23 and 2.24 show that the time evolution of particles and antiparticles are inversely proportional to their weak amplitudes and so the ratio of their states can be seen to be

$$\frac{\langle P_1(t)|P^0(t)\rangle}{\langle P_1(t)|\bar{P}^0(t)\rangle} \propto \frac{q}{p} \tag{2.57}$$

As we are looking at the time evolution of states and weak mixing amplitudes this tells us that we are describing the box diagrams shown in Figure 2.3 and we can find expressions for q/p

$$\frac{q}{p} \propto \frac{V_{t[d/s]}V_{tb}^*}{V_{tb}V_{t[d/s]}^*} \tag{2.58}$$

If we apply the same treatment to the decay amplitudes, A_f and $\bar{A}_f$, and take their ratio we see

$$\frac{\bar{A}_f}{A_f} \propto \frac{V_{ub}V_{u[d/s]}^*}{V_{u[d/s]}V_{ub}^*} \tag{2.59}$$

For B$\rightarrow h^+h'^-$ decays, this gives us an expression for λ

$$\lambda = \left(\frac{V_{t[d/s]}V_{tb}^*}{V_{tb}V_{t[d/s]}^*}\right)\left(\frac{V_{ub}V_{u[d/s]}^*}{V_{u[d/s]}V_{ub}^*}\right) \tag{2.60}$$

Under Standard Model conditions, the Unitarity triangles obey $\pi = \alpha + \beta + \gamma$ and so, using Equations 2.18 to 2.20, we can get a simple expression for λ in $\mathrm{B}^0 \rightarrow \pi^+\pi^-$ decays when, from the unitarity triangle and the Chau-Keung parametrisation of the CKM matrix, we note that $V_{ud}^* = V_{ud}$, $V_{tb}^* = V_{tb}$, $V_{ub}^* = |V_{\mathrm{ub}}|e^{i\gamma}$ and $V_{td}^* = |V_{\mathrm{td}}|e^{i\beta}$

$$\lambda_{\pi^+\pi^-} \propto e^{-2i(\beta+\gamma)} \tag{2.61}$$

Thus measurements of β or γ in the channel $\mathrm{B}^0 \rightarrow \pi^+\pi^-$ can be compared to the Standard Model prediction where deviations from predictions would imply that the Unitarity triangle is not closed. Interpretations of non-closed Unitarity triangles could be physics beyond the Standard Model.

A similar treatment can be applied to $\mathrm{B_s^0} \rightarrow \mathrm{K^+K^-}$ decays where $V_{us}^* = V_{us}$, $V_{ub}^* = V_{ub}e^{i\gamma} = V_{ub}e^{i\gamma\prime+\beta_\mathrm{s}}$ and $V_{ts}^* = V_{ts}e^{i\beta_\mathrm{s}}$ to obtain

$$\lambda_{\mathrm{K^+K^-}} \propto e^{2i(\beta_\mathrm{s}\ -\ \gamma)} \tag{2.62}$$

Thus $\mathrm{B_s^0} \to \mathrm{K^+K^-}$ decays are also sensitive to the angle β_s. To find a more robust method for extracting the CP observables we note that the decay amplitudes are given from the matrix elements defined in Equations 2.35 and 2.36 and will be given by the sum of the individual contributions scaled by their CKM elements [57]

$$A_{\pi^+\pi^-} = V_{ud}V_{ub}^*(A_\mathrm{tree}^u + A_\mathrm{loop}^u) + V_{cd}V_{cb}^*A_\mathrm{loop}^c + V_{td}V_{tb}^*A_\mathrm{loop}^t \tag{2.63}$$

where the superscript on the amplitude defines the decay involving a transition with up, charm or top quarks while the subscript defines if the decay was from tree or loop processes. Using the Wolfenstein parametrisation of the CKM matrix and the expression given in Equations 2.16 to 2.19 it is possible to derive an expression for the decay amplitude in terms of γ

$$A_{\pi^+\pi^-} = |V_{ud}V_{ub}^*|e^{i\gamma}\frac{|V_{cb}V_{cd}^*|}{|V_{cb}V_{cd}^*|}(A_\mathrm{tree}^u + A_\mathrm{loop}^u) + V_{cd}V_{cb}^*A_\mathrm{loop}^c + |V_{cb}V_{cd}^*|\left(\frac{|V_{td}V_{tb}^*|}{|V_{cb}V_{cd}^*|}e^{i\beta}\right)A_\mathrm{loop}^t. \tag{2.64}$$

This can be vastly simplified by noting that

$$|V_{cb}V_{cd}^*| = |V_{cd}V_{cb}^*| = V_{cb}V_{cd}^* = A\lambda^3 \tag{2.65}$$

and

$$\frac{|V_{td}V_{tb}^*|}{|V_{cb}V_{cd}^*|}e^{i\beta} = 1 - \bar{\rho} + i\bar{\eta} = 1 - \frac{|V_{ub}V_{ud}^*|}{|V_{cb}V_{cd}^*|}e^{-i\gamma}. \tag{2.66}$$

Using these relations and substituting the Wolfenstein parameters for the real elements of the CKM matrix, Equation 2.64 becomes

$$A_{\pi^+\pi^-} = e^{i\gamma}\left(1 - \frac{\lambda^2}{2}\right)A\lambda^3\frac{1}{\lambda}\frac{|V_\mathrm{ub}|}{|V_\mathrm{cb}|}(A_\mathrm{tree}^u + A_\mathrm{loop}^u - A_{loop}^t) - A\lambda^3(A_\mathrm{loop}^c + A_\mathrm{loop}^t), \tag{2.67}$$

where λ is defined from the Wolfenstein parametrisation of the CKM matrix. If we define the parameters R_b, $\mathcal{C}$ and $de^{i\theta}$ as

$$R_b = \frac{1}{\lambda}\frac{|V_\mathrm{ub}|}{|V_\mathrm{cb}|}, \tag{2.68}$$

$$\mathcal{C} = A\lambda^3 R_b(A_\mathrm{tree}^u + A_\mathrm{loop}^u - A_{loop}^t,) \tag{2.69}$$

$$de^{i\theta} = \frac{1}{R_b(1-\lambda^2/2)}\left(\frac{A_\mathrm{loop}^c + A_\mathrm{loop}^t}{A_\mathrm{tree}^u + A_\mathrm{loop}^u - A_{loop}^t}\right) \tag{2.70}$$

then Equation 2.67 becomes

$$A_{\pi^+\pi^-} = e^{i\gamma}\left(1 - \frac{\lambda^2}{2}\right)\mathcal{C}(1 - de^{i(\theta - \gamma)}). \tag{2.71}$$

The decay amplitude of the CP conjugate decay can be constructed by the same method where the amplitude is given by

$$\bar{A}_{\pi^+\pi^-} = V^*_{ud}V_{ub}(A^u_{\text{tree}} + A^u_{\text{loop}}) + V^*_{cd}V_{cb}A^c_{\text{loop}} + V^*_{td}V_{tb}A^t_{\text{loop}}. \tag{2.72}$$

It should be noted that the CKM elements are the complex conjugates of Equation 2.63. The final decay amplitude is

$$\bar{A}_{\pi^+\pi^-} = e^{-i\gamma}\left(1 - \frac{\lambda^2}{2}\right)\mathcal{C}(1 - de^{i(\theta+\gamma)}) \tag{2.73}$$

From inspecting Equations 2.71 and 2.73 it can be seen that γ differs by a factor of -1 but θ is unchanged. The decay rates are given by the probability density of the decay amplitudes as stated in Equations 2.33 and 2.34 so we obtain expressions for the decay rates of $\mathrm{B}^0 \to \pi^+\pi^-$ and $\bar{\mathrm{B}}^0 \to \pi^+\pi^-$

$$|A_{\pi^+\pi^-}|^2 = \left(1 - \frac{\lambda^2}{2}\right)^2 \mathcal{C}^2(1 - 2d\cos\theta\cos\gamma - 2d\sin\theta\sin\gamma + d^2) \tag{2.74}$$

$$|\bar{A}_{\pi^+\pi^-}|^2 = \left(1 - \frac{\lambda^2}{2}\right)^2 \mathcal{C}^2(1 - 2d\cos\theta\cos\gamma + 2d\sin\theta\sin\gamma + d^2). \tag{2.75}$$

At this stage it is also useful to define $|A^*_{\pi^+\pi^-}||\bar{A}_{\pi^+\pi^-}|$

$$|A^*_{\pi^+\pi^-}||\bar{A}_{\pi^+\pi^-}| = e^{-i2\gamma}\left(1 - \frac{\lambda^2}{2}\right)^2 \mathcal{C}^2(1 - de^{-i(\theta - \gamma)})(1 - de^{i(\theta+\gamma)}) \tag{2.76}$$

$$|A^*_{\pi^+\pi^-}||\bar{A}_{\pi^+\pi^-}| = \left(1 - \frac{\lambda^2}{2}\right)^2 \mathcal{C}^2(e^{-i2\gamma} - 2d\cos\theta e^{-i\gamma} + d^2). \tag{2.77}$$

It has previously been stated that C_f describes direct CP violation. If we inspect Equation 2.39 in the case that $|q/p| = 1$ (i.e. there is no CP violation in the mixing) then

$$C_{\pi\pi} = \frac{1 - \frac{|\bar{A}_{\pi^+\pi^-}|^2}{|A_{\pi^+\pi^-}|^2}}{1 + \frac{|\bar{A}_{\pi^+\pi^-}|^2}{|A_{\pi^+\pi^-}|^2}} = \frac{|A_{\pi^+\pi^-}|^2 - |\bar{A}_{\pi^+\pi^-}|^2}{|A_{\pi^+\pi^-}|^2 + |\bar{A}_{\pi^+\pi^-}|^2} \tag{2.78}$$

which is the definition of direct CP violation. If we use Equations 2.74 and 2.75 then the expression for direct CP violation in $\mathrm{B}^0 \rightarrow \pi^+\pi^-$ decays is

$$C_{\pi\pi} = \; - \; \frac{2d \sin\theta \sin\gamma}{1 \; - \; 2d\cos\theta\cos\gamma + d^2} \tag{2.79}$$

We can apply this to the expression for CP violation in the interference between the mixing and the decay, $S_{\pi\pi}$, to find

$$S_{\pi\pi} = \frac{2\mathrm{Im}\left(\frac{|\bar{\mathrm{A}}_{\pi^+\pi^-}|^2}{|\mathrm{A}_{\pi^+\pi^-}|^2}\mathrm{e}^{\mathrm{i}2\beta}\right)}{1 + \frac{|\bar{A}_{\pi^+\pi^-}|^2}{|A_{\pi^+\pi^-}|^2}} = \frac{2\mathrm{Im}(|\mathrm{A}^*_{\pi^+\pi^-}||\bar{\mathrm{A}}_{\pi^+\pi^-}|\mathrm{e}^{\mathrm{i}2\beta})}{|A_{\pi^+\pi^-}|^2 + |\bar{A}_{\pi^+\pi^-}|^2} \tag{2.80}$$

This results in a final expression for $S_{\pi\pi}$

$$S_{\pi\pi} = -\frac{\sin(2\beta + 2\gamma) - 2d\cos\theta\sin(2\beta+\gamma) + d^2\sin 2\beta}{1 \; - \; 2d\cos\theta\cos\gamma + d^2} \tag{2.81}$$

The above treatment can be applied to $\mathrm{B}^0_\mathrm{s} \rightarrow \mathrm{K}^+\mathrm{K}^-$ decays where the decay amplitudes are given by

$$A_{\mathrm{K}^+\mathrm{K}^-} = V_{us}V^*_{ub}(A^u_{\mathrm{tree}} + A^u_{\mathrm{loop}}) + V_{cs}V^*_{cb}A^c_{\mathrm{loop}} + V_{ts}V^*_{tb}A^t_{\mathrm{loop}} \tag{2.82}$$

$$\bar{A}_{\mathrm{K}^+\mathrm{K}^-} = V^*_{us}V_{ub}(A^u_{\mathrm{tree}} + A^u_{\mathrm{loop}}) + V^*_{cs}V_{cb}A^c_{\mathrm{loop}} + V^*_{ts}V_{tb}A^t_{\mathrm{loop}} \tag{2.83}$$

which results in the simplified expressions in terms of γ

$$A_{\mathrm{K}^+\mathrm{K}^-} = e^{i\gamma}\lambda\mathcal{C}'(1 \; - \; \left(\frac{1 \; - \; \lambda^2}{\lambda^2}\right) d' e^{i(\theta' \; - \; \gamma)}) \tag{2.84}$$

$$\bar{A}_{\mathrm{K}^+\mathrm{K}^-} = e^{-i\gamma}\lambda\mathcal{C}'(1 \; - \; \left(\frac{1 \; - \; \lambda^2}{\lambda^2}\right) d' e^{i(\theta'+\gamma)}) \tag{2.85}$$

where the primes are used to differentiate the expressions from those for $\mathrm{B}^0 \rightarrow \pi^+\pi^-$ decays. The expressions for C_{KK} and S_{KK} are obtained using the same methodology as for $C_{\pi\pi}$ $S_{\pi\pi}$. As the decay width difference is non-zero for B^0_s mesons, there is an additional CP observable, $\mathcal{A}^{\Delta\Gamma}_{\mathrm{KK}}$, which is defined in Equation 2.41. It can be seen that this is the real analogue to S_f and can be treated the same in obtaining an expression. The expressions for C_{KK}, S_{KK} and $\mathcal{A}^{\Delta\Gamma}_{\mathrm{KK}}$ are thus

$$C_{\mathrm{KK}} = \; - \; \frac{2\tilde{d}' \sin\theta' \sin\gamma}{1 \; - \; 2\tilde{d}'\cos\theta'\cos\gamma + d^2} \tag{2.86}$$

$$S_{\mathrm{KK}} = -\frac{\sin(2\beta_{\mathrm{s}} + 2\gamma) - 2\tilde{d}' \cos\theta \sin(2\beta_{\mathrm{s}} + \gamma) + \tilde{d}'^{2} \sin 2\beta_{\mathrm{s}}}{1 \; - \; 2\tilde{d}' \cos\theta \cos\gamma + \tilde{d}'^{2}} \tag{2.87}$$

$$\mathcal{A}^{\Delta\Gamma}_{\mathrm{KK}} = -\frac{\cos(2\beta_{\mathrm{s}} + 2\gamma) - 2\tilde{d}' \cos\theta \cos(2\beta_{\mathrm{s}} + \gamma) + \tilde{d}'^{2} \cos 2\beta_{\mathrm{s}}}{1 \; - \; 2\tilde{d}' \cos\theta \cos\gamma + \tilde{d}'^{2}} \tag{2.88}$$

where $\tilde{d}'$ is a shorthand for

$$\tilde{d}' = \frac{1 - \lambda^{2}}{\lambda^{2}} d'. \tag{2.89}$$

As $\mathrm{B}^0 \to \pi^+\pi^-$ and $\mathrm{B}^0_{\mathrm{s}} \to \mathrm{K}^+\mathrm{K}^-$ are related by U-spin symmetry which is a SU(2) subgroup of SU(3) where all d quarks are exchanged by s quarks [58, 59] then $d' = d$ and $\theta' = \theta$. Invoking U-spin symmetry is advantageous to this analysis strategy as both the photon and Z^0 boson involved in the loop level decays couple equally to d and s quarks and, if the U-spin symmetry-breaking corrections are fully factorizable, the decays should be insensitive to the final-state QCD interactions when using the ratios of different amplitudes and observables[6]. This links the expressions for the CP observables for the two decays and shows that their values are dependent on γ, $\beta_{\mathrm{s}}, \beta, d$, and θ. This motivates the simultaneous measurement of both of these channels.

The experimental status of the parameters of interest prior to the measurements presented in this thesis are given in Table 2.2. If the values of d and θ were well known it would be possible to constrain γ and β_{s} (though it should be pointed out that the opposite is true, knowing $C_{\pi\pi}$ and $S_{\pi\pi}$ well can be used to constrain these angles when studying d and θ). In practice however, the values of d and θ are not well known and a simultaneous fit for the angles must be performed using Equations 2.79, 2.81, 2.86 and 2.87 [60]. The LHCb collaboration previously used the measured values of $C_{\pi\pi}$, $S_{\pi\pi}$, C_{KK} and S_{KK} from $1\,\mathrm{fb}^{-1}$ of data collected at $7\,\mathrm{TeV}$ to place constraints on γ and β_{s} as a function of the allowed U-spin symmetry breaking, κ, between $\kappa = 0$ and $\kappa = 1$. The results of the constraints are given in Figure 2.5. The constraints on γ and β_{s} can be improved by invoking isospin symmetry and using $\mathrm{B}^0 \to \pi^0\pi^0$ and $\mathrm{B}^+ \to \pi^+\pi^0$ decays; however, the reconstruction of neutral pions is challenging at LHCb and is out of the scope of this thesis.

As an example of a 1D projection produced with measurements of the CP observables to constrain γ and β, Equation 2.79 was used to plot $C_{\pi\pi}$ as a function of

---

[6] Some non-factorizable corrections must be accounted for to properly constrain any CKM parameters.

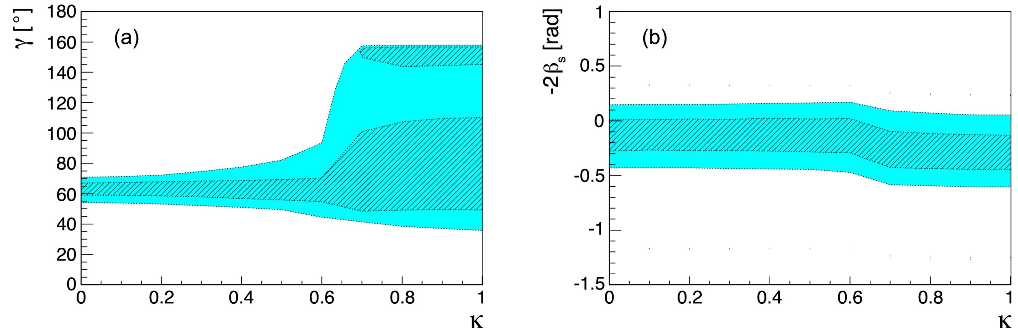

FIGURE 2.5: Constraints on unitarity triangle angles as a function of U-spin symmetry breaking using the measured values of $C_{\pi\pi}$, $S_{\pi\pi}$, C_{KK} and S_{KK} from $1\,\mathrm{fb}^{-1}$ of data collected at 7 TeV with the LHCb detector. The 1σ confidence limits are shown in the blue hatched area and the 2σ confidence limits are shown in the blue solid area. (a) Constraints on γ. (b) Constraints on β_{s} [60].

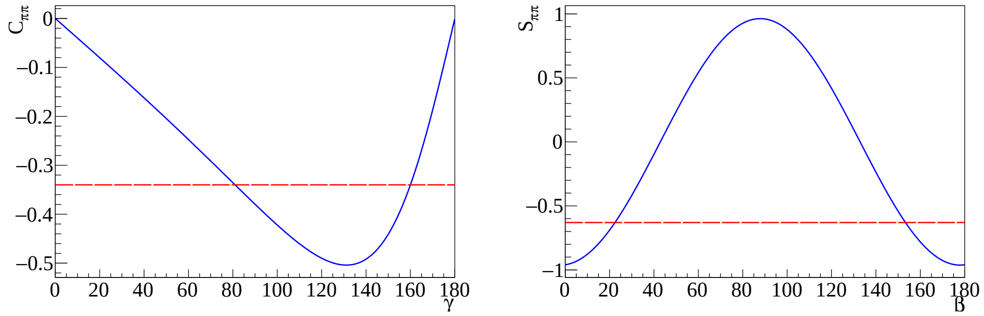

FIGURE 2.6: An example of how the CP observables can be used to constrain the Unitarity Triangle angles γ and β. Left - The value of $C_{\pi\pi}$ as a function of γ (in blue) assuming $d = 0.46$ and $\theta = 210°$. The red line shows the measurement of $C_{\pi\pi}$ prior to this thesis. Right - The value of $S_{\pi\pi}$ as a function of β (in blue) assuming $d = 0.46$, $\theta = 210°$ and $\gamma = 65.4°$. The red line shows the measurement of $S_{\pi\pi}$ prior to this thesis. It should be emphasised that the previous measurement of the observables did not give values for γ or β, that the values of these angles match current knowledge is just a coincidence due to the values of d and θ used to produce the plots. In practice, d and θ are not well known and a simultaneous fit using all the CP observables must be performed to extract γ or β_{s}.

γ assuming $d = 0.46$ and $\theta = 210°$ while Equation 2.81 was used to plot $S_{\pi\pi}$ as a function of β assuming $d = 0.46$, $\theta = 210°$ and $\gamma = 65.4°$ which can be seen in Figure 2.6.

Using the current knowledge of the observables [36, 61] and Equation 2.55 it is possible to show that the value of $A_{\mathrm{int}}^{\mathrm{CP}}$ for $\mathrm{B}^0 \to \pi^+\pi^-$ decays is approximately -0.09 while for $\mathrm{B}_{\mathrm{s}}^0 \to \mathrm{K}^+\mathrm{K}^-$ decays it is approximately 6.8×10^{-3}.

Parameter	Value
$S_{\pi\pi}$	-0.63 ± 0.05 (stat.) $\pm\, 0.01$(syst.) [61]
$C_{\pi\pi}$	-0.34 ± 0.06 (stat.) $\pm\, 0.01$(syst.) [61]
S_{KK}	0.18 ± 0.06 (stat.) $\pm\, 0.02$(syst.) [61]
C_{KK}	0.20 ± 0.06 (stat.) $\pm\, 0.02$(syst.) [61]
$\mathcal{A}^{\Delta\Gamma}_{\mathrm{KK}}$	-0.79 ± 0.07 (stat.) $\pm\, 0.10$(syst.) [61]
α	$(92.0^{+1.3}_{-1.1})^{\circ}$ [44]
β	$(22.60^{+0.36}_{-0.35})^{\circ}$ [44]
γ	$(65.40^{+0.97}_{-1.16})^{\circ}$ [44]
β_S	$(0.0185^{+0.00032}_{-0.00032})^{\circ}$ [44]

Table 2.2: The current experimental status of the observables within this thesis.

Chapter 3

The LHC and The LHCb Experiment

The European Organisation for Nuclear Research (Organisation Européenne pour la Recherche Nucléaire, CERN) is the largest particle physics laboratory in the world. It was created in 1954 as a response to the actions undertaken by physicists during World War II to allow them to pursue science without militaristic outcomes [62]. The main complex sits at the edge of Geneva, Switzerland and straddles the Franco-Suisse border where over 12,500 scientists and engineers conduct their research. CERN has made many life-changing inventions, such as the creation of the World Wide Web [63] and touch-screen technologies [64], and discoveries, such as weak neutral currents [65], the $W^{\pm}$ bosons [39, 40], the Z^0 boson [41, 42] and the Higgs boson [6, 7].

3.1 The CERN Accelerator Complex

To achieve a world leading standard, a series of particle accelerators have been created at CERN with increasing energy to allow physicists to push the boundaries of physics. The accelerators have been combined together to create an ever-increasing accelerator complex, as can be seen in Figure 3.1. The various accelerators are used for other experiments and for testing components before their use in detectors. Examples of other experiments running at CERN are the isotope mass separator on-line facility (ISOLDE) studying nuclear effects and, having been running since 1957, is the oldest experiment at CERN [66]. Another experiment is the neutron time-of-flight (n-ToF) experiment which uses neutron beams to study the effects of treating radioactive materials and contains the only vertical target line in the world [67]. There is also the Cosmics Leaving Outdoor Droplets (CLOUD) experiment which uses a special cloud chamber to create environments with different atmospheric conditions before bombarding it with particles to simulate cosmic ray effects on clouds to improve models of climate change over many years [68]. Finally, the Antiproton Cell Experiment (ACE) which looked at the effectiveness of antiprotons in cancer treatment [69].

The complex is also capable of producing heavy ions and nuclei for acceleration such as lead. This is achieved using electron cyclotron resonance (ECR) of a heated lead source (to obtain a gas). ECR uses microwaves with the same frequency as the orbital frequency of the valence electrons to increase their energy above ionisation. This results in a collection of lead ions (Pb^{22+}, Pb^{29+} and Pb^{32+}) of which Pb^{29+} is selected using a spectrometer before being accelerated by a radio-frequency quadrupole (RFQ) and a linear accelerator, Linac3, to 4.2 MeV/nucleon. The ions then pass through a 0.3 µm thick carbon foil to strip the ions to Pb^{54+} before entering the 78 m in circumference Low Energy Ion Ring (LEIR) to be accelerated to 72 MeV/nucleon. There are two final accelerators before lead particles arrive at the LHC; the 628 m Proton Synchrotron (PS) where they are accelerated to 5.9 GeV/nucleon and the 7 km Super Proton Synchrotron (SPS) where they are accelerated to 177 GeV/nucleon. There is a final 0.8 mm aluminium foil to strip the Pb^{54+} ions to lead nuclei. The LHC is capable of accelerating these nuclei to 5.5 TeV/nucleon (or 1.1 PeV/nuclei) and conducts proton-lead or lead-lead collisions for short periods typically at the end of each year.

3.1.1 From Hydrogen to the LHC

The data presented in this thesis was obtained from proton-proton collisions at the LHC. The protons are obtained using a different path from the lead nuclei. The starting point is a bottle of hydrogen gas from which a small volume is injected into a duoplasmatron. This device is capable of heating the gas and applying a high electric field to strip off the electrons, leaving behind a proton source. These protons are then accelerated using an RFQ and Linac2 to 50 MeV before they are injected into the Proton Synchrotron Booster (PSB).

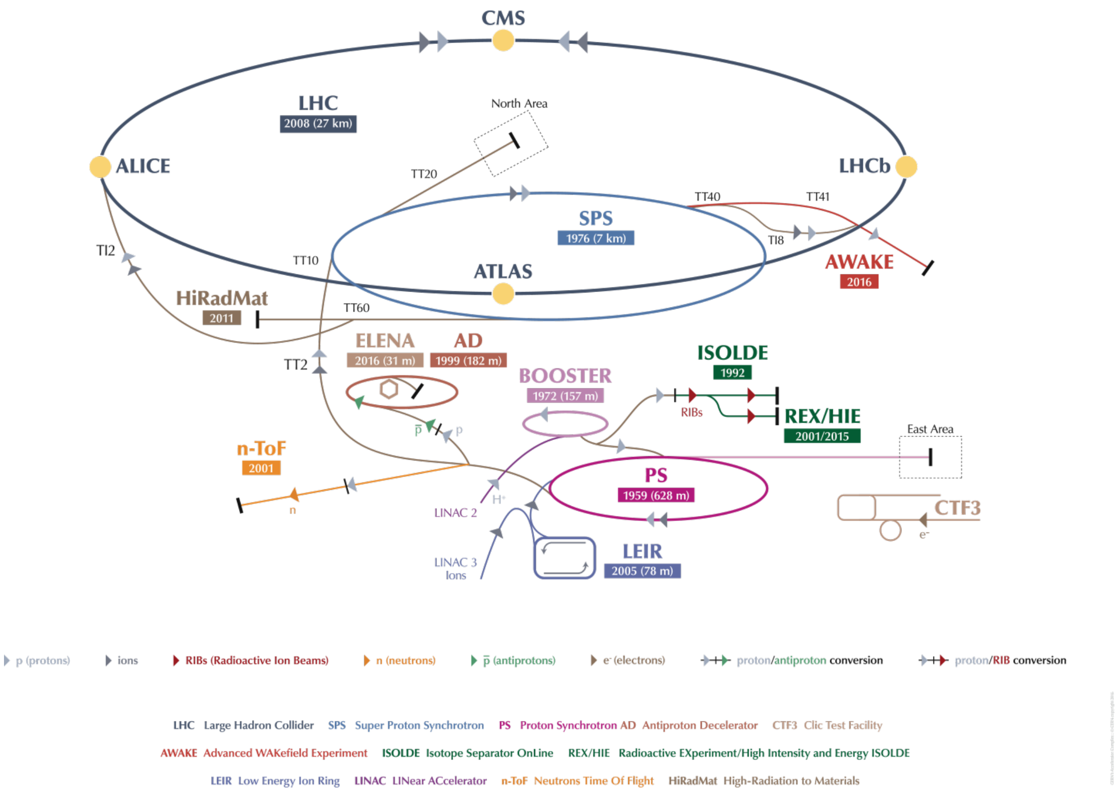

FIGURE 3.1: The CERN accelerator complex as of 2018. The protons that collide in the LHC start their journey at Linac2. Taken from [70].

The PSB is a 157 m circle consisting of four accelerators stacked on top of each other which are merged into one beam at the end of the acceleration process where the beam has an energy of 1.4 GeV. The beam then enters the PS which accelerates the protons to 26 GeV before entering the SPS to be accelerated to 450 GeV, the injection energy of the LHC.

During Long Shutdown II (LS2), Linac2 will be replaced by Linac4 which will use hydrogen ions (H^-) to increase the beam intensity for use with the high-luminosity LHC [71].

3.1.2 The Large Hadron Collider

At 27 km, the Large Hadron Collider (LHC) [72] is the largest, brightest and most powerful particle accelerator in the world and was initially turned on in 2009. The LHC was designed to accelerate 450 GeV protons from the SPS to 7 TeV to achieve 14 TeV centre-of-mass ($\sqrt{s}$) collisions although the energy has been limited to $\sqrt{s}$ = 13 TeV until at least Run III to ensure both the safety of the machine and to achieve consistency in the data sets collected in each year of Run II. These collisions occur in four caverns which supply a total of seven experiments; ALICE [73], ATLAS [74], CMS [75], LHCb [76], LHCf [77], TOTEM [78] and MoEDAL [79]. The LHC is housed inside the old Large Electron Positron (LEP) collider tunnel and is at an incline of 1.4% with an average depth of 100 m with the shallowest point at 45 m (ALICE) and the deepest at 170 m (LHCb is at a depth of 100 m).

The LHC consists of two counter-circulating beams which are injected at two points in the ring; one close to ALICE and the other close to LHCb's muon stations. The LHC is divided into octants known as points; point 1 hosts the ATLAS and LHCf experiments, point 2 hosts ALICE, point 4 hosts the accelerator cavities, point 5 hosts CMS and TOTEM, point 6 hosts the beam dump and point 8 hosts LHCb and MoEDAL. Each LHC beam can contain up to 2808 bunches of protons which in turn each contain 1.15×10^{11} protons, this results in a total stored energy of 723 MJ (the equivalent of 51 Bugatti Veyrons travelling at their full speed of 268 mph). The bunches are separated in time by 25 ns (7.5 m) with a 3 µs "abort gap" where there are no protons. This gap is to allow a "kicker" magnet to fully charge and eject the beam at the end of a fill or if it is deemed to be unsafe [72]. This ejection occurs at point 6 where the beam is fired into two graphite cylinders which weigh almost 27 tonnes to absorb all the energy. The abort gap is important as if the beam sees a magnetic field that is not at full strength then the protons will be bent at a smaller angle and can then damage the walls of the machine. The protons complete over 11,000 circuits every second.

The LHC is equipped with a host of devices to accelerate, focus, bend and tune the beam to produce a beam well suited to the physics goals of the experiments. The accelerator cavities, located at point 4, consist of 16 copper "bells" which accelerate the two beams (8 bells per beam) at a radio frequency, hence they are known as RF cavities.

The beams are kept on their circular path using 1232 15 m long dipole magnets whose energy increases in synchronicity with the beam energy. The LHC uses superconducting niobium-titanium magnets and fibres with an operational field strength of 0.54 T at 450 GeV and 8.33 T at 7 TeV. The magnets are kept at 1.9K using liquid helium in the superfluid phase (liquid nitrogen is used to bring the magnets from room temperature down to 80K). This field strength is obtained using a current of 11,800 A [80]. This current would be impractical to obtain using

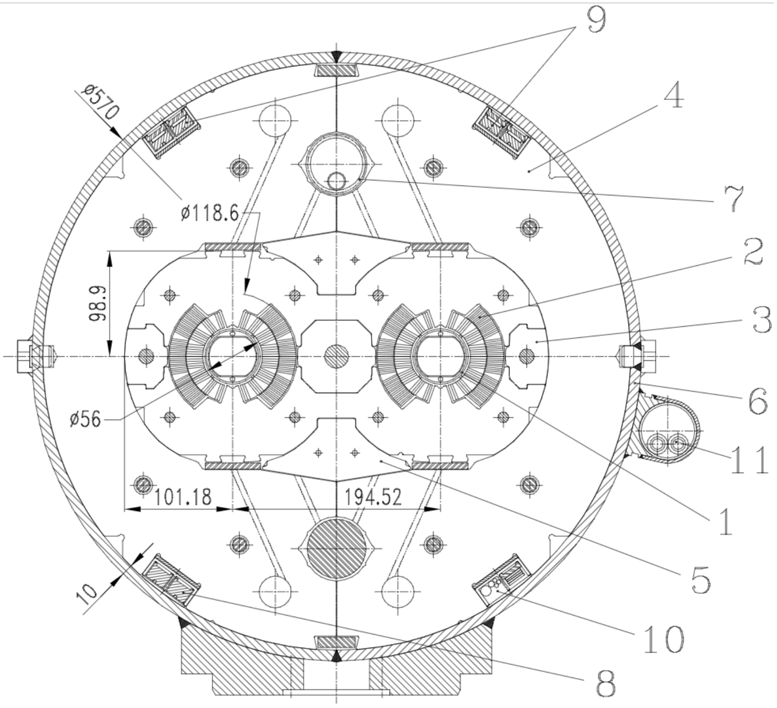

FIGURE 3.2: Cross section of the dipole used in the LHC. 1 - The beam screen. 2 - NbTi superconducting magnet. 3 - Steel collars. 4 and 5 - Iron yoke. 6 - Dipole wall. 7 - Heat exchange pipe. 8, 9 and 11 - Bus bars. 10 - Magnet wiring. Taken from [80].

copper as the diameter required would be approximately 12 cm thus superconducting niobium-titanium filaments inside copper (for mechanical strength) are used to supply the required current. The structure of the dipole can be seen in Figure 3.2.

Energy emitted by the beam as it circulates can strike the walls of the accelerator, releasing secondary electrons which can affect the quality of the beam by creating electron clouds within the vacuum. These electrons must be periodically removed using a technique known as scrubbing where a satellite proton bunch with lower intensity is used to condition the beam screen and removes slow electrons [81]. The LESS experiment is developing a laser etching technique to bring the ratio of secondary electrons to wall collisions to less than one, effectively halting the issue of electron clouds and is planned to be deployed during LS2 [82].

To protect the magnets from the secondary electrons, the LHC is equipped with beam screens made from steel doped with nitrogen and manganese. The screens have an internal copper lining with etches on two sides to try and absorb gases by allowing low velocity gas to pass from where the beam is to outside the screen. The screen is also cooled to 5-20K.

To focus the beam, the LHC has 392 10 m long quadrupole magnets with similar design characteristics to the dipoles. From optics calculations it can be shown that if a beam is focused in one plane, it will be defocused in its perpendicular plane thus the quadrupoles are placed in alternating magnetic field configurations to focus the beam faster than it can defocus. This allows the full-width at half maximum (FWHM) of the beam to be less than 16 µm [72].

When the beam leaves the dipoles it is shifted off centre. To put the beam back into the central position before the next magnet, higher order corrector magnets are used with special field configurations (sextupoles, octupoles and decapoles). The position of the beam is also determined using two methods; wire scanners and beam screens. Wire scanners involve passing a wire through the beam at a known velocity and measuring the integrated flux of particles displaced by the wire then converting time to position. The beam screen involves passing the beam through a material at 45° to the beam. This material emits photons which impact on a CCD and a picture of the beam is produced.

The magnets are connected by a bellow structure to absorb the shrinkage of the accelerator as it is cooled from 300K to 1.9K, since the LHC shrinks by around 80 m over this temperature difference. Collimators are placed on either side of each experimental cavern which are metal blocks separated by a small distance. As the beams pass by these devices, particles on the edges of the Gaussian beam profile are “shaved” off to avoid damage to the particle detectors.

3.2 The Large Hadron Collider beauty Experiment

µ The LHCb detector [21, 83], seen in Figure 3.3, is a forward arm spectrometer covering a pseudorapidity of $2 < \eta < 5$. It has been designed to maximise the yield of b-quarks which are produced predominantly in the forward-backwards region due to their boost, as can be seen in Figure 3.4. The $b\bar{b}$ cross section has been measured by LHCb to be 72.0 ± 0.3 (stat.) $\pm\, 6.8$ (syst.) µb at 7 TeV and 144 ± 1 (stat.) $\pm\, 21$ (syst.) µb at 13 TeV [84] in the acceptance of LHCb which has been scaled to a prediction of ∼295 µb and ∼560 µb for the full solid angle at 7 TeV and 13 TeV respectively. The detector covers a solid angle of 2% while containing 26% of b-quarks produced at 13 TeV. LHCb consists of a large set of sub-detectors

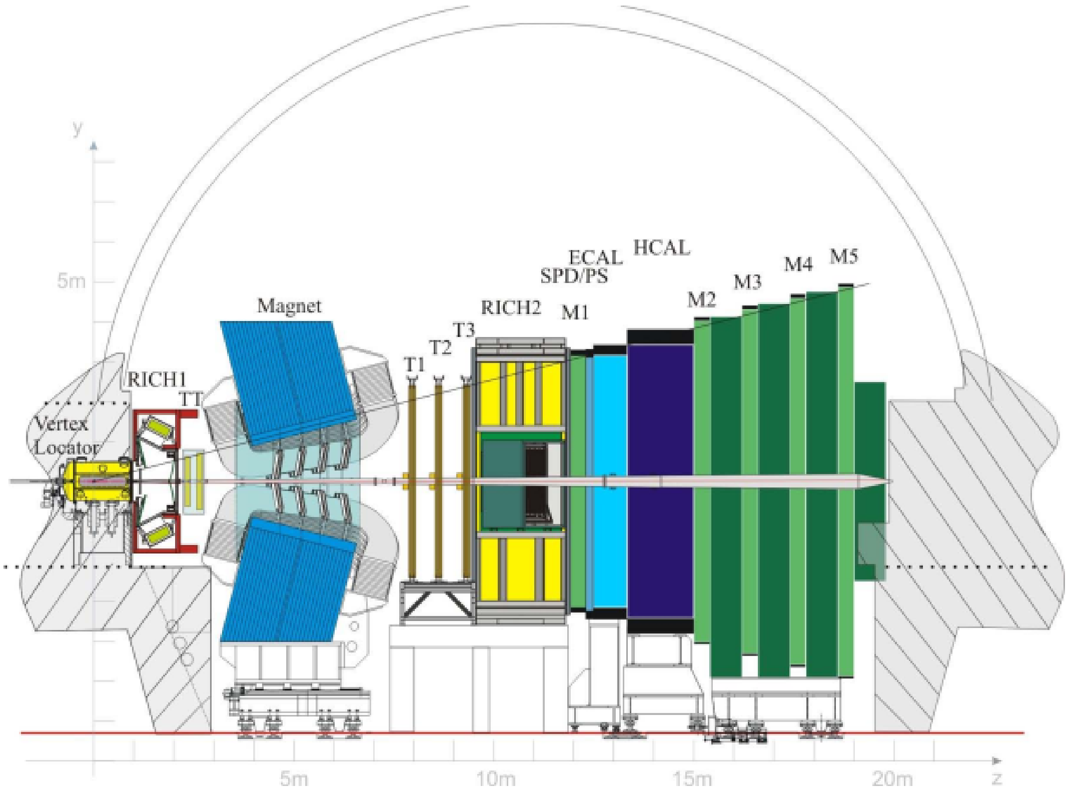

FIGURE 3.3: The LHCb detector at CERN. The interaction point is at the left most point of the Figure in the VELO. Another important feature are the two RICH detectors before and after the 4 Tm dipole magnet [85].

working together to select and measure a variety of parameters of the collisions produced in the LHC. The bunch crossing rate is currently 40 MHz so LHCb uses a set of sophisticated hardware and software triggers to reduce this rate to a manageable level, the first trigger reduces the rate to approximately 1 MHz [76].

At the LHC there are two major processes by which quarks are produced; gluon-gluon fusion and quark-antiquark annihilation, these processes are illustrated in Figure 3.5. These production mechanisms produce $b\bar{b}$ and $c\bar{c}$ pairs which is more important to LHCb's physics program than, for example, top-quark decay, as pair -production allows for flavour tagging which is required to understand CP violation. LHCb has taken data in seven years and at three different energies; $0.04\,\text{fb}^{-1}$ at $\sqrt{s}$ = 7 TeV in 2010, $1.11\,\text{fb}^{-1}$ at $\sqrt{s}$ = 7 TeV in 2011, $2.08\,\text{fb}^{-1}$ at $\sqrt{s}$ = 8 TeV in 2012, $0.33\,\text{fb}^{-1}$ at $\sqrt{s}$ = 13 TeV in 2015, $1.67\,\text{fb}^{-1}$ at $\sqrt{s}$ = 13 TeV in 2016, $1.71\,\text{fb}^{-1}$ at $\sqrt{s}$ = 13 TeV in 2017 and $1.85\,\text{fb}^{-1}$ at $\sqrt{s}$ = 13 TeV in 2018 at the time of submission. The data collected from 2010 to 2012 is known at Run I while the data collected from 2015 to 2018 is known as Run II. The data collected as a function of the time of year can be seen in Figure 3.6.

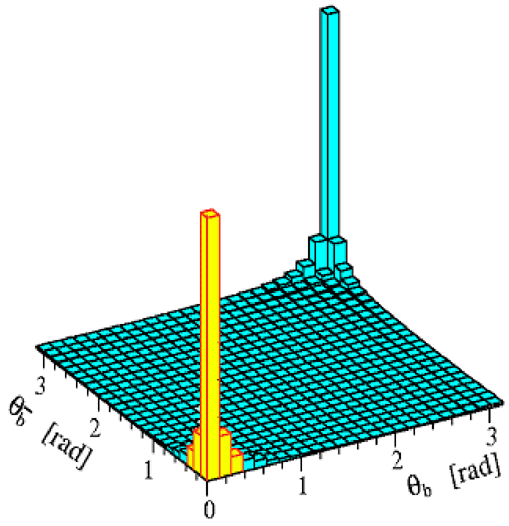

FIGURE 3.4: Angular distribution of b-quarks. The distribution of quarks can be seen to be predominantly in the forward-backwards direction [86].

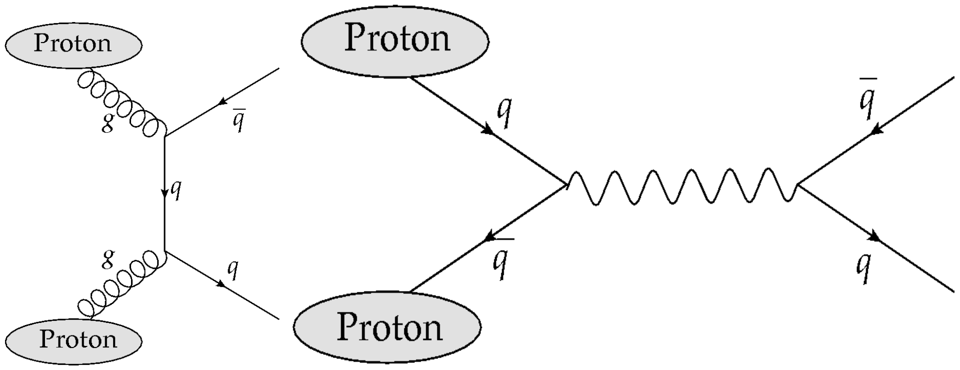

FIGURE 3.5: The main particle production methods at the LHC. Left - Gluon-Gluon fusion whereby the coloured quarks within the proton emit two gluons which hadronise to create observable particles. Right - Quark-antiquark annihilation whereby two quarks are produced by protons which then annihilate to emit a vector boson which in turn decays into observable particles.

Due to the complexity of reconstructing b-candidates and the requirement of a clean environment to be able to tag the flavour of B-mesons at production, LHCb operates in a lower luminosity environment than ATLAS or CMS. A process, known as *luminosity levelling* [87], is performed to displace the two beams at the proton-proton collision point to reduce the number of visible interactions, μ, by reducing the overlap of the beams. For Run I and II, the average value of μ was 1.1 visible interactions per crossing.

The VELO is the first detector traversed by the particles and is used to reconstruct the primary vertices and decay vertices of particles before they enter the first Ring Imaging Cherenkov detector (RICH1) for particle identification (PID). LHCb also

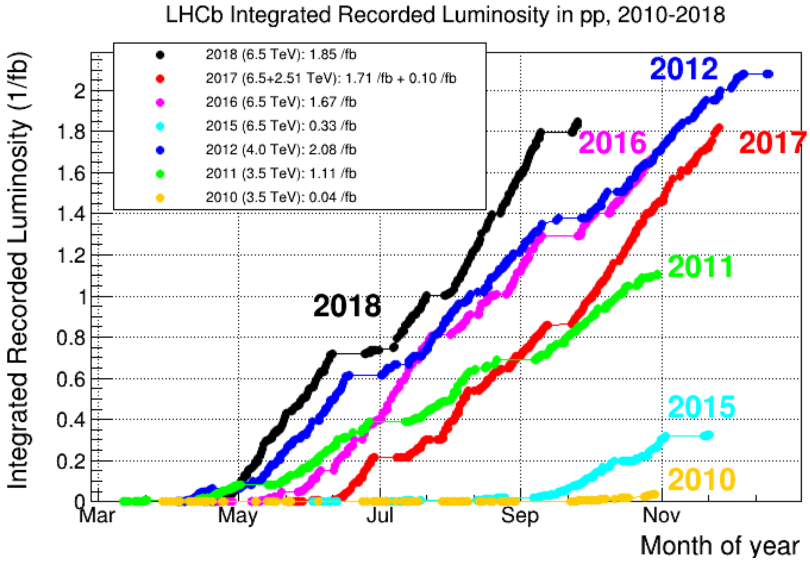

FIGURE 3.6: The recorded luminosity at LHCb as a function of the time of year [88].

uses a 4 Tm dipole magnet with trackers before and after to measure the charge and momentum of particles. Beyond the second RICH detector (RICH2) are the electromagnetic calorimeter (ECAL) used for electron and photon identification and energy measurements (taking advantage of the Bremsstrahlung and electron shower effects), the hadron calorimeter and the muon system. The muon system and calorimeters are of particular importance as they are also used as hardware triggers.

3.2.1 Tracking System

The need for good tracking is of the utmost importance for the physics programme of LHCb. B-mesons have a lifetime of about 1.5 ps which results in them travelling 1 cm before decaying on average. It is also important that the detector has good momentum and lifetime resolution; the B^0_s will oscillate to a $\bar{\mathrm{B}}^0_\mathrm{s}$ and back about 3 times every picosecond [56]. The tracking system consists of a vertex locator (VELO), a set of silicon strip detectors (the Tracker Turicensis, TT, and the inner tracker, IT, collectively known as the silicon tracker, ST) and a set of set of straw tube trackers (the outer tracker, OT). The IT and ST are grouped into three tracking stations, T1 - T3.

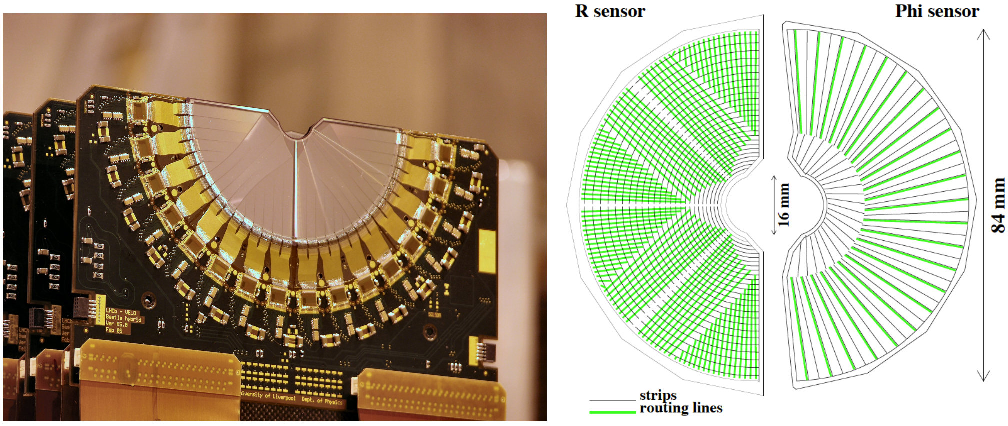

FIGURE 3.7: Left - Three completed VELO modules [92]. An r sensor can be seen at the front as well as the Beetle readout chips. Right - Silicon strip and routing line comparison for r and ϕ sensors [90].

3.2.1.1 The VELO

The VELO [89, 90] is a silicon strip detector located around the proton-proton interaction point and is built in two distinct halves. The first active part of the VELO takes data from 8 mm from the LHC beam but as this distance is designated to be unsafe outside stable beams the two halves are capable of retracting to 29 mm from the beam. The detector has two different sensor designs; one consists of strips extending from the inner to outer regions and is used for angular measurements (ϕ sensors) while the other has semicircular strips extending concentrically outwards for radial measurements (r sensors). The sensors are mounted onto modules with one r and ϕ sensor each. There are a total of 42 VELO modules (and 4 pile-up modules with only r sensors [91][1]) which gives 21 VELO stations. Each station is separated along the z-axis by 3 cm. The layout of the VELO can be seen in Figure 3.8. The sensors are 300 µm thick with a strip pitch varying from 38 µm to 102 µm to give a total of 172,000 readout strips.

The data from each sensor is collected by a 128 channel custom ASIC, the Beetle [93, 94], that has been tested up to 45 MRad with the peaking time increasing by less than 20% of the bunch separation of 25 ns after irradiation. The Beetle has a 160 event buffer [95] with a 16 event de-randomising buffer to account for the Poisson distribution of the L0 trigger [96] and a pulse length of approximately 100 ns, depending on the accumulated radiation, as can be seen in Figure 3.9. If the Beetle receives an L0 trigger decision the data is then sent to the off-detector

---

[1] The pile-up sensors consist of r-sensors and are used to veto events with too many visible interactions. These type of events would have a very large combinatorial background component.

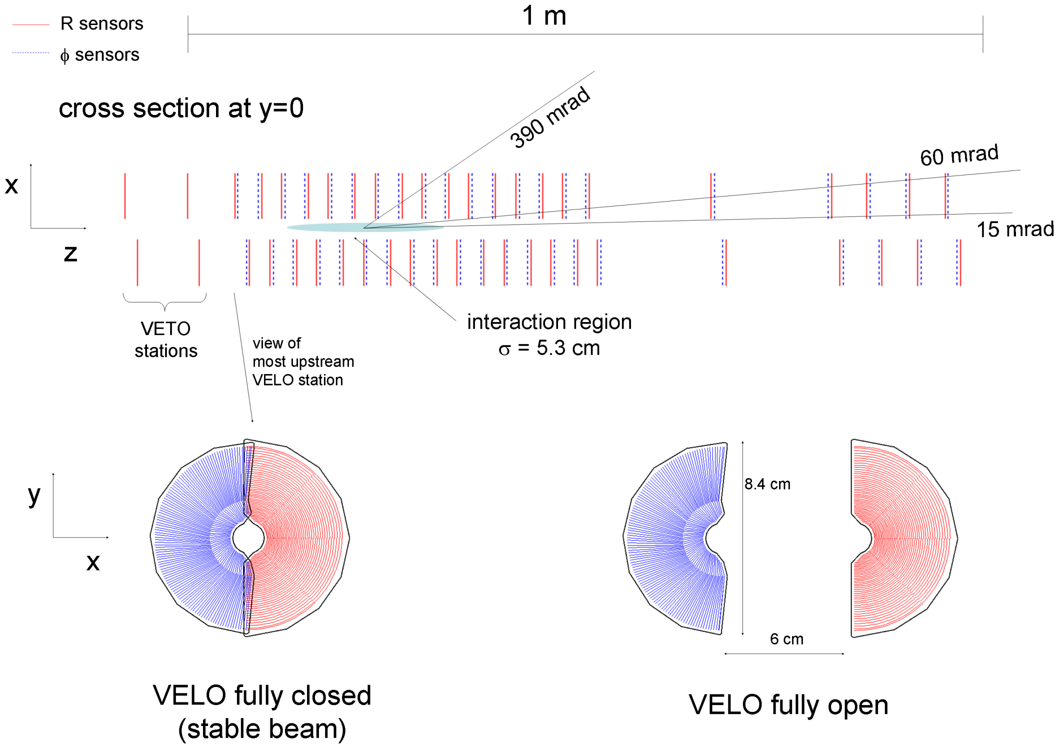

FIGURE 3.8: Layout of the VELO detector. The red solid lines represent r sensors while the blue dashed lines represent the ϕ sensors. The gaps in the layout exist in the true VELO and are there to reduce the material budget without significantly impacting the detector resolution. Taken from [76].

readout boards, the Tell1s [97], of which there are one per sensor. The data sent by the VELO is analogue so the Tell1s are equipped with an analogue receiver (A-Rx) which differs from the optical receivers (O-Rx) required by other subdetectors. The A-Rx's contain 16 10-bit ADC channels, there are 4 A-Rx's per Tell1 sampling at the bunch-crossing rate of 40 MHz to give a peak bit-rate of 25.6 Gbit/s per sensor.

The VELO is kept in a vacuum with a pressure of 10^{-7} mbar, which is two orders of magnitude higher than that of the LHC. To isolate the two vacuums, the VELO is equipped with a 300 µm thick aluminium RF foil which is the largest contributor to the material budget as seen in Figure 3.10. The RF foil is corrugated to allow the two halves to overlap, giving full coverage. To remove heat from the front-end electronics, avoid thermal runaway and detrimental annealing of the sensors (and hence to increase the lifetime of the detector), the sensors are kept at an operational temperature of approximately −8°C using CO_2 and at −30°C when the detector is not is use [76, 90].

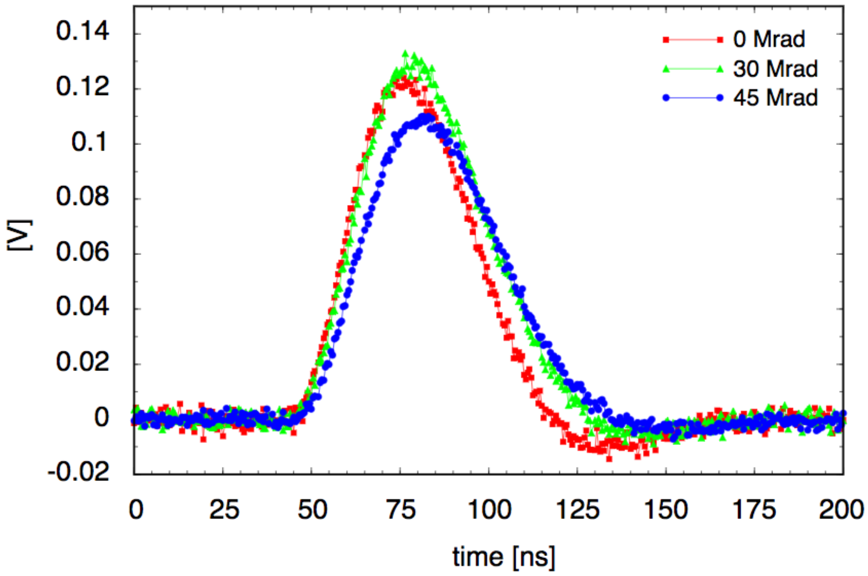

FIGURE 3.9: Event pulse shape from a Beetle chip for different radiation doses from a X-ray source. Red - no irradiation, green - 30 MRad, blue - 45 MRad. Taken from [93].

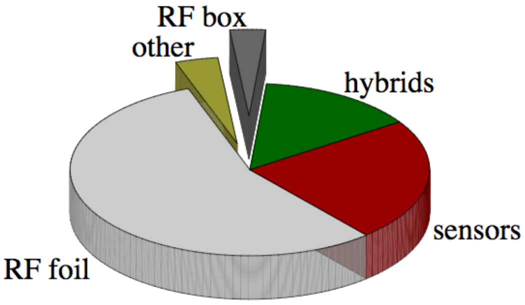

total material: 20.0%X_0

FIGURE 3.10: The total material budget of the current VELO, broken down by component. The largest contribution comes from the RF foil. Taken from [98].

The impact parameter is given as the shortest distance between a line and a point. For example, this could be the shortest distance between a daughter particle's track and the primary vertex in the $x - y$ plane (which is the common usage in particle physics). To accurately measure lifetimes, identify secondary vertices and tag particle flavours at production, the impact parameter resolution (σ_{IP}) must be kept to a minimum. This can be achieved in two main ways; by reducing the distance to the first active part of the detector (r_1) and reducing the material budget (x/X_0) as much as feasibly possible [98]. The form of the IP resolution as

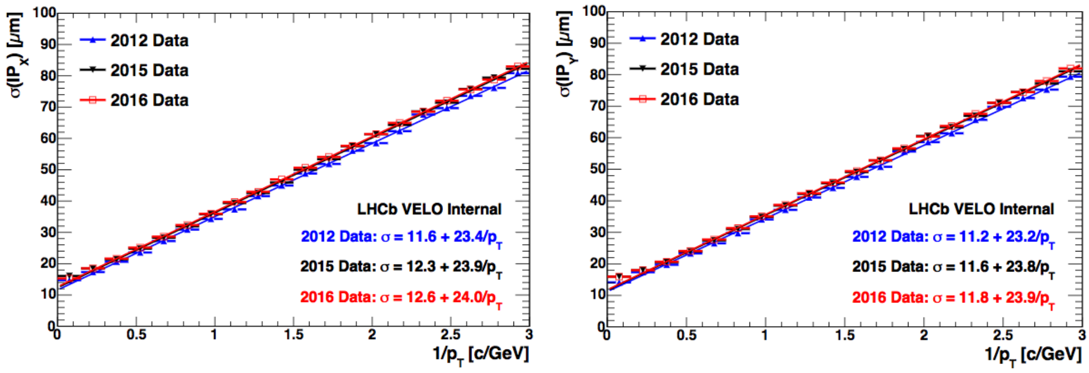

FIGURE 3.11: Left - The evolution for different running years of the x-direction (horizontal) IP resolution as a function of inverse transverse momentum. Right - The evolution in the y-direction (vertical).

a function of the transverse momentum can be written as

$$\sigma_{\mathrm{IP}} \propto \frac{r_1^2}{p_T^2}\left(0.0136\,\mathrm{GeV}/c\sqrt{\frac{x}{X_0}}\left(1+0.038\ln\frac{x}{X_0}\right)\right) \tag{3.1}$$

The IP resolution in the x and y directions can be seen in Figure 3.11 for 2012, 2015 and 2016 showing that we can achieve a resolution of about 12 μm at high p_T with little degradation in performance with increased fluence.

3.2.1.2 The Silicon Tracker

The silicon tracker [99] consists of two detectors; the Tracker Turicensis, TT, and the inner tracker, IT. The TT is located between RICH1 and the magnet. Its purpose is to help in track reconstruction between the VELO and further tracking stations where low momentum particles would be lost due to the bending of the magnet and to reconstruct decays which occur outside the VELO such as $\mathrm{K}^0_\mathrm{S}$and Λ^0. The IT consists of three stations located in front of the outer tracker. The silicon microstrips are used to increase the granularity of LHCb at high η where the track multiplicity is greater. Both the TT and IT stations have four detection layers with the inner two layers rotated at $\pm 5^{\circ}$ with respect to the y-axis to give a stereoscopic particle view.

The TT uses 500 μm thick sensors with a pitch of 198 μm. Each sensor is 780 mm wide with 384 strips per sensor for a total 143,360 readout channels. The first and second layers are separated from the third and fourth layers by a 30 cm gap to improve tracking ability without increasing the material budget.

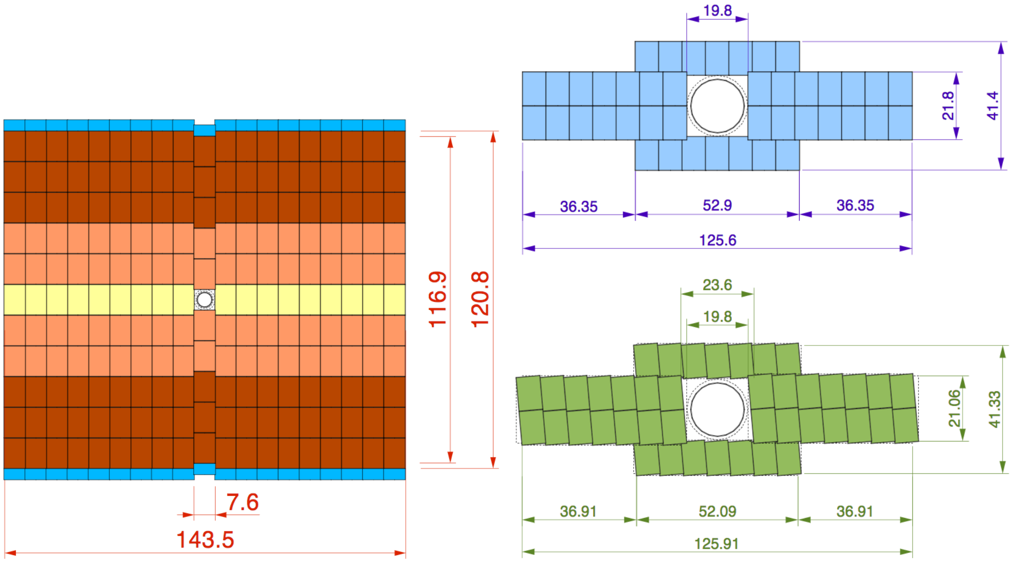

FIGURE 3.12: Left - Front view of 0°TT station. Top Right - Dimensions of an IT at 0°. Bottom Right - Dimensions of an IT at -5°. Dimensions are in centimetres. Taken from [99].

The IT has a similar silicon design to the TT, using 780 mm wide sensors with thickness of 320 µm and a strip pitch of 200 µm for a total of 129,024 readout channels. The sensors are attached in a cross shape around the beam pipe with the Outer Tracker extending from the IT to cover the full acceptance of LHCb. The IT covers 1.3% of the acceptance but 20% of the produced particles within that acceptance. The sensors are read out via Beetle chips while the data is read out by Tell1 boards, like the VELO. The IT is cooled using fluorocarbons (C_6F_{14}) supplied at -15°C to maintain a temperature below 5°C [76, 99]. The dimensions of the TT and IT can be seen in Figure 3.12.

3.2.1.3 The Outer Tracker

The three OT stations are located directly behind their corresponding IT station with their positions listed in Table 3.1. The OT uses straw tubes with a radius of 2.5 mm to measure the drift time. The counting gas is a mixture of Argon, CO_2 and O_2 in a 70:28.5:1.5 ratio to give a drift time of less than 50 ns. This drift time is required to keep the detectors occupancy below 10% at design luminosity. This requirement also determines the sizes of the IT and OT, with the two detectors having a 1 cm overlap region. The straw tubes have a bilayer design with an inner cathode layer of 40 µm thick carbon doped Kapton (Kapton-XC) and an outer insulating layer of 12.5 µm Kapton-XC and 12.5 µm aluminium laminate.

Tracking Stations z-positions				
	IT		OT	
	$z_{\min}$ [cm]	$z_{\max}$ [cm]	$z_{\min}$ [cm]	$z_{\max}$ [cm]
T1	767.3	782.8	783.8	803.8
T2	836.0	851.5	852.5	872.5
T3	905.0	920.5	921.5	941.5

TABLE 3.1: The locations of the tracker stations in cm, from the nominal interaction vertex. Taken from [99]

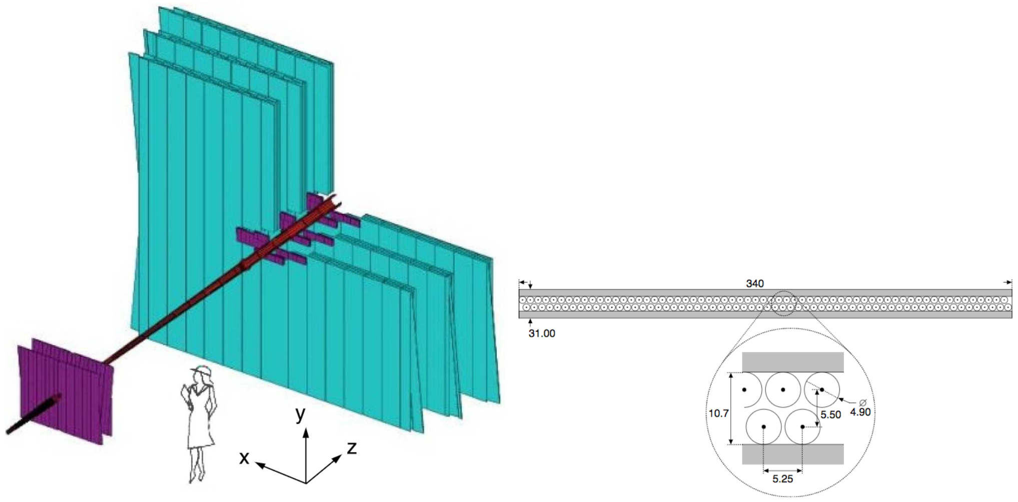

FIGURE 3.13: Left - View of the ST (in purple) and OT (in turquoise) with the beam pipe in the middle (in brown). Right - Schematic of the inside of an OT station. Taken from [76].

The anode wire is made of gold plated tungsten with a radius of 12.5 µm. Like the ST, the inner two layers of OT are rotated by ±5° to give full stereoscopic coverage [76, 100].

3.2.2 Particle Identification and Calorimetry

Particle identification at LHCb is performed by a variety of subdetectors working in unison. There are two Ring Imaging Cherenkov (RICH) detectors [101] located on either side of the magnet, a calorimetry system consisting of the preshower (PS), the scintillating pad detector (SPD), the electromagnetic calorimeter (ECAL) and the hadronic calorimeter (HCAL) [102] and, finally, the muon detector with five stations (M1 – M5) [103].

The identification of different species is of great importance to the collaboration as different decays will have different CP asymmetry properties. Thus, the ability to veto candidates based on their species assumption will greatly reduce systematic errors on measurements.

3.2.2.1 The RICH

The RICH detectors are used for particle identification, with RICH1 located directly after the VELO and RICH2 located between T3 and M1. PID is achieved by measuring the opening angle of Cherenkov radiation emitted by particles transitioning through the detectors. When a particle passes through a medium faster than the speed of light in that medium then it will emit photons at a characteristic angle given by

$$\cos\theta = \frac{1}{n\beta} \tag{3.2}$$

where θ is the angle that the photon makes with respect to the flight path of the particle, n is the refractive index [104]. The energy and momentum of a particle are given by

$$E = \gamma mc^2 \tag{3.3}$$

$$p = \gamma mv = \gamma mc\beta \tag{3.4}$$

where m is the mass of the particle and β is the fraction of the speed of light the particle is travelling at [105]. Equations 3.3 and 3.4 can be combined to give an expression for β,

$$\beta = \frac{pc}{E} \tag{3.5}$$

The relativistic energy equation is given by

$$E^2 = (pc)^2 + (mc^2)^2 \tag{3.6}$$

$$E = \sqrt{(pc)^2 + (mc^2)^2} = pc\sqrt{1 + \left(\frac{mc}{p}\right)^2} \tag{3.7}$$

Substituting Equation 3.7 into Equation 3.5 then substituting the resulting form into Equation 3.2 gives

$$\cos\theta = \frac{1}{n}\sqrt{1 + \left(\frac{mc}{p}\right)^2} \tag{3.8}$$

which allows you to identify particles in terms of their momentum and Cherenkov angle.

The RICH detectors can identify particles in the momentum range of $2 - 100\,\mathrm{GeV}/c$ across the full acceptance of LHCb, with the ability to discern between electrons, muons, pions, kaons and protons with a particular emphasis on the latter three particles[2]. In Run I, the RICH system used three radiators: silica aerogel for low-momentum tracks, C_4F_{10} for tracks with intermediate momentum values and CF_4 for high momentum tracks. The first two radiators were used in RICH1 while the third radiator was used in RICH2 as low-momentum tracks would be removed by the magnet system before reaching RICH2 [101]. The coverage of the RICH detectors for simulated $B^0 \to \pi^+\pi^-$ events can be seen in Figure 3.14. The silica aerogel was removed for Run II as it was found to block Cherenkov photons produced in certain areas of the detector and significantly increased the reconstruction time of candidates. The removal was important for the Run II trigger decisions as described in Section 3.2.5 [106].

The Cherenkov rings are reconstructed using Hybrid Photon Detectors (HPDs) which consist of a vacuum chamber and a silicon pixel sensor. The schematic of the HPDs can be seen in Figure 3.15. Cherenkov photons strike the quartz window, releasing a photoelectron into the vacuum. The quartz window has a bias of $-20\,\mathrm{kV}$ applied which accelerates the photoelectron to the silicon sensor which has an array of 256×32 pixels that are reduced to a 32×32 super-pixel array to reduce the read-out time. The super-pixels translate to a resolution of $2.5\times2.5\,\mathrm{mm}^2$ at the quartz window [107]. The HPD vacuum suffers from degradation over time which allows atoms and molecules to accumulate. The photoelectrons can strike and ionise these particles which are then accelerated to the photocathode and release secondary electrons. These electrons can give secondary signals but if the density of atoms or molecules is too great then this effect can become self-sustaining, known as ion feedback (IFB) [108]. To mitigate this effect, the HPDs are closely monitored and replaced at opportune moments when the IFB becomes problematic.

The photons are focused onto the HPDs using two sets of mirrors with spherical primaries and flat secondaries with a 90 % reflectivity between 200 and 600 nm. The material budget of RICH1 is 8 % of a radiation length while RICH2 is 15 % [109]. The efficiency and misidentification rate of LHCb's particle identification (PID)

---

[2] Electrons tend to produce "fuzzy" rings due to showering effects while muons are close in mass to the pion so information from the calorimeters and muon stations are used in combination with the RICH information to identify these particles.

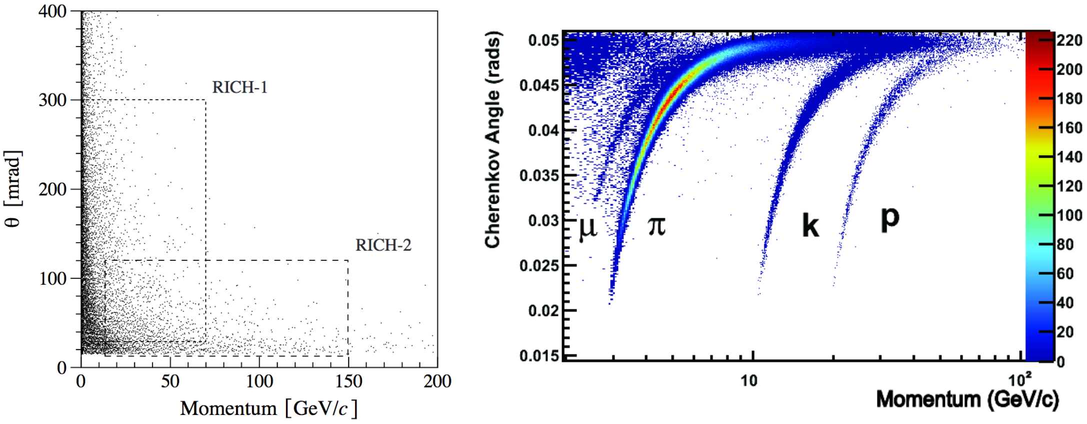

FIGURE 3.14: Left - Cherenkov angle versus momentum for simulated $B^0 \rightarrow \pi^+\pi^-$ events with the coverage of the two RICH detectors highlighted. Taken from [101]. Right - Particle identification efficiencies for the RICH detectors in LHCb with respect to the particle's momentum and the Cherenkov angle. Taken from [109].

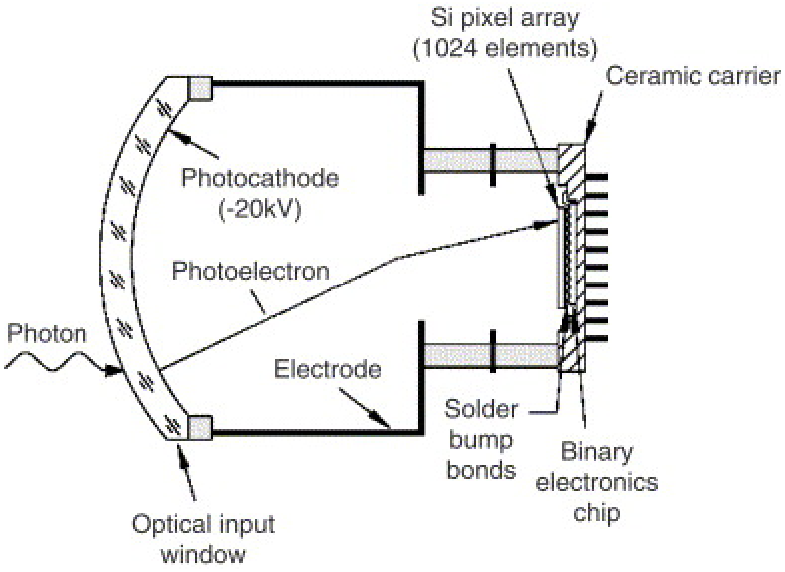

FIGURE 3.15: Schematic of the HPDs used in LHCb. Photons enter the quartz window on the left where a photoelectron is released. A 20 kV bias accelerates the electron to the pixel array where it produces secondary electrons. Occasionally ions within the vacuum will be accelerated to the quartz window where they can release electrons, giving ion feedback after-pulses about 200 ns after the initial pulse. Taken from [107].

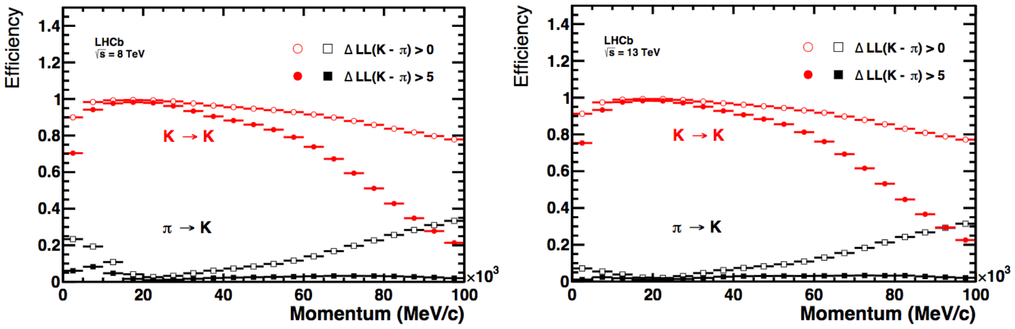

FIGURE 3.16: Left - Kaon identification efficiencies and pion misidentification for different likelihood cuts over a range of momenta in Run I. Right - Kaon identification efficiencies and pion misidentification for different likelihood cuts over a range of momenta in Run II. Taken from [106].

can be seen in Figure 3.14. The kaon identification efficiencies and pion misidentification for different likelihood cuts over a range of momenta can be seen in Figure 3.16.

3.2.2.2 The Calorimetry System

The calorimetry system consists of four detectors; the SPD, the PS, the ECAL and the HCAL in order of distance from the proton-proton collision point. The four detectors follow a common design principle with Wavelength Shifting (WLS) fibres running through scintillations pads. The WLS fibres are attached to photomultiplier tubes (PMTs). As the track density increases the closer you are to the beam pipe, the SPD, the PS, the ECAL use three cell sizes of increasing granularity while the HCAL uses two cell sizes to help distinguish particles.

The ECAL and HCAL are both sampling calorimeters. The ECAL is constructed using layers of 2 mm thick lead, 120 µm thick reflective paper and 4 mm thick scintillator tiles, forming a 42 cm thick module (see Figure 3.17) resulting in 25 X_0 and 1.1 λ_I where λ_I is the interaction length [102]. 25 X_0 was chosen to measure high energy photon showers. The cell sizes in the ECAL are the same as for the SPD and PS. The energy resolution of the ECAL is $\sigma_E/E = 10\%/\sqrt{E} \oplus 1\%$ and its electron-hadron separation can be seen in Figure 3.17.

The HCAL uses two cell sizes; $13{\times}13\,\mathrm{cm}^2$ and $26{\times}26\,\mathrm{cm}^2$, with an average of 4 mm of scintillating material and 16 mm of iron per layer to give an interaction length of 5.6 λ_I and an energy resolution of $\sigma_E/E = 80\%/\sqrt{E} \oplus 10\%$. λ_I was decided due to spatial restrictions within the LHCb cavern.

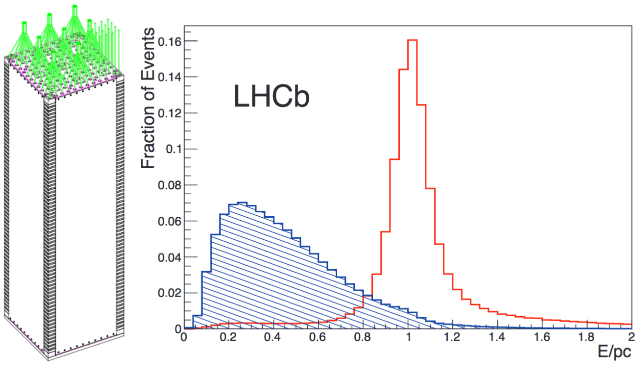

Figure 3.17: Left - The design of an ECAL inner module showing the sampling design. Right - Seperation of electrons (in red) and hadrons (in blue) for the ECAL using 340 pb^{-1} collected in 2011. Taken from [83].

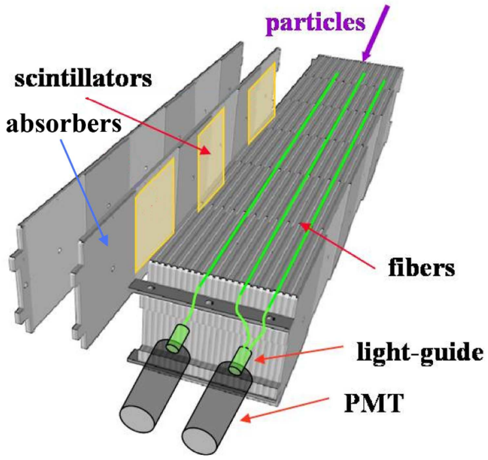

Figure 3.18: The design of an HCAL inner module showing the sampling design. The incoming particle direction is shown, highlighting the rotated design. Taken from [76].

The SPD and PS are placed either side of a 15 mm lead plate which has a thickness of 2.5 radiation lengths (X_0) and photon collection occurs using a multianode PMT. The cell sizes are $4{\times}4\,\mathrm{cm}^2$, $6{\times}6\,\mathrm{cm}^2$ and $12{\times}12\,\mathrm{cm}^2$. These detectors are used to help distinguish photons (γ), electrons (e^-) and neutral pions (π^0). π^0's will decay to two γ's 98.8 % of the time [36] which will be detected in the SPD while e^-'s will also deposit energy in the SPD but will also leave tracks in previous detectors. γ's that convert to an e^-e^+ pair before the PS will leave energy deposits and can be identified via track association. Measurements of the energy deposited in the PS will assist in the particle identification, e^-'s will deposit more energy due to Bremsstrahlung [76, 83]. The PS is capable of rejecting π^0's with over 99% efficiency while accepting e^-'s with over 91% efficiency.

3.2.2.3 The Muon System

Many of the Golden Channels under investigation by LHCb involve muons (i.e. B-meson decays where one of the daughters is a charmonium particle which will subsequently decay to a muon pair or rare decays such as $B^0_s \to \mu^+\mu^-$), hence a good muon detection system is required. This is achieved at LHCb using five muon stations with absorber material in between. M1 is located before the SPD and hence the absorber is the calorimetry system itself while M2 − M5 are separated by 80 cm of iron each, these layers give a thickness of 4.8 λ_I [103].

The muon stations each consist of 276 multi-wire proportional chambers (MWPCs) except the inner section of M1 which is equipped with 12 gas electron multipliers (GEMs) due to the increased track multiplicity at that location. The gas mixture used for detection is $Ar/CO_2/CF_4$ in a ratio of 40/55/5 for the MWPCs and 45/15/40 for the GEMs. The chambers are divided into detecting pads with increasing size with increasing distance from the beam axis, like the other detectors.

The stations are each divided into four regions (R1 − R4) with the pads becoming larger with increasing region. The pads are thinner in the horizontal direction which is the bending plane of the magnet thus requiring higher granularity. The design of a quadrant in M1 can be seen in Figure 3.19. M1 is used for the L0 trigger while tracks in all stations are required for muon reconstruction but the stations can be further broken down by specific purpose. M1 to M3 are used for P_T measurements while M4 to M5 are used for PID thus the final two stations were designed with a lower granularity. The pad width in these two stations is in fact double that of M1 while the width is halved in M2 and M3 with respect to M1 [110].

3.2.3 HeRSCheL

The High Rapidity Shower Counters for LHCb (HeRSCHeL) consist of five sets of scintillator panels either side of the interaction point, at a maximum distance of ± 114.0 m [111]. The HeRSCheL stations increase the pseudorapidity coverage of the detector to ± 5 to ± 10. The increase in η allows the LHCb collaboration to study Central Exclusive Production (CEP) of particles. CEP involves the production of particles without the destruction of the original protons, thus these productions tend to fly at very low angles with respect to the beam pipe. The HeRSCheL

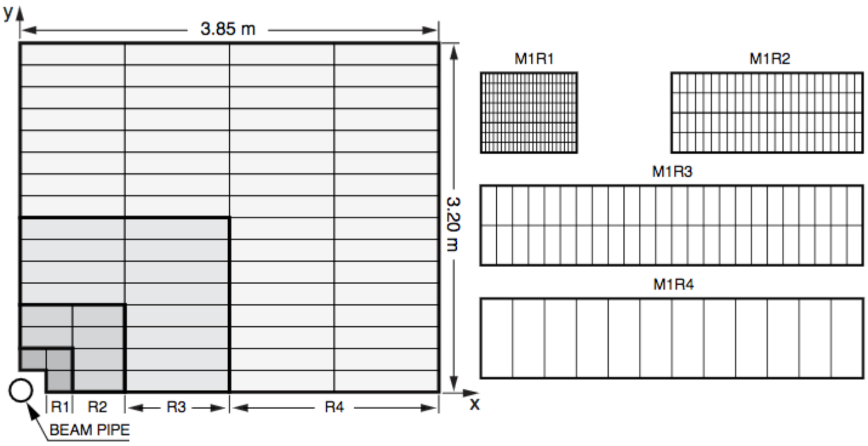

FIGURE 3.19: Left - A quandrant of M1 with a rectangle representing a chamber. Right - The division of pads within each type of chamber. Taken from [110].

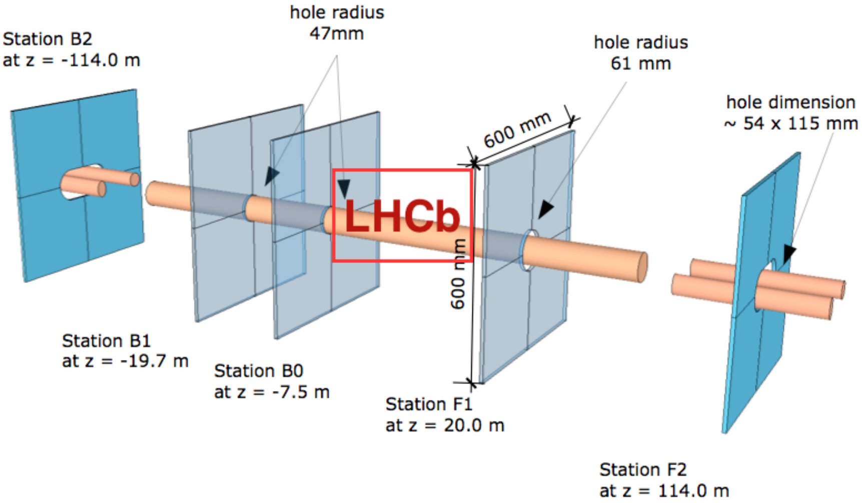

FIGURE 3.20: Exaggerated layout of the HeRSCheL stations with their z-positions from the proton-proton collision point indicated.

detectors were adding during LS1. As CEP is not a focus of this thesis, these stations will not be discussed in any further detail.

3.2.4 The Magnet

LHCb employs a warm dipole magnet with an integrated field of 4 Tm for momentum measurements and charge designation. The magnet consists of two water-cooled 27 ton trapezoidal aluminium coils angled at 45° housed within a 1450 ton iron yoke for a combined mass of 1504 ton. To reach the required field, a current of 5.8 kA flows through the coils. The water input temperature is 20°C and the output temperature is 60°C [112]. Using the expression for the Lorentz force on a particle in a magnetic field, the momentum of a particle (p) can be expressed in terms of its bending radius, r, as $p = (qB\sin\theta)r$ where q is the charge of the particle, B is the magnetic field strength and θ is the angle of the particle in the $y-z$ (vertical) plane. The magnet is used in two polarities designated as UP, achieved using a negative current (−5.8 kA), and DOWN, achieved using a positive current (+5.8 kA). The aim of LHCb is for 50% of the data to be taken in each polarity to cancel charge dependent detection asymmetries.

3.2.5 The Trigger

LHCb employs a staggered trigger system as it would not be possible to read out at the bunch crossing rate of 40 MHz. The trigger system reduces the read-out rate to a manageable level of up to 12.5 kHz and is split into three parts; Level-0 (L0), High Level Trigger 1 (HLT1) and High Level Trigger 2 (HLT2). L0 is a hardware trigger while the HLT's are software based.

The latency of L0 is fixed at 4 µs with the minimum required time for a decision being 900 ns which results in a maximum trigger rate of 1.11 MHz. The L0 trigger is capable of accepting or rejecting events based on simple decisions such as the L0 Decision Unit (L0DU) which uses the previously mentioned pile-up sensors to measure μ and the SPD to measure track multiplicity as a method to reject events which would contain an unmanageable track multiplicity. Decay products from heavy flavour events typically have large p_{T} and/or E_{T}, this allows measurements from the muon system and calorimeters to be used in the L0 decision to identify these events [113]. A schematic of the trigger system explaining the different L0 decisions at the time of design can be seen in Figure 3.21.

The HLT systems employ a set of trigger lines which contain physics requirements to select candidates for specific analyses. The requirements can either be optimised for signal efficiency but at the cost of introducing biases which must be corrected for by the analyst (such as detector acceptances which introduce lifetime biases) or they can reduce biases at the cost of reduced signal efficiency. The HLT runs on the Event Filter Farm which contained ∼29,000 logical cores in Run I and contains ∼52,000 in Run II. The HLT is capable of online reconstruction and HLT1 performs a partial event reconstruction using information from the tracking system and has a rate of the order of 100 kHz [114]. To reduce background rates, the HLT1 trigger lines typically cut on the impact parameter (i.e. any tracks originating very close

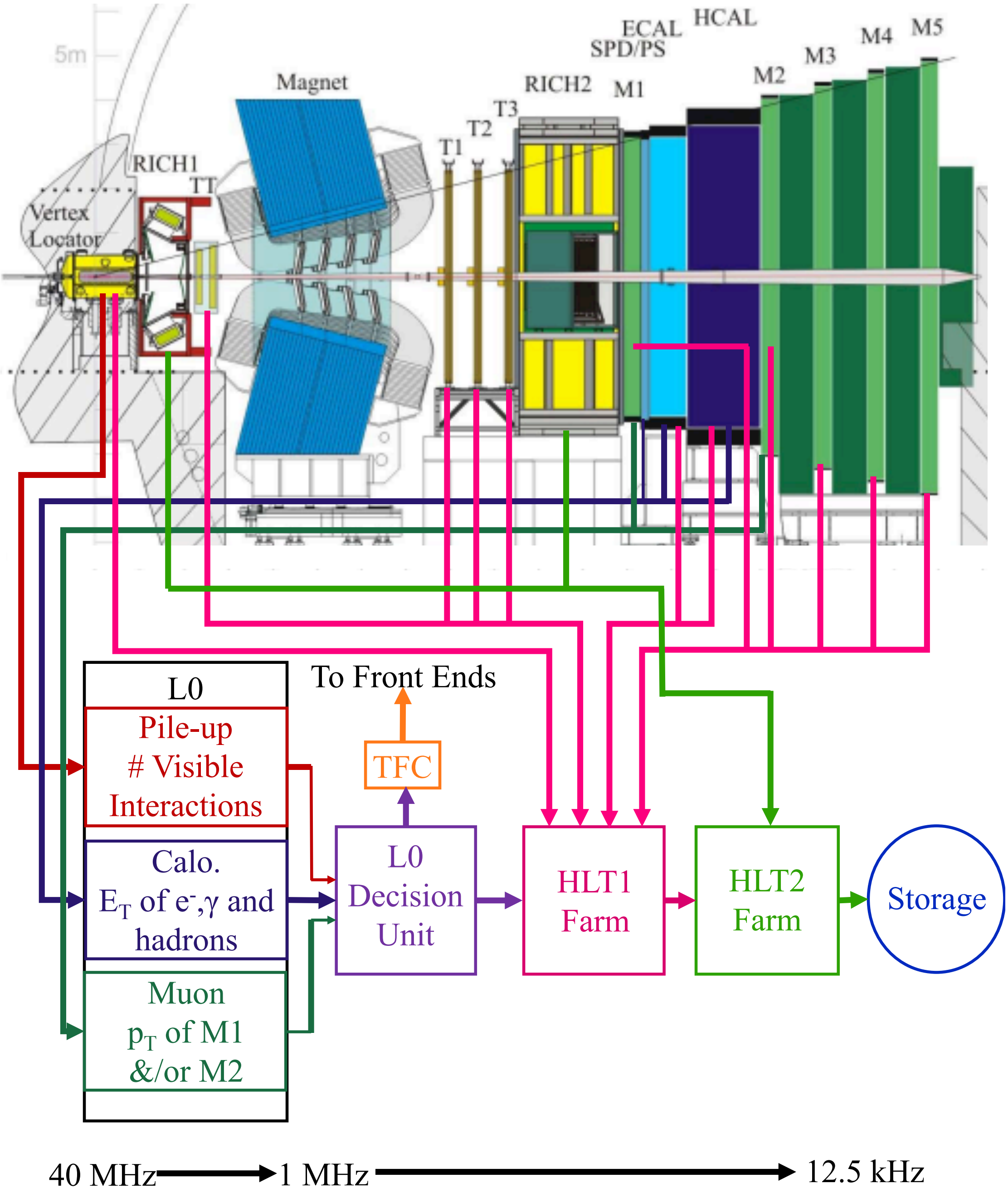

FIGURE 3.21: Structure of the LHCb trigger system in Run II. The Run I trigger was very similar apart from the storage rate and no RICH information was used in HLT2. Adapted from [113].

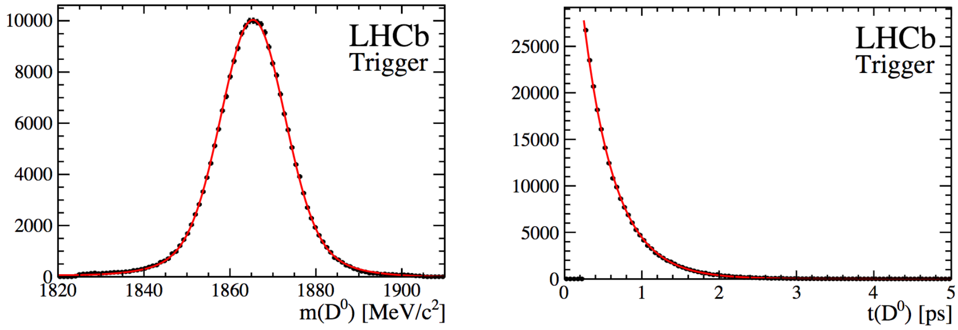

FIGURE 3.22: Left - The invariant mass distribution of $K^+\pi^-$ candidates that fired the HLT1CALIBTRACKINGKPI trigger line. Right - The lifetime distribution of $K^+\pi^-$ candidates that fired the HLT1CALIBTRACKINGKPI trigger line. The red exponential is the world average overlayed on the data points. Taken from [115].

to the *pp* collision point are rejected) but this has an adverse affect of biasing lifetime measurements (as distance from the collision point is proportional to a particle's lifetime). To correct for this, the lifetime acceptance must be modelled which can introduce significant systematic errors into the final measurement. Due to the increased farm size and subsequent alterations to the HLT trigger lines, new lines without these IP cuts were introduced for Run II, known as Lifetime Unbiased Trigger lines [115]. The mass and lifetime distribution of $\mathrm{D}^0 \rightarrow \mathrm{K}^+\pi^-$ candidates that fired the HLT1CALIBTRACKINGKPI line can be seen in Figure 3.22. The red line is an overlay of the world average.

In Run I, HLT2 used a simpler event reconstruction based on VELO tracks due to time constraints [116]. HLT2 trigger requirements typically include a cut on the invariant mass distribution, cuts at small lifetimes (for background reduction) and track quality cuts (Track χ^2/nDoF). Significant alterations were made to the HLT system between Runs I and II. It was previously mentioned that the farm size was significantly increased and real-time alignment and calibration of the detector was performed at the start of stable beams for every fill of the LHC. These improvements made it possible to apply full event reconstruction of offline quality between HLT1 and HLT2, significantly decreasing the time between collisions and when an event is available for user analysis. The real time alignment of the RICH detectors made it possible to apply particle identification to Run II HLT2 trigger lines, further improving the quality of offline stored data. the differences in trigger architecture from Run I to Run II can be seen in Figure 3.23.

A further alteration to the trigger system between Run I and Run II was the

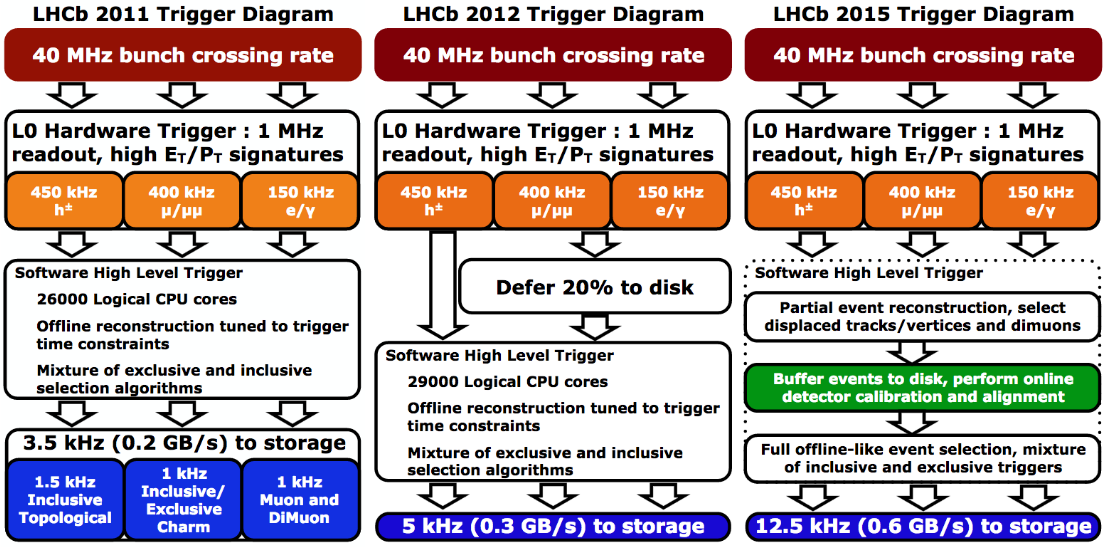

FIGURE 3.23: Structure of the LHCb trigger system in 2011, 2012, and 2015. No alterations were made to the structure of the trigger in 2016 except the removal of the duplication of events. Taken from [114].

separation of HLT1 and HLT2 processes allowing HLT1 processed events to be buffered then processed by HLT2 in between LHC fills (the typical LHC physics delivery accounts for ∼30% of the running period). The maximum time to process an event through HLT1 is 35 ms while it is 650 ms for HLT2. This has also improved the data collection for the experiment. The trigger system underwent minimal alterations between 2015 and 2016. In 2015, the storage size was 5 PB as the events were duplicated but as the error rate was only 0.1%, the mirroring was dropped and the full 10 PB storage was used. A description of the trigger requirements used in the analyses in this thesis will be given in Sections 7.1.1 and 8.2.1.

Part II

Studies of Vertex Detectors at LHCb

Chapter 4

VELO Operations

The VELO has performed exceptionally throughout its use in the LHCb experiment. However, it was designed to withstand a radiation dose of 7×10^{14} 1 MeV $n_{\mathrm{eq}}\,\mathrm{cm}^{-2}$ at its most intense point [98]. To ensure its optimal performance, careful monitoring of the system is required. To aid in this, duties were undertaken to monitor the evolution of the high voltage (HV) system and maintain its operation. This is of particular importance as radiation flux through silicon sensors will increase the leakage current in a system via Frenkel defects [117]. This effect can be mitigated through the production of Schottky defects at low temperature which act as a sink to the dislocated atom, known as beneficial annealing. Before the start of the 2015, 2016 and 2017 running periods, the candidate validated the operation of the HV system and produced software to monitor the increase in leakage current throughout the runs.

Understanding the behaviour of the HV system is of high importance to the LHCb collaboration as studies have shown that at the end of Run II in 2018 the effective depletion voltage of the VELO is predicted to be over 450 V as can be seen in Figure 4.1. The operational high voltage levels are decided by performing a charge collection efficiency (CCE) scan of the VELO. These are performed periodically throughout the running period and involve lowering the voltage of every 5th module then sequentially ramping the voltage up beyond operational voltages. The track finding efficiency is then measured at every voltage step by using the preceding and succeeding two sensors as a telescope to predict the position of the track on the module under test. This allows a plot of track finding efficiency to be produced as a function of voltage and radius whereby the voltage at which a

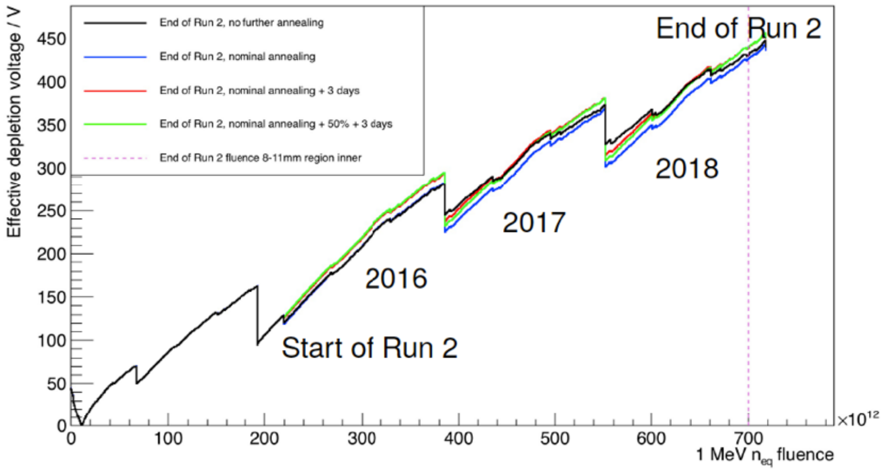

FIGURE 4.1: Predictions for the effective depletion of the VELO for Run II with different annealing periods. We were expected to reach 300 V by the end of 2016 and approach 450 V by the end of Run II. Credit to Jon Harrison.

sensor becomes fully depleted can be obtained. The high voltage must be set at a level above this threshold to maintain a good signal-to-background ratio within the VELO. Results of the HV tests have shown that sensor trips could occur when operating above 300 V which was predicted to occur towards the end of 2016.

4.1 Leakage Currents Within The VELO

The 88 sensors of the VELO are supplied with their HV by a set of 6 ISEG EHQ 607n-F modules which are capable of supplying up to 700 V to an individual channel [118]. One of the ISEGs currently used can be seen in Figure 4.2. As the LHCb cavern is a highly irradiated area during collisions which would interfere with the operation of sensitive read-out and control devices, many components of the detector are kept behind a concrete shielding wall. This requires long cables to connect detector electronics around the collision point to their off detector counterparts. The majority of VELO sensors use n^+-on-n semiconductors which have been shown to have higher efficiencies than p^+-on-n sensors for an equivalent depletion depth, producing 99% signal efficiency with a depletion of about 55% at a fluence of 2.5×10^{14} 1 MeV $n_{\text{eq}}\,\text{cm}^{-2}$ [119].

The change in leakage current, ΔI, will increase proportionally to the fluence, Φ where the infinitesimal change in leakage current is given by

$$dI = \alpha(T) dV \Phi \tag{4.1}$$

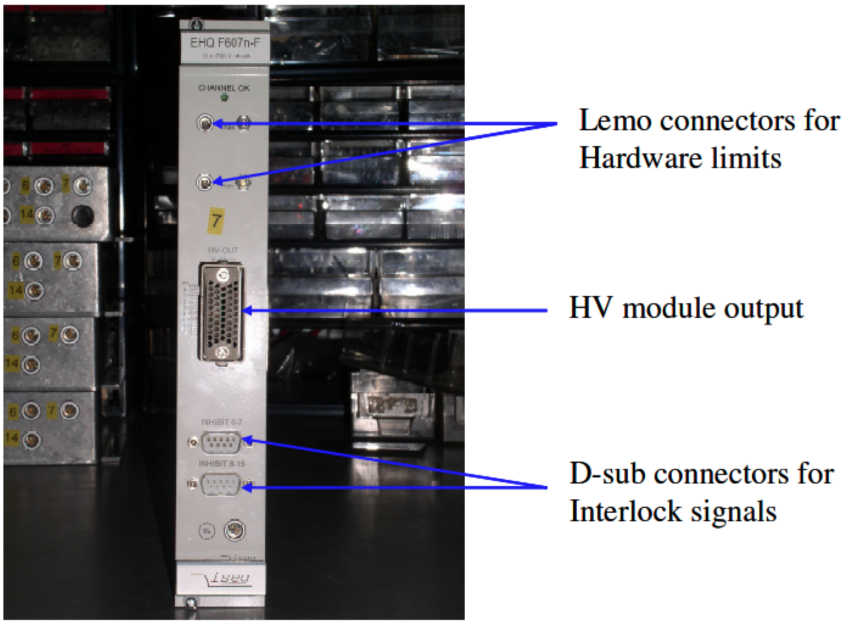

FIGURE 4.2: The current VELO ISEG HV supply [120].

where $\alpha(T)$ is the temperature-dependent damage rate and dV is the infinitesimal volume of the irradiated area [121]. The leakage current in a semicircular VELO sensor is thus given by the integral of Equation 4.1 over the radius. We can also scale the fluence with respect to the maximum fluence at the sensor tip, $\Phi = \Phi_{\rm I} \times (r_{\rm I}/r)^2$

$$\Delta I = \int dI = \int_{r_{\rm I}}^{r_{\rm O}} \alpha(T)\Phi_{\rm I}\pi t r_{\rm I}^2 \frac{dr}{r} \tag{4.2}$$

$$\Delta I = \alpha(T)\Phi_{\rm I}\pi t r_{\rm I}^2(\ln(r_{\rm O}) \ - \ \ln(r_{\rm I})) \tag{4.3}$$

where t is the thickness of the sensor, 300 µm, $r_{\rm I/O}$ is the inner/outer radius of the silicon, 8.2/42.0 mm. $\Phi_{\rm I}$ is given as the maximum fluence expected, $7{\times}10^{14}$ 1 MeV $n_{\rm eq}$ cm^{-2}. Established radiation damage models [121] have shown that the value of $\alpha(T)$ is $\approx 4.0 \times 10^{-17}$ at 20°C. To avoid thermal runaway and keep the drawn currents low, the VELO is pumped with CO$_2$ at -30°C, resulting in an operational ("with beam") temperature of about -10°C. We can rescale temperature dependent parameters such as $\alpha(T)$ or the current using

$$f(T_{\rm New}) = f(T_{\rm Old}) \left(\frac{T_{\rm New}}{T_{\rm Old}}\right)^2 e^{\frac{-E_{\rm gap}}{2k_{\rm B}}\left(\frac{1}{T_{\rm New}} \ - \ \frac{1}{T_{\rm Old}}\right)} \tag{4.4}$$

where $f(T)$ is a temperature dependent parameter, $E_{\rm gap}$ is the band gap energy, measured to be 1.12 eV, k_B is Boltzmann's constant, given as $8.62{\times}10^{-5}$eV/K [122]. Using these equations results in a maximum predicted leakage current at -10°C of

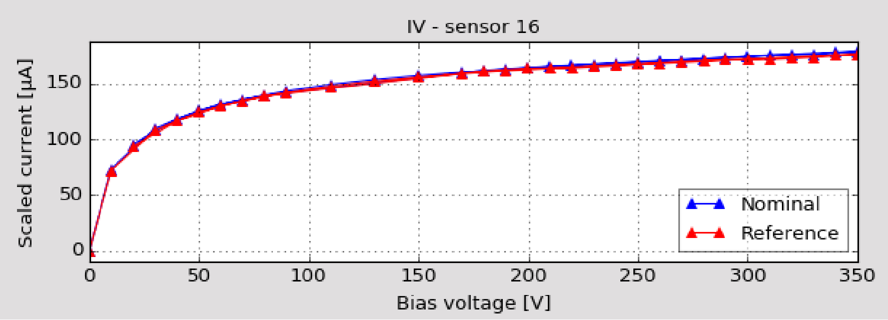

FIGURE 4.3: Two IV scans from the VELO taken towards the end of 2017. Both scans are corrected to -10°C with the red plot being the reference scan and the blue plot being the newer scan to be compared to. The blue scan has a higher point-by-point current than the red scan due to larger delivered luminosity at the time of measurement which is to be expected. Both scans are below the maximum predicted leakage current of 187 mA.

approximately 187 µA.

Current-Voltage (IV) scans can be performed to monitor the leakage current in the VELO. Software was developed and deployed to allow different IV scans to be compared immediately after they have been taken using the VELO offline monitoring software. This analysis software is currently used by the experts on-call for the VELO to continuously monitor the evolution of the radiation damage. As scans taken on different dates can be taken at different temperatures this can have an impact on the measured current as can be seen from Equation 4.4. To circumvent this issue, the ability to temperature correct the results to $-10°$C was added to the monitoring. The overlaid results from two IV scans taken late in 2017 can be seen in Figure 4.3. These results were corrected to $-10°$C and it can be seen that the plateau of the current is below the predicted level of 187 µA at end-of-life. An overview of the temperature corrected currents recorded at 200 V from all the VELO sensors at their positions from the stated interaction point of the LHC can be seen in Figure 4.4.

4.2 Status of the VELO High Voltage system

All of the LHC experiments were turned off during Long Shutdown I (LSI) from February 2013 to March 2015. After such an extensive period in shutdown mode, all aspects of LHCb were required to undergo evaluation to ensure they were ready for data taking in Run II. When the high voltage system was turned on, it was

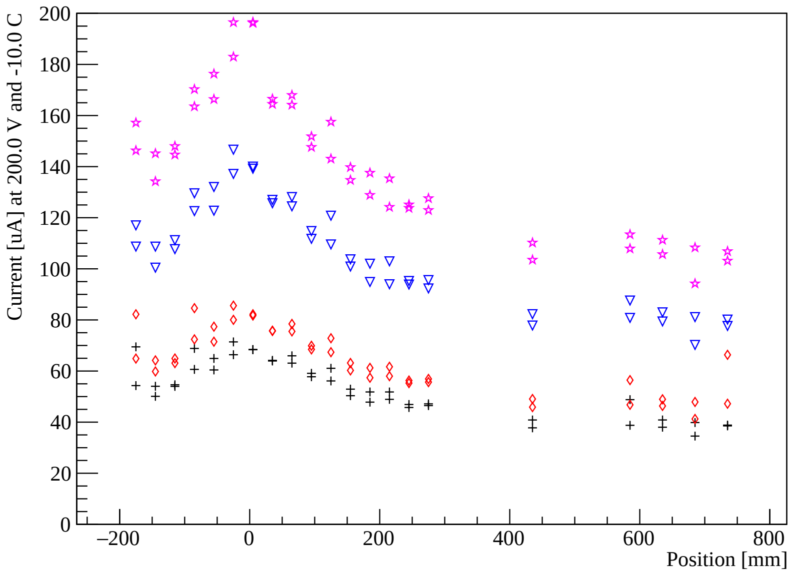

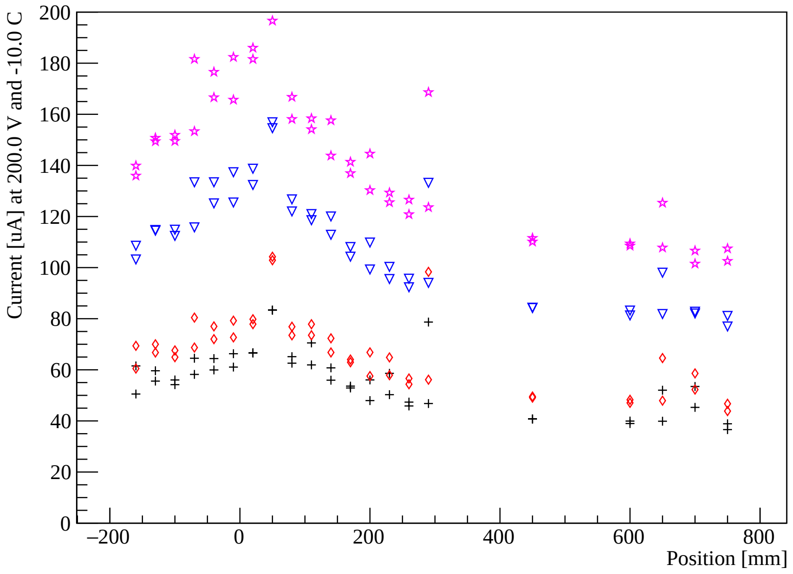

FIGURE 4.4: The leakage current drawn from all VELO sensors corrected to -10°C and taken at 200 V at their stated positions within the VELO at different periods in Run II of the LHC. 0 mm corresponds to the stated interaction point of the LHC. Top - Currents recorded on the A-side of the VELO. Bottom - Currents recorded on the C-side of the VELO. Black crosses - Start of Run II. Red diamonds - end of year shutdown, 2015-2016. Blue triangles - end of year shutdown 2016 - 2017. Pink stars - end of year shutdown 2017 - 2018.

found that sensors appeared to randomly trip with no immediately obvious cause, thus tests were devised and performed to discover and correct this effect. The only obvious pattern to the trips appeared to be that a sensor would trip at higher voltages every time, as though it was some type of “training”. The effect would reappear after a period in which the high voltage system was not in use and could appear as rapidly as two weeks without use.

Before the start of Run II, two cables were constructed with resistors to enable diagnostics of the high voltage system; a plug with 16×3 MΩ resistors that could be connected at the output of the ISEG to monitor the voltage directly from the module and one socket with a 2.3 MΩ resistor that could be attached to the end of the long distance cables at the VELO hood to monitor the voltage before it enters the VELO detector. These cables allowed VELO sensors to be removed from the testing procedure to avoid damaging them and isolate effects from the ISEG supplies from the rest of the system. The results of an IV curve taken from the output of an ISEG module using the 3 MΩ resistors can be seen in Figure 4.5 which show a linear relationship between the current and voltage, consistent with Ohm’s Law. Thus it was demonstrated that the ISEG supplies were capable of reaching their maximum specified voltage of 700 V, well above the maximum quoted operational voltage of 500 V for the VELO sensors. A second set of tests were performed at the VELO hood to inspect whether the long distance cables were causing the behaviour but this test also failed to replicate the tripping behaviour.

During the end of year shut down from 2015 to 2016 a second round of testing was performed. Initially the tests from the previous year were repeated to check whether near-continuous running of the HV system had sorted the problem, but it was discovered that the problem persisted and the tripping behaviour had reverted to occurring at the initial value of 300 V. A list of the trips that were observed over all sensors, including their voltages can be seen in Figures 4.6 and 4.7. The first column gives the name of the VELO sensor, the second gives the number of “current limits” that caused the channel to stop supplying a voltage and the third gives the number of “current trips” that caused the channel to stop supplying a voltage. The final four columns show the voltage that each trip occurred at. These columns are colour coded to emphasise the voltage range at which the sensor tripped at; from red at lower voltages (300 to 320 V) to green at higher voltages (420 V and above). This colour scheme was chosen as the VELO was

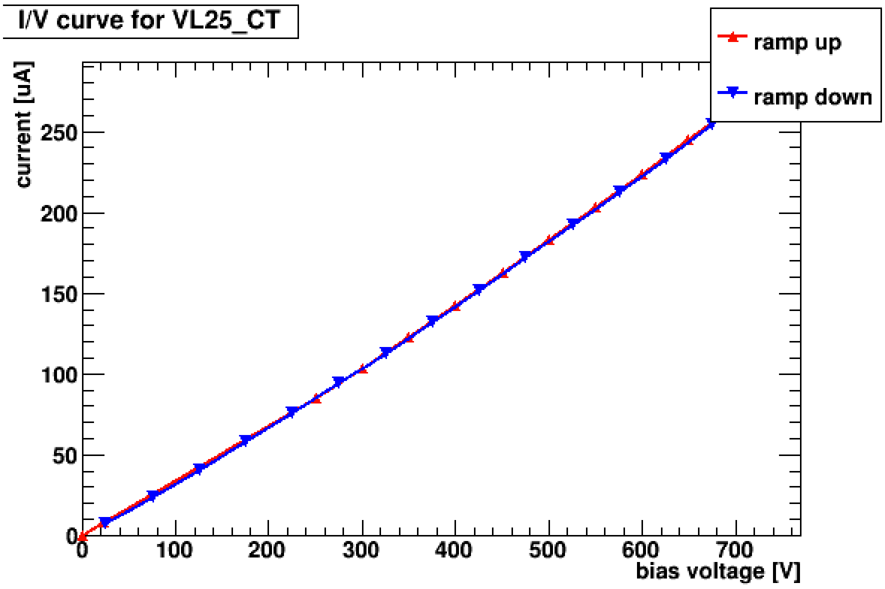

Figure 4.5: I/V curve for the voltage supplied from the ISEG directly to a male SLA.H51.LLZG plug.

expected to operate at 300 V after these tests. After a few ramps it was possible to get an IV scan to 450 V of the whole VELO, the results from 4 sensors can be seen in Figure 4.8.

The three most problematic channels (VL14_AB, VL08_CB and VL14_CT) were then tested with a new power supply, a Keithley 2410, to see if any strange behaviour could be observed but none was seen. The comparison between the Keithley and ISEG power supplies for these three channels can be seen in Figure 4.9. The voltage sourced from the ISEG in these channels was also spied using an oscilloscope in case of fast spikes that the VELO monitoring was unable to pick up but nothing was observed. The currents observed in one channel can be seen in Figure 4.10 which reveals no abnormal behaviour, the small overshoot in the current just before 12:12:20 was due to an inductive response from the change in voltage.

The control software was altered to allow for auto-recovery of the high voltage in case of an "event" which was defined as either exceeding a voltage limit or 500 V or a current limit of 320 µA. If either of these limits were exceeded within a period of ten minutes, then that high voltage channel would automatically ramp down and would have to be manually recovered. This was implemented after a discussion with experts revealed that the value of the internal currents as the voltage changes could cause the module to report a current trip condition. A second software

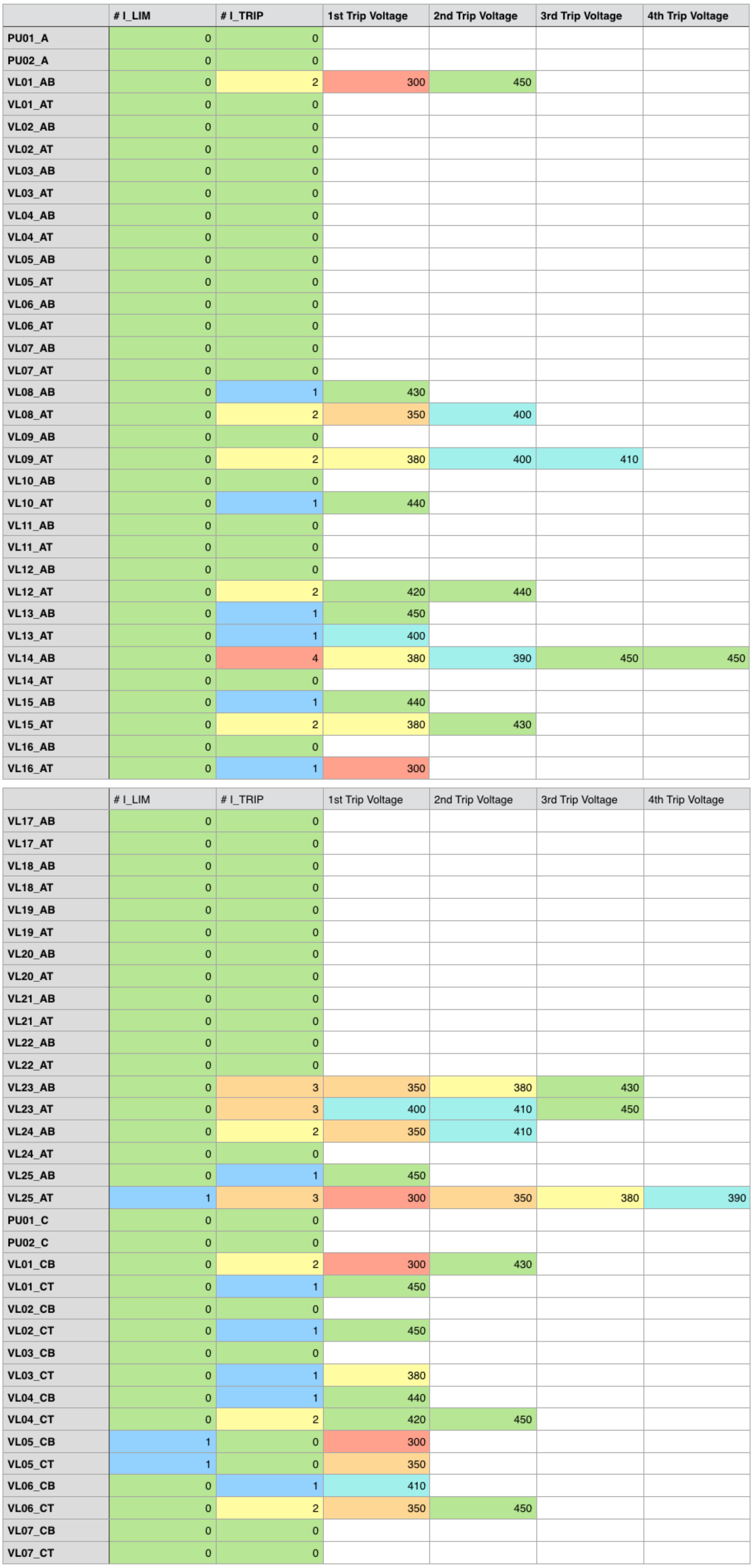

	# I_LIM	# I_TRIP	1st Trip Voltage	2nd Trip Voltage	3rd Trip Voltage	4th Trip Voltage
PU01_A	0	0				
PU02_A	0	0				
VL01_AB	0	2	300	450		
VL01_AT	0	0				
VL02_AB	0	0				
VL02_AT	0	0				
VL03_AB	0	0				
VL03_AT	0	0				
VL04_AB	0	0				
VL04_AT	0	0				
VL05_AB	0	0				
VL05_AT	0	0				
VL06_AB	0	0				
VL06_AT	0	0				
VL07_AB	0	0				
VL07_AT	0	0				
VL08_AB	0	1	430			
VL08_AT	0	2	350	400		
VL09_AB	0	0				
VL09_AT	0	2	380	400	410	
VL10_AB	0	0				
VL10_AT	0	1	440			
VL11_AB	0	0				
VL11_AT	0	0				
VL12_AB	0	0				
VL12_AT	0	2	420	440		
VL13_AB	0	1	450			
VL13_AT	0	1	400			
VL14_AB	0	4	380	390	450	450
VL14_AT	0	0				
VL15_AB	0	1	440			
VL15_AT	0	2	380	430		
VL16_AB	0	0				
VL16_AT	0	1	300			
VL17_AB	0	0				
VL17_AT	0	0				
VL18_AB	0	0				
VL18_AT	0	0				
VL19_AB	0	0				
VL19_AT	0	0				
VL20_AB	0	0				
VL20_AT	0	0				
VL21_AB	0	0				
VL21_AT	0	0				
VL22_AB	0	0				
VL22_AT	0	0				
VL23_AB	0	3	350	380	430	
VL23_AT	0	3	400	410	450	
VL24_AB	0	2	350	410		
VL24_AT	0	0				
VL25_AB	0	1	450			
VL25_AT	1	3	300	350	380	390
PU01_C	0	0				
PU02_C	0	0				
VL01_CB	0	2	300	430		
VL01_CT	0	1	450			
VL02_CB	0	0				
VL02_CT	0	1	450			
VL03_CB	0	0				
VL03_CT	0	1	380			
VL04_CB	0	1	440			
VL04_CT	0	2	420	450		
VL05_CB	1	0	300			
VL05_CT	1	0	350			
VL06_CB	0	1	410			
VL06_CT	0	2	350	450		
VL07_CB	0	0				
VL07_CT	0	0				

Figure 4.6: Trips observed from the VELO HV system during the March 2016 tests. Each line corresponds to one high voltage channel. It can be seen that the trips occurred at higher voltages each time.

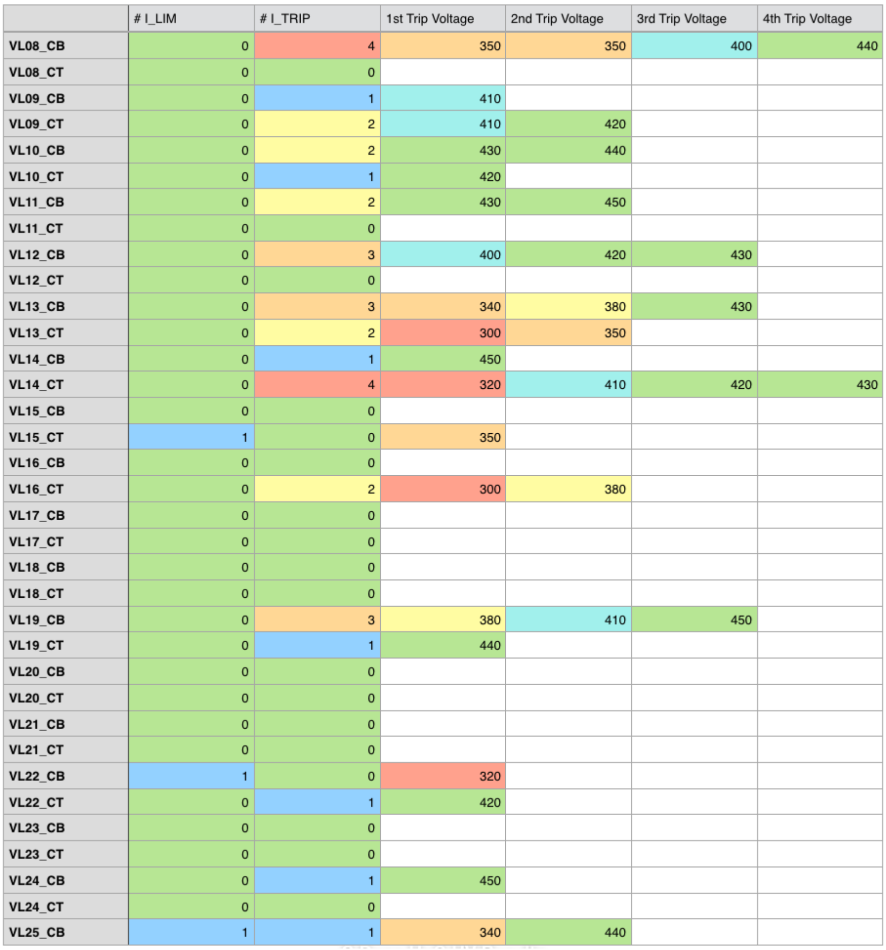

	# I_LIM	# I_TRIP	1st Trip Voltage	2nd Trip Voltage	3rd Trip Voltage	4th Trip Voltage
VL08_CB	0	4	350	350	400	440
VL08_CT	0	0				
VL09_CB	0	1	410			
VL09_CT	0	2	410	420		
VL10_CB	0	2	430	440		
VL10_CT	0	1	420			
VL11_CB	0	2	430	450		
VL11_CT	0	0				
VL12_CB	0	3	400	420	430	
VL12_CT	0	0				
VL13_CB	0	3	340	380	430	
VL13_CT	0	2	300	350		
VL14_CB	0	1	450			
VL14_CT	0	4	320	410	420	430
VL15_CB	0	0				
VL15_CT	1	0	350			
VL16_CB	0	0				
VL16_CT	0	2	300	380		
VL17_CB	0	0				
VL17_CT	0	0				
VL18_CB	0	0				
VL18_CT	0	0				
VL19_CB	0	3	380	410	450	
VL19_CT	0	1	440			
VL20_CB	0	0				
VL20_CT	0	0				
VL21_CB	0	0				
VL21_CT	0	0				
VL22_CB	1	0	320			
VL22_CT	0	1	420			
VL23_CB	0	0				
VL23_CT	0	0				
VL24_CB	0	1	450			
VL24_CT	0	0				
VL25_CB	1	1	340	440		

FIGURE 4.7: Trips observed from the VELO HV system during the March 2016 tests. It can be seen that the trips occurred at higher voltages each time.

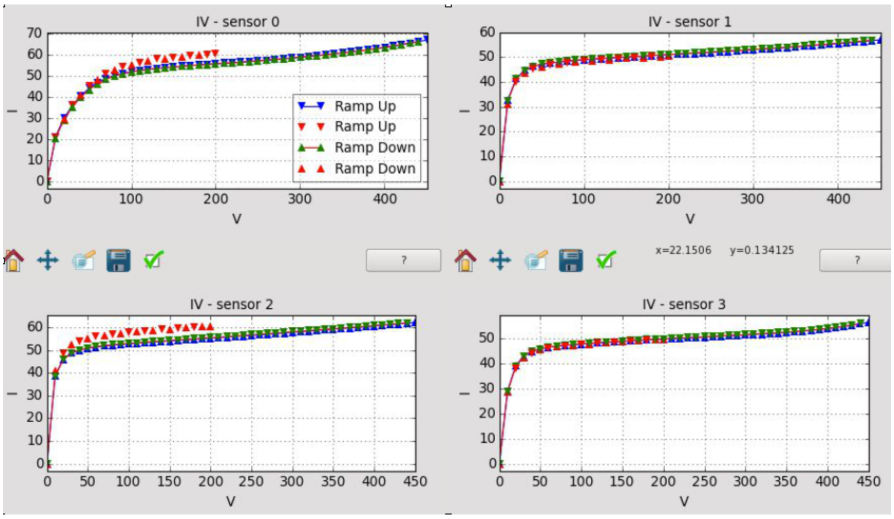

FIGURE 4.8: A successful IV scan to 450 V of 4 VELO sensors using the ISEG Power supply. The y-axis is given in µA.

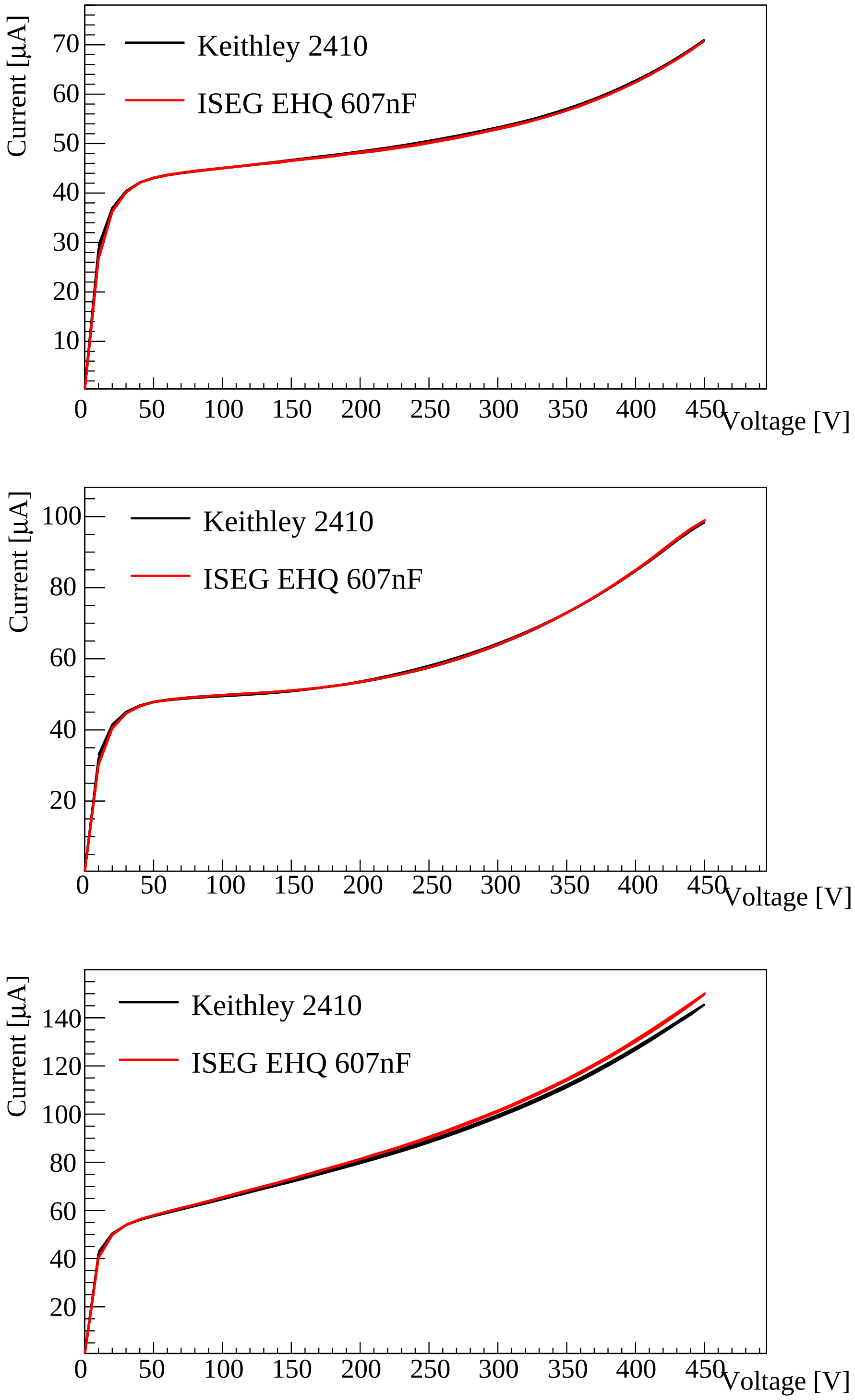

Figure 4.9: Comparison of IV scans performed on three VELO channels. No significant difference can be observed between the sources.

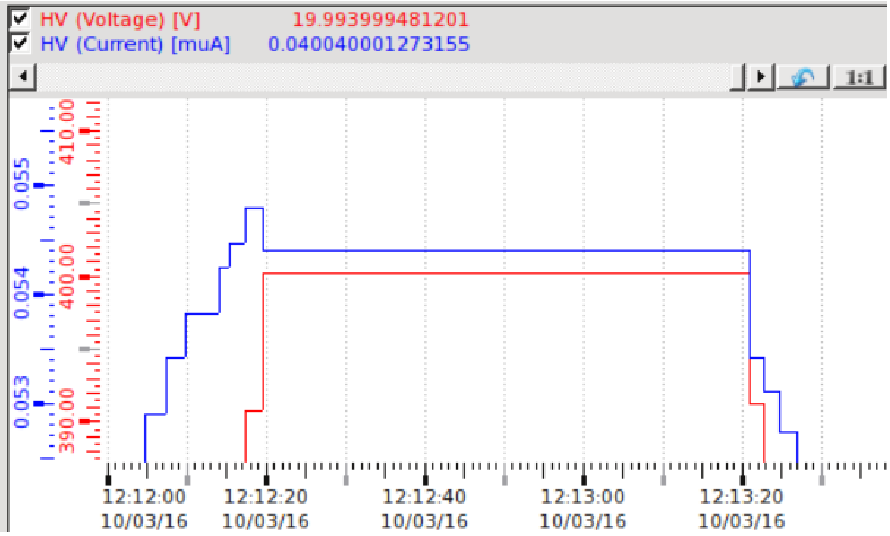

Figure 4.10: The voltage and current in one of the channels that tripped. No abnormal behaviour was observed from the monitoring software.

update was added to the global LHCb system to act as a watchdog to monitor the system and alert those in the control room of any potential issues. This watchdog also has the ability to analyse and recover the channel if deemed to be safe to minimise the loss of data and need for human intervention. It should be noted that this watchdog was not implemented by the candidate but by another member of the VELO team, Manuel Schiller.

The tests performed on the high voltage system of the VELO were designed in such a way as to study individual components of the system in an attempt to discern the origin of the tripping behaviour. This involved testing the power supply modules in isolation, the long distance cables with the power supply but without a detector module and the long distance cables with a detector module but without the power supply. None of these tests conclusively revealed the source of the behaviour but it was felt that it was due to a cumulative effect of the three components. The results of the CCE scans performed have shown that the expected effective depletion voltage of the sensors in expected to exceed 400 V by the end of Run II. The results of the tests have shown that the “training” effect and the implementation of the watchdog will ensure the successful operation of the VELO until the end of Run II.

Chapter 5

The Upgraded LHCb Detector

LHCb has had a very successful physics program which has in no small part been achieved due to the exceptional performance of the detector which was described in Section 3.2. The LHCb detector was initially designed to withstand a radiation dose of $7{\times}10^{14}$ 1 MeV $n_{\mathrm{eq}}\,\mathrm{cm}^{-2}$ at its most intense point over its lifetime, which will be reached by the end of Run II [98]. This requires a redesign of several of the subdetectors that have either reached their end of life or are not compatible with the requirements of the upgrade. During Long Shutdown III, the LHC will also undergo an upgrade, significantly increasing its peak luminosity from $1.58{\times}10^{34}\,\mathrm{cm}^{-2}\mathrm{s}^{-1}$ [123] to $5{\times}10^{34}\,\mathrm{cm}^{-2}\mathrm{s}^{-1}$ [124]. This increased luminosity will also mean altering the architecture of the experiment significantly to cope. The LHCb upgrade is a significant project with its installation scheduled for LS2 which begins at the end of 2018.

5.1 The LHCb Upgrade

As stated in Chapter 3, LHCb uses luminosity levelling to achieve its physics goals. After the upgrade of the detector, levelling will still be used but the instantaneous luminosity will be increased to $2{\times}10^{33}\mathrm{cm}^{-2}\mathrm{s}^{-1}$, increasing the number of visible interactions (μ) from 1.1 to 5.2 per bunch crossing as can be seen in Figure 5.1 [21]. The readout rate of the detector will be increased from 1 MHz to the full bunch crossing rate of 40 MHz. As it has been shown that the minimum time for an L0 decision is 900 ns this limits the trigger rate to 1 MHz. To circumvent this

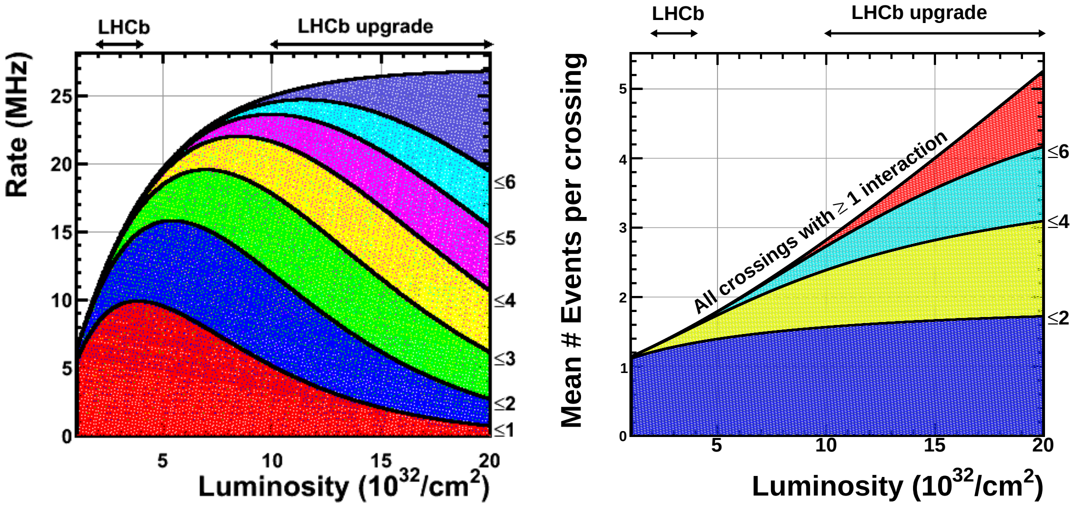

FIGURE 5.1: Left - Evolution of the interaction rate expected in LHCb as a function of the luminosity, split into bands of number of interactions per bunch crossing. Right - Evolution of the pileup as a function of the luminosity.

constraint, the L0 trigger will be removed which will result in LHCb being the first detector at a hadron collider with a fully software based trigger [125].

LHCb has made many physics discoveries in the first two runs of the LHC such as the observation of the first doubly charmed baryon, the Ξ_{cc}^{++} [126]. However, many of the analyses conducted at LHCb would benefit from increased signal yields. By removing the hardware trigger and reading out at 40 MHz, the collaboration would obtain these higher yields sooner than it would take using the current detector design. This requires not only changing the VELO but also all of the readout electronics. Other detectors will also undergo changes to improve on the current design such as the replacement of the HPDs in the RICH with Hamamatsu R13742 and R13743 multi-anode photomultiplier tubes (MaPMTs) [127]. The HPDs have a built in readout limit of 1 MHz and suffer from degradation of their vacuum which requires periodic interventions to replace or rotate the positions of the devices. The MaPMTs should not require the same interventions as the HPDs. The only other major change to the RICH system will involve moving the focal plane of RICH1 back to decrease the peak occupancy within the detector. This is not required in RICH2 which lies beyond the bending magnet and thus has a lower occupancy due to low-momentum particles being swept out the the detectors acceptance.

The OT and IT will be replaced by the Scintillating Fibre tracker (SciFi) due to their degradation and the increased multiplicity in the higher luminosity environment. The SciFi upgrade will consist of 250 µm thick Kuraray SCSF-78MJ fibres

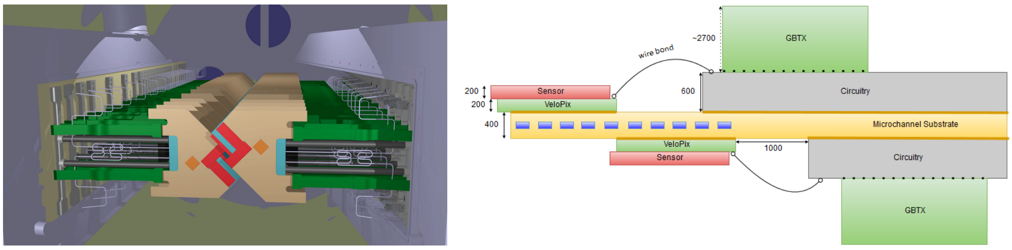

FIGURE 5.2: Left - Rendering of the VELO upgrade in the closed position. Right - Side view of a VELO Upgrade module [89].

with a maximum length of 2.4 m which was chosen due its long attenuation length of 4 m [128]. Also, with the L0 trigger being removed, the detectors components that it uses will also be removed, which includes the PS, SPD and M1.

5.2 The VELO Upgrade

To cope with the new conditions the current VELO will be replaced with a hybrid pixel detector with a pixel pitch of 55 µm, the distance from the beam to the closest pixel will be reduced to 5.1 mm and the RF foil will be changed to a thickness of 250 µm. The upgraded VELO will operate in a harsher radiation environment thus the radiation hardness will be improved to withstand a dose of $8{\times}10^{14}$ 1 MeV $n_{\rm eq}\,{\rm cm}^{-2}$ compared to the current requirement of $7{\times}10^{14}$ 1 MeV $n_{\rm eq}\,{\rm cm}^{-2}$ [89]. An upgraded VELO module will consist of a 200 μm silicon sensor bump bonded to the custom designed VeloPix ASIC [129], which is why the detector is described as *hybrid*, and will be actively chilled by evaporative CO_2 microchannel cooling [130]. The design of the upgrade can be seen in Figure 5.2. Each detector module will contain twelve VeloPix ASICs in an L-shaped configuration to maximise coverage. The twelve ASICs will be divided between two hybrids which are designated "Front" and "Back". The layout of the VeloPix ensures maximum coverage without overlap of the front and back sensors as can be seen in Figure 5.2.

5.2.1 Physics Motivation

The current VELO has performed fantastically, beyond its design luminosity of $2 \times 10^{32}{\rm cm}^{-2}{\rm s}^{-1}$ and up to $4 \times 10^{32}{\rm cm}^{-2}{\rm s}^{-1}$ however, at the specifications of the upgrade luminosity, $2 \times 10^{33}{\rm cm}^{-2}{\rm s}^{-1}$, the performance of the current VELO will degrade. The new VELO design gives several advantages over the current design to both recover the excellent physics performance and to improve in some areas. The reduced material budget and distance from the beam significantly improves the impact parameter resolution (σ_{IP}) at low values of transverse momentum (p_{T}) as can be seen in Figure 5.3. The resolution at high p_{T} is comparable for both the current VELO and the upgrade due to the increased pitch of the pixels when compared with the silicon strips that are currently used. There is also an improved efficiency at upgrade conditions with $\varepsilon > 99\,\%$ across most regions[1], which is seen in Figure 5.3, and a reduced ghost rate[2]: from 6.2% in the current VELO at μ=1.2 to 2.5% at μ=5.2 for the upgrade. A significant change is seen in the ϕ efficiency due to the change from silicon strips to pixels and the L-shaped geometry avoiding the reduced efficiency present in the overlap regions of the current VELO.

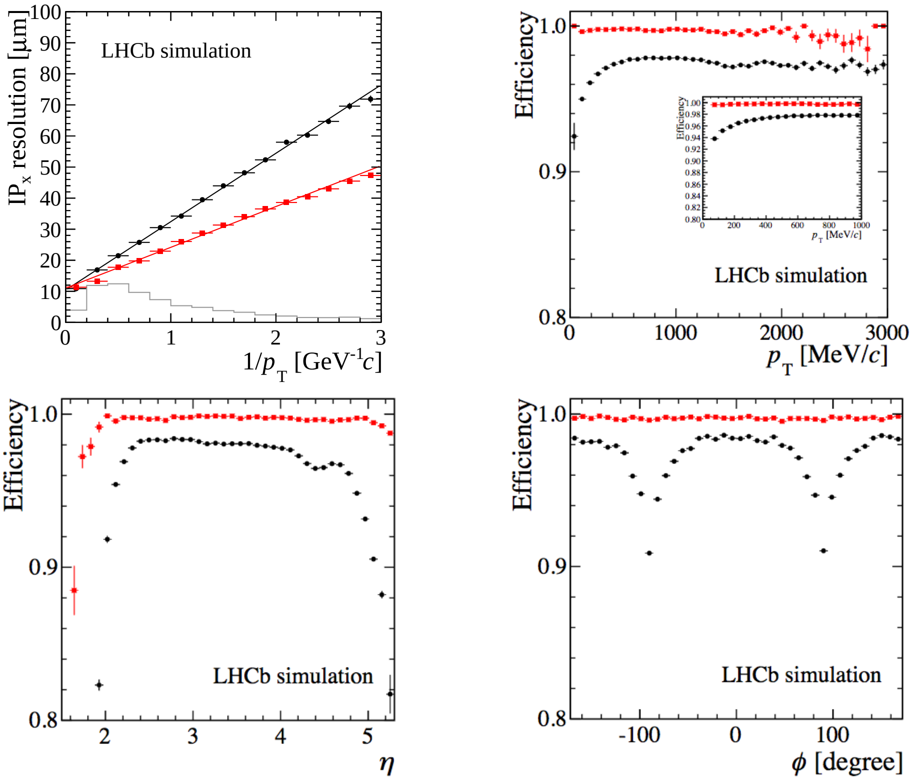

FIGURE 5.3: A comparison of several detector properties at the upgrade conditions of $\mu = 5.2$ and $\sqrt{s} = 14$ TeV for the current VELO in black and the upgraded VELO in red. Top Left - Impact parameter resolution. The histogram shows the relative population of events in each bin. Top Right - Efficiency vs p_T (the smaller plot shows a higher resolution of the low p_T region). Bottom Left - Efficiency vs η. Bottom Right - Efficiency vs Track Angle [98].

---

[1] The tracking efficiency decreases as the distance from the beam pipe increases, hence low η tracks have a slightly reduced efficeincy.

[2] The ghost rate is produced from tracks reconstructed from random hits within the detector.

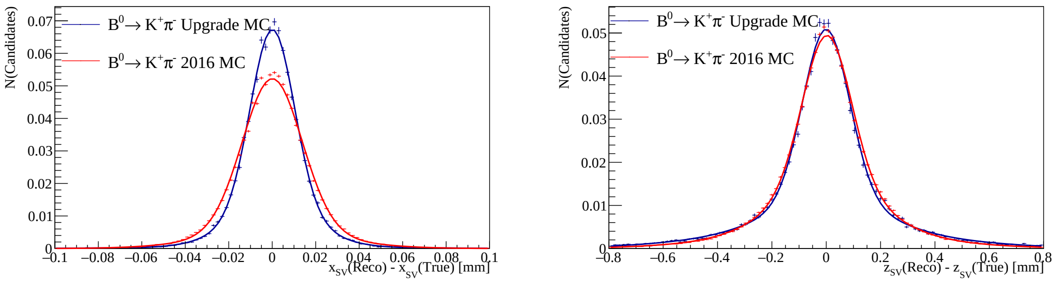

FIGURE 5.4: Comparison of the secondary vertex resolution for simulated $B^0 \to K^+\pi^-$ decays under Run II conditions in red and Upgrade conditions in blue. Left - The x-axis secondary vertex resolution. Right - The z-axis secondary vertex resolution.

The improvement in physics performance for $B \to h^+h'^-$ decays was investigated by producing a sample of $B^0 \to K^+\pi^-$ MC events under Run II and Upgrade conditions. A comparison of the secondary vertex resolution between the two detectors shows that the z-resolution of the current VELO is $129.68 \pm 0.54\,\mu m$ compared to $126.81 \pm 0.24\,\mu m$ for the upgrade, an improvement of approximately 2 % while the x-resolution was measured to be $15.29 \pm 0.23\,\mu m$ for the current VELO and $11.88 \pm 0.10\,\mu m$ for the upgrade, an improvement of approximately 24 %. The resolutions were measured as the weighted mean of the individual resolutions from a triple Gaussian. The x and z secondary vertex resolutions are shown in Figure 5.4. It can be seen that although the conditions in the upgrade are far more challenging, the upgraded detector shows a better performance than the current VELO.

5.2.2 Sensor Studies

The sensors are required to withstand 1000 V bias without signs of breakdown after receiving the full fluence and produce a signal of 6000 e^- to maintain a good S/N ratio. Several sensors were tested and have shown that they achieve the required 6000 e^- below the 1000 V limit imposed with no breakdown after the full irradiation [22]. Sensors that were exposed to half the fluence were tested and shown to collect 6000 e^- at a lower bias than the fully irradiated sensors as expected.

The upgrade sensors will consist of 200 µm thick silicon bump-bonded to three custom designed ASICs, the VeloPix, and will have dimensions of 14 × 43 mm. The nominal implant width is 39 µm with a guard ring width of 450 µm. Prototype

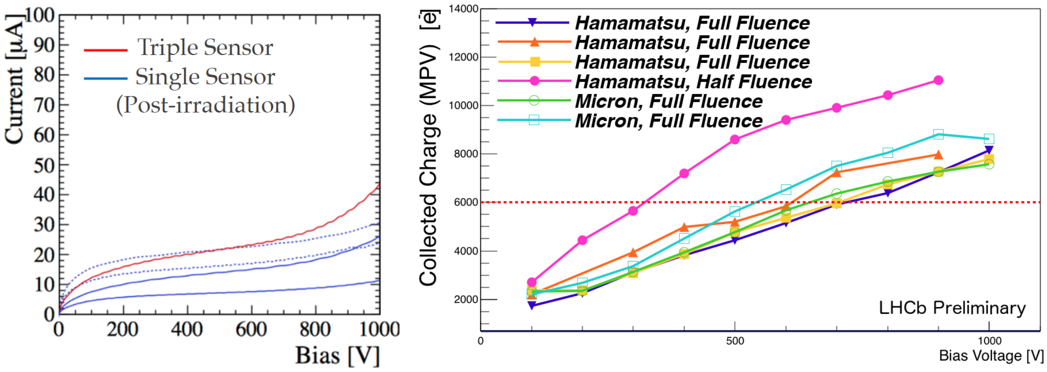

FIGURE 5.5: Left - IV scan from fully irradiated sensors (a *Single Sensor* is one which covers a single ASIC while a *Triple Sensor* covers three ASICs). Right - Charge collection results from a variety of irradiated sensors. The 6000e$^-$ requirement is marked with the dashed line. The pink plot with filled circles is from a sensor that had been exposed to half the expected fluence, the others are irradiated to the full expected fluence [22].

sensors have been produced by Micron (who provided sensors with a 36 μm implant) and Hamamatsu and extensively tested before and after irradiation to half (4×10^{14} 1 MeV $n_{\mathrm{eq}}\,\mathrm{cm}^{-2}$) and the full expected fluence (8×10^{14} 1 MeV $n_{\mathrm{eq}}\,\mathrm{cm}^{-2}$).

Sensor testing was conducted using the Timepix3 Telescope at CERN's Super Proton Synchrotron (SPS). The telescope consists of 8 Timepix3 ASICs [131] bump bonded to silicon sensors with a device under test (DUT) in the centre capable of x, y and θ motion. The telescope has a resolution of 2 μm with a hit rate of 80 Mhits/s using a 180 GeV beam. The results from measurements of prototype sensors are seen in Figures 5.5 to 5.7.

As the telescope has a resolution of ~2 μm it is possible to obtain the intrapixel efficiency by extrapolating the track position from the arms of the telescope while looking for a hit in the corresponding pixel of the DUT then superimposing all the pixels on top of each other. With a pixel size of 55×55 μm this allows the efficiency to be split into a 25×25 matrix. After full irradiation, at low voltages the pixels showed a large drop in efficiency at the edges due the distance of the track from the implant requiring the charge to travel further. High efficiency was recovered when the bias was increased towards 1000 V. The results from prototype sensors are shown in Figure 5.6.

The DUT is capable of rotating with respect to the beam hence it is possible to obtain the sensor resolution as a function of beam angle. This is obtained from the standard deviation of the residual between the cluster in the DUT and the

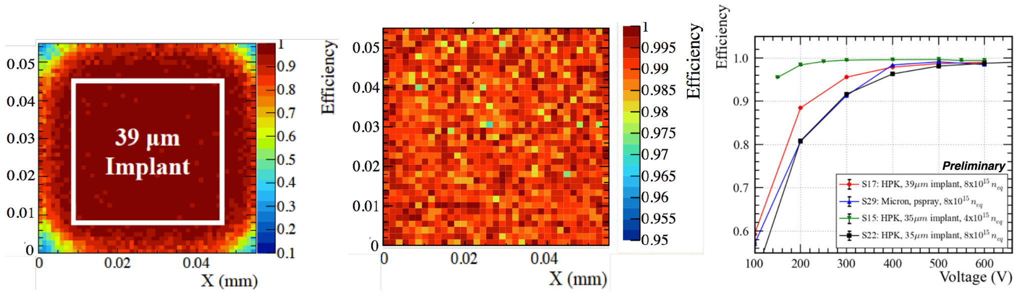

FIGURE 5.6: (left) The intrapixel efficiency for a Hamamatsu sensor at 300 V after being exposed to the full expected fluence. (middle) The intrapixel efficiency for the same sensor at 1000 V. (right) The average efficiency for three fully irradiated sensors and one sensor with half the irradiation (green with triangles) [22].

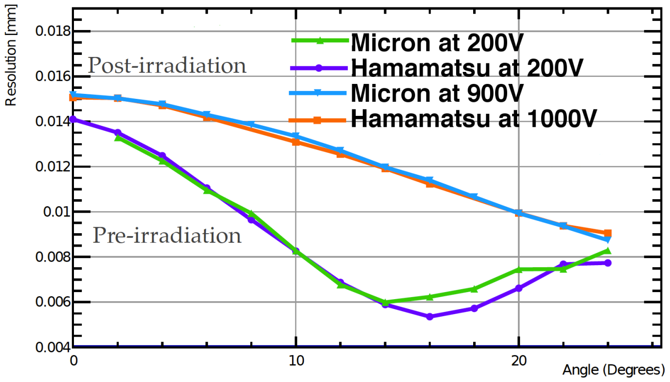

FIGURE 5.7: The resolution of sensors before and after irradiation as a function of beam angle. Purple - Pre-irradiation Hamamatsu, Green - Pre-irradiation Micron, Orange - Post-irradaition Hamamatsu, Blue - Post-irradiation Micron [22].

position of the track from the arms of the telescope. Figure 5.7 shows that the resolution of the sensors degrades after irradiation, caused by charge trapping.

5.2.3 The VeloPix

The VELO upgrade will use a custom-designed ASIC, the VeloPix, to handle the huge data rate that will be produced (up to 15.1 Gbit/s from the hottest ASIC) and is based on the Timepix3 that has been used to characterise the sensors in testbeam.

The VeloPix uses 130 nm CMOS technology with a 256 × 256 pixel array. These pixels are grouped in smaller 4 × 2 pixel arrays known as super pixels. Each pixel uses time-over-threshold (ToT) to register a hit with the threshold being programmable for a super pixel [129]. Each super pixel writes a data packet if

Feature	Timepix3	VeloPix
Readout	ToT	Binary
Max. Power	1 W/cm^2	1.5 W/cm^2
Pixel Matrix/Size	256×256/55 µm ×55 µm	256×256/55 µm ×55 µm
Hit Rate	80 Mhit/s	900 Mhit/s
Data Rate	5.12 Gbit/s	20.48 Gbit/s (4×5.12)
Technology	130 nm CMOS	130 nm CMOS

Table 5.1: Comparison of the key features and differences between Timepix3 and VeloPix.

any of the 8 associated pixels register a hit. The data packet consists of an 8 bit hitmap, a 9 bit time stamp and a 13 bit address. The data packets are sent in groups of four with a header (of 1010 in binary or 0xA in hexadecimal) for frame alignments and a four bit parity check resulting in a total frame size of 128 bits. These frames are sent at 40 MHz, thus the data rate of each serial data output is 5.12 Gb/s. There are 4 of these outputs on every VeloPix [132].

The VeloPix has been delivered and initial tests have shown that the ASIC works to the required specifications. A comparison of the key features and difference between the two chips is presented in Table 5.1 while the internal chip architecture explaining the pixels, super pixels packets and frames is shown in Figure 5.8.

5.2.4 The Electronics for the VELO Upgrade

A significant challenge for the VELO upgrade is in handling the rate of data being sent from the detector. As said in the previous section, each of the four data outputs from a VeloPix will send data at a constant rate of 5.12 Gbit/s with the peak data rate from the full detector being 2.85 Tb/s. The deliverables from the Glasgow LHCb group for the project are the off-module electronics. This requires the design, qualification and production of flexible high-speed data transmission cables, vacuum feedthroughs (VF) to pass signals through the vacuum wall and optoelectrical power boards (OPB) [133] for local control of the detector and the conversion of electrical signals to optical for the 300 m transfer to the off detector electronics. The final design of the OPB and cables were made at Glasgow while the VF was designed externally[3], however the responsibility for integrity of the high-speed signals remains in Glasgow.

---

[3] The first prototype of the VF was designed by the Glasgow LHCb group.

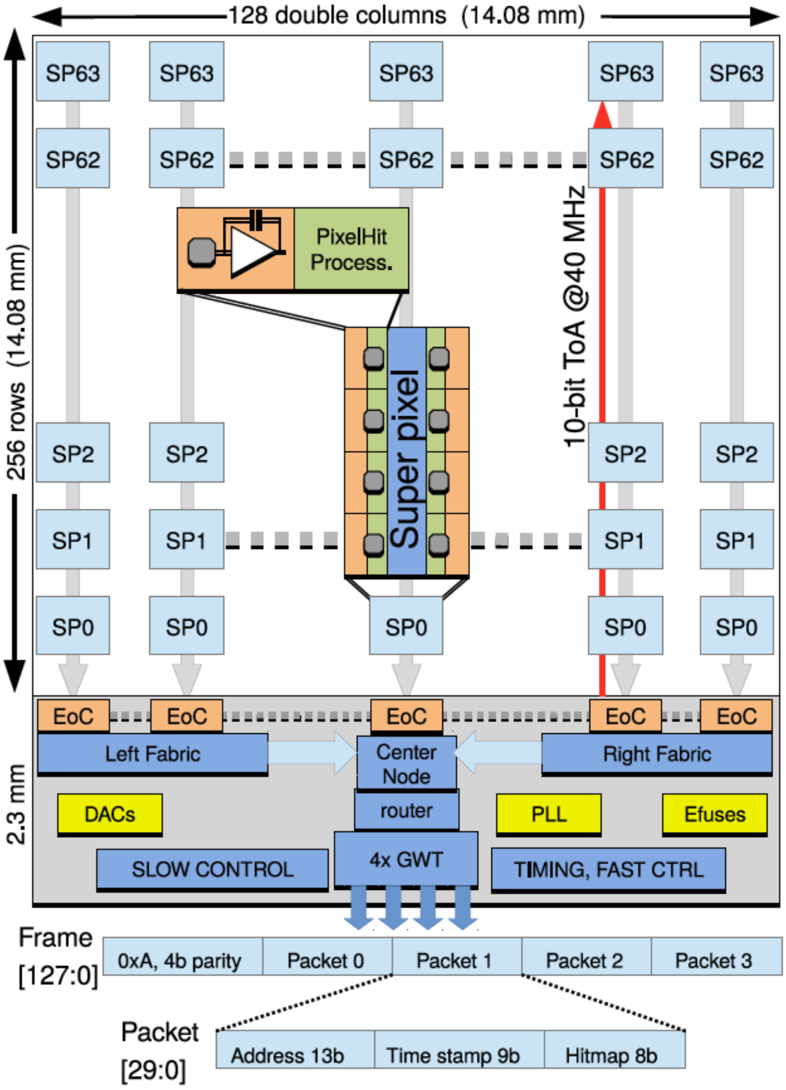

FIGURE 5.8: The architecture of the VeloPix ASIC explaining the layout and data structure of the chip [132].

The aim for the electronics is to have a loss of ∼10 dB at the Nyquist frequency of 2.56 GHz [134] for the full system, a characteristic impedance of 100 Ω to avoid impedance mismatch (and thus introducing reflections to the system) and a minimal rate of errors in the transmission of the bits, set to be $< 10^{-13}$. The project requires the production of 208 data cables, 52 OPBs and 52 VFs for installation in the final detector plus spares of each component. Full scale prototype designs can be seen in Figure 5.9.

The OPB provides optical-electrical conversion of the serial data from the VeloPix and to/from the control ASIC, the GigaBit Tranceivers (GBTx) located on the OPB and on the detector module. The optical conversions are carried out by two

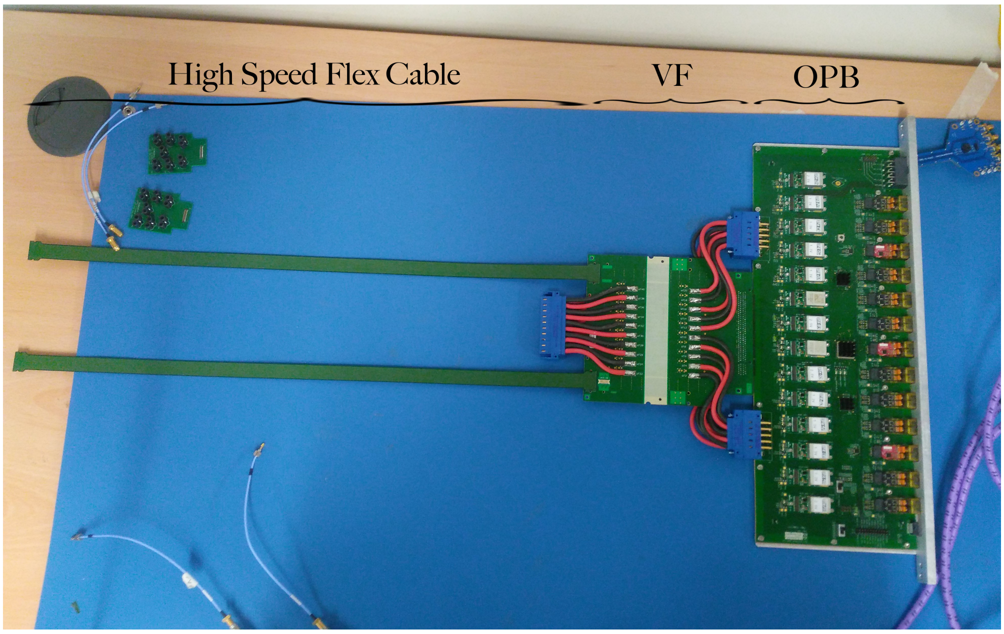

Figure 5.9: Full scale picture of the opto-power board, vacuum feedthrough and two flex cables. The red and black cables connected to the blue plugs are the low voltage lines. The column of 14 DC/DC converters can be seen near the left hand side of the OPB. The GBTx is visible as the central black ASIC with its two SCAs located above and below. The ten VTTx modules can be seen on the far right of the OPB (in black) along with the three VTTx modules (in red).

modules; the Versatile Twin Transmitter (VTTx) converts the signal from two data links while the Versatile Transceiver (VTRx) converts the control signals [135]. Each detector module has an associated OPB thus each OPB services two GBTx's on the detector module and twelve VeloPix with an additional GBTx for control of the OPB itself. The GBTx on the OPB distributes control via two slow control adaptors (SCA). The OPB also performs the DC/DC conversions for the VeloPix and the control electronics.

As the hit occupancy decreases approximately as an inverse square law, the true data output[4] decreases further from the innermost region thus less data links are required to carry data from those VeloPix. In total, one module requires 20 data links (10 per hybrid) and 3 control links resulting in each OPB requiring 10 VTTx's and 3 VTRx's. The OPB's also supply the low voltage (the red and black cables in Figure 5.9) required to power the ASIC's on the hybrids.

---

[4] A brief distinction is made here between *true data output* and *data output*. Each channel of the VeloPix emits a constant stream of bits at 5.12 Gb/s but true information from collisions can and will result in less data than the constant rate.

The ten data links from each hybrid are sent using differential transmission pairs. The cables each contain seven differential pairs thus four of them are required per module. The signals are transmitted along copper traces with a width and pitch on the order of a few hundred microns using different dielectrics suited for each of the component design requirements. The OPB and VF were produced using Isola I-Tera[5] while the flex cables were produced using DuPont Pyralux AP8575[6]. The signal traces for both the OPB and cables are constructed from copper with a height of 36 µm. For the OPB these traces are separated from the ground trace on the same plane by 185 µm while for the cables they are separated by 230 µm. This difference in separations is due to the different dielectric materials used. These separations were chosen as they were predicted to result in the same characteristic impedance between the OPB and cables. The dielectric thickness above and below the signal traces for the cable is 175 µm before they meet extra sheets of grounded copper while the dielectric thickness of the OPB was 168 µm above and 125 µm below the traces. The cables use through-drilled vias while the OPB uses back-drilled vias to avoid extra reflections from the stubs produced during the manufacturing process. The deliverables use TaiFlex BT40 Cast epoxy adhesive[7].

A cartoon (not to scale) of the cross section for the OPB and cables is given in Figure 5.10 to help visualise the discussion of the stack up. Schematics of trace paths of the two cable variations and the OPB are given in Figure 5.11. A cartoon (not to scale) of the signal path in the VELO Upgrade is given in Figure 5.12.

5.2.5 Continuous Time Linear Equalisation

Transmitted signals lose amplitude due to conductive losses, dielectric losses, reflections and dispersions of the waves. These losses increase with frequency and hence can prove to be significant at the Nyquist frequency of the upgrade. The distortion of the signal can also cause problems with components that require a specific input swing or with reading data at the output (if the signal degrades too much then there is no way to differentiate between a 0 and a 1). This problem can

---

[5] http://www.isola-group.com/wp-content/uploads/data-sheets/i-tera-mt40.pdf

[6] http://www.dupont.com/content/dam/dupont/products-and-services/electronic-and-electrical-materials/flexible-rigid-flex-circuit-materials/documents/PyraluxAPclad_DataSheet.pdf

[7] http://www.msc-polymer.com/en/component/jdownloads/send/1-root/117-taiflex-overview.html

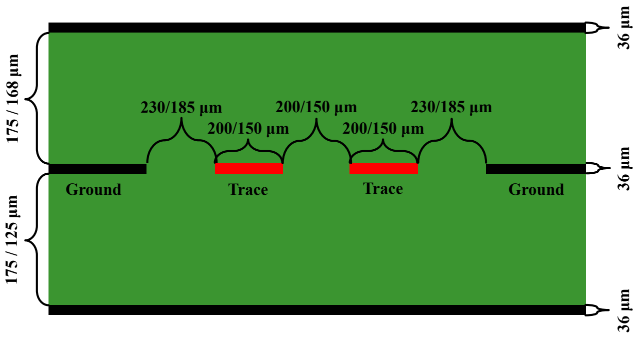

FIGURE 5.10: A mock-up of the stack-up of the OPB and cables (not to scale). The ground layers are given in black, the dielectrics are given in green and the traces are highlighted in red. The dimensions of the data cables/OPB are also given.

be solved by applying an equaliser to the circuit. In the VELO Upgrade passive Continuous Time Linear Equaliser (CTLE) circuits were added to the OPB for each data trace and for the control down-link while the circuits were added to the hybrid for the control up-link. The CTLE attenuates the signal as a function of the frequency and acts in essence as a band-pass filter [136] where it should give a constant signal attenuation up to a determined frequency.

A passive differential CTLE circuit is designed as a typical filter circuit with the transfer function, $H(i\omega, R, C)$, which describes the frequency-dependent modification to the attenuation being defined as

$$H(i\omega, R, C) = \frac{1 + i\omega RC}{1 + \frac{2R}{Z_{\text{in}}} + i\omega RC} \tag{5.1}$$

where R is the value of the resistors on the CTLE circuit, C is the value of the capacitor on the CTLE circuit, ω is the signal frequency and Z_{in} is the input impedance of the gigabit laser driver (GBLD). Hence the transfer function can be maximised at the Nyquist frequency with specific choices of the resistors and capacitors used. The circuit diagram of the CTLE circuit implemented on the electronics is given in Figure 5.13. The input impedance of the CTLE circuit, Z_C, is given by

$$Z_C = \frac{Z_{\text{in}}}{H(i\omega, R, C)}. \tag{5.2}$$

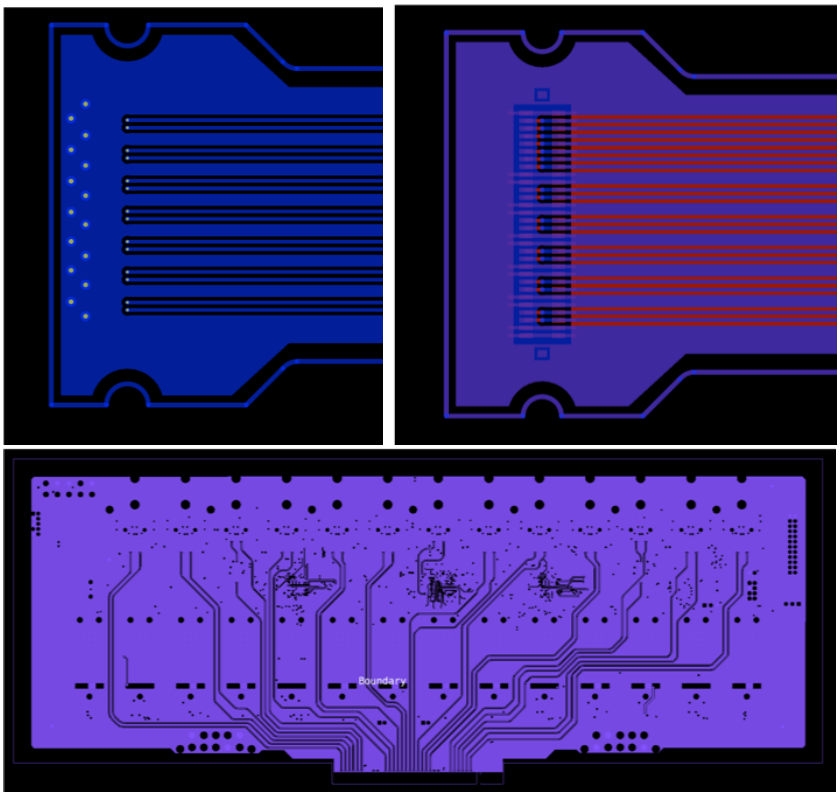

Figure 5.11: The design of the signal traces in the Glasgow deliverables. Top Left - The design of the cable with only data traces. Top Right - The design of the cable with data and control traces. Bottom - The design of the OPB. Credit to Lars Eklund, Sneha Naik and Phil Collins.

To compensate for this, an L-R-L circuit (where L is an inductor) can be added to bridge the two traces with the inductor and resistor values determined by

$$L = \frac{Z_{\text{in}}^2 C}{2} \tag{5.3}$$

$$R_L = Z_{\text{in}} + \frac{Z_{\text{in}}^2}{2R}. \tag{5.4}$$

The predicted response of the transfer function for the data and control links are given in Figure 5.13 with the component values used from the control and data signals given in Table 5.2.

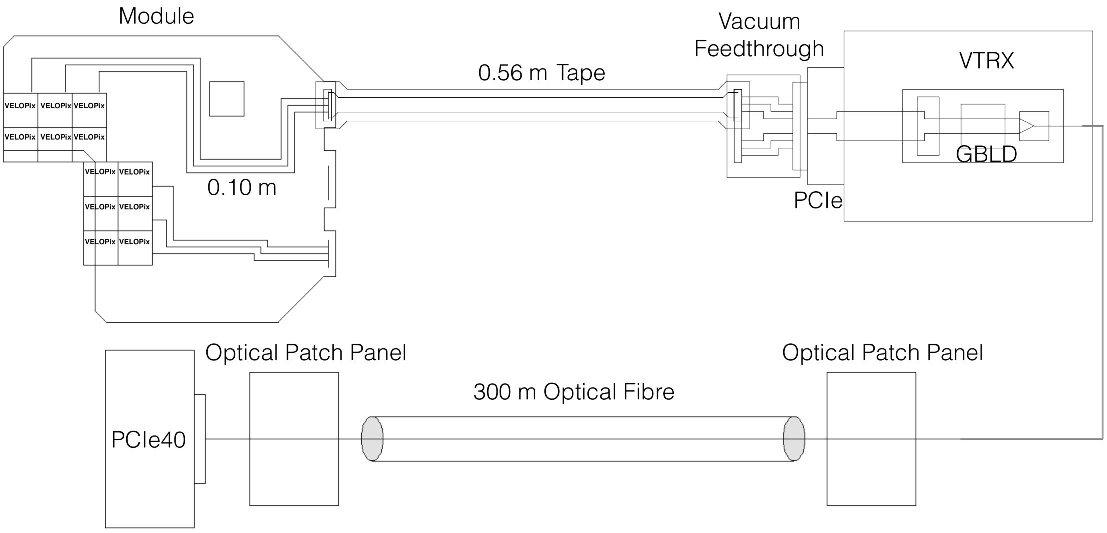

FIGURE 5.12: Sketch of the path the data signals take through a VELO module. Signals will be produced from the VeloPix which will then travel to a VTTX chip where they undergo electrical to optical conversions before travelling 300 m in fibre optic cables to the off-detector readout boards, the PCIe40. It should be noted that the VeloPix has been rotated by 45° since this sketch was produced.

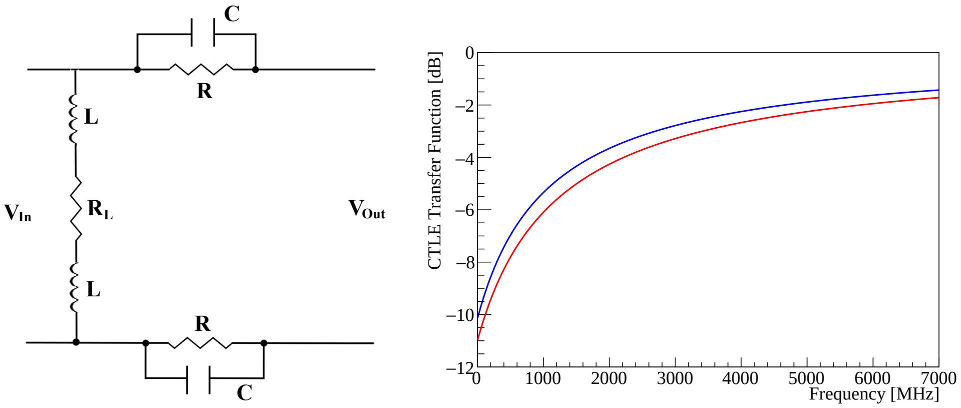

FIGURE 5.13: Left - The circuit diagram for the CTLE with the L-R-L circuit to correct for the impedance of the equaliser. Right - The transfer functions for the data links in red and the control links in blue.

Component	Data Link	Control Link
R	100 Ω	88 Ω
C	2.2 pF	2.7 pF
R_L	150 Ω	161 Ω
L	11 nH	13.5 nH

TABLE 5.2: The values of the components used to construct the CTLE circuit for the data and control links.

Chapter 6

Electronics Characterisation for the VELO Upgrade

To ensure the best possible performance of the electronics in the upgraded VELO it was necessary to produce several prototypes of the deliverables. The first round of prototypes was produced by CERN and were used to test the basic principles of operation of the electronics. This allowed us to discover the dominant features of the electronics before the designs were refined for further prototyping with an industrial partner. The theory behind the measurements is presented in this chapter before the setups used to measure the desired parameters are explained. Finally, the results of these measurements on the various prototypes are discussed which has led to the final design specifications.

6.1 The Theory of Electronics Characterisation

The measurements conducted by the candidate involved characterising the high-speed transmission properties of the prototypes such as the signal losses over the length of transmission, the impedance of the individual components, the properties of the transmission eye diagrams produced by the components and the bit error rates that were recorded.

6.1.1 Sources of High-speed Signal Loss

The typical sources of error in a system such as the one designed for the upgrade are cross-talk, jitter and intersymbol interference [137]. Cross-talk occurs when the signal of one trace interferes with that of another as its propagation induces charge and thus waves on nearby lines. This is minimised in the design by the use of differential signals with extra grounding traces between them and the separation between the traces. Intersymbol interference is caused when a bit on a trace interferes with a later bit causing constructive (or destructive) interference. For example, a “1” can be reflected from a material transition or a discontinuity where it meets a “0” and increases its voltage, potentially above the threshold to be recognised as a “1”. This effect can typically be minimised through high-quality production and avoidance of impedance mismatches (or at least minimise them to reduce the reflected amplitudes).

6.1.2 Scattering Parameters

In circuit theory, a port is defined as point on a system where electrical energy can enter and exit the circuit and thus requires a *pair* of terminals [138]. To truly be a port, the terminals must satisfy the *port condition* that the current of the two terminals is equal in magnitude but opposite in direction. As the VELO upgrade uses differential signals then the network consists of a four-port system. An example of such a system is shown in Figure 6.1.

The typical method to measure signal properties in a system is to stimulate one port with a known voltage then measure the resulting voltage on the other ports, the ratio of these measurements would then describe the signal loss if the measured port is on the same line as the stimulation, cross-talk if it is on a different line or reflection if the measurement is on the same port as the stimulation. In the radio frequency (RF) range that is used for the upgrade, where the signal wavelengths are of the same order as the circuit dimensions, it is no longer useful to characterise data transmission as currents and voltages, instead the parameters are measured in terms of power and energy [139]. In networks, these scattering parameters are measured by stimulating port j with a known amplitude, a_j, and measuring the amplitude at port i, b_i. Once these parameters are measured, their ratio, the scattering parameter (s_{ij}), is obtained and stored within a matrix, the

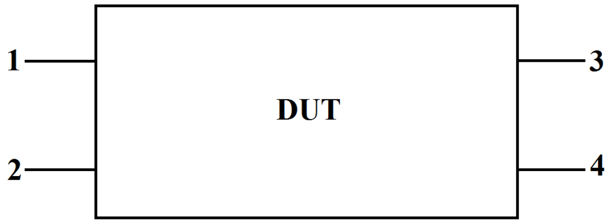

Figure 6.1: Schematic of a differential network with port assignments set as in Equation 6.1.

scattering matrix (S-matrix). If the measurements are repeated over a range of frequencies then the frequency dependent behaviour of a network can be fully characterised [140, 141].

For a 4-port system this results in a 4×4 S-matrix

$$\boldsymbol{S} = \begin{pmatrix} s_{11} & s_{12} & s_{13} & s_{14} \\ s_{21} & s_{22} & s_{23} & s_{24} \\ s_{31} & s_{32} & s_{33} & s_{34} \\ s_{41} & s_{32} & s_{43} & s_{44} \end{pmatrix} \tag{6.1}$$

corresponding to the network setup shown in Figure 6.1. This results in the output signals, **b** being related to the input signals, **a**, by

$$\boldsymbol{b} = \boldsymbol{S}\boldsymbol{a} \tag{6.2}$$

where

$$\boldsymbol{a} = \begin{pmatrix} a_1 \\ a_2 \\ a_3 \\ a_4 \end{pmatrix} \qquad \boldsymbol{b} = \begin{pmatrix} b_1 \\ b_2 \\ b_3 \\ b_4 \end{pmatrix}. \tag{6.3}$$

These results can then be combined to measure differential and common mode transmission and reflection where differential mode is the difference between the two ports and common mode is the average of them. Hence the s-parameters supply information about the differential-differential, differential-common, common-differential and common-common mode signals where the former term comes from the stimulated end and the latter from the receiving end of the network. Differential-differential mode signals are used in high-speed transmissions thus all measurements presented here are of the differential-differential type and are referred to simply as "differential signal[s]" throughout.

The losses of the system are described in terms of their decibel loss

$$\mathrm{Loss[dB]} = -10\log_{10}\left(\frac{P_{\mathrm{out}}}{P_{\mathrm{in}}}\right) \tag{6.4}$$

where $P_{[\mathrm{in/out}]}$ is the measured power of the [input/output] signal. This is measured in practice as the input and output voltage, where

$$P = V^2/R, \tag{6.5}$$

so Equation 6.4 becomes

$$\mathrm{Loss[dB]} = -10\log_{10}\left(\frac{V_{\mathrm{out}}^2 R}{V_{\mathrm{in}}^2 R}\right) = -20\log_{10}\left(\frac{V_{\mathrm{out}}}{V_{\mathrm{in}}}\right) \tag{6.6}$$

The signal losses can be described in terms of the conductive and dielectric losses where the conductive losses are due to the skin effect. These losses can be quantified as [142, 143]

$$-\mathrm{Loss[dB]} = \mathrm{a}\frac{1}{\mathrm{w}}\sqrt{\mathrm{f}} + (1-\mathrm{a})2.3\,\mathrm{D_f}\sqrt{\mathrm{D_k}}\mathrm{f} \tag{6.7}$$

where w is the trace width in millimetres, f is the frequency in gigahertz, D_f is the dissipation factor, D_k is the dielectric constant and a is the conductive loss fraction. The first term describes the conductive losses while the second term describes the dielectric losses. As the skin depth is inversely proportional to the frequency, conductive losses dominate at lower frequency while dielectric losses dominate at higher frequency.

6.1.3 Measuring the Impedance

It was previously discussed that it is important to know the value of the network's impedance, Z, to avoid mismatches in different areas of the system and hence introduce reflections. Also, if it is possible to measure the impedance as a function of propagation time then it is possible to discern the behaviour of the system at different physical points. This can aid in finding areas of the design that could be improved, such as impedance mismatches at interfaces or unexpected changes in trace widths of spacings which will alter the impedance at those regions.

The impedance of a system is given in terms of the inductance and capacitance [141]

$$Z_0 = \sqrt{\frac{L}{C}}. \tag{6.8}$$

As the VELO upgrade uses differential signals, the traces also have a mutual induction, M, which acts to reduce the overall inductance (as the currents in the two traces are equal and opposite) and a mutual capacitance, C_M, which modifies the impedance [137]

$$Z = \sqrt{\frac{L - M}{C + C_M}}. \tag{6.9}$$

As the capacitance scales inversely with the distance between the plates then traces with a smaller separation should have a smaller impedance.

Measurements of the impedance were performed using two methods as a cross check of their reliability. The first technique is to perform a time domain reflectometry (TDR) measurement. This involves stimulating a port at a range of frequencies using step functions then measuring the time for the signal to return to the port. As the impedance of the system changes (whether due to D.C. resistance or the signal transitions into new components, such as between the OPB and VF) the wave is reflected back at varying percentages depending on the reflection coefficient. This allows for a position-dependent measurement of the differential impedance, $Z(x)$, as

$$Z(x) = Z\left(\frac{V(2x/v)}{1 - V(2x/v)}\right) \tag{6.10}$$

where v is the propagation velocity of the wave.

The second technique involves the inverse Fourier Transform of the s-parameters from the frequency to the time domain, this is referred to as a "pseudo-TDR" measurement as it requires the measurement of the s-parameters to be accurate. This technique results in the s-parameters becoming a step-signal which can be converted into an impedance measurement using Equation 6.10.

6.1.4 Measuring Signal Height and Width

The losses and reflections in the system distort the signal quality, hence it is important to understand the signal output. A system could have minimal losses and a perfectly matched impedance between the components, but without the ability to discern 0's and 1's this system would not be suitable. The quality of the signal can be measured via *eye diagrams* which involves repetitively sampling the signal produced and overlaying the results with respect to a clock, the signal amplitude is given on the y-axis and the time on the x-axis. Typically the displayed time is one signal period. This allows for the rise and fall time of the signal, the variations in the signal amplitude and offsets between the measured and expected arrival time of the signal to be measured, amongst other parameters.

The clock is recovered using a phase-locked loop (PLL) which uses the input signal and a negative feedback circuit to obtain the frequency. This is achieved at a fundamental level by using a phase detector and a voltage-controlled oscillator. The signal output from the voltage-controlled oscillator is passed back to the phase detector where its phase is compared to that of the input signal, the phase difference between the two signals is used to alter the input voltage of the oscillator and hence give a different output frequency. This process is then repeated until the phase difference between the two signals is zero and the system becomes "phase locked" [138].

The typical bit pattern used to qualify the signal is a pseudorandom binary sequence (PRBS) [144]. A PRBS-n signal uses a polynomial of order n to generate a pseudorandom sequence using a feedback shift register. A true random sequence can not be produced as it would require infinite memory allocation. It is possible with some setups to add a colour scale to an eye diagram to display the number of signals that pass an amplitude-time coordinate which will display the signal distribution in terms of limits in the standard deviation (σ) of the signal. As the signal offset is Gaussian distributed then a measure of the one σ width of the rise (or fall) of the signal would measure the jitter. Due to the standardisation of the PRBS signal then it is possible to compare the results from different measurements. The eye width and height is important as it gives a qualitative feel for how error prone the system is. However it is important to note that a rigorous test of this is required to quantify the error rate. The peak to peak amplitude of the system will also define the voltage available to power active components so it is

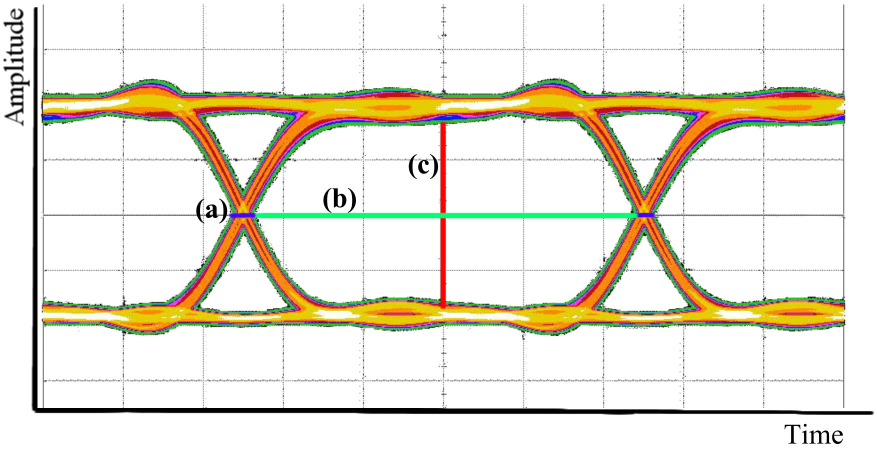

Figure 6.2: An eye diagram produced at 5.12 Gb/s with a PRBS-7 signal. The typical features on an eye diagram of interest for the characterisation of the VELO upgrade are shown. (a) in blue is the jitter of the signal. (b) in green is the eye width. (c) in red is the eye height.

important that this value is within the operating point of these components. A typical eye diagram and its main features are shown in Figure 6.2.

To ensure that the measurements of the eye are accurate it is important to reduce the noise originating from sources other than the DUT. This is achieved by simultaneously observing the incoming signal and its Fourier transform. A gate is then placed around the signal to observe a single bit which is triggered from the rising edge of the signal. The bandwidth of the oscilloscope is then reduced until just before the rise time of the signal becomes dampened.

6.1.5 Measuring the Bit Error Rate

It is also possible to measure the probability of a bit error in the system. This was achieved in these measurements by passing the signal from the pattern generator to a bit error rate tester located on the same module. The clock was recovered using a second order phase-locked loop and each error made at the output was recorded.

As the error is a Poisson process then recording a specific number of errors, $N(\mathrm{Err})$, would lie within the confidence limit, σ,

$$\sigma = 1 \; - \; e^{-N(\mathrm{Err})} = 1 \; - \; e^{-N(\mathrm{Bits})\times\mathrm{BER}} \tag{6.11}$$

where $N(\text{Bits})$ is the number of transferred bit and BER is the measured bit error rate. Thus the number of bits required to establish a confidence limit is

$$N(\text{Bits}) = \frac{-\ln(1-\sigma)}{\text{BER}} \tag{6.12}$$

which will be reached after an acquisition time of

$$T(\text{Acquisition}) = \frac{-\ln(1-\sigma)}{\text{BER} \times \text{Bit Rate}} \tag{6.13}$$

Hence, if you record for $T(\text{Acquisition})$ without seeing an error then you can say that your system has a BER less than the desired rate at that confidence level.

6.2 Experimental Setup

To measure the required parameters, a new lab was set up in the School of Physics and Astronomy at the University of Glasgow. The lab consists of a 13.5 GHz Keysight N5231A PNA-L Network Analyser[1] to meaure the s-parameters and impedance, a 13.5 GHz Keysight DSA91304A Digital Signal Analyser[2] for measuring the eye parameters and a Keysight N4903B J-BERT[3] which is capable of both producing the required high-speed patterns and measuring the bit error rate. A Keysight N4431B Electronic Calibration Kit is used to calibrate the network analyser to remove the effects of the analyser and cables attached to the device under test (DUT). 3.5 mm cables with air dielectric adapters capable of operation at the required frequency range are used to make precise measurements of the signal loss in the network. The air dielectric is used to reduce measurement errors from thermal expansion of the insulating material. The lab setup can be seen in Figure 6.3 along with one of the prototype cables under test.

The results from the network analyser are passed to Keysight's 2015 Physical Test Layer Software (PLTS). PLTS has a built-in feature, the Automatic Fixture Removal, capable to analysing results from open circuits and through circuits to remove extra features in the network that the calibration kit cannot itself remove.

---

[1] https://literature.cdn.keysight.com/litweb/pdf/N5235-90004.pdf?id=2755232
[2] https://literature.cdn.keysight.com/litweb/pdf/5989-7819EN.pdf?id=1364807
[3] https://literature.cdn.keysight.com/litweb/pdf/5990-3217EN.pdf?id=1876866

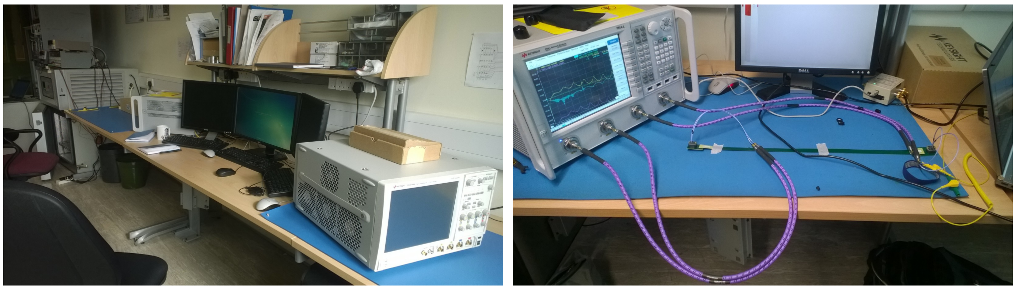

FIGURE 6.3: Left - The current setup of the Glasgow LHCb upgrade lab. Right - One of the new data tapes set up for testing.

This would allow us to remove the effects of the 3.5 mm connecting cables and any adapter boards required to extract the signals from the DUTs.

Two TDR modules were used at CERN, a LeCroy SDA100G[4] and a Tektronix TDS8000[5] to measure the impedance of the first prototyped data cables. The results from these modules were compared with the results from the pseudo-TDR measurements from the network analyser and were found to be compatible with each other. See Section 6.3.2 for further details.

6.3 Results of the Characterisation

6.3.1 Transmission Results

The signal at the Nyquist frequency was required to have an overall loss of approximately 10 dB. The signal losses were measured as a function of frequency between 0.01 GHz and 13.5 GHz in steps of 10 MHz using a 1 kHz bandwidth. This was to allow for sufficient resolution to measure low frequency waves and enough range to notice the modes of the components.

The prototyping of the electronics was conducted in several stages to allow for the gradual refinement of features. The first set of prototypes produced were only the data cables in three variants, the dimensions of the traces in these variants are given in Table 6.1. These prototypes were also produced with a very short variant which consisted of only the Molex connectors and a short length of copper to connect the two ends. These “stubs” could be used to remove the features of

---

[4] http://www.recontest.com/pdf/rte_pdf_1106.pdf

[5] https://uk.tek.com/oscilloscope/csa8000b-manual/csa8000-tds8000-user-manual

Version	Trace Width [µm]	Trace Spacing [µm]	Ground Spacing [µm]
1	200	200	200
2	150	250	225
3	100	100	350

TABLE 6.1: The trace dimensions for the VELO Upgrade cable prototypes produced at CERN.

the connectors from the measurement which allowed for the losses from the traces to be disentangled from the losses from the Molex connectors. The comparison of the three variants with and without the losses due to the Molex connectors are given in Figure 6.4.

When observing the losses when the connectors are still a part of the measurement a regular sinusoidal change in transmission with a frequency of ∼ 150 MHz can be noted (See Figure 6.4). If the transmission speed of copper (used in the links) is taken to be $\sim 2{\times}10^{8}$ m/s then this results in a wavelength of ≈ 1 m with the length of the first mode being ∼ 0.5 m. The length of the cables here are 0.56 m, so this change is due to reflected signals from impedance mismatches at the boundaries of the cables causing frequency dependent constructive and destructive interference of the current signal pulse with the previous one..

It can be seen that version three, the cable with both the thinnest trace width and spacing, appears to perform poorer than versions one and two with the cable connectors attached and also when removed. This substandard behaviour persisted when observing transmission along other traces on the same cables and also when testing the transmission on cables created using a different sheet of kapton. From Equation 6.7 that thinner trace widths will cause an increase in the signal attenuation and hence this variant was expected to result in a larger signal loss.

It was also possible to fit Equation 6.7 to the losses due to the traces to measure whether the attenuation at the Nyquist frequency is dominated by dielectric or conductive losses as can be seen in Figure 6.5. The distribution of the measured transition frequency when measuring the losses shows that at the Nyquist frequency the cables are dominated by conductive losses with the transition to dielectric dominated losses occurring at 8.1 ± 3.6 GHz. The large error is due to both the small sample size and the difficulty in achieving full removal of the losses from the Molex connectors without introducing a high frequency resonance.

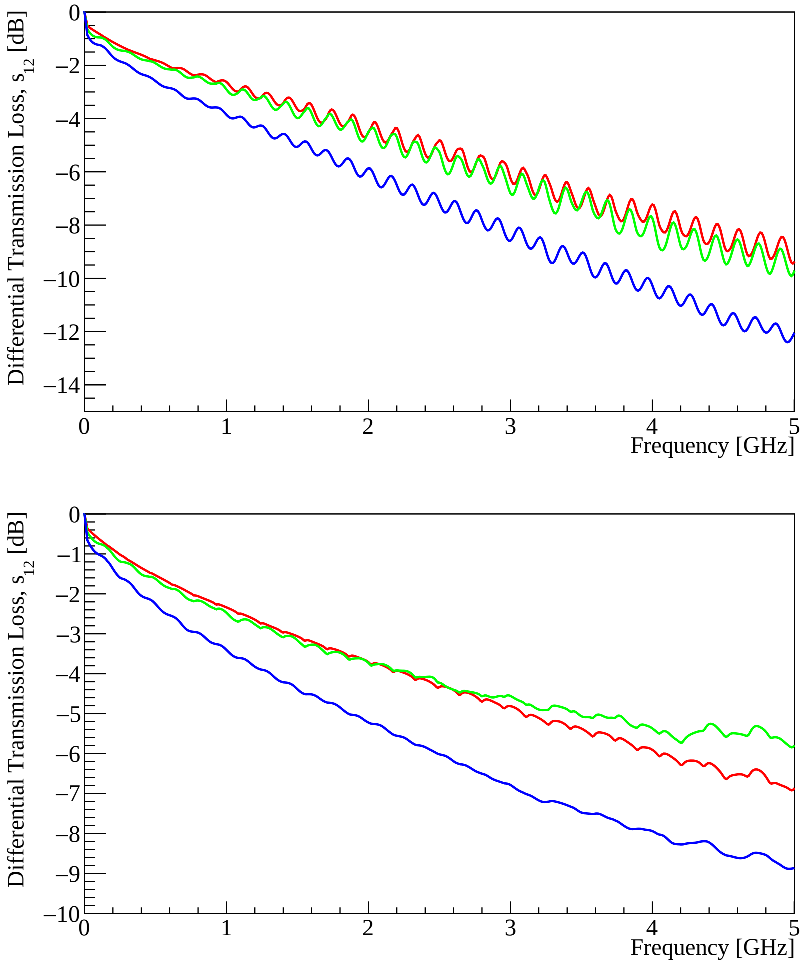

Figure 6.4: Transmission results comparing the three prototype cables produced by CERN along channel three. Top - The losses due to the full cable. Bottom - The losses due to the traces. The red distribution shows the losses with a trace width and spacing of 200 µm. The green distribution shows the looses with a trace width of 150 µm and a trace spacing of 250 µm. The blue distribution shows the losses with a trace width and spacing of 100 µm.

From the results of the losses for the three variants produced by CERN, combined with the measured impedances (see Section 6.3.2), it was decided that a trace width and spacing of 200 µm should be the best option in the VELO upgrade. At this stage, a set of prototype OPB's were produced along with a prototype hybrid which would be capable of mounting a VeloPix to for testing purposes. The prototype hybrid also had a dummy differential trace to emulate the trace length to be expected in the final design. It was possible to measure the cable and hybrid separately while the OPB and VF had to be measured together as there was no PCIe adapter to extract signals from them individually. The cable was found to have a loss of −3.9 dB, the hybrid was found to have a loss of −2.3 dB

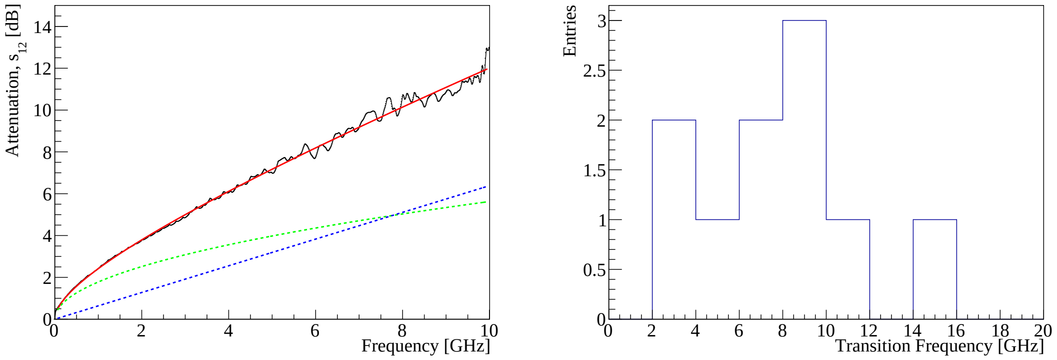

Figure 6.5: Left - Fit to the attenuation in a prototype version one cable produced by CERN using Equation 6.7 with the fit (red), the extracted conductive losses (green dashed) and dielectric losses (blue dashed). Right - Distribution of the measured transition frequency from conductive to dielectric losses for the prototype version one cables.

while the VF and OPB were found to have a combined loss of -3.1 at the Nyquist frequency with a combined transmission loss of -9.4 dB. The signal losses as a function of frequency for the individual and combined components along with the sum of the components are given in Figure 6.6. When comparing the measurement of the full system to the sum of the components there appears to be no significant extra losses coming from signal transition between the connectors in the system. These connectors are hence felt to be suitable for use in the final design.

It is not practically feasible to produce the volume of components required internally at CERN for the upgrade project so an industrial partner was sought that would be able to cope with the demand. The results from the previous tests were used to refine the designs before producing a set of pre-production prototypes. The OPB and VF were produced with a trace width and spacing of 150 µm while the cables were produced with the version one specifications. The CTLE circuit was added to the up-links of the OPB to the VeloPix to have constant transmission loss with respect to the frequency in the region of the Nyquist frequency. Further CTLE circuits were added to the the control links of the hybrid. This was advantageous as it allowed for a comparison between traces with and without CTLE circuits. The full scale pre-production of the cables, VF and OPB that were tested is shown in Figure 5.9. Measurements of the losses across all traces of this setup with a CTLE circuit found that the mean loss was -11.25 dB with a standard deviation of 0.72 dB. The results of the differential transmission losses including a trace without a CTLE circuit can be seen in Figure 6.7 along with the

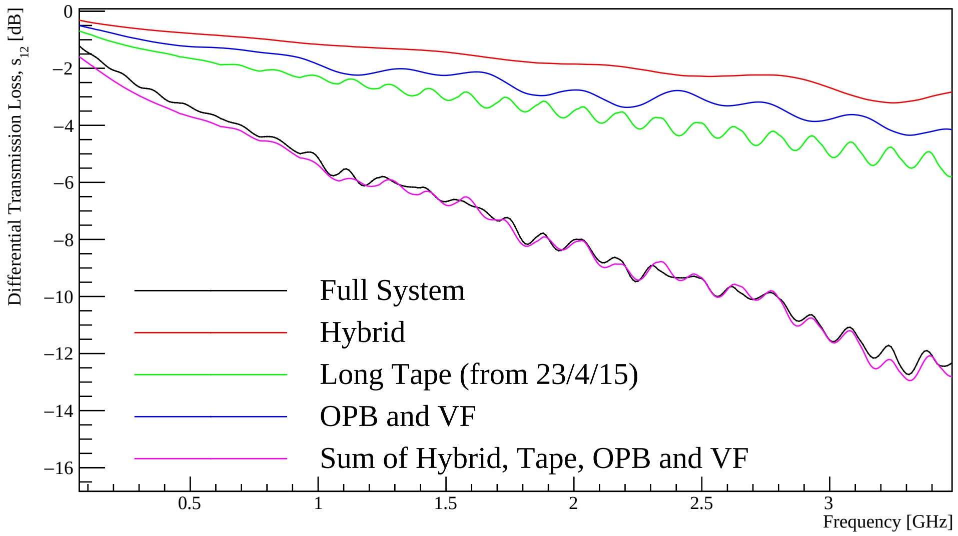

FIGURE 6.6: The measured transmission losses as a function of the signal frequency for the initial prototypes of the full electrical system produced. The overall loss was measured to be less than 10 dB. Red - the losses from the hybrid. Green - the losses from the data cable. Blue - the losses from the VF and OPB. Black - the losses of the combined system. Purple - the sum of the red, green and blue distributions.

distribution of measured losses at the Nyquist frequency for those traces with a CTLE circuit.

The specifications of the CTLE circuit were designed to give a 10 dB loss up to the Nyquist frequency at which point the losses would increase again as for the traces without a CTLE circuit. This behaviour is apparent in Figure 6.7, the result in red is for a trace without an attached CTLE circuit. These results show that the circuit does indeed give a flatter attenuation at frequencies at or below the Nyquist frequency. The response of the CTLE circuit can be determined by taking the ratio of the trace without the circuit and the mean of the traces with the circuit. As there are three traces on the pre-production prototypes with a circuit, it would be possible in theory to use the mean of those traces however in practice the other two traces were unavailable during testing.

6.3.2 Impedance Results

To avoid mismatches and hence the introduction of reflections within the signal, each component was required to have a characteristic impedance of 100 Ω. The impedance of the prototypes produced by CERN were measured using the two

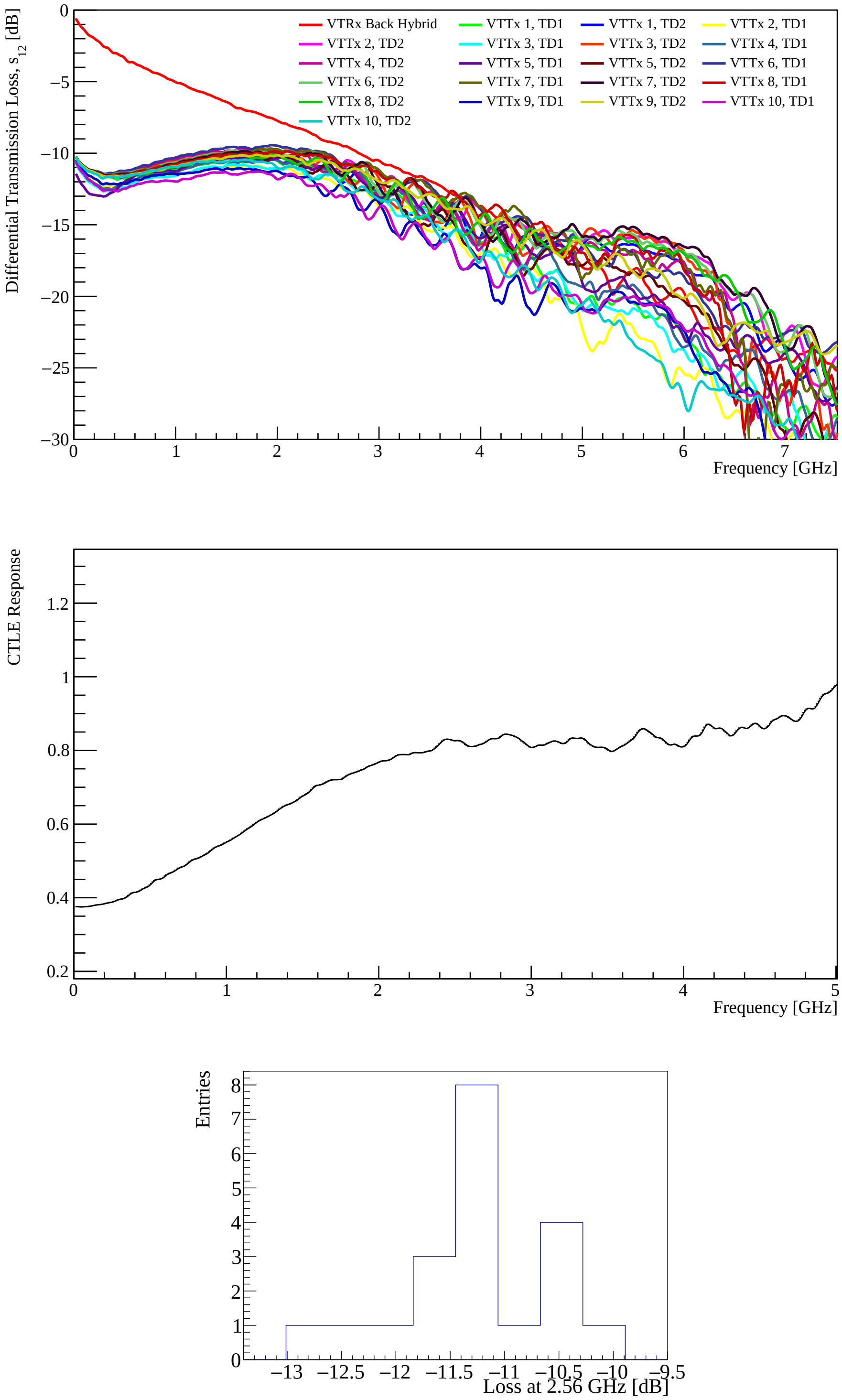

Figure 6.7: Top - The measured differential transmission losses for the full scale pre-production prototype across 20 traces. The red trace does not have a CTLE circuit attached while the rest of the traces do. Bottom - The ratio of the differential transmission losses for a trace without a CTLE circuit to the mean of the traces with a CTLE circuit, showing its response from the pre-production prototype. A 10 decibel loss is equivalent to a signal degrading to 33% of its initial amplitude. The CTLE circuit was designed to peak at approximately the Nyquist frequency to give the best performance.

		Z_{Diff} [Ω]			
Trace	DUT	LeCroy SDA100G	Tektronix TDS800	Fourier Transform	Simulation
0	V1	101.7→107.1	98.9	101.1→107.4	86
	V2	117.4→124.7	116.2	117.4→125.7	102
	V3	116.4→129.5	115.6	115.9→131.1	101
6	V1	101.7→107.6	-	100.9→107.6	-
	V2	117.2→127.0	-	117.0→126.9	-
	V3	117.4→131.6	-	118.6→132.4	-

Table 6.2: Impedance measurements performed on the three cable versions produced by CERN using three independent machines and compared to the simulation predictions. Both machines give similar results to the Fourier transform but they are not similar to the simulation. The magnitude difference between each of the variants is the same for both the simulation and the prototypes.

physical TDR modules previously described and compared with the inverse Fourier transform of the equivalent s-parameters measured using the network analyser, the results of which are given in Table 6.2. It was discovered that version one of the prototypes meets the impedance requirements while versions two and three are more that 15% over the specification. The results are surprising as versions two and three were predicted to be closer to the specification than version one. The magnitude difference in the impedance between the variants is the same in both simulation and the prototypes which led us to believe that there was something we did not understand about the physical properties of the cables produced. The simulation was improved by increasing the quantity of glue used in the simulations and minor alterations to the geometry of the traces from rectangles to trapezoids.

When the differences between the simulation and what was observed in the cross section of the cable were incorporated into the simulation studies, version one of the cable was predicted to have a characteristic impedance closer to 100 Ω while the value for versions two and three increased. From these results and those of the transmission losses it was decided that a trace width and spacing of 200 µm would give the best performance for the upgrade.

Once the full scale prototypes had been produced it was also possible to measure the impedance of this full system from the pseudo-TDR measurements of the s-parameters. The resulting measurement of the characteristic impedance as a function of signal transmission time for the available traces is shown in Figure 6.8. The first structure visible on the far left is the adapter board used to connect the cable to the network analyser. The signal transition across the Molex connector

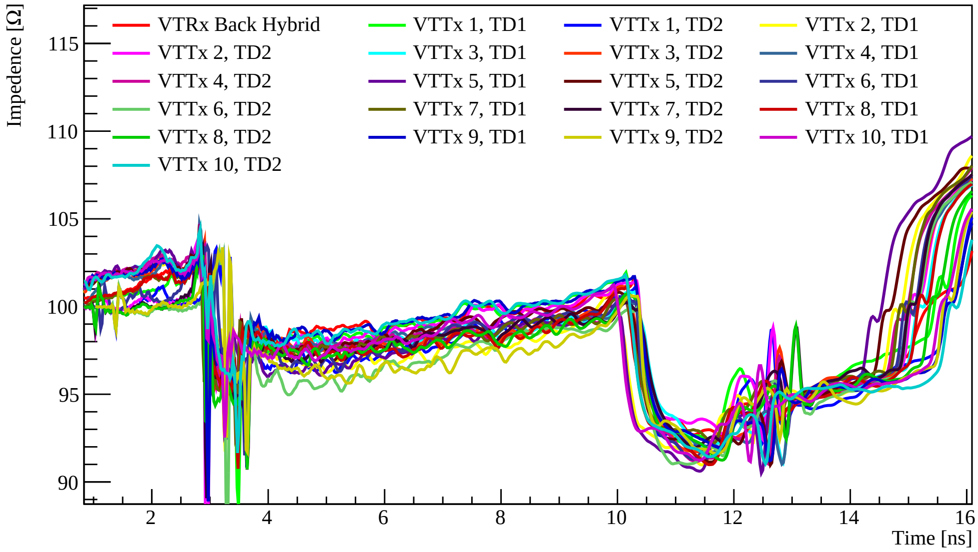

FIGURE 6.8: The measured impedance of the pre-production prototypes of the cables, VF and OPB for all available traces. This measurement was performed via the Fourier transform of the s-parameters.

is then visible as a sharp change in impedance. The long structure from approximately 3.8 ns to 10 ns is the measured impedance of the cables before the transition into the VF which is of lower impedance. A small increase in the impedance of the VF can be seen just before the transition to the OPB which is thought to be due to a widening of the traces as they move from the outer edge of the VF to the inside to meet the PCIe connector, decreasing the capacitance and hence increasing the impedance as per Equation 6.9. The last structure visible on the far right is the impedance of the OPB.

6.3.3 Eye Measurements and Jitter

The eyes produced by the prototypes were created under as realistic a scenario as feasible. The upper and lower voltages were set to ±300 mV which is the expected output of the GWT in the VeloPix, resulting in a 1.2 V input swing with a data rate of 5.12 Gb/s. The data pattern sent was a PRBS-31 signal. To avoid high frequency noise from the oscilloscope, the bandwidth was limited to 4 GHz by the method described in Section 6.1.4 which is above the Nyquist frequency. The clock recovery was achieved via a second order phase locked loop. The oscilloscope was setup to simultaneously display the incoming bit pattern and its measured offset which is the difference between the measured and predicted arrival time of the signal. This offset was then stored in a histogram where the full width at half maximum gives the jitter of the DUT. Finally the real time eye was produced and its width and height were recorded.

The eye properties were measured for each of the traces from the pre-production prototypes which had a CTLE circuit attached. A screenshot from a typical test can be seen in Figure 6.9. It can be seen that even though a swing of 1.2 V was applied, the measured swing at the output of the eye is 400 mV from peak to peak which is to be expected as the CTLE circuit results in a 10 dB loss in the region of interest. The mean eye height was measured to be 147.1 mV with a standard deviation of 9.1 mV while the mean eye width was measured to be 142.3 ps with a standard deviation of 5.3 ps. There was no strong correlation observed between the eyes height and width as can be seen in Figure 6.10. The signal jitter for each trace was measured by a Gaussian fit to the histogram of the offset of each bit. The observed offset for each trace is shown in Figure 6.11 where the mean jitter was measured to be 6.7 ps with a standard deviation of 0.5 ps.

6.3.4 Measuring the Bit Error Rate

The requirement for the BER was to have an error rate of $< 10^{-13}$ at a $2\,\sigma$ confidence level. Using Equation 6.13 this means that there should be less than 1 error for every 100 minutes of acquisition time. The first prototyped cables produced by CERN were found to achieve this requirement, however when the OPB, VF and hybrid produced by CERN were measured they were found to have a BER $= 3.72 \times 10^{-9}$ and hence were unsuitable at that stage. Observations of the eye diagram for this setup showed it to have just closed at the bit rate which can be seen in Figure 6.12. As CTLE circuits are known to improve eye openings then it was felt that these results justified the pursuit of constructing the CTLE circuits. After the pre-production prototypes were delivered with the specified CTLE parameters the traces were measured and found to meet the requirements of the BER by recording their error rate using a PRBS signal at 5.12 Gb/s for an acquisition time of 100 minutes.

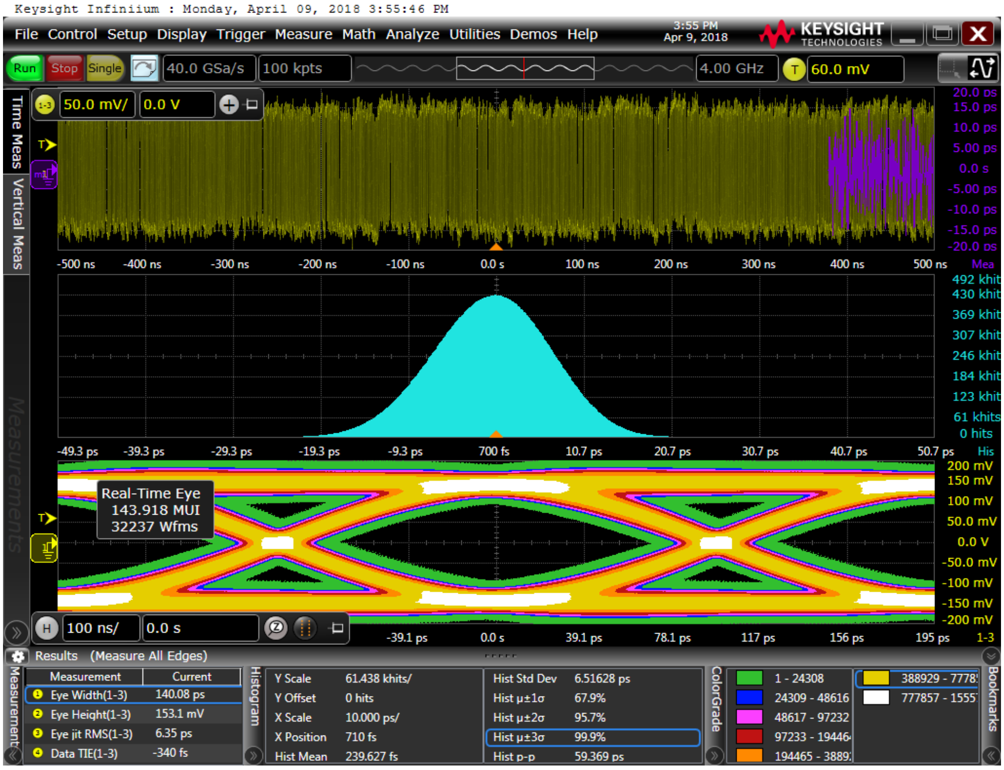
Keysight Infiniium : Monday, April 09, 2018 3:55:46 PM

Results (Measure All Edges)

Measurement	Current
❶ Eye Width(1-3)	140.08 ps
❷ Eye Height(1-3)	153.1 mV
❸ Eye jit RMS(1-3)	6.35 ps
❹ Data TIE(1-3)	-340 fs

Y Scale	61.438 khits/
Y Offset	0 hits
X Scale	10.000 ps/
X Position	710 fs
Hist Mean	239.627 fs

Hist Std Dev	6.51628 ps
Hist μ±1σ	67.9%
Hist μ±2σ	95.7%
Hist μ±3σ	99.9%
Hist p-p	59.369 ps

🟩	1 - 24308	🟨	388929 - 7778
🟦	24309 - 48616	⬜	777857 - 1555
🟪	48617 - 97232		
🟥	97233 - 19446		
🟧	194465 - 3889		

FIGURE 6.9: A screenshot of a typical trace under test from the pre-production prototype using a PRBS-31 signal at 5.12 Gb/s. The top distribution shows the incoming data pattern in yellow and the offset of the signal from the difference between the measured and predicted arrival time of the signal in purple. The middle plot shows the timing distribution of the signal with respect to the threshold. The bottom plot shows the eye produced by the prototypes. The bottom left box shows the measured parameters of the eye, the middle box shows the measured parameters of the signal offset and the bottom right box shows the numbers of signals corresponding to each colour scale in the eye diagram.

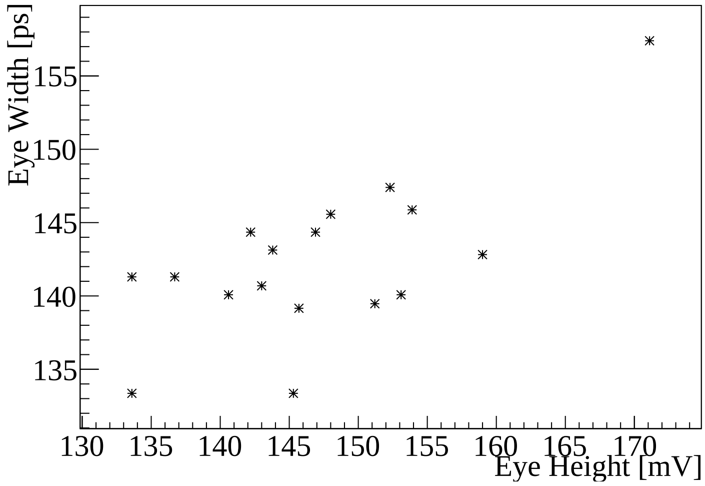

FIGURE 6.10: Scatter plot of the measured eye height and width for each measured trace.

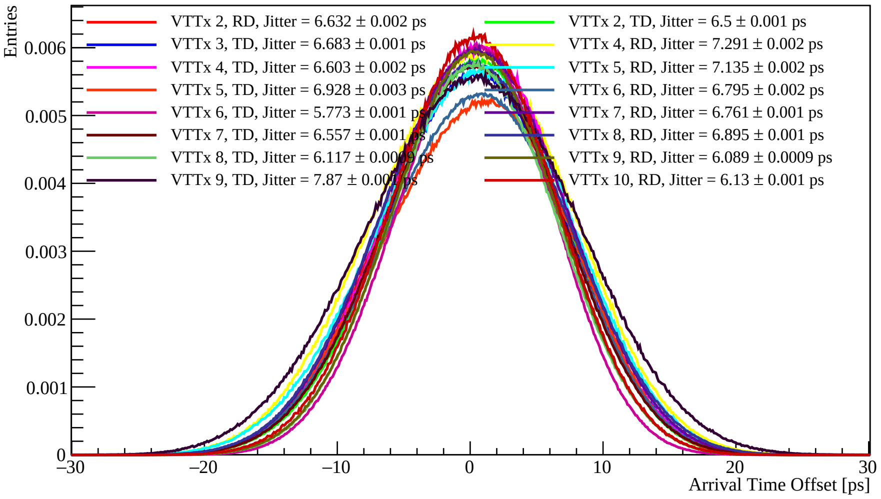

FIGURE 6.11: The overlayed histograms of the signal offsets for each trace and their corresponding measured jitter. To avoid overcrowding the figure, the fit to each offset is not drawn.

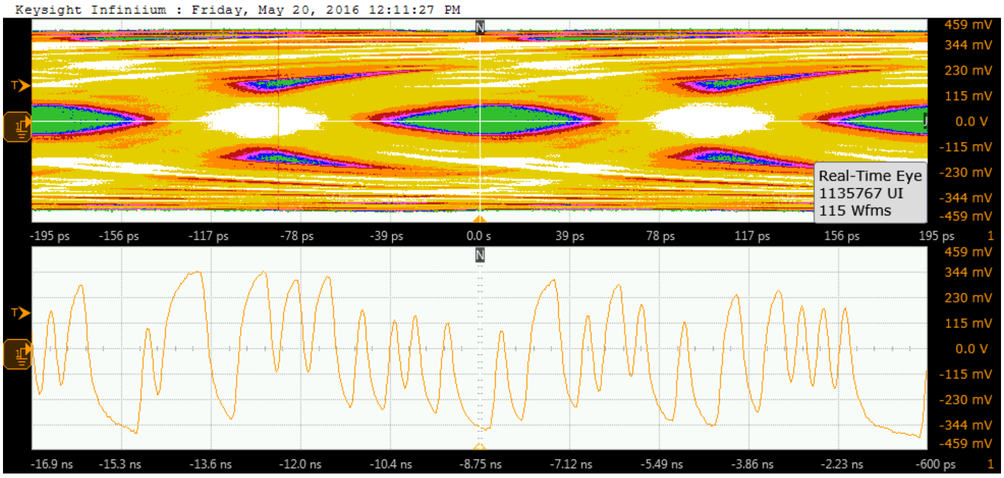

FIGURE 6.12: Top - The eye diagram produced by the half-scale prototypes produced by CERN using a PRBS-7 signal at 5.12 Gb/s. It can be seen that the eye has just closed (green is the lowest valued colour scale) which resulted in a large bit error rate. Bottom - The bit pattern measured at the output of the setup.

6.3.5 The Effect of Repeated Bending

The VELO is the closest subdetector to the LHC beam and as a safety precaution it is retracted from the beam until the conditions for stable beams are met and physics data is ready to be collected. As the rest of the electrical components in the VELO upgrade will be rigid[6], the cables are required to absorb forces from the motion, hence they are designed as flexible circuits.

We devised a structure to test the effect of repeated bending on the tapes in case they fracture or their performance degrades. A bed was created to secure a cable to and then a program was written to bend the tape by a specified horizontal distance a number of times. We performed the bends over a distance of 3 cm for a period of three minutes per bend which is similar to the distance that will be covered in the upgrade and the closing time of the VELO. The cable was bent 3000 times. This value was chosen to represent the expected number of opening and closing motions they are expected to endure, with a large safety margin added (8 years of operation × 8 months use per year × 1 open and close per day $\approx$ 2000 bends, then add 50% for commissioning, shorter fills and reopenings during fill). After 3000 bends no noticeable change in performance was observed as can be seen in Figure 6.13.

Overall, the results from the testing of components for the VELO upgrade have demonstrated that they are capable of transmitting signals of the required quality. The average signal loss at the Nyquist frequency was 1.25 ± 0.72 dB greater than the desired losses however the quality of the eyes produced, the minimal bit error rate and the measured impedance of the system is all within the requirements and more than compensates for the extra signal loss. The results presented here should ensure that the upgrade project meets its goals and ensure the best possible physics performance for LHCb.

---

[6] This is true except for some small flex cables on the rigid module which were added to avoid thermal deformations during heating or cooling. The small cables are not involved in the motion of the detector.

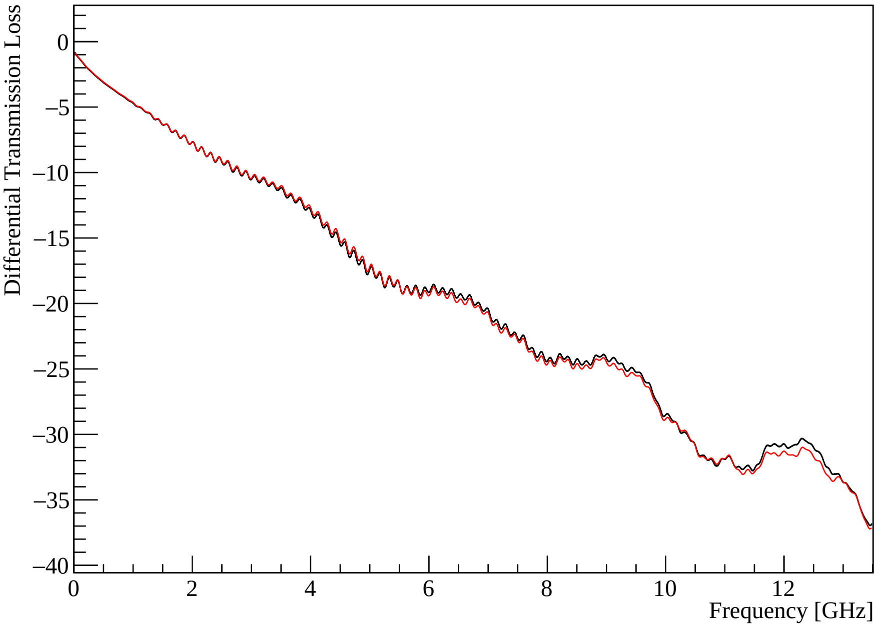

FIGURE 6.13: Results from repeated bending for a differential trace of one of the data cables. The signal losses across all traces of this tape were measured before and after 3000 bends. Black - before bending. Red - after bending.

Part III

Time Dependent Studies of B$\rightarrow h^{+}h^{'-}$ Decays

Chapter 7

$\mathrm{B}\!\to\! h^+h'^-$ Lifetime Analysis

The studies of $\mathrm{B}\to h^+h'^-$ decays can reveal a depth of interesting results. It was shown in Chapter 2 that the decays of neutral mesons show different behaviour depending on their flavour at production, where the decay rates are described by

$$\Gamma_f = e^{-\Gamma t}\left[\cosh\left(\frac{\Delta\Gamma}{2}t\right) + \mathcal{A}_f^{\Delta\Gamma}\sinh\left(\frac{\Delta\Gamma}{2}t\right) + C_f\cos(\Delta m t) \;-\; S_f\sin(\Delta m t)\right] \tag{7.1}$$

and

$$\bar{\Gamma}_f = e^{-\Gamma t}\left[\cosh\left(\frac{\Delta\Gamma}{2}t\right) + \mathcal{A}_f^{\Delta\Gamma}\sinh\left(\frac{\Delta\Gamma}{2}t\right) \;-\; C_f\cos(\Delta m t) + S_f\sin(\Delta m t)\right]. \tag{7.2}$$

If the flavour cannot be discerned the trigonometric terms vanish but as long as $\Delta\Gamma$ is non-zero then the hyperbolic terms remain. This is the case for B_s^0 mesons where $\Delta\Gamma = 0.088 \pm 0.006$ [36] showing that it is possible to measure $\mathcal{A}_{\mathrm{KK}}^{\Delta\Gamma}$ via a lifetime measurement of the $\mathrm{B}_s^0\to \mathrm{K}^+\mathrm{K}^-$ system. The channels $\mathrm{B}^0\to \mathrm{K}^+\pi^-$ and $\mathrm{B}_s^0\to \pi^+\mathrm{K}^-$ make up part of the "$\mathrm{B}\to \mathrm{K}\pi$ puzzle" where a set of these decays display inconsistencies between the combination of their branching fractions and CP asymmetries [145]. The decay $\mathrm{B}^0\to \mathrm{K}^+\pi^-$ differs from the decay $\mathrm{B}^+\to \mathrm{K}^+\pi^0$ by the change of the d-quark to a u-quark with the tree and loop decay amplitudes expected to have the same value for each decay hence they should have the same values of A^{CP}. However, A^{CP} ($\mathrm{B}^+\to \mathrm{K}^+\pi^0$) has been measured to be 0.037 ± 0.021 [36] while a recent LHCb measurement using Run I data has found A^{CP} ($\mathrm{B}^0\to \mathrm{K}^+\pi^-$) to be -0.084 ± 0.004 (stat.) ± 0.003 (syst.) [61].

This chapter describes measurements of the effective lifetimes of various B→ $h^+h'^-$ decays. They were performed as an update to a previous analysis by LHCb Glasgow which used $1\,\mathrm{fb}^{-1}$ of data collected in 2011 [146] whereas this analysis presents $3\,\mathrm{fb}^{-1}$ of data collected at the LHCb detector during Run I of the LHC. The work was conducted in collaboration with Lars Eklund, Michael Alexander and Sarah Karodia , who carried out a PhD on this topic [147]. As such a significant portion of the analysis was performed by other members of the group. The candidate performed the PID selection and the studies of the invariant mass distribution of the pK^- and $\mathrm{p}\pi^-$ decay spectra. The multivariate analysis used to reduce the combinatorial background contamination, the invariant mass fits to the other final states, the effective lifetime measurements and the systematics studies were performed by Sarah Karodia. The lifetime acceptance correction was performed by Vladimir Gligorov. The fitting software was developed by members of the LHCb collaboration while the specific lifetime fitter was developed by Michael Alexander.

The techniques used to measure the effective lifetimes of B → $h^+h'^-$ decays are similar to those used to measure CP observables, which is the topic of Chapter 8. The purpose of this chapter is to describe the underlying methods and implementation of these techniques within LHCb before describing their specific application to measure CP violation in B→ $h^+h'^-$ decays in the following chapter. The final measurements of the effective lifetimes of these decays are presented at the end of this chapter for completeness only.

7.1 Candidate Selection

7.1.1 Trigger and Stripping Selections

The effective lifetime of six B→ $h^+h'^-$ decay channels; $\mathrm{B}^0\to\pi^+\pi^-$, $\mathrm{B}^0\to\mathrm{K}^+\pi^-$, $\mathrm{B}^0_\mathrm{s}\to\pi^+\mathrm{K}^-$, $\mathrm{B}^0_\mathrm{s}\to\mathrm{K}^+\mathrm{K}^-$, $\Lambda^0_\mathrm{b}\to\mathrm{pK}^-$ and $\Lambda^0_\mathrm{b}\to\mathrm{p}\pi^-$ and their corresponding charge-conjugate states were studied. To observe suitable candidates from the significant volume of data collected we are required to apply a preselection. We initially impose trigger cuts on the mother particle in the decay chain. LHCb can trigger on the signal candidate (TOS) or trigger independently of the signal candidate (TIS). To select the candidates, two L0 trigger lines (`L0Global_TIS` or `L0Hadron_TOS`), one HLT1 trigger line (`Hlt1TrackAllL0Decision_TOS`) and one

HLT2 trigger line (`Hlt2B2HHDecision_TOS`) are applied to the LHCb data set. The definitions of several variables used to select the candidates are given in Table 7.1 and the trigger requirements are defined in Tables 7.2 to 7.4.

The triggered data sample is further processed to produce smaller data samples for use in offline analysis. This process is known as “stripping”. The candidates used in this analysis are selected by the `Hb2Charged2BodyB2Charged2BodyLine` stripping line in the `BHADRONCOMPLETEEVENT` stream from the Stripping20 pass. This stripping line was designed specifically to select B$\rightarrow h^+h'^-$ candidates. The line reconstructs all candidates using the $\pi^+\pi^-$ decay hypothesis. The selection requirements are listed in Table 7.5. The selected candidates are then re-fitted under the correct mass hypothesis before being passed on to the offline selection. Inverting the mass hypothesis of the daughters will change the mass range of the sample. For example, as the kaon and proton are both more massive than the pion then this will increase the mass range due the change in the time component of the 4-momentum.

Variable	Definition
$m_{\mathrm{d_1d_2}}$	The invariant mass of the daughter particles.
IP	The minimum distance between the primary vertex and the particle track. This is taken with respect to all primary vertices in the event.
IPχ^2	The difference in χ^2 of the primary vertex fit with and without the track.
DOCA	The distance of closest approach between two tracks in the event.
DIRA	The cosine of the angle between the direction and momentum vectors.
Flight Distance χ^2	The χ^2 from the flight distance vector and its associated covariance matrix.
Ghost Probability	The probability of a track being reconstructed from random hits within the detector.

Table 7.1: The definitions of several variables used to select the decays of interest.

7.1.2 Particle Identification

To select the desired channels, we decided on suitable particle identification (PID) selections. This involves combining the likelihood distributions for different particles using well calibrated (pure) data samples and observing the resulting efficiency

Trigger Line	Cuts Imposed
`L0Global_TIS`	
`L0Hadron_TOS`	$E_T > 3240$ MeV $SPD_{Mult} < 450$

Table 7.2: L0 trigger requirements imposed on the daughters in the LHCb 2011, 2012, 2015 and 2016 data sets.

Trigger Line	Cuts Imposed
`Hlt1TrackAllL0`	$p > 3$ GeV/c $p_T > 1.6$ GeV/c Track χ^2/nDoF < 2 IP > 0.1 mm IP$\chi^2 > 16$

Table 7.3: `Hlt1TrackAllL0` trigger requirements imposed on the daughters in the LHCb 2011 and 2012 data sets.

Cut Type	Cuts Imposed
Combination	Sum $p_T >$ 4500 MeV $4700 \leq m_{d_1d_2} \leq 6200$ MeV/c^2 DOCA $\chi^2 < 9$
Daughter	$p_T >$ 1000 MeV min(IPχ^2) > 16 Track χ^2/NDOF < 3
Mother	DIRA > 0.99 IP $\chi^2 < 9$ Flight Distance $\chi^2 > 100$ $p_T >$ 0 MeV

Table 7.4: `Hlt2B2HH` trigger requirements imposed on the LHCb 2011, 2012, 2015 and 2016 data sets.

in each of the final states for different cut combinations when using Monte Carlo (MC) signal samples.

Particle identification is achieved at LHCb using combined information from the RICH detectors, the calorimetry system and the muon detectors as described in Section 3.2.2. Calorimeters and muon detectors are standard parts of modern HEP experiments. However, unlike the general purpose detectors at the LHC, LHCb's geometry allows for the addition of the RICH detectors which vastly improves particle identification, compensating for the lower integrated luminosity with respect

Cut Type	Cuts Imposed
Combination Cuts	$4600 \leq m_{\mathrm{d_1d_2}} \leq 6000\,\mathrm{MeV}/c^2$ IP > 0.27 mm `OR` IP $\chi^2 > 200$ $p_{\mathrm{T}} > 2700\,\mathrm{MeV}/c$ DOCA < 0.08 mm
Daughter Cuts	$p_{\mathrm{T}} > 1100\,\mathrm{MeV}/c$ IP $> 0.15\,\mathrm{mm}$ `OR` IP $\chi^2 > 100$ Track $\chi^2/\mathrm{nDoF} < 3$ Track Ghost Prob. < 0.8
Mother Cuts	$4800 \leq m_{\mathrm{d_1d_2}} \leq 5800\,\mathrm{MeV}/c^2$ $p_{\mathrm{T}} > 1200\,\mathrm{MeV}/c$ $\tau_{\mathrm{B}} > 0.6$ ps IP $< 0.08\,\mathrm{mm}$ `OR` IP $\chi^2 < 12$

TABLE 7.5: `Hb2Charged2BodyB2Charged2BodyLine` Stripping Requirements for B→ $h^+h'^-$ candidates.

to ATLAS and CMS[1]. This is especially apparent for separating pions and kaons. The likelihood of the particle identity for each track is constructed using the combined information of the previously mentioned subdetectors, and the difference in likelihood of the particle hypothesis is used to separate the different final states of decays.

The PIDCALIB package [148] was developed by LHCb to assist in particle identification within analyses. PIDCALIB uses well-calibrated data samples of pions, kaons, protons, muons and electrons taken under various conditions such as magnet polarity and run year without any PID information to calculate the event-by-event efficiency of a data set under different particle hypotheses which can be combined into a global efficiency. Using true event data for the calibration samples is preferable to using MC which can be poorly modelled for PID discriminants. For example, an event's track multiplicity can be large so modelling these discriminants can be both CPU intensive and storage heavy. PID cuts can be applied to the calibration samples and the number of events passing the cut can be used to give an efficiency.

These efficiencies are known to vary as a function of several other variables hence it is necessary to compute the cut efficiencies in a multi-dimensional space of those variables, where the binning is chosen such that the cut efficiency is roughly

---

[1] ALICE also has a Cherenkov detector but a comparison between the physics goals of LHCb and ALICE is out of the scope of this thesis.

constant within them. The same binning scheme can be applied to the channel under investigation and compared to the calibration sample to give the event-by-event efficiencies.

Final-state selection efficiencies were obtained by separating events from signal MC into bins of pseudorapidity and momentum. The discrimination between different particles as a function of momentum in the RICH detectors can be seen in Figure 3.14. The pseudorapidity range was taken to cover the full detector acceptance of LHCb while the momentum of the daughters was required to be between $3\,\mathrm{MeV} \leq p \leq 100\,\mathrm{MeV}$ to avoid saturation of the Cherenkov angles within the RICH detectors which can be seen in Figure 3.14. A 3D binning with track multiplicity was previously used but later discarded as it was found that, without reweighting, multiplicity is poorly modelled in MC. The same procedure was repeated to measure the background contaminations using MC samples of the channels expected to be dominant within the analysis. The variation in the predicted signal efficiency for the final states as a function of different $\Delta\log(\mathcal{L}_{\mathrm{p_1p_2}})$ cuts are shown in Figure 7.1.

7.1.3 Final-state Contaminations

As particle identifications are based on likelihood distributions, it is possible to misidentify one or both daughters in the selection of the candidates. The dominant source of these decays is believed to be due to other B$\to h^+h'^-$ channels (excluding $\mathrm{B}^0 \to p\bar{p}$ decays which have a branching fraction of $(1.25 \pm 0.32) \times 10^{-8}$ [149] compared to the branching fractions of the other $\mathrm{B} \to h^+h'^-$ decays which are of order $\mathcal{O}(10^{-6})$ to $\mathcal{O}(10^{-5})$ [36]). An event-by-event misidentification efficiency was calculated using the same method to estimate the signal efficiencies using dedicated samples of the background decays. The relative contamination, k^{mid}_{chann}, of these backgrounds in each final state was quantified for each cut combination, where *chann* is the channel being probed and *mid* is the misidentified channel contaminating the signal. The generic form of the equation for obtaining the contamination fraction is

$$k^{\mathrm{mid}}_{\mathrm{chann}} = \frac{f_{\mathrm{mid}}}{f_{\mathrm{chann}}}\frac{\mathcal{B}_{\mathrm{mid}}}{\mathcal{B}_{\mathrm{chann}}}\frac{\omega_{\mathrm{mid}}}{\varepsilon_{\mathrm{chann}}} \tag{7.3}$$

where f_{P} is the hadronization fraction of the mother particle, $\mathcal{B}_{\mathrm{P}}$ is the branching fraction of the decay, ω_{mid} is the misidentification efficiency and $\varepsilon_{\mathrm{chann}}$ is the

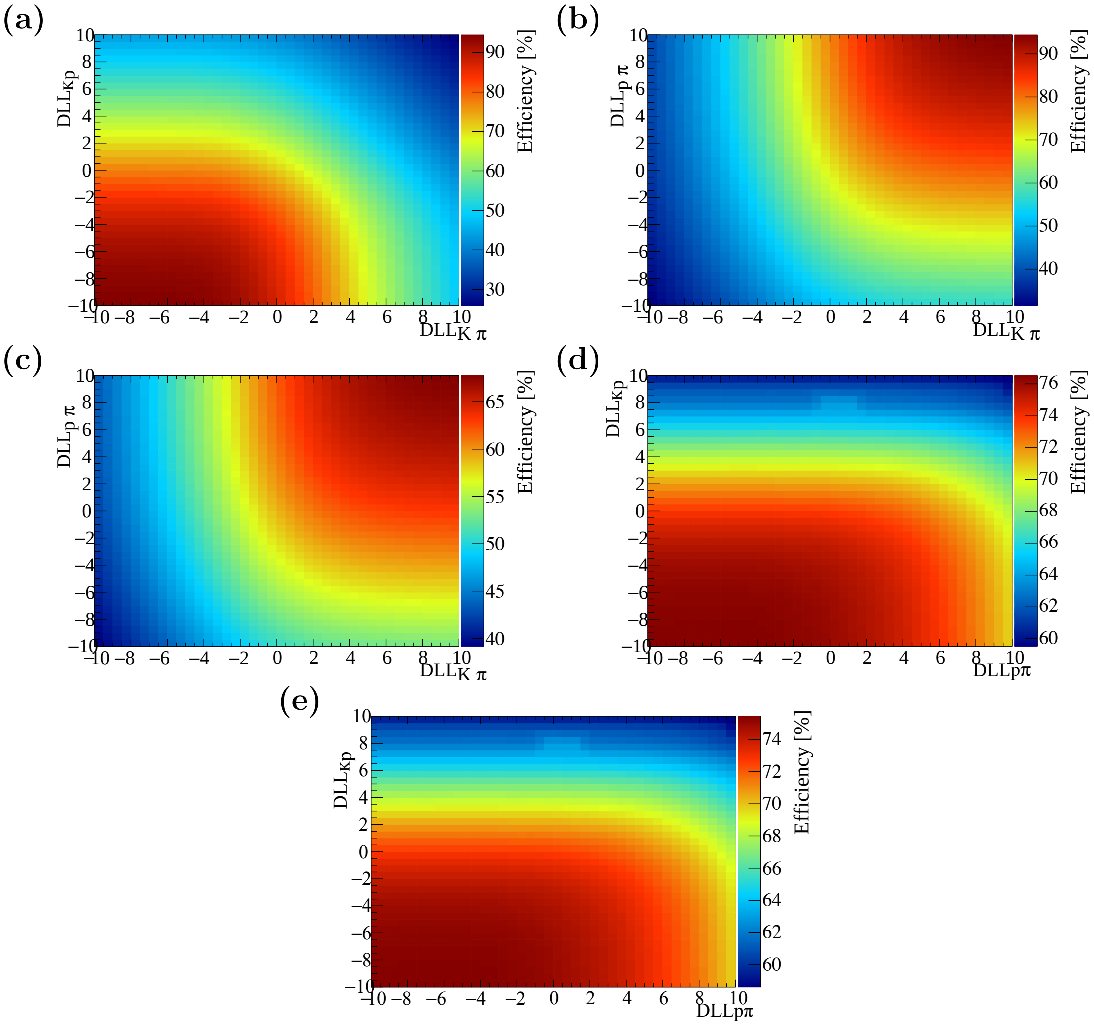

FIGURE 7.1: The predicted signal efficiencies of the five final states of interest. (a) K^+K^- selection efficiencies for $K^+\pi^-$ and K^+p separation for both of the daughter tracks. (b) $\pi^+\pi^-$ selection efficiencies for $K^+\pi^-$ and $p\pi^-$ separation for both of the daughter tracks.(c) $K^+\pi^-$ final state selection efficiencies for $K^+\pi^-$ and $p^+\pi^-$ separation for the pion daughter track, keeping the kaon track cut the same as for K^+K^-. (d) $p\pi^-$ selection efficiencies for π^+p and K^+p separation for different cuts on the proton track, keeping the pion cuts the same as for $\pi^+\pi^-$. (e) pK^- selection efficiencies for $K^+\pi^-$ and $p^+\pi^-$ separation for the proton track, keeping the cuts on the kaon track the same as that for K^+K^-.

signal efficiency. The contamination is estimated by passing MC samples of the decays believed to contribute to the backgrounds present (i.e. other $\mathrm{B} \to h^+h'^-$ decays) through the same selection requirements as the signal class and then using PIDCalib to obtain a global misidentification efficiency for the sample.

The hadronization fractions [150] are shown in Table 7.6, the branching fractions for the signal channels and main contaminations are shown in Table 7.7 and the final cuts used in the analysis are given in Table 7.8. These cuts were chosen to keep the contaminations of the two-body backgrounds below 10 % if possible to reduce the associated systematic uncertainties in the final measurement while simultaneously maximising the signal yield within this constraint. The predicted signal efficiencies and relevant predicted two-body contaminations are shown in Table 7.9 for the chosen cuts while the predicted contaminations for the different cuts considered are given in Appendix C. Charge conjugation is unimportant for daughter-symmetric final states (i.e. $\mathrm{K}^+\mathrm{K}^-$ and $\pi^+\pi^-$) as altering the misidentified tracks will cancel with the symmetrical final state. The charge conjugate misidentified tracks become important for daughter asymmetric final states (i.e. $\mathrm{K}^+\pi^-$, $p\pi^-$ and pK^-) where swapping the misidentified tracks will not cancel with the asymmetrical final state. This requires doubling the contamination from symmetrical misidentifications (i.e. $\mathrm{K}^+\mathrm{K}^-$ and $\pi^+\pi^-$)[2] to account for anti-particle mothers (i.e. B^0_s and $\bar{\mathrm{B}}^0_s$) and recalculating efficiencies from charge-conjugate MC samples for daughter asymmetric mis-ID. The latter effect can have huge impacts for some decays, most notably there is a large contamination from $\bar{\mathrm{B}}^0 \to \mathrm{K}^-\pi^+$ in the $\mathrm{p}^+\mathrm{K}^-$ final state but a small contamination from $\mathrm{B}^0 \to \mathrm{K}^+\pi^-$. This arises from requiring the mis-ID of a single track in $\bar{\mathrm{B}}^0 \to \mathrm{K}^-\pi^+$ (the pion is misidentified as a proton) which is much more likely than the mis-ID of two tracks in $\mathrm{B}^0 \to \mathrm{K}^+\pi^-$ (the pion must be misidentified as a kaon while the kaon must be misidentified as a proton).

7.1.4 Multivariate Analysis

The combinatorial background in the samples was reduced using a multivariate analysis technique (MVA) devised by Sarah Karodia.

---

[2] PIDCalib relies on identifying the daughter species, not the mother species

Ratio	Value
$f_{\mathrm{B_s^0}}/f_{\mathrm{B^0}}$	0.256 ± 0.020
$f_{\mathrm{B_s^0}}/f_{\Lambda_\mathrm{b}^0}$	0.481 ± 0.013
$f_{\mathrm{B^0}}/f_{\mathrm{B_s^0}}$	1.878 ± 0.030
$f_{\mathrm{B^0}}/f_{\Lambda_\mathrm{b}^0}$	1.797 ± 0.008
$f_{\Lambda_\mathrm{b}^0}/f_{\mathrm{B^0}}$	0.556 ± 0.025
$f_{\Lambda_\mathrm{b}^0}/f_{\mathrm{B_s^0}}$	2.080 ± 0.057

Table 7.6: The $b\bar{b}$ hadronization ratios where f_x/f_y is the production of x with respect to y [150].

Channel	$\mathcal{B}$ [$\times 10^{-6}$]
$\mathrm{B_s^0} \rightarrow \mathrm{K^+K^-}$	24.9 ± 1.7
$\mathrm{B^0} \rightarrow \mathrm{K^+K^-}$	0.13 ± 0.05
$\mathrm{B_s^0} \rightarrow \pi^+\mathrm{K^-}$	5.5 ± 0.6
$\mathrm{B^0} \rightarrow \mathrm{K^+}\pi^-$	19.6 ± 0.5
$\mathrm{B_s^0} \rightarrow \pi^+\pi^-$	0.76 ± 0.19
$\mathrm{B^0} \rightarrow \pi^+\pi^-$	5.12 ± 0.19
$\Lambda_\mathrm{b}^0 \rightarrow \mathrm{p}\pi^-$	4.1 ± 0.8
$\Lambda_\mathrm{b}^0 \rightarrow \mathrm{pK^-}$	4.9 ± 0.9

Table 7.7: The 2-body branching fractions relevant to the channels being studied [151].

A boosted decision tree with a gradient boost (BDTG) was used to reduce background contamination for all final states by employing a wide range of variables to efficiently discriminate between signal and background events.

A decision tree is created by having two samples, for example one of signal and the other of background events which is typical for an analysis of this type. A set of variables, V_j, are chosen which have good signal and background discrimination, then a cut is placed on one of the variables for both signal and background at some value, a_i, and the number of events on each side of the cut for both of samples is noted. This is repeated for each of the variables and for different cuts for each variable to find the best possible combination to reduce the background and keep the signal [152]. This is shown schematically in Figure 7.2. Decision trees can then be *boosted* by assigning weights to each event depending on whether it is sorted in a signal (+1) or background decision (-1). The creation of a tree is then repeated with the new weights with successive assignments summed for each of the tree iterations. Thus in theory a signal-like event should finish with a very positive weight while a background event should have a very negative weight.

Final State	Track	Cuts
K^+K^-	Kaon	$\Delta\log(\mathcal{L}_{K\pi}) > 5.0$ $\Delta\log(\mathcal{L}_{Kp}) > 0.0$ $\Delta\log(\mathcal{L}_{Ke}) > 0.0$ $\Delta\log(\mathcal{L}_{K\mu}) >$ -1.0
$K^+\pi^-$	Kaon	$\Delta\log(\mathcal{L}_{K\pi}) > 5.0$ $\Delta\log(\mathcal{L}_{Kp}) > 0.0$ $\Delta\log(\mathcal{L}_{Ke}) > 0.0$ $\Delta\log(\mathcal{L}_{K\mu}) >$ -1.0
$K^+\pi^-$	Pion	$\Delta\log(\mathcal{L}_{K\pi}) <$ -4.0 $\Delta\log(\mathcal{L}_{p\pi}) < 3.0$ $\Delta\log(\mathcal{L}_{e\pi}) < 0.0$ $\Delta\log(\mathcal{L}_{\mu\pi}) < 1.0$
$\pi^+\pi^-$	Pion	$\Delta\log(\mathcal{L}_{K\pi}) <$ -4.0 $\Delta\log(\mathcal{L}_{p\pi}) < 3.0$ $\Delta\log(\mathcal{L}_{e\pi}) < 5.0$ $\Delta\log(\mathcal{L}_{\mu\pi}) < 5.0$
pK^-	Proton	$\Delta\log(\mathcal{L}_{p\pi}) > 3.0$ $\Delta\log(\mathcal{L}_{pK}) > 5.0$ $\Delta\log(\mathcal{L}_{pe}) > 0.0$ $\Delta\log(\mathcal{L}_{p\mu}) > 0.0$
pK^-	Kaon	$\Delta\log(\mathcal{L}_{K\pi}) > 5.0$ $\Delta\log(\mathcal{L}_{Kp}) > 0.0$ $\Delta\log(\mathcal{L}_{Ke}) > 0.0$ $\Delta\log(\mathcal{L}_{K\mu}) >$ -1.0
$p\pi^-$	Proton	$\Delta\log(\mathcal{L}_{p\pi}) > 3.0$ $\Delta\log(\mathcal{L}_{pK}) > 9.0$ $\Delta\log(\mathcal{L}_{pe}) > 0.0$ $\Delta\log(\mathcal{L}_{p\mu}) > 0.0$
$p\pi^-$	Pion	$\Delta\log(\mathcal{L}_{K\pi}) <$ -4.0 $\Delta\log(\mathcal{L}_{p\pi}) < 3.0$ $\Delta\log(\mathcal{L}_{e\pi}) < 5.0$ $\Delta\log(\mathcal{L}_{\mu\pi}) < 5.0$

TABLE 7.8: The $\Delta\log(\mathcal{L})$ cuts applied to the Run I data sample. The cuts are initial taken against the pion hypothesis, for example $\Delta\log(\mathcal{L}_{pe}) = \log(\mathcal{L}_p) - \log(\mathcal{L}_\pi) - (\log(\mathcal{L}_e) - \log(\mathcal{L}_\pi))$

Channel	$B_s^0 \rightarrow K^+K^-$	$B^0 \rightarrow \pi^+\pi^-$	$B^0 \rightarrow K^+\pi^-$	$\Lambda_b^0 \rightarrow pK^-$	$\Lambda_b^0 \rightarrow p\pi^-$
ε or ω [%]					
K^+K^-	56.03 ± 0.07	$(1.78 \pm 0.05)\times10^{-2}$	0.91 ± 0.02	1.95 ± 0.02	$(1.08 \pm 0.03)\times10^{-2}$
$\pi^+\pi^-$	$(2.9 \pm 0.06)\times10^{-2}$	58.32 ± 0.80	1.19 ± 0.02	$(6.28 \pm 0.10)\times10^{-2}$	2.09 ± 0.01
$K^+\pi^-$	1.26 ± 0.02	0.98 ± 0.02	53.36 ± 0.07	$(4.47 \pm 0.08)\times10^{-2}$	0.60 ± 0.01
π^+K^-	1.26 ± 0.02	0.98 ± 0.02	$(2.12 \pm 0.05)\times10^{-2}$	2.83 ± 0.02	$(3.39 \pm 0.07)\times10^{-2}$
pK^-	2.44 ± 0.39	$(2.64 \pm 1.42)\times10^{-2}$	$(4.21 \pm 0.67)\times10^{-2}$	66.60 ± 0.98	1.05 ± 0.03
$\bar{p}K^+$	2.44 ± 0.39	$(2.64 \pm 1.42)\times10^{-2}$	1.10 ± 0.71	-	$(1.14 \pm 0.78)\times10^{-2}$
$p\pi^-$	$(5.29 \pm 0.90)\times10^{-2}$	1.31 ± 0.80	2.31 ± 0.37	1.49 ± 0.03	61.95 ± 0.93
$\bar{p}\pi^+$	$(5.29 \pm 0.90)\times10^{-2}$	1.31 ± 0.80	$(2.49 \pm 1.61)\times10^{-2}$	0.10 ± 0.02	-
k [%]					
$B_s^0 \rightarrow K^+K^-$	-	$(3.84 \pm 0.39)\times10^{-2}$	0.56 ± 0.05	7.19 ± 1.43	$(5.08 \pm 1.07)\times10^{-2}$
$\bar{B}_s^0 \rightarrow K^+K^-$	-	$(3.84 \pm 0.39)\times10^{-2}$	0.56 ± 0.05	7.19 ± 1.43	$(5.08 \pm 1.07)\times10^{-2}$
$B^0 \rightarrow K^+K^-$	2.16 ± 0.79	$(8 \pm 3)\times10^{-4}$	$(1.14 \pm 0.44)\times10^{-2}$	0.14 ± 0.06	$(1 \pm 3)\times10^{-3}$
$\bar{B}^0 \rightarrow K^+K^-$	2.16 ± 0.79	$(8 \pm 3)\times10^{-4}$	$(1.14 \pm 0.44)\times10^{-2}$	0.14 ± 0.06	$(1 \pm 3)\times10^{-3}$
$B_s^0 \rightarrow \pi^+\pi^-$	$(1.59 \pm 0.41)\times10^{-3}$	3.84 ± 1.00	$(2.24 \pm 0.58)\times10^{-2}$	$(7.05 \pm 2.20)\times10^{-3}$	0.30 ± 0.10
$\bar{B}_s^0 \rightarrow \pi^+\pi^-$	$(1.59 \pm 0.41)\times10^{-3}$	3.84 ± 1.00	$(2.24 \pm 0.58)\times10^{-2}$	$(7.05 \pm 2.20)\times10^{-3}$	0.30 ± 0.10
$B^0 \rightarrow \pi^+\pi^-$	$(4.13 \pm 0.41)\times10^{-2}$	-	0.56 ± 0.03	0.17 ± 0.03	7.58 ± 1.51
$\bar{B}^0 \rightarrow \pi^+\pi^-$	$(4.13 \pm 0.41)\times10^{-2}$	-	0.56 ± 0.03	0.17 ± 0.03	7.58 ± 1.51
$B_s^0 \rightarrow \pi^+K^-$	0.50 ± 0.06	0.47 ± 0.06	$(2.89 \pm 0.37)\times10^{-3}$	2.30 ± 0.50	$(3.54 \pm 0.80)\times10^{-2}$
$\bar{B}_s^0 \rightarrow \pi^-K^+$	0.50 ± 0.06	0.47 ± 0.06	7.27 ± 0.82	$(3.63 \pm 0.79)\times10^{-2}$	0.63 ± 0.14
$B^0 \rightarrow K^+\pi^-$	6.85 ± 0.64	6.43 ± 0.31	-	0.48 ± 0.09	8.37 ± 1.66
$\bar{B}^0 \rightarrow K^-\pi^+$	6.85 ± 0.64	6.43 ± 0.31	-	30.54 ± 5.69	0.47 ± 0.09
$\Lambda_b^0 \rightarrow pK^-$	1.78 ± 0.45	$(2.41 \pm 1.38)\times10^{-2}$	0.011 ± 0.0027	-	1.13 ± 0.55
$\bar{\Lambda}_b^0 \rightarrow \bar{p}K^+$	1.78 ± 0.45	$(2.41 \pm 1.38)\times10^{-2}$	0.29 ± 0.19	-	$(1.22 \pm 1.61)\times10^{-2}$
$\Lambda_b^0 \rightarrow p\pi^-$	$(3.0 \pm 0.8)\times10^{-2}$	1.00 ± 0.64	0.50 ± 0.13	1.04 ± 0.50	-
$\bar{\Lambda}_b^0 \rightarrow \bar{p}\pi^+$	$(3.0 \pm 0.8)\times10^{-2}$	1.00 ± 0.64	$(5.43 \pm 3.67)\times10^{-3}$	$(7 \pm 4)\times10^{-2}$	-

Table 7.9: Predicted signal efficiencies and contaminations for the five final states studied. ε is the signal selection efficiency, ω is the misidentification efficiency and k is the background contamination with respect to the signal.

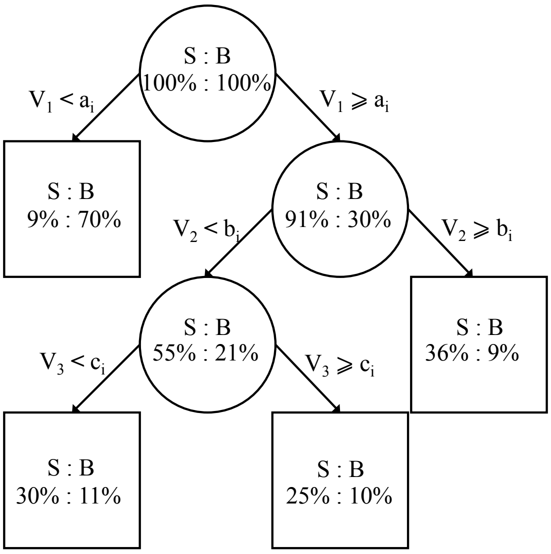

FIGURE 7.2: A mock up of a decision tree with three variables, V_1, V_2 and V_3 and one cut per variable, a_i, b_i and c_i. For each variable these cuts are altered to find new signal and background retentions. Adapted from [152].

The BDTG was trained using the ROOT package TMVA [153]. The BDTG was trained using the 2012 $\mathrm{B^0_s} \to \mathrm{K^+K^-}$ MC sample for the signal events and the upper mass sideband of the 2012 $\mathrm{K^+K^-}$ invariant mass distribution for the background events. Two BDTG's were produced, one using even numbered data events and the other using odd numbered data events to avoid biasing the MVAs. The output MVAs were then applied to the opposite numbered event samples. It was decided to use the following input variables for event discrimination; the logarithm of the IPχ^2 of the mother, the DIRA of the mother, both the maximum and minimum p_T of the daughters, both the maximum and minimum logarithm of the IPχ^2 of the daughters and both the maximum and minimum logarithm of the χ^2 per degree of freedom of the track of the daughters. A comparison of the signal and background distributions of the variables used for the training of the BDTG can be seen in Figure 7.3 with the measured correlations between the variables given in Figure 7.4. The optimal cut point of the BDTG was believed to be at the maximum significance where the significance, Z, is defined as

$$Z = \frac{S}{\sqrt{S+B}} \tag{7.4}$$

where S is the number of signal events and B is the number of combinatorial background events. The response of the BDTG and the measured significance on $\mathrm{B^0_s} \to \mathrm{K^+K^-}$ events is given in Figure 7.5, where it was decided to require that the BDTG response > -0.80.

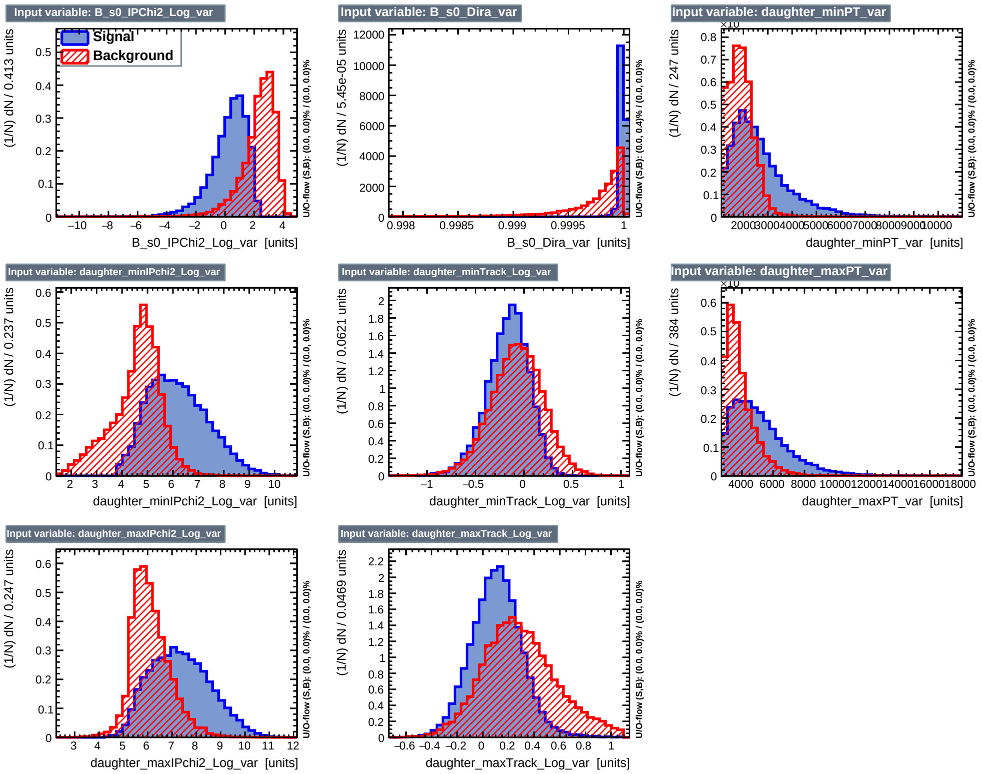

FIGURE 7.3: Comparison of variables used for the BDTG trained on $B_s^0 \rightarrow K^+K^-$ events. Blue - Simulated signal events, red - data events from the upper mass sideband.

7.2 Mass Fits

Once the selection had been finalised the invariant mass spectrum of the five different final states were studied as they provide a good method to separate signal from background events. The fits to the $p\pi^-$ and pK^- spectra were performed by the candidate while the other final states were performed by Sarah Karodia. For the $\Lambda_b^0 \rightarrow p\pi^-$ and $\Lambda_b^0 \rightarrow pK^-$ fits, the invariant mass window of the daughters was reduced to $5300 < m_{ph} < 5800\,\text{MeV}$ from the window imposed by the HLT2 trigger and stripping line. The fits were performed using G-FACT which is a general purpose fitting package developed by the Glasgow group using a maximum likelihood fit to measure the relative fractions of the invariant mass contributions, $\varepsilon((\text{class})$, and the parametrisation of their shapes, $f((\text{m}|(\text{class})$. The total invariant

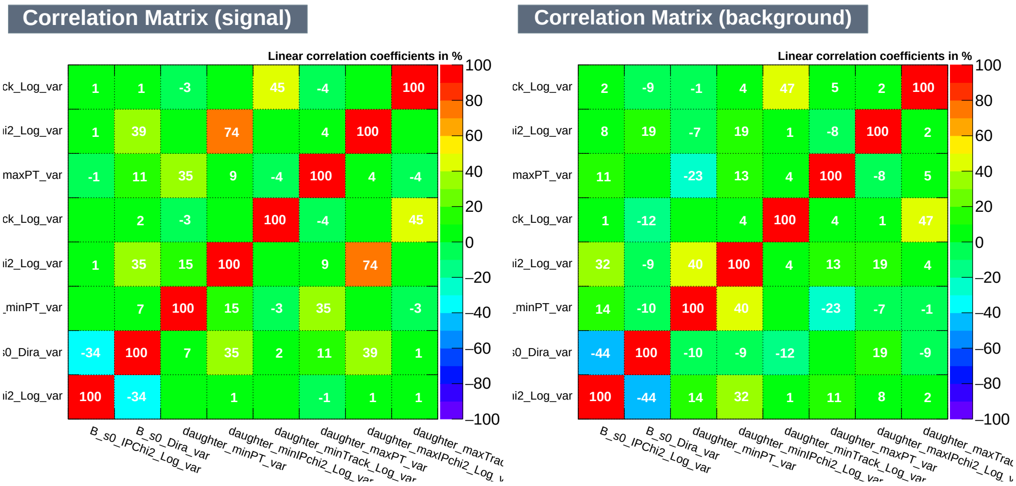

FIGURE 7.4: The measured correlations between variables used to train the BDTG for $B_s^0 \to K^+K^-$ candidates with an odd event number. Left - Correlations apparent in variables from the signal MC sample. Right - Correlations apparent in variables from the upper mass side band of the K^+K^- invariant mass spectrum. Variables without a value for their correlation were measured to have a correlation of zero.

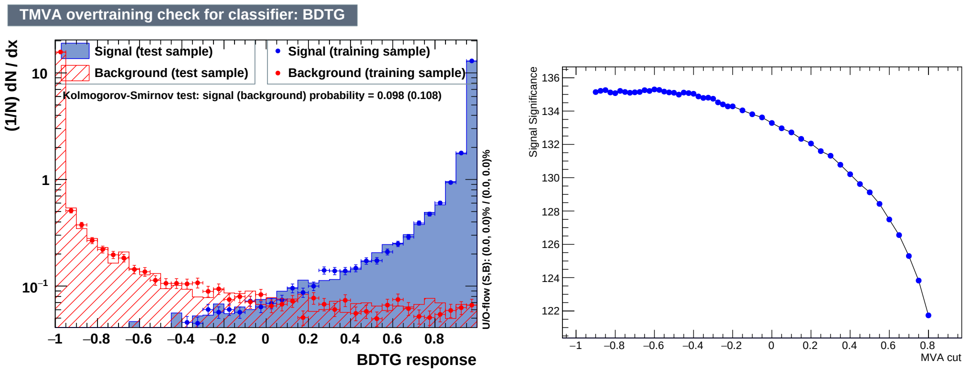

FIGURE 7.5: The measured responses of the BDTG used in the analysis. The training samples are given as data points while the testing samples are given as solid histograms. The signal events are given in blue while the background events are given in red. Left - The response of the BDTG trained on $B_s^0 \to K^+K^-$ candidates. Right - The measured signal significance of $B_s^0 \to K^+K^-$ events as a function of BDTG cut.

mass probability density function (PDF), $f(\mathrm{m})$, is thereby

$$f(\mathrm{m}) = \sum_{\mathrm{class}} f(\mathrm{m}|\mathrm{class}) \cdot \varepsilon(\mathrm{class}). \tag{7.5}$$

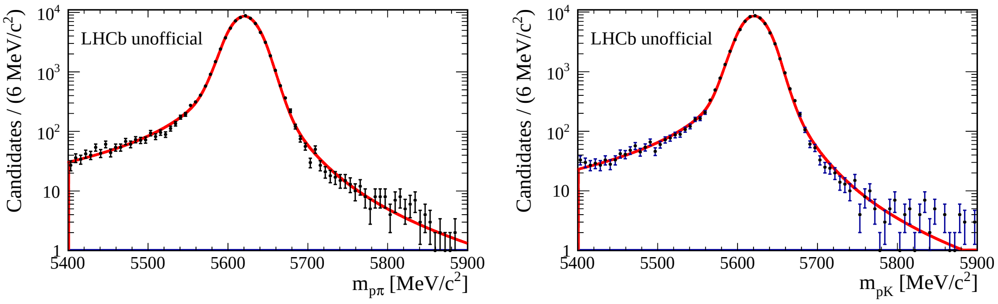

FIGURE 7.6: Double Crystal Ball fit to simulated Λ_b^0 decay events under Run I conditions with the full event selection applied. Left - The fit to $\Lambda_b^0 \to p\pi^-$ signal candidates. Right - The fit to $\Lambda_b^0 \to pK^-$ signal candidates.

7.2.1 Signal Shapes

The full event selection was applied to MC samples of the signal channels to parametrise the invariant mass. The distributions were modelled using a double Crystal Ball function which is composed of two single Crystal Ball functions [154] sharing a common mean and width. One of the Crystal Ball tails is used to parametrise the low mass distribution while the other is used for the high mass distribution. There is also a final parameter to describe the relative fractions of the two distributions in the final fit. The double Crystal Ball function is given by

$$f(x;\alpha_{\mathrm{L}},n_{\mathrm{L}},\alpha_{\mathrm{H}},n_{\mathrm{H}},\mu,\sigma) = N\cdot\begin{cases}\exp(-\frac{(x-\mu)^2}{2\sigma^2}), & \text{for } -\alpha_{\mathrm{L}} < \frac{x-\mu}{\sigma} < -\alpha_{\mathrm{H}}\\ A_{\mathrm{L}}\cdot(B_{\mathrm{L}} - \frac{x-\mu}{\sigma})^{-n_{\mathrm{L}}}, & \text{for } -\alpha_{\mathrm{L}} \geqslant \frac{x-\mu}{\sigma}\\ A_{\mathrm{H}}\cdot(B_{\mathrm{H}} - \frac{x-\mu}{\sigma})^{-n_{\mathrm{H}}}, & \text{for } \frac{x-\mu}{\sigma} \geqslant -\alpha_{\mathrm{H}}\end{cases} \tag{7.6}$$

where

$$A_{[\mathrm{L/H}]} = \left(\frac{n_{[\mathrm{L/H}]}}{\left|\alpha_{[\mathrm{L/H}]}\right|}\right)^{n_{[\mathrm{L/H}]}} \cdot \exp\left(-\frac{\left|\alpha_{[\mathrm{L/H}]}\right|^2}{2}\right) \tag{7.7}$$

$$B_{[\mathrm{L/H}]} = \frac{n_{[\mathrm{L/H}]}}{\left|\alpha_{[\mathrm{L/H}]}\right|} - \left|\alpha_{[\mathrm{L/H}]}\right|. \tag{7.8}$$

The mean and width of the central Gaussian distribution are given by μ and σ respectively while L and H refer to the parameters defining the low and high mass regions of the distribution. The parameter $\alpha_{[\mathrm{L/H}]}$ describes the boundary between the Gaussian and power law components while $n_{[\mathrm{L/H}]}$ describes the order of the power law (it is not necessarily an integer value).

7.2.2 Background Studies

As the selection requirements for the decays of interest involve cutting on regions of interest for several variables then it is possible for events of similar topologies and kinematics of the channel of interest to contaminate the final sample. There are three main types of background that appear.

- Two-body misidentified backgrounds
- Partially reconstructed backgrounds
- Combinatorial background

The contributions of each of these backgrounds to the five final states were studied with their relative contaminations quantified via the invariant mass fit. The causes, make-up and parametrisation of each are discussed here.

7.2.2.1 Two-body Contaminations

The two-body misidentified backgrounds are caused by an incorrect particle ID attached to one or more of the daughter particles in the decay and the measurement of their contamination in each of the final states was discussed in Section 7.1.3. After the relative contaminations were quantified, the background MC samples were required to undergo the same selections as the full data. This includes a substitute particle identification where the species of each component was exchanged for that of the signal channel. For example, a sample of $\Lambda_{\mathrm{b}}^0 \to \mathrm{pK}^-$ MC would have the Λ_{b}^0 exchanged for a $\mathrm{B}_{\mathrm{s}}^0$ and the proton exchanged for a kaon to match the $\mathrm{B}_{\mathrm{s}}^0 \to \mathrm{K}^+\mathrm{K}^-$ decay.

As the invariant mass distribution of the events that pass the selection requirements tend to become non-parametric due to the selection requirements and the invariant mass substitutions imposed on the sample, then the shape of the PDFs are extracted using the kernel density estimation method with an adaptive bandwidth [155]. The use of kernel density estimation to describe non-parametric distributions in invariant masses was proposed by the D0 collaboration for analysis of the Higgs boson [156] but has been developed for use in other collaborations.

In a kernel estimation the events of a distribution are substituted for a kernel function so that the distribution, $\hat{f}_0(x)$, can be described as

$$\hat{f}_0(x) = \frac{1}{nh}\sum_{\mathrm{i}=1}^{n} K\left(\frac{x-t_i}{h}\right) \tag{7.9}$$

where t_i is the value of event i and h is the bandwidth or smoothing parameter. It has been suggested [156] that a suitable kernel function for use in describing the invariant mass distribution would be a Gaussian as it is positive definite and infinitely differentiable.

To avoid issues of function overspill at boundaries, underestimations of the distribution within regions with low event density, and overestimation within regions of high density then the bandwidth is allowed to alter on an event-by-event basis which is known as an *adaptive kernel estimation* where the per-event bandwidth is given by [157]

$$h_i = \frac{h}{\sqrt{\hat{f}_0(x)}}. \tag{7.10}$$

The PDFs determined by the kernel method used in the pK^- fit are shown in Figure 7.7 while the kernels used for the $p\pi^-$ fit are shown in Figure 7.8. The size of these PDFs within the fit was determined using the predictions from PIDCalib and then allowed to vary within a Gaussian constraint.

7.2.2.2 Partially Reconstructed Background

The partially reconstructed background (PRB) is composed of B-hadron decays with more than two daughter tracks, where only two of the tracks contribute to the signal candidate reconstruction. As these candidates involve missing tracks their measured momentum is lower than their true momentum. Thus they tend to lie towards lower regions of the invariant mass spectrum. The predicted composition of the PRB was produced from a cocktail of MC samples. Like the two-body contaminations, these samples were required to undergo the full selection requirements then scaled by their selection efficiency, relative hadronisation fractions and branching ratios. The observed weighted distributions of the PRB in the pK^- and $\mathrm{p}\pi^-$ spectra are shown in the upper two plots of Figure 7.9. After observing the distributions it was noted that the PRB contribution could be removed from the pK^- sample by changing the lower mass limit to 5400 MeV. Using this same

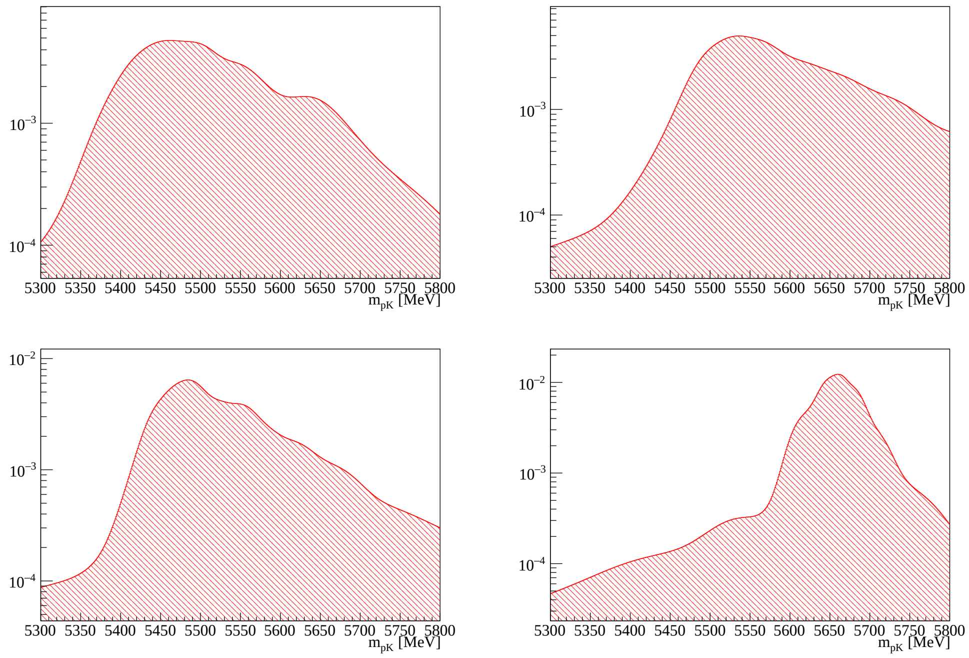

FIGURE 7.7: Kernelised histograms produced from MC samples constructed using the $\Lambda_b^0 \rightarrow pK^-$ decay selection used in the Run I analysis. Top Left - The $B^0 \rightarrow K^+\pi^-$ contamination. Top Right - The $B_s^0 \rightarrow \pi^+K^-$ contamination. Bottom Left - The $B_s^0 \rightarrow K^+K^-$ contamination. Bottom Right - The $\Lambda_b^0 \rightarrow p\pi^-$ contamination.

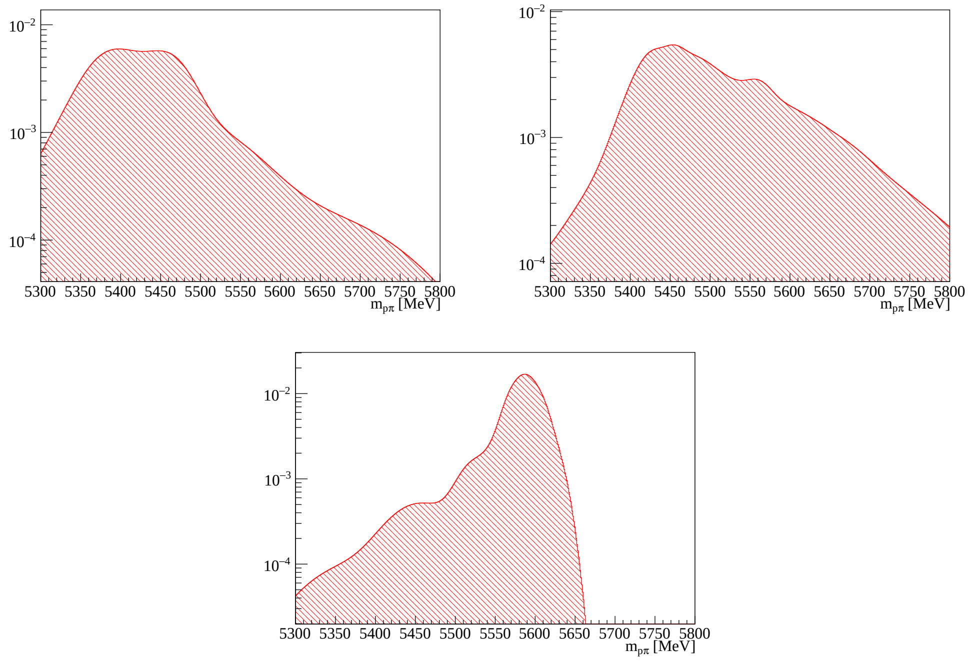

FIGURE 7.8: Kernelised histograms produced from MC samples constructed using the $\Lambda_b^0 \rightarrow p\pi^-$ decay selection used in the Run I analysis. Top Left - The $B^0 \rightarrow K^+\pi^-$ contamination. Top Right - The $B^0 \rightarrow \pi^+\pi^-$ contamination. Bottom - The $\Lambda_b^0 \rightarrow pK^-$ contamination.

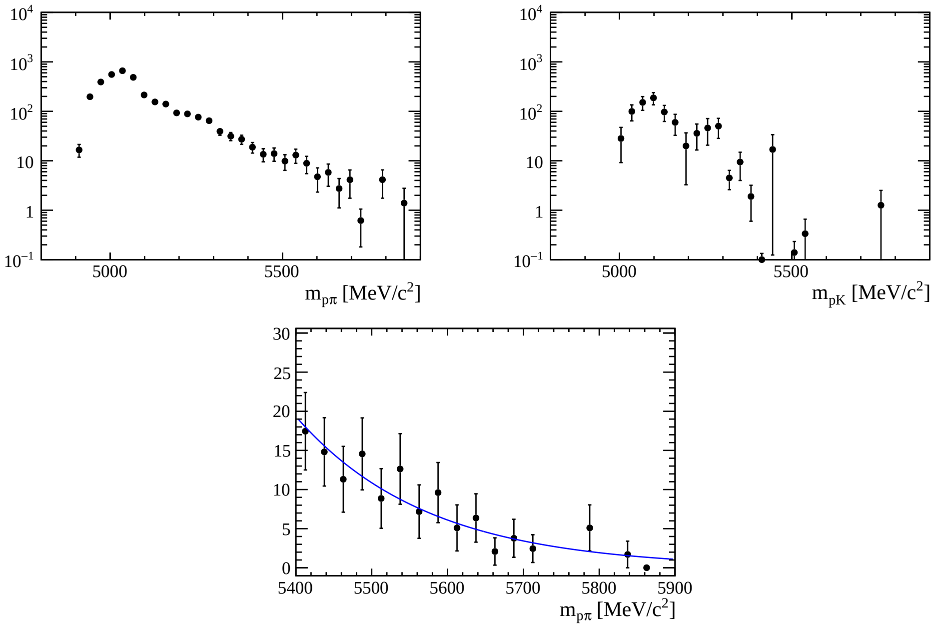

FIGURE 7.9: The predicted distribution of the partially reconstructed background events in the pK^- and $p\pi^-$ spectra. Top Left - The prediction for the full invariant mass window for the $p\pi^-$ spectra. Top Right - The prediction for the full invariant mass window for the pK^- spectra. Bottom - The distribution in the reduced mass window for the $p\pi^-$ spectra and the resulting exponential fit.

Partially Reconstructed Background Samples		
Channel	BF [10^{-6}]	in $p\pi^-$
$B^0 \to \pi^+\pi^-\pi^0$	< 720	12.97%
$\bar{B}^0 \to \pi^-\pi^+\pi^0$	< 720	0.62%
$B^0 \to K^+\pi^-\pi^0$	37.8 ± 3.2	0.05%
$B^+ \to \pi^+\pi^-\pi^+$	15.2 ± 1.4	0.09 %
$\bar{B}^+ \to \pi^-\pi^+\pi^-$	15.2 ± 1.4	0.01 %
$\Lambda_b^0 \to \Lambda_c^+\pi^-$	5700^{+4000}_{-2600}	85.51%
$\Lambda_b^0 \to pD^0\pi^-$	590^{+400}_{-320}	0.74 %

TABLE 7.10: The partially reconstructed background samples used to determine the $\Lambda_b^0 \to p\pi^-$ contamination and the volume of contamination present in the mass window under investigation.

window for the $p\pi^-$ spectra it was found that the distribution was well described by an exponential decay from approximately 5150 MeV with a free decay constant, λ_{PRB}, but to further reduce the background contamination without removing signal candidates the lower bound on the fit range was increased to 5400 MeV. The predicted contributions from various three-body decays in this range is given in Table 7.10.

7.2.2.3 Combinatorial Background

The combinatorial background is produced by close association of random tracks in the detector which results in a fake signal or incorrect decays being accepted by the selection. The background was modelled as an exponential function with the decay constant, $\lambda_{\mathrm{Comb.}}$, being left free in the fit.

7.2.3 Results

The fits were performed using the shapes described previously. The mean and width of the double Crystal Ball were left floating along with the decay constant of the combinatorial background. The decay constant of the PRB in the $\mathrm{p}\pi^-$ spectrum was fixed to the results from Section 7.2.2.2. The distributions for the two-body backgrounds were used from the results of Section **??** but were shifted by the difference between the fitted mean mass of the Λ_b^0 and the PDG value [36]. The relative contamination of these backgrounds with respect to the signal were Gaussian constrained to the predictions given in Table 7.9. The results of the fits to the $\mathrm{p}\pi^-$ and pK^- spectra are given in Table 7.11. The fits to the other final states were performed by Sarah Karodia and their parameters are listed in that thesis [147]. In the $\mathrm{p}\pi^-$ sample, 34306 candidates passed selection and were used in the fit, resulting in 4319 ± 106 $\Lambda_b^0 \to \mathrm{p}\pi^-$ signal candidates. In the pK^- sample, 27149 candidates passed the selection and were used in the fit, resulting in 6002 ± 123 $\Lambda_b^0 \to \mathrm{pK}^-$ signal candidate. The final fits to the $p\pi^-$ and pK^- spectra are shown in Figure 7.10 while the results of the $\mathrm{K}^+\mathrm{K}^-$, $\pi^+\pi^-$ and $\mathrm{K}^\pm\pi^\mp$ spectra are shown in Figure 7.11. The yields of the other four channels were determined to be 27849 ± 201 for the $\mathrm{B}_s^0 \to \mathrm{K}^+\mathrm{K}^-$ sample, 22601 ± 237 for the $\mathrm{B}^0 \to \pi^+\pi^-$ sample, 78375 ± 311 for the $\mathrm{B}^0 \to \mathrm{K}^+\pi^-$ sample and 5596 ± 148 for the $\mathrm{B}_s^0 \to \pi^+\mathrm{K}^-$ sample.

7.3 Acceptance Corrections

The decay of a particle is a stochastic process and so follows an exponential decay law where the decay constant is inversely proportional to the lifetime. In an ideal world a measurement of this parameter would allow for a measurement of the decay time. However, the kinematic selection of the events, which is performed

Parameter	$\Lambda_b^0 \rightarrow p\pi^-$	$\Lambda_b^0 \rightarrow pK^-$	Description	Origin
$f_{\Lambda_b^0}$	$15.12 \pm 0.45\,\%$	$23.02 \pm 0.41\,\%$	Λ_b Signal	Data
$k_{B_s^0 \rightarrow K^+K^-}$	N/A	$14.02 \pm 1.82\,\%$	$B_s^0 \rightarrow K^+K^-$ Contamination	Data
$k_{B^0 \rightarrow \pi^+\pi^-}$	$18.46 \pm 2.10\,\%$	N/A	$B^0 \rightarrow \pi^+\pi^-$ Contamination	Data
$k_{B^0 \rightarrow K^+\pi^-}$	$15.28 \pm 1.57\,\%$	$55.00 \pm 4.51\,\%$	$B^0 \rightarrow K^+\pi^-$ Contamination	Data
$k_{B_s^0 \rightarrow \pi^+K^-}$	N/A	$2.06 \pm 0.48\,\%$	$B_s^0 \rightarrow \pi^+K^-$ Contamination	Data
$k_{\Lambda_b^0 \rightarrow p\pi^-}$	N/A	$0.66 \pm 0.49\,\%$	$\Lambda_b^0 \rightarrow p\pi^-$ Contamination	Data
$k_{\Lambda_b^0 \rightarrow pK^-}$	$1.12 \pm 0.55\,\%$	N/A	$\Lambda_b^0 \rightarrow pK^-$ Contamination	Data
f_{PRB}	$7.84 \pm 1.82\ \%$	N/A	Partially Reconstructed Fraction	Data
μ	$5625.03 \pm 0.60\,\mathrm{MeV}/c^2$	$5625.99 \pm 0.40\,\mathrm{MeV}/c^2$	Λ_b Mass	Data
σ	$21.66 \pm 0.66\,\mathrm{MeV}/c^2$	$19.67 \pm 0.39\,\mathrm{MeV}/c^2$	Λ_b Mass Resolution	Data
α_{L}	1.58 ± 0.10	1.46 ± 0.17	Low CB Boundary	MC
α_{H}	1.84 ± 0.09	1.94 ± 0.08	High CB Boundary	MC
n_{L}	$1.55\ \pm 0.09$	1.70 ± 0.10	Low CB Tail	MC
n_{H}	2.77 ± 0.21	3.08 ± 0.21	High CB Tail	MC
f_{DCB}	$54.36 \pm 8.50\,\%$	$35.13 \pm 6.63\,\%$	CB Fraction	MC
λ_{PRB}	142.86 ± 4.47	N/A	Partially Reconstructed Coefficient	MC
$\lambda_{\mathrm{Comb.}}$	$2843 \pm 1217\ \mathrm{MeV}/c^{2^{-1}}$	$865 \pm 75\ \mathrm{MeV}/c^{2^{-1}}$	Combinatorial Coefficient	Data

TABLE 7.11: The fit parameters used in the $p\pi^-$ and pK^- invariant mass distributions.

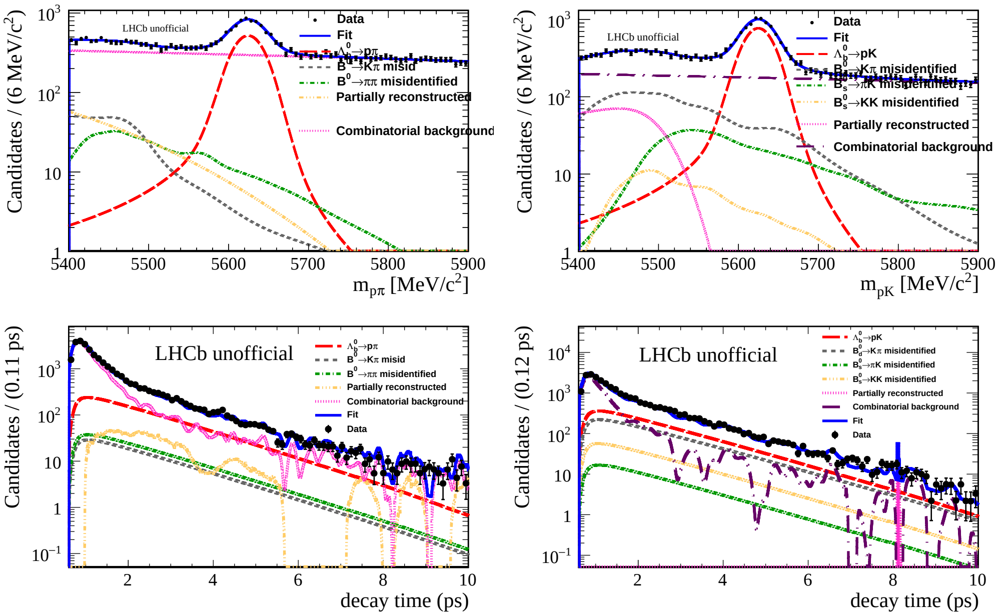

FIGURE 7.10: Top - The fit to the invariant mass distributions containing decays from Λ_b^0 baryons. Bottom - The fit to the decay time distributions containing decays from Λ_b^0 baryons. Left - The results of the $\Lambda_b^0 \to p\pi^-$ analysis. Right - The results of the $\Lambda_b^0 \to pK^-$ analysis.

to reduce the large number of background events, introduces biases in the lifetime distribution which must be corrected for. An example of a bias introduced is requiring that the particle is sufficiently displaced from the PV by applying a cut on the impact parameter. While this is an effective method for reducing the background, requiring a minimum IP rejects events with a small flight distance. As the flight distance is proportional to the lifetime this then rejects quickly decaying particles.

It is possible to model the detector acceptance as an asymmetric function that sharply decays to 0 at low decay times and decays slower at higher decay times [158] of the form

$$\varepsilon(t) = \frac{(1-at)[b(t-t_0)]^n}{1+[b(t-t_0)]^n}. \tag{7.11}$$

With suitably chosen starting parameters a typical distribution of the decay time acceptance for B-decays using Equation 7.11 is given in Figure 7.12

The drawback to this method is that it involves a good understanding of the true decay time of the channel and a good simulation of the decay in order to extract the fit parameters and hence it can lead to extra systematic uncertainties. To avoid

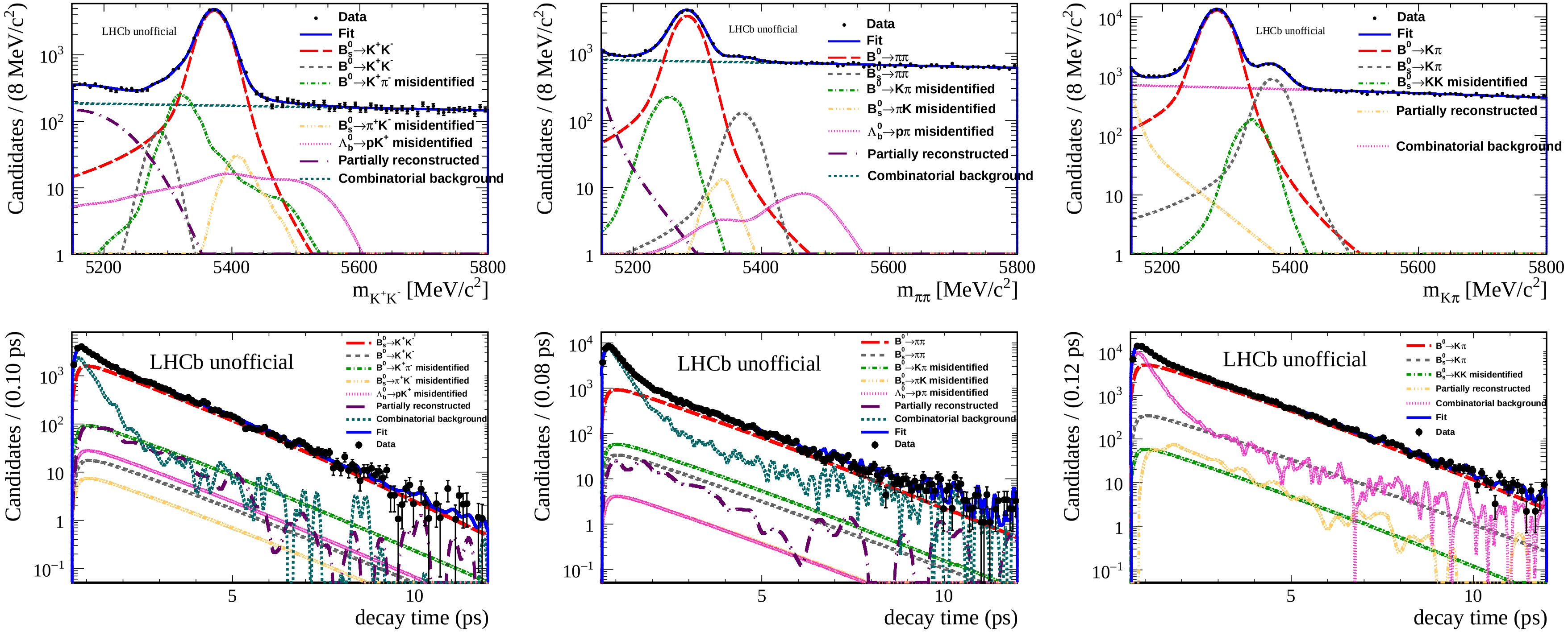

FIGURE 7.11: Top - The fit to the invariant mass distributions containing decays from B mesons. Bottom - The fit to the decay time distributions containing decays from B-mesons. Left - The results of the $B_s^0 \to K^+K^-$ analysis. Middle - The results of the $B^0 \to \pi^+\pi^-$ analysis. Right - The results of the $B^0 \to K^+\pi^-$ and $B_s^0 \to \pi^+K^-$ analyses.

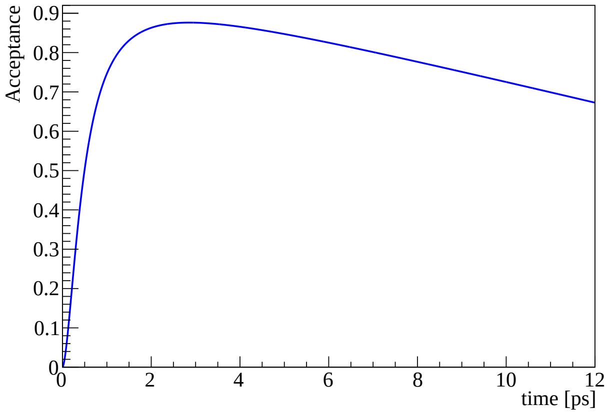

FIGURE 7.12: A typical distribution for the decay time acceptance in LHCb using Equation 7.11 with starting parameters $a = 0.027$, $b = 2.05$, $t_0 = 0$ and $n = 1.66$.

these issues, a data driven method for extracting the acceptance on an event-by-event basis known as *swimming* was developed by the NA11 collaboration [159] and extended for use by the LHCb collaboration [160].

The swimming method involves re-evaluating the decay time of the mother and determining whether the event would have been accepted by the lifetime-biasing selections. If the event would still be selected then a value of 1 is assigned but if not then a value of 0 is assigned. The point at which this decision changes is known as a *turning point*. By repeating this method for several hypothetical decay times then a series of top hat functions will be constructed for each event as it transitions from being accepted to not being accepted[3]. As the L0 trigger only requires measurements of a particle's transverse momentum and transverse energy, which are independent of a particle's decay time, then this selection does not need to be swum but the HLT1, HLT2, stripping and offline (multi-variate analysis selection) decisions must be re-evaluated for each hypothetical decay time. This method can be safely used to evaluate the acceptance of an event as the daughter kinematics of the decay are unaffected by the decay time of the mother.

For this analysis, the swimming is performed in two steps. The first step is to match the event to the tracks in the trigger and the stripping line, and then requiring that this matching produces an overlap of more that 70% of the tracks. For the trigger, this requires that the event was triggered on the signal candidate. The second stage consists of varying the decay time of the mother. As this is computed

---

[3] A series of top hat functions is produced as each event can have more than one primary vertex.

via the flight distance of the mother then this can be achieved in two ways. The first is to change the position of the decay vertex but this would involve altering how the daughter tracks interact with different regions of the detector and would thus require good knowledge of the track parameters as they traverse different regions of the detector. The second method is to keep the decay vertex location constant and to vary the PV along the direction of the mother's momentum. This second method is the one implemented as it is far less resource intensive due to the PV determination being the first step in the event reconstruction. After the PV has been moved the trigger, stripping and offline requirements can be re-evaluated within the LHCb framework to determine whether the event would be accepted or not.

Two additional requirements are imposed on each event along with the selection requirements to account for reconstruction efficiency effects. The first requires that the radial flight distance is below a maximum value to avoid interactions with the VELO material and was calculated by a previous analysis to be 4.0 mm [146].

The second requirement is on the minimum number of VELO modules[4] that the daughter tracks traverse. This requirement is required globally by all HLT trigger lines (referred to here as online) and during offline reconstruction where the tracks are required to traverse five sensors at the online stage and three sensors at the offline stage. Different module requirements are imposed due to a simpler detector model and fitter being used in the online reconstruction [90]. When evaluating the VELO module requirement, the model is moved with the PV and the number of traversed modules is recalculated. As the separation of the PV and SV increases, the daughter tracks will traverse fewer modules, and thus this requirement will produce an upper acceptance effect. This mainly affects longer lived B-candidates which will have traversed more VELO modules before decaying than short lived B-candidates.

For this analysis, the PV granularity was initially set to 4 mm then the granularity was decreased in steps of 1 mm to evaluate whether an event would be accepted or not by the selection at that location. The time at which an event starts to be accepted is referred to as t_{min} while the time that it is no longer accepted is referred to as t_{max}. The probability of a particle decaying at time, t, given a mean

---

[4] Recall that a VELO module consists of two VELO sensors; an r and a ϕ sensor.

lifetime τ is then

$$P(t|\tau) = \frac{1}{\tau}\frac{e^{-\frac{t}{\tau}}}{e^{-\frac{t_{\mathrm{min}}}{\tau}} - e^{-\frac{t_{\mathrm{max}}}{\tau}}}. \tag{7.12}$$

It should be noted that Equation 7.12 simplifies greatly in the limit that $t_{\mathrm{max}} \gg t$ to

$$P(t|\tau) = \frac{1}{\tau}e^{-\frac{t-t_{\mathrm{min}}}{\tau}}. \tag{7.13}$$

A simplified example of how the swimming algorithm works is given in Figure 7.13 where the impact parameter of each of the daughters is used to determine whether the event is accepted or not. In practice there can be numerous turning points for each event as there can be multiple primary vertices. For this analysis, the swimming was performed within the full LHCb framework where the trigger and stripping decisions could be re-evaluated using the same software that gave the initial acceptance condition, thus if the detector conditions are known at the time at which the event was recorded then the swimming method should determine the events acceptance intervals with high precision. It should be noted that this method takes approximately one minute to swim each event and hence will be a long process if the number of events to swim is large. To reduce the run time, the final event selection is decided upon before beginning the swimming process. The acceptance correction for the Run I analysis was not performed by the candidate but its applicability to the study undertaken was previously demonstrated in another analysis [146].

7.4 Lifetime Results

The lifetime measurements of all the final states were performed by Sarah Karodia and are given here for completeness only.

The lifetime measurements were performed sequentially from the mass fits for each of the final states. During the mass fit, each candidate was assigned a weight determining its likelihood to belong to each class. This technique is known as *sWeighting* [161] which involves maximising a likelihood function for a discriminating variable (such as an event's mass) where each candidate's contribution to a specific class is determined by calculating the likelihood with and without that event then assigning an event probability where the probabilities of an event belonging to that class are required to sum to one over all classes in the model. These

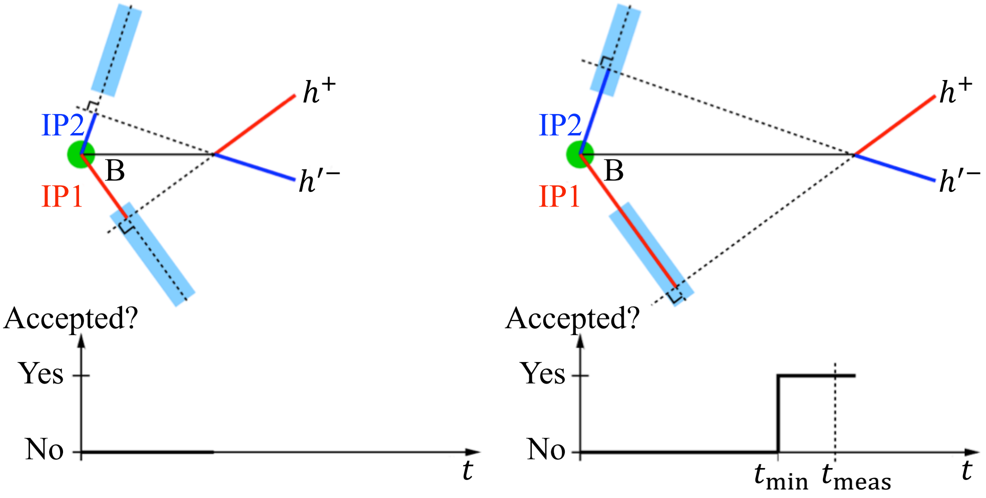

FIGURE 7.13: A simplified example of the decision making within the swimming method where the PV of the mother is moved and the IP decision is re-evaluated. In the left figure it can be seen that for the PV position, the daughter in red meets the IP requirement (the light blue shaded area) but the daughter in blue does not, so this event is not accepted for this decay time. In the right plot both daughters meet the requirement and the event is accepted.

weights can then be applied to a control variable (such as a particle's lifetime) assuming there is no correlation between the two variables.

The fit fractions of the individual components in the lifetime distribution were taken from the results of the mass fit. All signals and two-body backgrounds were modelled using an exponential function convolved with a Gaussian[5] where the decay time resolution of the Gaussian was fixed to 40 fs[6]. The partially reconstructed and combinatorial backgrounds cannot be easily described parametrically thus the shapes of these decays are extracted via the *sWeights* obtained for the appropriate class from the mass fit.

As $\mathrm{B_s^0} \to \mathrm{K^+K^-}$ decays have been observed to show time-dependent CP violation [61] and $\mathrm{B_s^0}$ mesons have a non-zero value of $\Delta\Gamma_\mathrm{s}$ [36] then it is possible to use the fitted value of $\tau_{\mathrm{B_s^0}\to\mathrm{K^+K^-}}$ to extract a value for $\mathcal{A}^{\Delta\Gamma}_{\mathrm{KK}}$ from [162],

$$\frac{\tau_{\mathrm{B_s^0}\to\mathrm{K^+K^-}}}{\tau_{\mathrm{B_s^0}}} = 1 + \mathcal{A}^{\Delta\Gamma}_{\mathrm{KK}} y_s + [2 \; - \; (\mathcal{A}^{\Delta\Gamma}_{\mathrm{KK}})^2] y_s^2 + \mathcal{O}(y_s^3) \tag{7.14}$$

where

$$y_s = \frac{\Delta\Gamma_s}{2\Gamma_s}. \tag{7.15}$$

---

[5] See Section 8.7.1

[6] See Section 8.5

Parameter	Value
$\tau_{B_s^0\to K^+K^-}$	1.410 ± 0.009 (stat.) ± 0.011 (syst.)
$\tau_{B^0\to \pi^+\pi^-}$	1.495 ± 0.012 (stat.) ± 0.007 (syst.)
$\tau_{B^0\to K^+\pi^-}$	1.504 ± 0.006 (stat.) ± 0.023 (syst.)
$\tau_{B_s^0\to \pi^+K^-}$	1.548 ± 0.028 (stat.) ± 0.023 (syst.)
$\tau_{\Lambda_b^0\to pK^-}$	1.477 ± 0.022 (stat.) ± 0.022 (syst.)
$\tau_{\Lambda_b^0\to p\pi^-}$	1.511 ± 0.028 (stat.) ± 0.012 (syst.)
$\mathcal{A}_{KK}^{\Delta\Gamma}$	-0.975 ± 0.092 (stat.) ± 0.113 (syst.) ± 0.082 (ext.)

Table 7.12: The final results from the Run I lifetime analysis.

The fit to the lifetime distributions of the five final states are shown in Figures 7.10 and 7.11. The final fit results are given in Table 7.12.

7.5 Conclusions

This chapter presented a study of the effective lifetime in B→ $h^+h'^-$ decays using 3 fb^{-1} of data collected at $\sqrt{s} = 7$ and 8 TeV at LHCb. The effective lifetime of $B_s^0 \to K^+K^-$, $B^0 \to K^+\pi^-$ and $B_s^0 \to \pi^+K^-$ have previously been published by the LHCb collaboration [146] at 7 TeV using 1 fb^{-1} of data. Several techniques were used to optimise the selection of the events. Specific stripping lines were used to select the different final states. Data-driven methods were used to predict the level of background contaminations to be expected in the sample at different log-likelihood cuts on the daughter species. The combinatorial background was reduced using multi-variate analysis techniques which was cut at the location corresponding to the greatest signal significance. Fits to the invariant mass distribution were performed to discriminate signal from background events and event weights were applied to assign events to the relevant decay classes. These weights then assign the contribution of different components of the data sample to the proper lifetime distribution. This allowed for the effective lifetimes of the channels to be measured.

The final results were measured to be

$$\begin{aligned}
\tau_{\mathrm{B_s^0\to K^+K^-}} &= 1.410 \pm 0.009(\mathrm{stat.}) \pm 0.011(\mathrm{syst.}) \\
\tau_{\mathrm{B^0\to \pi^+\pi^-}} &= 1.495 \pm 0.012(\mathrm{stat.}) \pm 0.007(\mathrm{syst.}) \\
\tau_{\mathrm{B^0\to K^+\pi^-}} &= 1.504 \pm 0.006(\mathrm{stat.}) \pm 0.023(\mathrm{syst.}) \\
\tau_{\mathrm{B_s^0\to \pi^+K^-}} &= 1.548 \pm 0.028(\mathrm{stat.}) \pm 0.023(\mathrm{syst.}) \\
\tau_{\mathrm{\Lambda_b^0\to pK^-}} &= 1.477 \pm 0.022(\mathrm{stat.}) \pm 0.022(\mathrm{syst.}) \\
\tau_{\mathrm{\Lambda_b^0\to p\pi^-}} &= 1.511 \pm 0.028(\mathrm{stat.}) \pm 0.012(\mathrm{syst.})
\end{aligned}$$

which are compatible with previous measurements. It is possible to measure the CP parameter, $\mathcal{A}^{\Delta\Gamma}_{\mathrm{KK}}$, from the effective lifetime of the $\mathrm{B_s^0} \to \mathrm{K^+K^-}$ decay which was found to be $\mathcal{A}^{\Delta\Gamma}_{\mathrm{KK}} = -0.975 \pm 0.092$ (stat.) $\pm$ 0.113 (syst.) $\pm$ 0.082 (ext.) and is compatible with the Standard Model unitarity condition of the CP observables.

Chapter 8

CP Violation in $\mathrm{B}\rightarrow h^{+}h^{'-}$ Decays

As was previously discussed in Section 2.4, the decays $\mathrm{B_s^0} \rightarrow \mathrm{K^+K^-}$ and $\mathrm{B^0} \rightarrow \pi^+\pi^-$ have similar contributions from loop topologies as they do from tree topologies so they are promising channels to search for physics beyond the Standard Model. These two decays are related by U-spin symmetry[1] and so can be used to make several complimentary measurements such as the Unitarity Triangle angles γ and -2β_s from measurements of CP violation within the decays. Measurements of the CP observables in $\mathrm{B^0} \rightarrow \pi^+\pi^-$ decays have previously been made by the BaBar [163] and Belle [164] collaborations while the LHCb collaboration has measured the observables for both $\mathrm{B^0} \rightarrow \pi^+\pi^-$ and $\mathrm{B_s^0} \rightarrow \mathrm{K^+K^-}$ decays at 7 TeV [165] and a combined measurement at 7 and 8 TeV [61]. The latest results from these experiments are given in Table 8.1. The latest LHCb study found 4.0 σ evidence for time-dependent CP violation in the $\mathrm{B_s^0}$ sector. This motivates further analysis of these channels using data collected during 2015 and 2016 at LHCb using 2 fb^{-1} of data. This is a smaller integrated luminosity than what is available from Run I, however the increased $b\bar{b}$ production cross-section at 13 TeV results in a larger available data set.

8.1 Simulation Studies

In the analysis of CP violation in the channels of interest from Run I it was felt that several of systematic errors could be reduced by increasing the statistical size of the

---

[1] The d-quarks in the $\mathrm{B^0} \rightarrow \pi^+\pi^-$ decay are replaced by s-quarks in the $\mathrm{B_s^0} \rightarrow \mathrm{K^+K^-}$ decay.

Parameter	Belle	BaBar	LHCb
$S_{\pi\pi}$	$-0.64 \pm 0.08 \pm 0.03$	$-0.68 \pm 0.10 \pm 0.03$	$-0.63 \pm 0.05 \pm 0.01$
$C_{\pi\pi}$	$-0.33 \pm 0.06 \pm 0.03$	$-0.25 \pm 0.08 \pm 0.02$	$-0.34 \pm 0.06 \pm 0.01$
S_{KK}	–	–	$0.18 \pm 0.06 \pm 0.02$
C_{KK}	–	–	$0.20 \pm 0.06 \pm 0.02$
$\mathcal{A}_{\mathrm{KK}}^{\Delta\Gamma}$	–	–	$-0.79 \pm 0.07 \pm 0.10$

Table 8.1: The measured values of the CP observables of interest from previous experimental searches where the first error is statistical and the second is systematic [61, 163, 164].

Monte Carlo (MC) samples. Hence, the first step performed in the Run II analysis was to update the simulation of the experiment to reflect the current understanding of the channels at the time as the values of previously generated observables were taken before they had been experimentally measured. To improve the available number of MC events without excessively using the limited disk space afforded to LHCb it was decided to produce a *filtered* sample. This involved requiring that the MC events passed a predefined set of criteria, in this case each event was required to pass any of the following stripping lines:

- StrippingHb2Charged2BodyB2Charged2BodyLine
- StrippingB2HHBDTLine
- StrippingBs2MuMuLinesNoMuIDLine
- StrippingBs2MuMuLinesWideMassLine
- StrippingBs2MuMuLinesBs2KKLTUBLine
- StrippingBs2MuMuLinesLTUBLine

The first two lines are of interest for $\mathrm{B} \rightarrow h^{+}h'^{-}$ decays and are described in Tables 7.5 and 8.4 while the remaining four lines are of interest to the decay channels $B^{0}_{\mathrm{d/s}} \rightarrow \mu^{+}\mu^{-}$, the requirements of which are not given here (the MC production was conducted in collaboration with the Rare Decays group hence the extra lines). It was decided to produce approximately 2.2×10^{6} events for $\mathrm{B}^{0} \rightarrow \pi^{+}\pi^{-}$, $\mathrm{B}^{0}_{\mathrm{s}} \rightarrow \mathrm{K}^{+}\mathrm{K}^{-}$ and $\mathrm{B}^{0} \rightarrow \mathrm{K}^{+}\pi^{-}$ and 6×10^{5} events for $\mathrm{B}^{0} \rightarrow \mathrm{K}^{+}\mathrm{K}^{-}$, $\mathrm{B}^{0}_{\mathrm{s}} \rightarrow \pi^{+}\pi^{-}$, $\mathrm{B}^{0}_{\mathrm{s}} \rightarrow \pi^{+}\mathrm{K}^{-}$, $\Lambda^{0}_{\mathrm{b}} \rightarrow \mathrm{p}\pi^{-}$ and $\Lambda^{0}_{\mathrm{b}} \rightarrow \mathrm{pK}^{-}$. The splitting of events by data-taking year is detailed in Table 8.2.

Channel	2015 Conditions	2016 Conditions
$\mathrm{B_s^0} \rightarrow \mathrm{K^+K^-}$	600,000	1,800,000
$\mathrm{B^0} \rightarrow \mathrm{K^+K^-}$	150,000	450,000
$\mathrm{B_s^0} \rightarrow \pi^+\pi^-$	150,000	450,000
$\mathrm{B^0} \rightarrow \pi^+\pi^-$	600,000	1,800,000
$\mathrm{B_s^0} \rightarrow \pi^+\mathrm{K^-}$	150,000	450,000
$\mathrm{B^0} \rightarrow \mathrm{K^+}\pi^-$	600,000	1,800,000
$\Lambda_\mathrm{b}^0 \rightarrow \mathrm{p}\pi^-$	150,000	450,000
$\Lambda_\mathrm{b}^0 \rightarrow \mathrm{pK^-}$	150,000	450,000

TABLE 8.2: The requested number of MC events to be produced for the Run 2 analysis. Each sample was split evenly between an LHCb configuration with magnet up and magnet down polarity.

The values of the CP observables were taken from [166]. The decays were produced with EVTGEN[167] using the EvtSSDCP model which can fully describe CP violation from the mass difference (Δm_q), the ratio of $\Delta\Gamma/\langle\Gamma\rangle$, the magnitude and phase of the mixing amplitudes ($|q|$,$|p|$ and $\phi_{\frac{\mathrm{q}}{\mathrm{p}}}$) and the magnitude and phase of the decay amplitudes ($|\bar{A}_f|$, $|A_f|$, $\phi_{\bar{\mathrm{A}}_\mathrm{f}}$ and $\phi_{\mathrm{A_f}}$) describing the decay[2]. The values used in the simulation were

- $$\Delta m_\mathrm{q} = \begin{cases} 17.8\,\mathrm{ps}^{-1} \text{ for } \mathrm{B_s^0} \rightarrow \mathrm{K^+K^-} \\ 0.507\,\mathrm{ps}^{-1} \text{ for } \mathrm{B^0} \rightarrow \pi^+\pi^- \end{cases}$$
- $$2y = \frac{\Delta\Gamma}{\langle\Gamma\rangle} = \begin{cases} 0.179518 \text{ for } \mathrm{B_s^0} \rightarrow \mathrm{K^+K^-} \\ 0 \text{ for } \mathrm{B^0} \rightarrow \pi^+\pi^- \end{cases}$$
- $$\left|\frac{q}{p}\right| = \begin{cases} 1 \text{ for } \mathrm{B_s^0} \rightarrow \mathrm{K^+K^-} \\ 1 \text{ for } \mathrm{B^0} \rightarrow \pi^+\pi^- \end{cases}$$
- $$\phi_{\frac{\mathrm{q}}{\mathrm{p}}} = \begin{cases} 0.04 \text{ for } \mathrm{B_s^0} \rightarrow \mathrm{K^+K^-} \\ -0.775 \text{ for } \mathrm{B^0} \rightarrow \pi^+\pi^- \end{cases}$$
- $$|A_f| = \begin{cases} 9.6 \text{ for } \mathrm{B_s^0} \rightarrow \mathrm{K^+K^-} \\ 1 \text{ for } \mathrm{B^0} \rightarrow \pi^+\pi^- \end{cases}$$
- $$\phi_{\mathrm{A_f}} = \begin{cases} -0.8 \text{ for } \mathrm{B_s^0} \rightarrow \mathrm{K^+K^-} \\ 0.6 \text{ for } \mathrm{B^0} \rightarrow \pi^+\pi^- \end{cases}$$

---

[2] See Section 2.3 for further information.

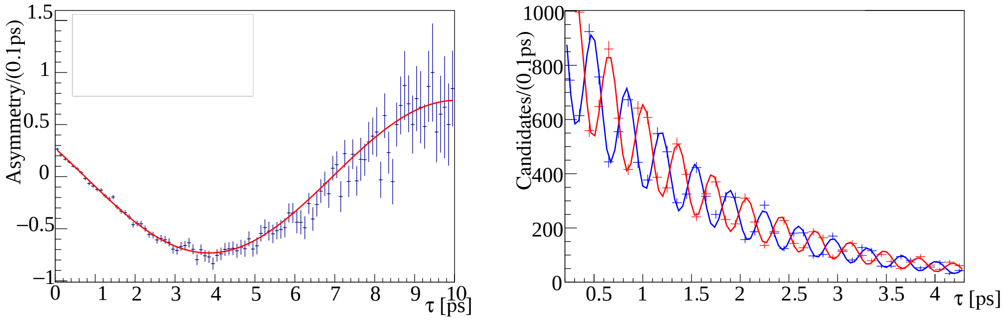

FIGURE 8.1: Results of the fit to the true decay time of simulated two-body b-hadron decays using EVTGEN and PYTHIA8. Left - $\mathrm{B}^0 \to \pi^+\pi^-$. Right - $\mathrm{B}^0_\mathrm{s} \to \mathrm{K}^+\mathrm{K}^-$.

- $|\bar{A}_f| = \begin{cases} 7.52 \text{ for } \mathrm{B}^0_\mathrm{s} \to \mathrm{K}^+\mathrm{K}^- \\ 1.32 \text{ for } \mathrm{B}^0 \to \pi^+\pi^- \end{cases}$
- $\phi_{\bar{\mathrm{A}}_\mathrm{f}} = \begin{cases} -0.61 \text{ for } \mathrm{B}^0_\mathrm{s} \to \mathrm{K}^+\mathrm{K}^- \\ 0.59 \text{ for } \mathrm{B}^0 \to \pi^+\pi^- \end{cases}$
- $\tau = \begin{cases} 1.509\,\mathrm{ps} \text{ for } \mathrm{B}^0_\mathrm{s} \\ 1.519\,\mathrm{ps} \text{ for } \mathrm{B}^0 \end{cases}$
- $A_\mathrm{CP} = \begin{cases} -0.082 \text{ for } \mathrm{B}^0 \to \mathrm{K}^+\pi^- \\ 0.263 \text{ for } \mathrm{B}^0_\mathrm{s} \to \pi^+\mathrm{K}^- \end{cases}$

These amplitudes were chosen to produce $S_{\pi\pi} = -0.68$, $C_{\pi\pi} = -0.27$, $S_\mathrm{KK} = 0.22$, $C_\mathrm{KK} = 0.24$ and $\mathcal{A}^{\Delta\Gamma}_\mathrm{KK} = -0.95$. 95,000 $\mathrm{B}^0 \to \pi^+\pi^-$ and 30,000 $\mathrm{B}^0_\mathrm{s} \to \mathrm{K}^+\mathrm{K}^-$ were produced from this model using PYTHIA8 [168] with an LHC configuration to simulate collisions at 13 TeV with no pileup. The LHCb detector was removed from this simulation to avoid smearing effects and to give perfect tagging performance. The results of the simulation can be seen in Figure 8.1. The results of the fit give $S_{\pi\pi} = -0.6809 \pm 0.0072$, $C_{\pi\pi} = -0.2705 \pm 0.0049$, $S_\mathrm{KK} = 0.2219 \pm 0.0045$ and $C_\mathrm{KK} = 0.2349 \pm 0.0045$ which is in agreement with the predicted values.

When the new MC samples had begun to be produced these events were reconstructed to validate the production against real data. 18508 $\mathrm{B}^0_\mathrm{s} \to \mathrm{K}^+\mathrm{K}^-$ and 14802 $\mathrm{B}^0 \to \pi^+\pi^-$ events were used, created with 2015 conditions, and the transverse momentum, p_T, and pseudorapidity, η, were compared. The MC production was found to be in good agreement with data when the same selection requirements had been applied to both. The comparisons are shown in Figure 8.2.

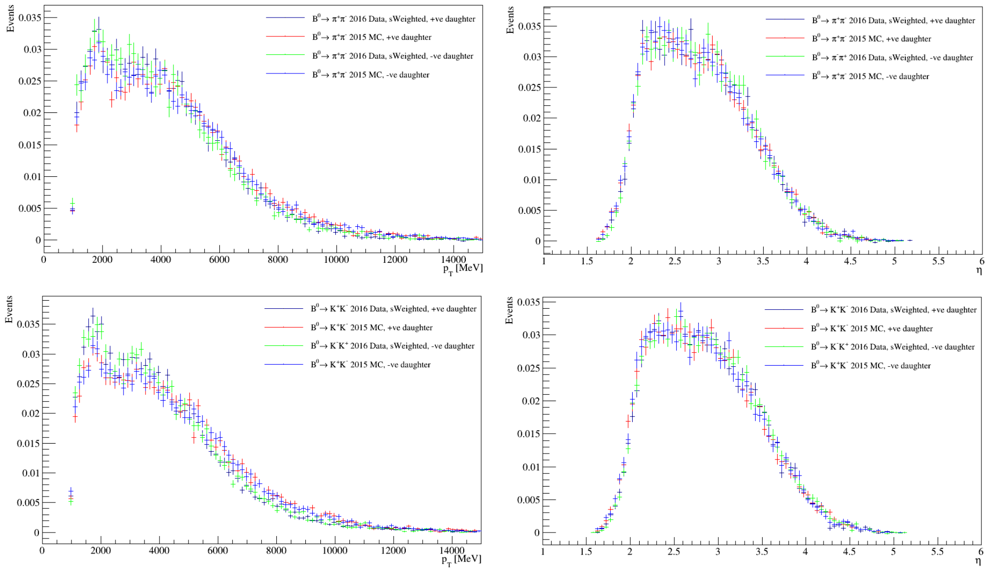

FIGURE 8.2: Comparison of variables between data and Monte Carlo samples produced using Run II conditions. Top Left - Comparison of the transverse momentum of the pions in $\mathrm{B}^0\rightarrow \pi^+\pi^-$ decays. Top Right - Comparison of the pseudorapidity of the pions in $\mathrm{B}^0\rightarrow \pi^+\pi^-$ decays. Bottom Left - Comparison of the transverse momentum of the kaons in $\mathrm{B}^0_s \rightarrow \mathrm{K}^+\mathrm{K}^-$ decays. Bottom Right - Comparison of the pseudorapidity of the kaons in $\mathrm{B}^0_s\rightarrow \mathrm{K}^+\mathrm{K}^-$ decays.

8.2 Candidate Selection

8.2.1 Trigger and Stripping Selections

The trigger and stripping lines were altered in the Run II analysis from the Run I analysis to improve the expected signal yield. The same L0 combination, `L0Global_TIS` || `L0Hadron_TOS`, and HLT2 line, `Hlt2B2HHDecision_TOS`[3], were used but the HLT1 line was altered to the combination `Hlt1TrackMVADecision_TOS` || `Hlt1TwoTrackMVADecision_TOS`. The definition of these triggers is given in Table 8.3

Trigger Line	Cuts Imposed
`Hlt1TrackMVA`	Track χ^2/nDOF $<$ 2.5 Track Ghost Prob. < 0.2 p > 5 GeV/c (if p_{T} > 25 GeV/c, IP χ^2 > 7.4 OR if $0.6 \leq$ p_{T} ≤ 25 GeV/c $\ln(\mathrm{IP}\ \chi^2)\ >\ \frac{1}{(\mathrm{p_T}-1)^2} + \frac{1.1}{25}(25 - \mathrm{p_T}) + \ln(7.4)$)
`Hlt1TwoTrackMVA`	Track χ^2/nDOF < 2.5 Track Ghost Prob. < 0.2 p_{T} > 0.6 GeV/c p > 5 GeV/c IP χ^2 > 4 Vertex χ^2 $<$ 10 DIRA > 0 MVA Decision > 0.95

TABLE 8.3: HLT1 trigger requirements imposed on the daughters in the LHCb 2015 and 2016 data sets.

The data set was stripped using the `B2HHBDTLine` with the cuts it applies given in Table 8.4. The stripping line was changed with respect to Run I as `B2HHBDTLine` was found to increase the signal retention with respect to `Hb2Charged2BodyB2Charged2BodyLine`. This was confirmed using a sample of 10000 $\mathrm{B_s^0} \rightarrow \mathrm{K^+K^-}$ Monte Carlo events produced locally under 2016 conditions. The retention rate of `Hb2Charged2BodyB2Charged2BodyLine` was measured to be $28 \pm 1\%$ compared to $31 \pm 1\%$ for `B2HHBDTLine`.

---

[3] The name of this line was altered to `Hlt2B2HH_B2HHDecision` for 2016 but was physically unchanged

Cut Type	Cuts Imposed
Combination Cuts	Sum p_T $> 4500\,\mathrm{MeV}/c$ $4700 \leq$ $m_{\mathrm{d_1d_2}}$ $\leq 6200\,\mathrm{MeV}/c^2$ DOCA χ^2 < 9
Daughter Cuts	p_T $> 1000\,\mathrm{MeV}/c$ min IP χ^2 > 16 Track χ^2/nDOF $<$ 4 Track Ghost Prob. $<$ 3
Mother Cuts	DIRA > 0.99 IPχ^2 < 9 Flight Distance χ^2 > 100 p_T $> 0\,\mathrm{MeV}/c$ $4800 \leq$ $m_{\mathrm{d_1d_2}}$ $\leq 6200\,\mathrm{MeV}/c^2$
MVA Decision	BDT > -1

TABLE 8.4: `B2HHBDTLine` Stripping Requirements for $\mathrm{B}\to h^+h'^-$ candidates. The definitions of several variables given here are detailed in Table 7.1

8.2.2 Particle Identification

The PID selection methodology was kept similar to that of the Run I analysis as described in Section 7.1.2 in that a two-dimensional phase space of DLL distributions was scanned for signal efficiency and background contaminations. However, as it was found that lepton (electron and muon) separations decreased the signal retention by a few percent without any significant decrease in background rejection, these cuts were dropped, leaving only kaon, pion and proton separations.

PIDCALIB was again used to estimate the contaminations with a specific Run II configuration. All samples were created using data collected at 13 TeV, the pion samples were obtained from $\mathrm{K^0_S}\to\pi^+\pi^-$ decays, and the kaon samples were obtained from $\phi\to\mathrm{K^+K^-}$ decays. Extra samples for the pion and kaon calibration for tracks with high p and p_T were obtained from $\mathrm{D^0}\to\mathrm{K^+}\pi^-$ decays. The proton samples were obtained for high and low p and p_T events from $\Lambda\to\mathrm{p}\pi^-$ decays with an additional sample of $\Lambda_\mathrm{c}^+\to\mathrm{pK^-}\pi^+$ decays used to increase the coverage for high p and p_T events. Invariant mass distributions of the samples used in the calibration can be found in Figure 8.3.

The same technique from the Run I analysis to determine the background contaminations was used with updated branching fractions. The largest contamination still comes from $\mathrm{B^0}\to\mathrm{K^+}\pi^-$ decays and it was decided that this contamination

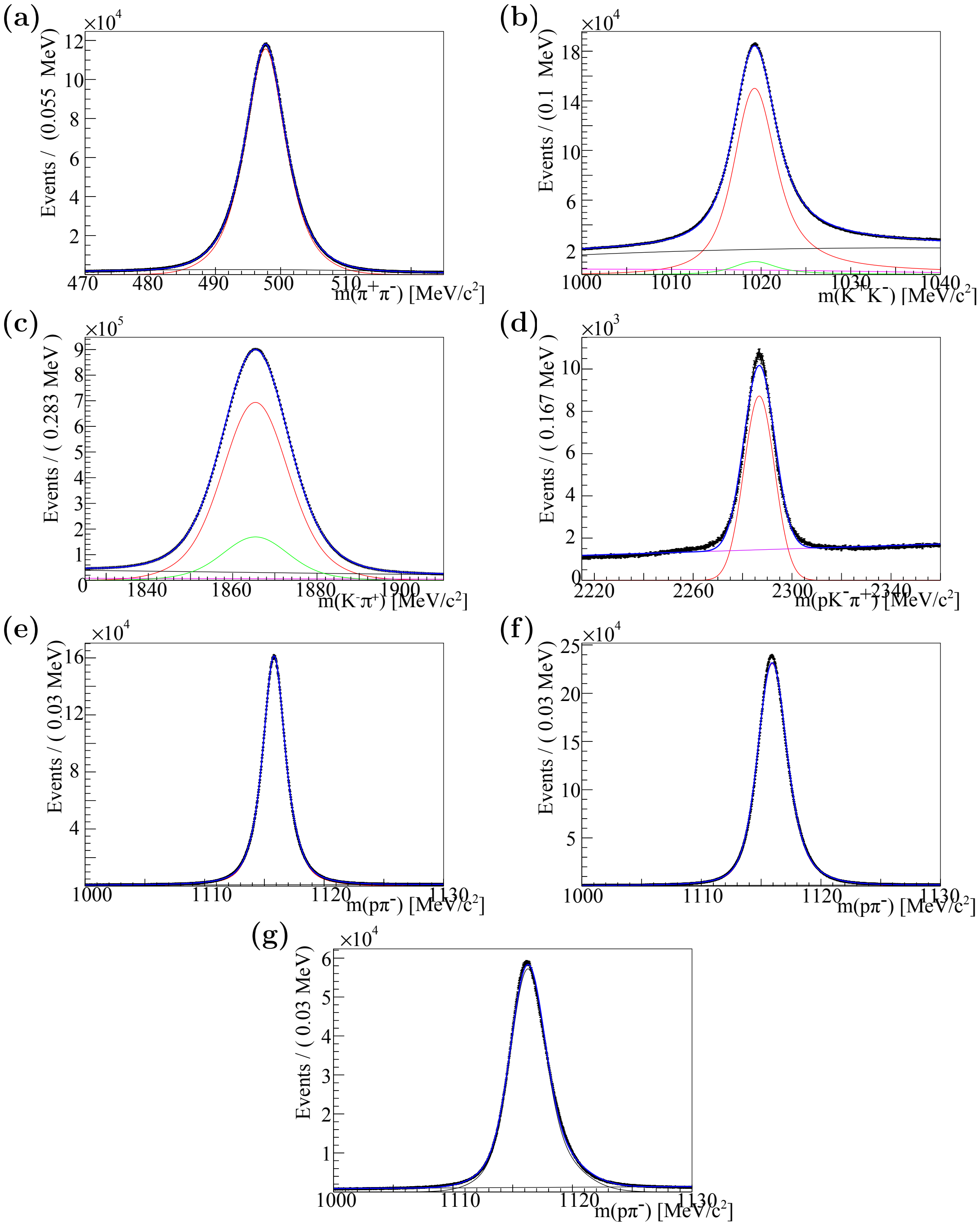

FIGURE 8.3: The calibration samples used to estimate background contaminations in the Run II analysis. (a) The $K^0_S \rightarrow \pi^+\pi^-$ sample. (b) The $\phi \rightarrow K^+K^-$ sample. (c) The $D^0 \rightarrow K^+\pi^-$ sample. (d) The $\Lambda_c^+ \rightarrow pK^-\pi^+$ sample. (e) The $\Lambda \rightarrow p\pi^-$ sample. (f) The high p_T $\Lambda \rightarrow p\pi^-$ sample. (g) The very high p_T $\Lambda \rightarrow p\pi^-$ sample.

Ratio	Value
$\frac{f_s}{f_d}$	$0.267^{+0.021}_{-0.020}$
$\frac{f_s}{f_u+f_d}$	$0.134^{+0.012}_{-0.011}$
$\frac{f_{\Lambda_b}}{f_u+f_d}$	0.240 ± 0.022

TABLE 8.5: The $b\bar{b}$ hadronization ratios used in the Run II analysis [150].

Channel	$\mathcal{B}$ $[\times 10^{-6}]$
$\mathrm{B^0_s} \to \mathrm{K^+K^-}$	24.8 ± 1.7
$\mathrm{B^0} \to \mathrm{K^+K^-}$	0.08 ± 0.01
$\mathrm{B^0_s} \to \pi^+\pi^-$	0.67 ± 0.08
$\mathrm{B^0} \to \pi^+\pi^-$	5.10 ± 0.19
$\mathrm{B^0_s} \to \pi^+\mathrm{K^-}$	5.5 ± 0.5
$\mathrm{B^0} \to \mathrm{K^+}\pi^-$	19.57^{+53}_{-52}
$\Lambda^0_\mathrm{b} \to \mathrm{p}\pi^-$	3.5 ± 1.0
$\Lambda^0_\mathrm{b} \to \mathrm{pK^-}$	5.5 ± 1.4

TABLE 8.6: The 2-body branching fractions relevant to the channels being studied [151].

should be kept to a maximum of 10 % if possible. A further large background comes from $\Lambda^0_\mathrm{b} \to \mathrm{pK^-}$ and $\Lambda^0_\mathrm{b} \to \mathrm{p}\pi^-$ decays in the $\mathrm{K^+K^-}$ and $\pi^+\pi^-$ spectra respectively which require good proton-kaon and proton-pion discrimination

The hadronization fractions are shown in Table 8.5 [150], the branching fractions for the signal channels and main contaminations are shown in Table 8.6 [151]. The initial efficiency studies were performed using 2016 MC samples from the Stripping 26 campaign. After the study, this campaign was found to have a bug in certain stripping lines which did not affect the channels under study, hence it was felt the results found here were still applicable to the data sets. The signal selection efficiencies for $\mathrm{B^0_s} \to \mathrm{K^+K^-}$ and $\mathrm{B^0} \to \pi^+\pi^-$ are given in Figure 8.4. The $\mathrm{B^0_s} \to \mathrm{K^+K^-}$ efficiency is given as a 2D phase space distribution of $\Delta\log(\mathcal{L}_{\mathrm{K}\pi})$ and $\Delta\log(\mathcal{L}_{\mathrm{Kp}})$ while the $\mathrm{B^0} \to \pi^+\pi^-$ efficiency is given as a 2D phase space distribution of $\Delta\log(\mathcal{L}_{\mathrm{K}\pi})$ and $\Delta\log(\mathcal{L}_{\mathrm{p}\pi})$. The discontinuity apparent in the $\mathrm{B^0_s} \to \mathrm{K^+K^-}$ efficiency is due to new algorithms implemented for Run II which creates a discontinuity at $\Delta\log(\mathcal{L}_{\mathrm{Kp}}) = 0$[4]. The $\mathrm{B^0} \to \mathrm{K^+}\pi^-$ and $\Lambda^0_\mathrm{b} \to \mathrm{pK^-}$ contaminations with respect to the $\mathrm{B^0_s} \to \mathrm{K^+K^-}$ signal are given in Figure 8.5 while the $\mathrm{B^0} \to \mathrm{K^+}\pi^-$ and $\Lambda^0_\mathrm{b} \to \mathrm{p}\pi^-$ contaminations with respect to the $\mathrm{B^0} \to \pi^+\pi^-$ signal are given in Figure 8.6.

---

[4] Recall that $\Delta\log(\mathcal{L}_{\mathrm{Kp}})$ is difference between two variables; $\Delta\log(\mathcal{L}_{\mathrm{K}\pi})$ and $\Delta\log(\mathcal{L}_{\mathrm{p}\pi})$

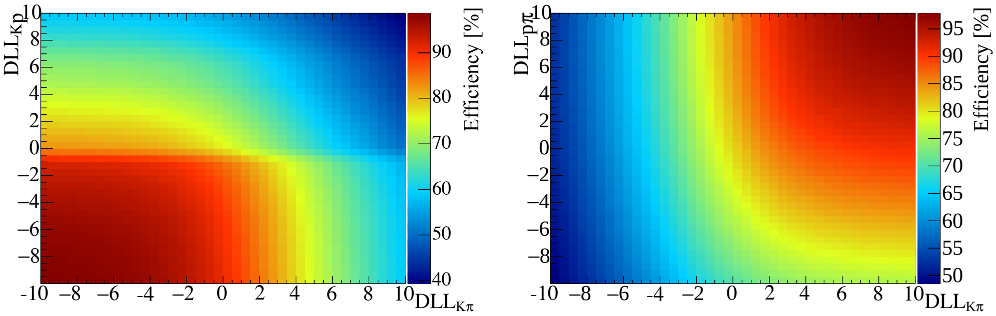

FIGURE 8.4: 2D phase space distributions of signal particle identification efficiency using 2016 MC. Left - The selection efficiency for $B^0_s \to K^+K^-$ candidates. Right - The selection efficiency for $B^0 \to \pi^+\pi^-$ candidates.

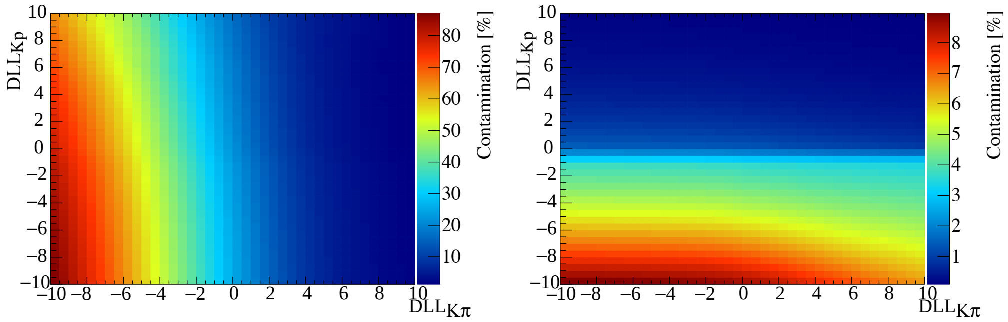

FIGURE 8.5: 2D phase space distributions of background contaminations with respect to the $B^0_s \to K^+K^-$ signal using 2016 MC. Left - $B^0 \to K^+\pi^-$ contamination. Right - $\Lambda^0_b \to pK^-$ contamination.

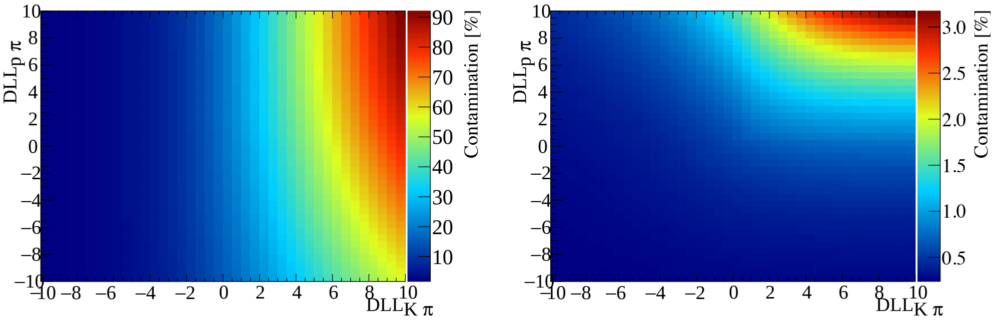

FIGURE 8.6: 2D phase space distributions of background contaminations with respect to the $B^0 \to \pi^+\pi^-$ signal using 2016 MC. Left - $B^0 \to K^+\pi^-$ contamination. Right - $\Lambda^0_b \to p\pi^-$ contamination.

8.2.3 Multivariate Analysis

Several methods of reducing the combinatorial background were investigated using TMVA to decide which technique would be most effective for the channels under investigation. The MVAs were trained using MC events for the signal and the

Channel	$\mathrm{K^+K^-}$	$\pi^+\pi^-$
	ε [%]	
Signal	60.20 ± 0.09	58.49 ± 0.10
	k [%]	
$\mathrm{B_s^0\rightarrow K^+K^-}$	-	$(4.83\pm0.55)\times10^{-2}$
$\mathrm{B^0\rightarrow K^+K^-}$	2.02 ± 0.78	$(5.96\pm0.80)\times10^{-4}$
$\mathrm{B_s^0}\rightarrow\pi^+\pi^-$	$(2.06\pm0.53)\times10^{-3}$	3.45 ± 1.00
$\mathrm{B^0}\rightarrow\pi^+\pi^-$	$(8.05\pm2.10)\times10^{-3}$	-
$\mathrm{B_s^0}\rightarrow\pi^+\mathrm{K^-}$	0.58 ± 0.06	0.54 ± 0.08
$\mathrm{B^0\rightarrow K^+}\pi^-$	7.88 ± 0.26	7.38 ± 0.37
$\Lambda_\mathrm{b}^0\rightarrow\mathrm{pK^-}$	3.82 ± 0.76	$(1.38\pm0.29)\times10^{-2}$
$\Lambda_\mathrm{b}^0\rightarrow\mathrm{p}\pi^-$	$(8.36\pm0.16)\times10^{-2}$	0.53 ± 0.11

Table 8.7: The predicted signal efficiencies and background contaminations present in the 2016 $\mathrm{B_s^0\rightarrow K^+K^-}$ and $\mathrm{B^0}\rightarrow\pi^+\pi^-$ before applying an MVA. The background contaminations are quoted with respect to the signal efficiencies.

upper mass sideband of the invariant mass of the daughters for the background[5]. Three variables from the mother (the decay vertex χ^2, flight distance χ^2 and the cosine of the angle between the momentum and the direction of flight) and six variables from the daughters (the minimum and maximum p_T, the minimum and maximum IP χ^2 and the minimum and maximum track χ^2 per number of degrees of freedom) were used to train the MVAs. The invariant mass distributions for the $\mathrm{K^+K^-}$ and $\pi^+\pi^-$ final states used in the training and testing of the MVAs can be seen in Figure 8.7, with the predicted signal efficiencies and background contaminations present in the samples given in Table 8.7[6]. The signal and background event distributions used to train the $\mathrm{B^0}\rightarrow\pi^+\pi^-$ MVAs on odd events can be seen in Figure 8.8. The receiver operating characteristic (ROC) curve comparing the signal versus background rejection as the classifier response is varied for the MVA techniques applied to the data sets are shown in Figure 8.9 where it can be seen that a boosted decision tree (BDT) gives the best performance [152]. To improve the selection efficiency each final state had a specific BDT trained for it using MC corresponding to the signal of interest and the upper mass side band from the channel of interest. To avoid biases in selecting events, two BDTs are created for each final state, one BDT is created from even numbered events to be applied to odd numbered events and vice versa for the other events.

---

[5] The upper mass sideband for both the $\pi^+\pi^-$ and $\mathrm{K^+K^-}$ was defined to be in the range $5550\leq m_{\mathrm{d_1d_2}}\leq 5850\,\mathrm{MeV}$

[6] The PID cuts applied to the training samples were chosen to lie within the contaminations region of interest for these cuts.

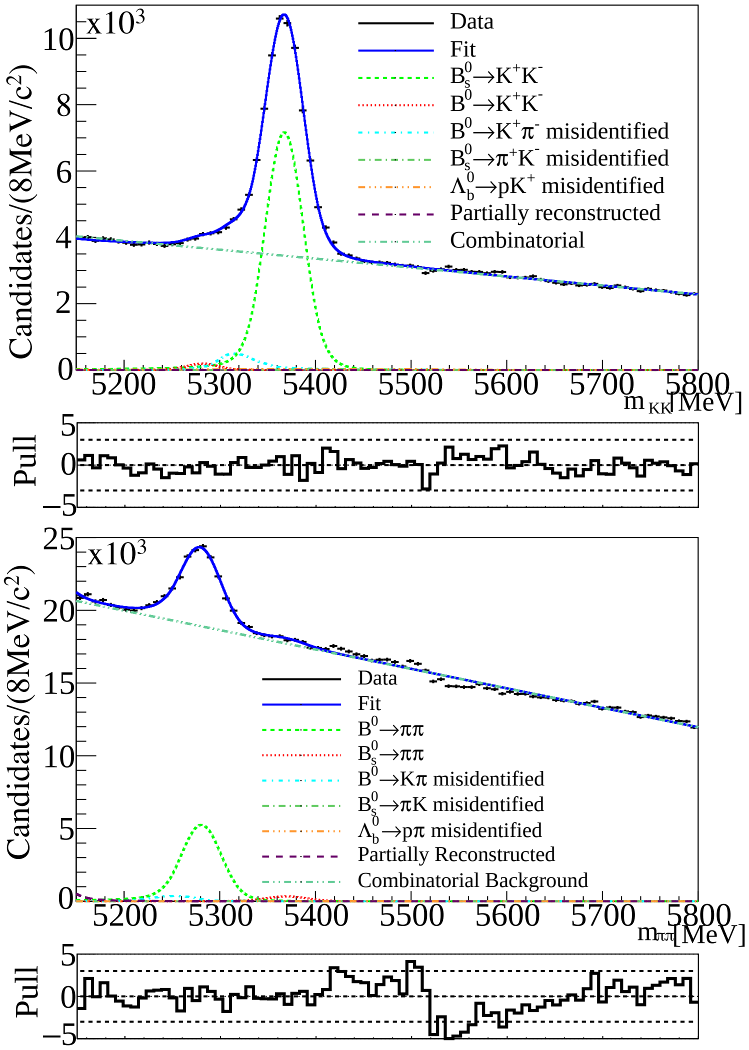

FIGURE 8.7: Pre-BDT invariant mass distributions for $B_s^0 \to K^+K^-$ events (top) and $B^0 \to \pi^+\pi^-$ events (bottom) from the 2016 data set used to train and test the BDTs. The contamination predictions were taken from Table 8.7, the background models and signal PDF parameters were taken from the Run I analysis.

The difference in the distributions of the variables for the different BDT trainings cannot be discerned by eye, however tests performed to measure combinatorial background rejection for the $B^0 \to \pi^+\pi^-$ decay channel found that using a BDT trained on $\pi^+\pi^-$ events rejected 98.02% of background events under the mass peak compared to 96.80% when using a BDT trained on K^+K^- events for the equivalent cuts[7].

---

[7] Pions are produced in a greater quantity than other hadrons in proton-proton collisions, thus the $B^0 \to \pi^+\pi^-$ channel suffers from a larger combinatorial background contamination than other channels and hence requires harsher MVA cuts to compensate for this.

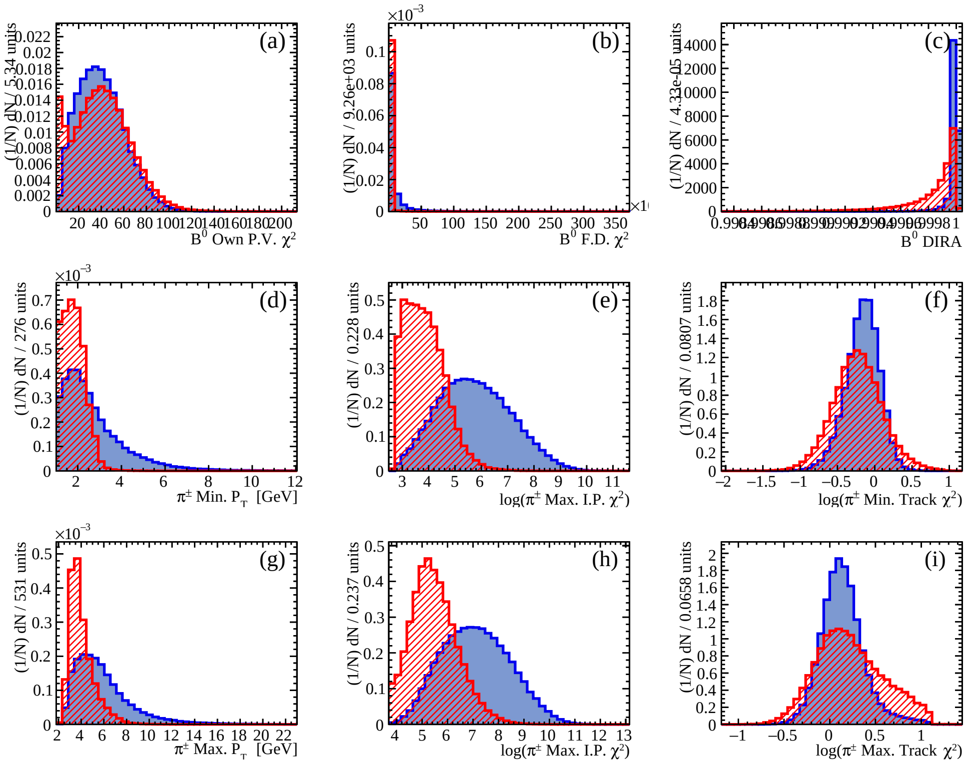

FIGURE 8.8: Comparison of variables used for the BDT trained on $\mathrm{B}^0 \to \pi^+\pi^-$ events with an odd Event Number. Blue - Simulated signal events, red - data events from the upper mass sideband. (a) The primary vertex χ^2 distribution of the mother, (b) the flight distance χ^2 of the mother, (c) the cosine of the angle between the momentum and the direction of flight of the mother, (d) the minimum daughter transverse momentum, (e) the minimum daughter I.P. χ^2, (f) the minimum daughter track χ^2 per number of degrees of freedom, (g) the maximum daughter transverse momentum, (h) the maximum daughter I.P. χ^2, (i) the maximum daughter track χ^2 per number of degrees of freedom.

To ensure optimal response of the BDT's it is important that the correlations between training variables are reduced as far as is reasonably possible. These correlations are given in Figure 8.10. The high correlation between the minimum and maximum I.P. χ^2 of the daughter tracks for the signal sample is to be expected as the daughters originate from the same secondary vertex. This correlation is reduced for the upper mass side band sample as the tracks are randomly matched. The high correlation between the mother's flight distance χ^2 and the daughter's I.P. χ^2 can also be explained via similar reasoning as the flight distance is derived from the secondary vertex. To ensure proper training of the samples, the response of the training events was compared with the response of a testing sample with opposite event number for both signal and background and overlayed together. This test can be useful to get a qualitative feel of how much signal and background can be reject as a function of MVA cut. The results of the comparison are given

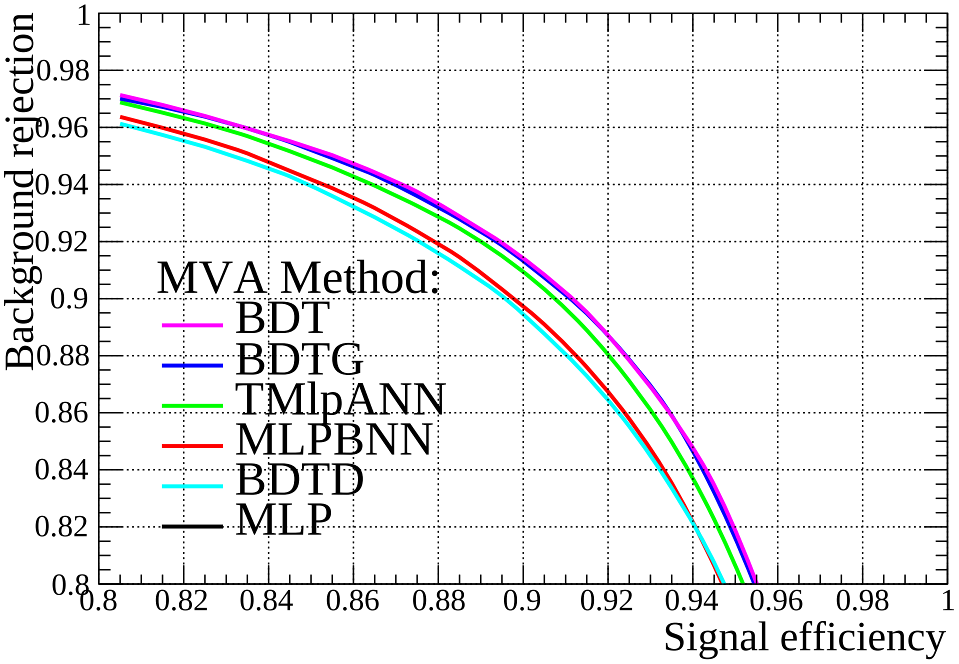

FIGURE 8.9: Comparison of several multi-variate analysis techniques for rejecting combinatorial background events. This ROC curve was produced using $B^0 \to \pi^+\pi^-$ MC for the signal and $\pi^+\pi^-$ events from the upper mass side band of the decay channel. These events were required to have an odd event number.

in Figure 8.11.

The optimal cut point of the BDT is believed to be in a region within 10% of the maximum significance where the significance, Z, is defined as

$$Z = \frac{S}{\sqrt{S + B}} \tag{8.1}$$

where S is the number of signal events and B is the number of combinatorial background events. As it was felt it was important to understand the combinatorial background contamination under the signal peak, small regions around the signal mass quoted from the Particle Data Group were measured for their signal and combinatorial background yields. In the $\pi^+\pi^-$ invariant mass spectrum the yields were measured between 5220 and 5340 MeV which is $3\,\sigma$ off the mass peak of the B^0, while for the K^+K^- mass spectrum the range was between 5320 and 5430 MeV. The upper mass limit is still $3\,\sigma$ off the mass peak of the B_s^0 but the lower limit was tightened to $2.5\,\sigma$ to avoid contamination from $B^0 \to K^+\pi^-$ events. The true significances of the BDTs were measured for even and odd event numbers and compared to the predicted significance. This was to ensure that

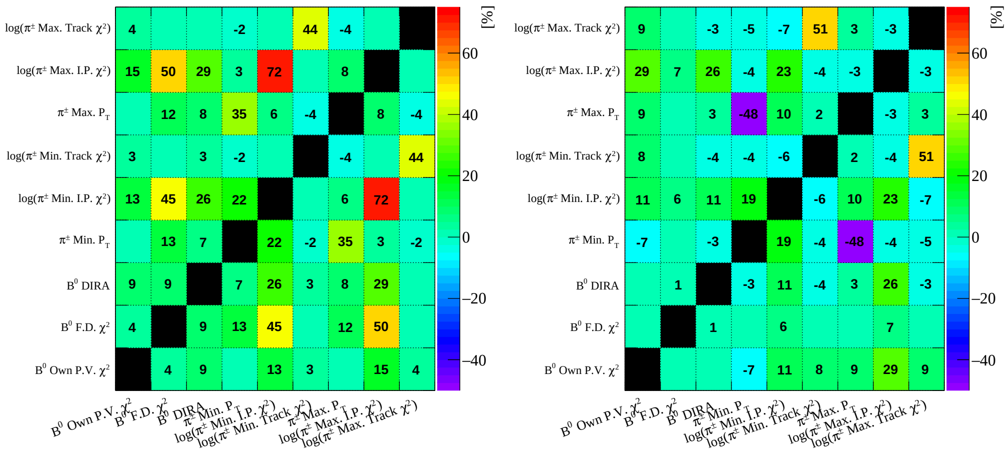

FIGURE 8.10: The measured correlations between variables used to train the BDT for $B^0 \to \pi^+\pi^-$ candidates with an odd Event Number. Left - Correlations apparent in variables from the signal MC sample. Right - Correlations apparent in variables from the upper mass side band of the $\pi^+\pi^-$ invariant mass spectrum. Variables without a value for their correlation were measured to have a correlation of zero.

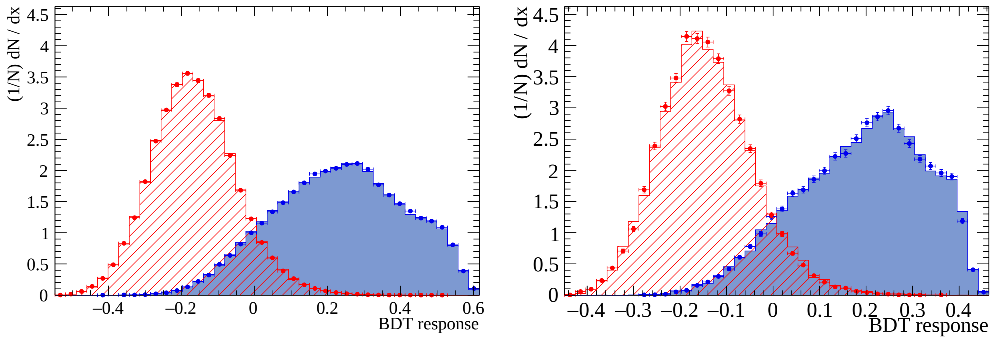

FIGURE 8.11: The measured responses of the BDTs used in the analysis. The training samples are given as data points while the testing samples are given as solid histograms. The signal events are given in blue while the background events are given in red. Left - The response of the BDT trained on $B^0 \to \pi^+\pi^-$ candidates with an odd Event Number. Right - The response of the BDT trained on $B_s^0 \to K^+K^-$ candidates with an odd Event Number.

the true point of maximum was known and that both BDTs treated the data sample consistently. The measured significance of the BDTs used compared to their predicted significance are shown in Figure 8.12 where it can be seen that they all show the same trend with the maximum significances of the BDTs trained on even and odd event numbers appearing at the same BDT cut.

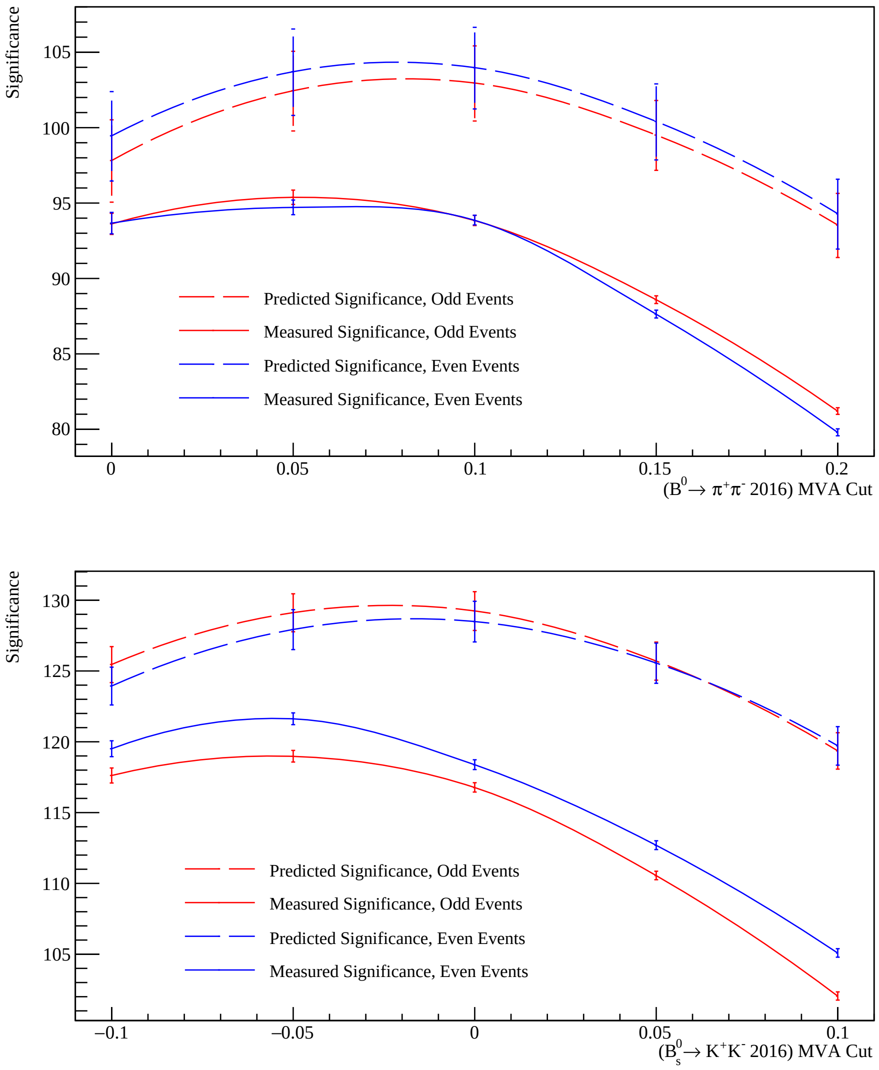

FIGURE 8.12: Comparison of the predicted significance in dashed lines to the measured significance in solid lines. The results for the BDT applied to odd events are given in red while those for even events are given in blue. Top - Significance comparison for the $B^0 \rightarrow \pi^+\pi^-$ event selection. Bottom - Significance comparison for the $B_s^0 \rightarrow K^+K^-$ event selection.

8.2.4 Simultaneous Optimisation of the PID and BDT

While it has previously been assumed that the greatest sensitivity on the A^{CP} parameters S_f, C_f and $\mathcal{A}_f^{\Delta\Gamma}$ could be achieved by maximising the signal significance there is no reason to believe this is truly the case. For example, due to the relatively slow oscillation of the B^0, the rising edge of the sine term in the decay is sensitive at low decay times, where the decay time acceptance is most apparent, while the parameter and $\mathcal{A}_{\mathrm{KK}}^{\Delta\Gamma}$, with its hyperbolic sine dependence, is sensitive at higher decay times where the event acceptance begins to decrease. It is also known that most combinatorial background events have a short decay time and the training variables of the BDT will reject more short-lived events than long-lived ones. The effect of misidentified backgrounds under the signal peak on the A^{CP} parameters is also unknown. Hence a simultaneous optimisation of the PID and BDT selection was performed to measure the predicted sensitivity on $S_{\pi\pi}$, $C_{\pi\pi}$, S_{KK}, C_{KK} and $\mathcal{A}_{\mathrm{KK}}^{\Delta\Gamma}$.

This optimisation was achieved by measuring the signal and background yields of both channels at different values of BDT response and $\Delta\log(\mathcal{L}_{\mathrm{K}\pi})$ then producing several simplified simulations (or pseudo-experiments) of the samples before measuring the errors on the parameters of interest. From studies of pseudo-experiments it was found that the error distribution for the parameters was approximately a few percent of the mean error hence only 10 pseudo-experiments were required to be produced at each point in the optimisation phase space. The search areas for the BDT and PID cuts were decided from the results found in Figures 8.4, 8.5, 8.6 and 8.12.

For the $\mathrm{B}^0\to\pi^+\pi^-$ selection the variation of the channel was studied for a PID range between $-5 \leq \Delta\log(\mathcal{L}_{\mathrm{K}\pi}) \leq 0$ in unit steps and a BDT range between $-0.05 \leq$ BDT Response ≤ 0.15 in response steps of 0.02 while for the $\mathrm{B}_\mathrm{s}^0\to\mathrm{K}^+\mathrm{K}^-$ selection the variation of the channel was studied for a PID range between $0 \leq \Delta\log(\mathcal{L}_{\mathrm{K}\pi}) \leq 5$ in unit steps and a BDT range between $-0.19 \leq$ BDT Response ≤ 0.05. It can be seen from Figures 8.4 to 8.6 that the signal efficiency and background rejection for proton contamination has a low variation in this region hence a cut of $\Delta\log(\mathcal{L}_{\mathrm{Kp}}) > -2$ was applied to the $\mathrm{B}_\mathrm{s}^0\to\mathrm{K}^+\mathrm{K}^-$ selection and a cut of $\Delta\log(\mathcal{L}_{\mathrm{p}\pi}) < 3$ was applied to the $\mathrm{B}^0\to\pi^+\pi^-$ selection.

To ensure the models were as realistic as possible, the variation of several background and signal parameters that can affect the measurement of A^{CP} observables

Parameter	Loose PID, Loose BDT	Loose PID, Tight BDT	Tight PID, Loose BDT	Tight PID, Tight BDT
Combinatorial Background τ	0.43 ps	1.04 ps	0.37 ps	1.05 ps
P.R.B. Background τ	1.31 ps	1.31 ps	1.26 ps	1.28 ps
Signal Mean $\delta(t)$	38.35 fs	38.60 fs	40.39 fs	37.96 fs
Signal R.M.S. $\delta(t)$	0.96 fs	1.00 fs	1.04 fs	0.93 fs
Background Mean $\delta(t)$	43.16 fs	42.08 fs	44.89 fs	40.67 fs
Background R.M.S. $\delta(t)$	1.30 fs	1.37 fs	1.40 fs	1.10 fs
Signal Mean Mistag	0.3614	-	-	0.3615
Background Mean Mistag	0.3577	-	-	0.3407

TABLE 8.8: The measured value of several parameters thought to vary as a function of BDT and PID selection for data in the K^+K^- invariant mass spectrum. The parameters were measured in the four corners of the optimisation phase space.

were studied at the four corners of the optimisation parameter space to see if any cut-dependent models must be accounted for in the generation of the pseudo-experiments. It was found that the decay time of combinatorial background varies as a function of BDT cut but not PID cut. This is expected due to the training variables that were used to produce the BDT. It was also seen that the decay time of the partially reconstructed background did not vary with either the BDT or PID cuts. This was also the same for the mistag distributions of signal and background events. The decay time error[8] which is required to calculate the correct decay time resolution was found not to vary with the cuts imposed however the distributions were found to be different for signal and combinatorial background events with the background events having a higher mean and R.M.S. decay time error. This is likely due to poorer impact parameter measurements for combinatorial background events than for signal events. These findings are summarised in Table 8.8 and Appendix D.

A data set for the $\mathrm{B_s^0} \to \mathrm{K^+K^-}$ and $\mathrm{B^0} \to \pi^+\pi^-$ selection was produced with the trigger cuts and stripping line applied using the 2015 and 2016 data collected. A cut of $\Delta\log(\mathcal{L}_{\mathrm{Kp}}) >$ -2 was applied to the $\mathrm{B_s^0} \to \mathrm{K^+K^-}$ selection and a cut of $\Delta\log(\mathcal{L}_{\mathrm{p}\pi}) < 3$ was applied to the $\mathrm{B^0} \to \pi^+\pi^-$ selection. The flavour tagging[9] calibration was performed using taggers trained on Run I data, which was felt to be similar enough to the final Run II optimised tagger for the requirements of

---

[8] See Section 8.5

[9] Flavour tagging is a method to discern whether the B-hadron contained a b or a $\bar{b}$ quark at the point of production and is discussed in depth in Section 8.6

the study. The taggers were used to divide each sample by their flavour to be able to measure the variation of signal and background events between the three tagged states. The invariant mass distribution was constructed by requiring that the mother candidate comes from the primary vertex. This distribution was then fitted for every combination of BDT and $\Delta\log(\mathcal{L}_{\mathrm{K}\pi})$ in the range $5000 \leq m_{\mathrm{d_1 d_2}} \leq 5800$ MeV. The backgrounds present in the samples were assumed to be:

- For $\mathrm{B}^0 \to \pi^+\pi^-$: $\mathrm{B}^0 \to \mathrm{K}^+\pi^-$, partially reconstructed and combinatorial background,
- For $\mathrm{B}^0_\mathrm{s} \to \mathrm{K}^+\mathrm{K}^-$: $\mathrm{B}^0 \to \mathrm{K}^+\pi^-$, $\mathrm{B}^0_\mathrm{s} \to \pi^+\mathrm{K}^-$, $\Lambda^0_\mathrm{b} \to \mathrm{p}\pi^-$, partially reconstructed and combinatorial. background

The measured $\mathrm{B}^0_\mathrm{s} \to \mathrm{K}^+\mathrm{K}^-$ yield, significance[10], and tagging power[11] for the $\mathrm{B}^0_\mathrm{s} \to \mathrm{K}^+\mathrm{K}^-$ optimisation are shown in Figure 8.13 while the equivalent plots for the $\mathrm{B}^0 \to \pi^+\pi^-$ optimisation are shown in Figure 8.14. These results were used to produce pseudo-experiments with the measured mass shapes and a per-event mistag and decay time error. The calibration of the flavour tagging was taken from a previous LHCb analysis [166] while the calibration of the decay time resolution using the decay time error was taken from a study on prompt $\mathrm{J}/\psi \to \mu^+\mu^-$ decays at 13 TeV described in Section 8.5.2. Each decay component of the sample was generated with the appropriate tag probabilities that had been measured in data.

The results of the predicted sensitivities to S_{KK}, C_{KK} and $\mathcal{A}^{\Delta\Gamma}_{\mathrm{KK}}$ are given in Figure 8.15 while the predicted sensitivities to $S_{\pi\pi}$ and $C_{\pi\pi}$ are given in Figure 8.16. It should be noted that, while every care was taken to ensure the toys were as faithful to true data as feasible, these values might not reflect the true sensitivities. However this study gives a stronger justification to the final selection over maximising the signal significance of the samples. These results combined with those detailed in Figures 8.13 and 8.14 were used to finalise the selection. The cuts were chosen at a point where the statistical uncertainty on the observables and the background contaminations were reduced while tagging power was kept high to reduce the resulting systematic uncertainty. The final cuts are summarised in Table 8.9. The selections for the two final states were predicted to give a statistical

---

[10] The significance this time was measured across the full invariant mass range of study.

[11] Equivalent to the fraction of signal candidates available for use in measuring the CP observables if they were perfectly tagged.

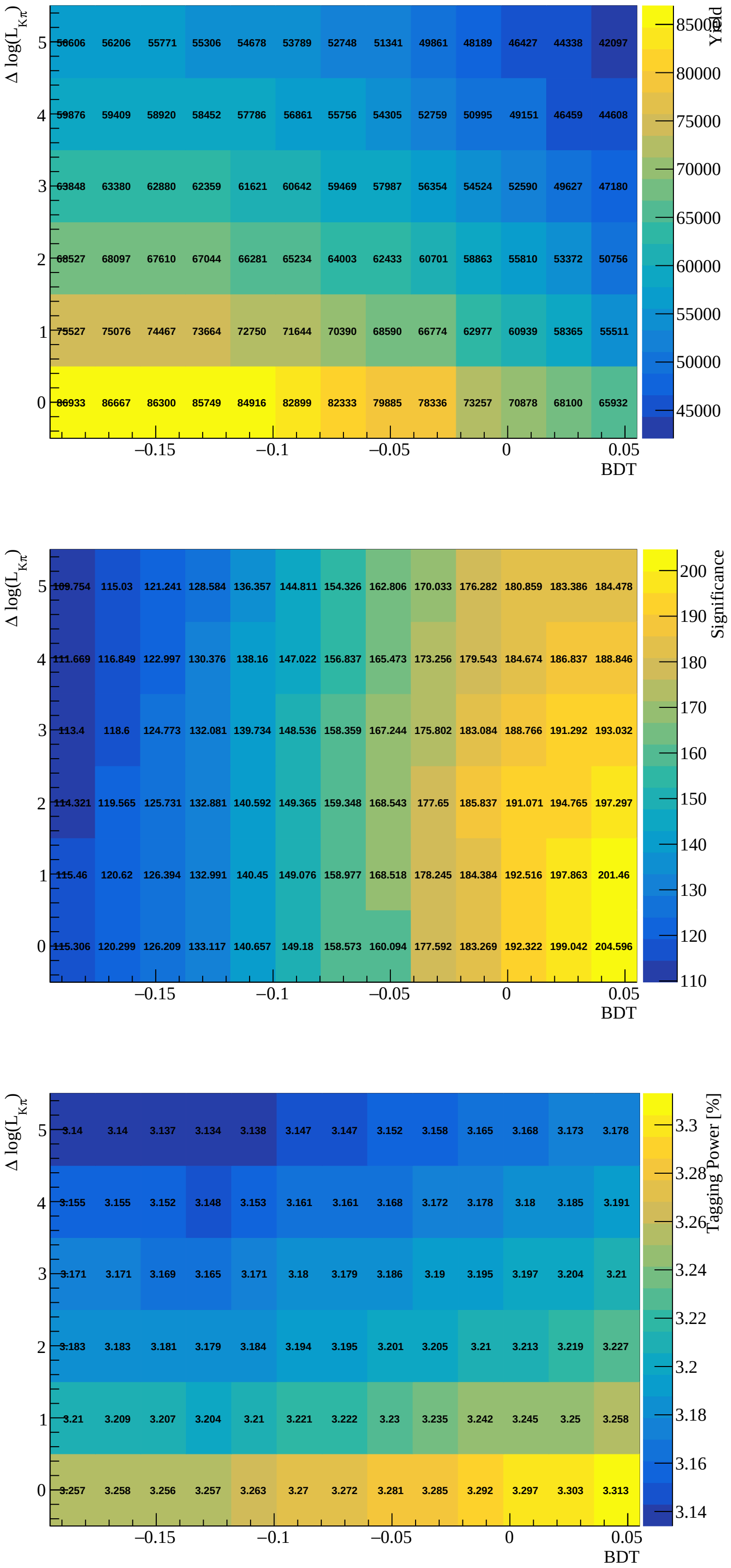

FIGURE 8.13: Top - The measured $B_s^0 \rightarrow K^+K^-$ signal yield for different BDT responses and $\Delta\log(\mathcal{L}_{K\pi})$. contaminations dle The measured $B_s^0 \rightarrow K^+K^-$ significance for different BDT responses and $\Delta\log(\mathcal{L}_{K\pi})$ cuts. Bottom - The measured $B_s^0 \rightarrow K^+K^-$ tagging power for different BDT responses and $\Delta\log(\mathcal{L}_{K\pi})$. It should be noted that approximately 5% of the total integrated luminosity from 2015 and 2016 is missing from these samples. This was corrected for in the toy generation.

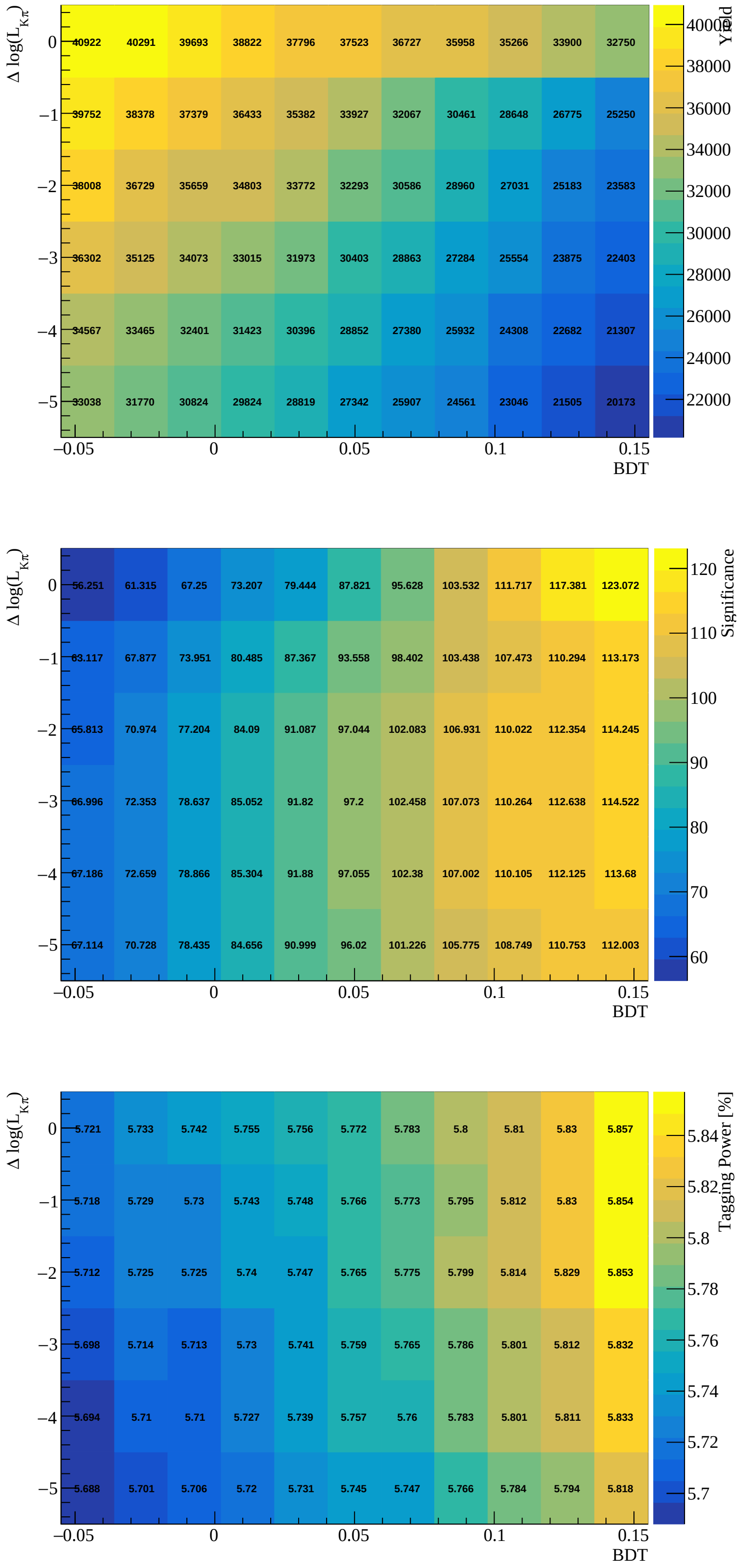

0	40922	40291	39693	38822	37796	37523	36727	35958	35266	33900	32750
−1	39752	38378	37379	36433	35382	33927	32067	30461	28648	26775	25250
−2	38008	36729	35659	34803	33772	32293	30586	28960	27031	25183	23583
−3	36302	35125	34073	33015	31973	30403	28863	27284	25554	23875	22403
−4	34567	33465	32401	31423	30396	28852	27380	25932	24308	22682	21307
−5	33038	31770	30824	29824	28819	27342	25907	24561	23046	21505	20173

0	56.251	61.315	67.25	73.207	79.444	87.821	95.628	103.532	111.717	117.381	123.072
−1	63.117	67.877	73.951	80.485	87.367	93.558	98.402	103.438	107.473	110.294	113.173
−2	65.813	70.974	77.204	84.09	91.087	97.044	102.083	106.931	110.022	112.354	114.245
−3	66.996	72.353	78.637	85.052	91.82	97.2	102.458	107.073	110.264	112.638	114.522
−4	67.186	72.659	78.866	85.304	91.88	97.055	102.38	107.002	110.105	112.125	113.68
−5	67.114	70.728	78.435	84.656	90.999	96.02	101.226	105.775	108.749	110.753	112.003

0	5.721	5.733	5.742	5.755	5.756	5.772	5.783	5.8	5.81	5.83	5.857
−1	5.718	5.729	5.73	5.743	5.748	5.766	5.773	5.795	5.812	5.83	5.854
−2	5.712	5.725	5.725	5.74	5.747	5.765	5.775	5.799	5.814	5.829	5.853
−3	5.698	5.714	5.713	5.73	5.741	5.759	5.765	5.786	5.801	5.812	5.832
−4	5.694	5.71	5.71	5.727	5.739	5.757	5.76	5.783	5.801	5.811	5.833
−5	5.688	5.701	5.706	5.72	5.731	5.745	5.747	5.766	5.784	5.794	5.818

FIGURE 8.14: Top - The measured $B^0 \to \pi^+\pi^-$ signal yield for different BDT responses and $\Delta\log(\mathcal{L}_{K\pi})$. contaminations dle The measured $B^0 \to \pi^+\pi^-$ significance for different BDT responses and $\Delta\log(\mathcal{L}_{K\pi})$. Bottom - The measured $B^0 \to \pi^+\pi^-$ tagging power for different BDT responses and $\Delta\log(\mathcal{L}_{K\pi})$ cuts. It should be noted that approximately 5% of the total integrated luminosity from 2015 and 2016 is missing from these samples. This was corrected for in the toy generation.

	Requirement
L0	`L0Global_TIS` ‖ `L0Hadron_TOS`
HLT1	`Hlt1TrackMVADecision_TOS` ‖ `Hlt1TwoTrackMVADecision_TOS`
HLT2	`Hlt2B2HHDecision_TOS`
Stripping Line	`B2HHBDTLine`
PID ($\mathrm{B_s^0}\to \mathrm{K^+K^-}$ Only)	$\Delta\log(\mathcal{L}_{K\pi}) > 2$ and $\Delta\log(\mathcal{L}_{Kp}) > -2$
PID ($\mathrm{B^0}\to \pi^+\pi^-$ Only)	$\Delta\log(\mathcal{L}_{K\pi}) < -2$ and $\Delta\log(\mathcal{L}_{p\pi}) < 3$
BDT ($\mathrm{B_s^0}\to \mathrm{K^+K^-}$ Only)	Response > -0.04
BDT ($\mathrm{B^0}\to \pi^+\pi^-$ Only)	Response $> +0.04$

Table 8.9: The final selection requirements for selecting $\mathrm{B_s^0}\to \mathrm{K^+K^-}$ and $\mathrm{B^0}\to \pi^+\pi^-$ events used in the Run II analysis.

uncertainty on the CP observables of $\delta S_{\mathrm{KK}} = 0.035$, $\delta C_{\mathrm{KK}} = 0.035$, $\delta\mathcal{A}^{\Delta\Gamma}_{\mathrm{KK}} = 0.078$, $\delta S_{\pi\pi} = 0.023$, $\delta C_{\pi\pi} = 0.039$.

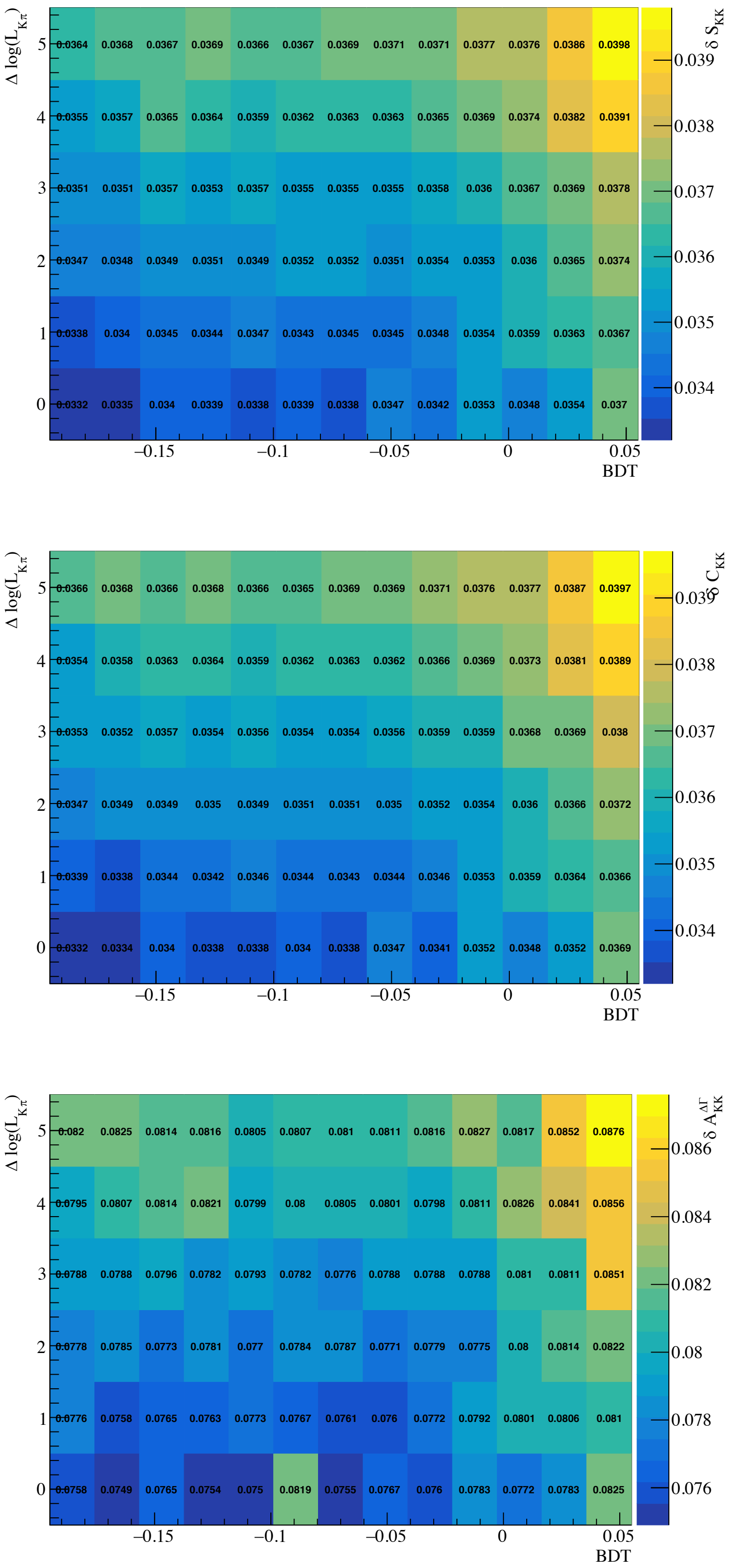

FIGURE 8.15: The predicted sensitivities on the CP observables for $\mathrm{B}_s^0 \to \mathrm{K}^+\mathrm{K}^-$ for different BDT responses and $\Delta\log(\mathcal{L}_{\mathrm{K}\pi})$ cuts. Top - The predicted sensitivity on S_{KK}. contaminations dle - The predicted sensitivity on C_{KK}. Bottom - The predicted sensitivity on $\mathcal{A}_f^{\Delta\Gamma}$.

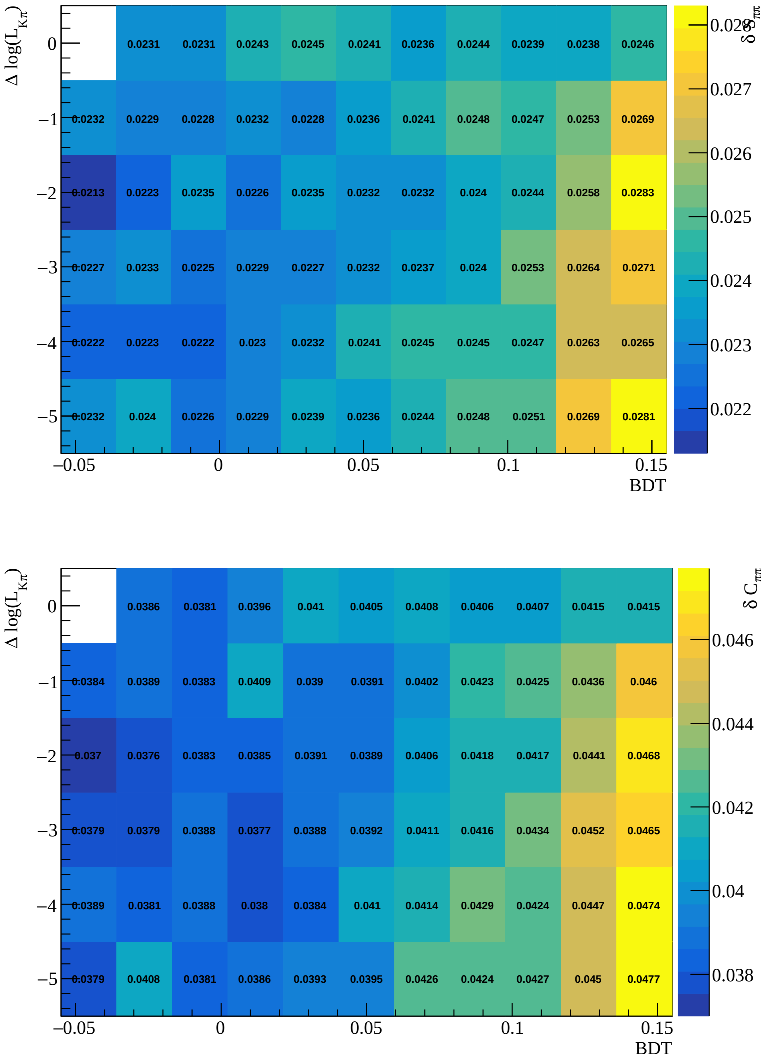

FIGURE 8.16: The predicted sensitivities on the CP observables for $\mathrm{B}^0 \to \pi^+\pi^-$ for different BDT responses and $\Delta\log(\mathcal{L}_{\mathrm{K}\pi})$ cuts. Top - The predicted sensitivity on $S_{\pi\pi}$. Bottom - The predicted sensitivity on $C_{\pi\pi}$.

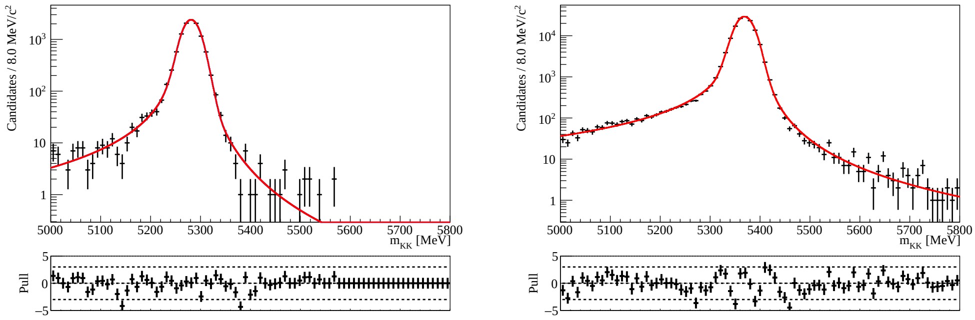

FIGURE 8.17: Fit to the K^+K^- invariant mass distribution for the MC samples produced for the Run II analysis. Left - The fit to $B^0 \rightarrow K^+K^-$ MC. Right - The fit to $B^0_s \rightarrow K^+K^-$ MC.

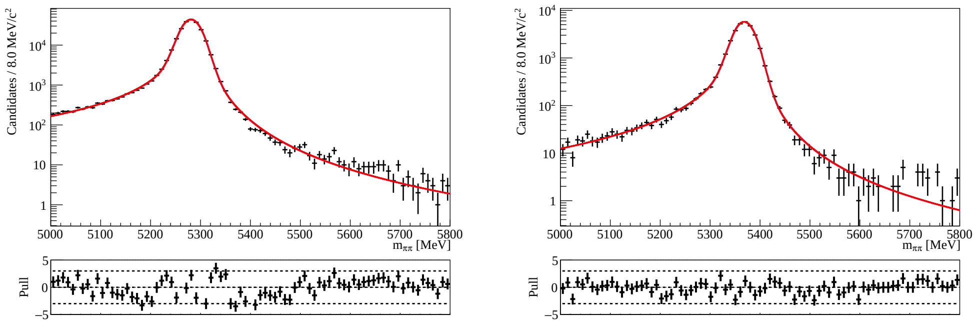

FIGURE 8.18: Fit to the $\pi^+\pi^-$ invariant mass distribution for the MC samples produced for the Run II analysis. Left - The fit to $B^0 \rightarrow \pi^+\pi^-$ MC. Right - The fit to $B^0_s \rightarrow \pi^+\pi^-$ MC.

8.3 Mass Fits

8.3.1 Signal Shapes

After the data selection was finalised, the invariant mass of the two final states was fitted to help distinguish signal events from background events. The shape of the signal was taken from Monte Carlo produced under 2015 and 2016 data-taking conditions. A double Crystal Ball was fit to these distributions as for the Run I analysis with their fitted distributions given in Figures 8.17 and 8.18, while their fitted parameters are given in Tables 8.10 and 8.11.

8.3.2 Background Studies

Knowledge of the contributing backgrounds to the $\pi^+\pi^-$ and K^+K^- mass spectra from the Run I analysis was used to understand the Run II spectra. There were no

Parameter	Description	$\mathrm{B^0 \to K^+K^-}$	$\mathrm{B^0_s \to K^+K^-}$
μ	Mass	$5281.16 \pm 0.21\,\mathrm{MeV}/c^2$	$5368.54 \pm 0.06\,\mathrm{MeV}/c^2$
σ	Mass Resolution	$17.38 \pm 0.19\,\mathrm{MeV}/c^2$	$17.72 \pm 0.05\,\mathrm{MeV}/c^2$
α_L	Low CB Boundary	-1.71 ± 0.15	1.48 ± 0.06
n_L	Low CB Tail	1.74 ± 0.15	1.57 ± 0.05
α_H	High CB Boundary	1.69 ± 0.28	2.09 ± 0.04
n_H	High CB Tail	3.04 ± 0.47	2.50 ± 0.09
f_DCB	CB Fraction	0.677 ± 0.167	0.382 ± 0.039

TABLE 8.10: The fit results to the $\mathrm{B^0 \to K^+K^-}$ and $\mathrm{B^0_s \to K^+K^-}$ invariant mass distributions from MC produced under 2015 conditions. The fits were performed using a double Crystal Ball shape for both distributions.

Parameter	Description	$\mathrm{B^0 \to \pi^+\pi^-}$	$\mathrm{B^0_s \to \pi^+\pi^-}$
μ	Mass	$5280.90 \pm 0.06\,\mathrm{MeV}/c^2$	$5368.11 \pm 0.16\,\mathrm{MeV}/c^2$
σ	Mass Resolution	$19.29 \pm 0.06\,\mathrm{MeV}/c^2$	$19.87 \pm 0.15\,\mathrm{MeV}/c^2$
α_L	Low CB Boundary	1.28 ± 0.04	1.21 ± 0.11
n_L	Low CB Tail	1.65 ± 0.04	1.87 ± 0.11
α_H	High CB Boundary	1.71 ± 0.03	1.79 ± 0.09
n_H	High CB Tail	2.87 ± 0.07	2.52 ± 0.17
f_DCB	CB Fraction	0.466 ± 0.027	0.479 ± 0.079

TABLE 8.11: The fit results to the $\mathrm{B^0 \to \pi^+\pi^-}$ and $\mathrm{B^0_s \to \pi^+\pi^-}$ invariant mass distributions from MC produced under 2015 conditions. The fits were performed using a double Crystal Ball shape for both distributions.

new backgrounds expected to be present, however the differences in the selection required studying the quantitative contributions of the dominant backgrounds.

8.3.2.1 Two-body Contaminations

For the Run I analysis, the shapes of the two-body contaminations present were obtained by applying the full selection to MC samples of the background of interest[12]. However it was found that applying the PID cuts to these samples resulted in statistically limited distributions. This introduced areas of the background with a deficiency of events and thus resulted in overly complex shapes (this effect is still apparent in the $\mathrm{\Lambda^0_b \to pK^-}$ shape under the $\mathrm{B^0_s \to K^+K^-}$ reconstruction). To improve on this problem in the Run II analysis it was decided to apply all the selection except for the PID requirements to the background samples. The events

---

[12] See Section 7.2.2.1.

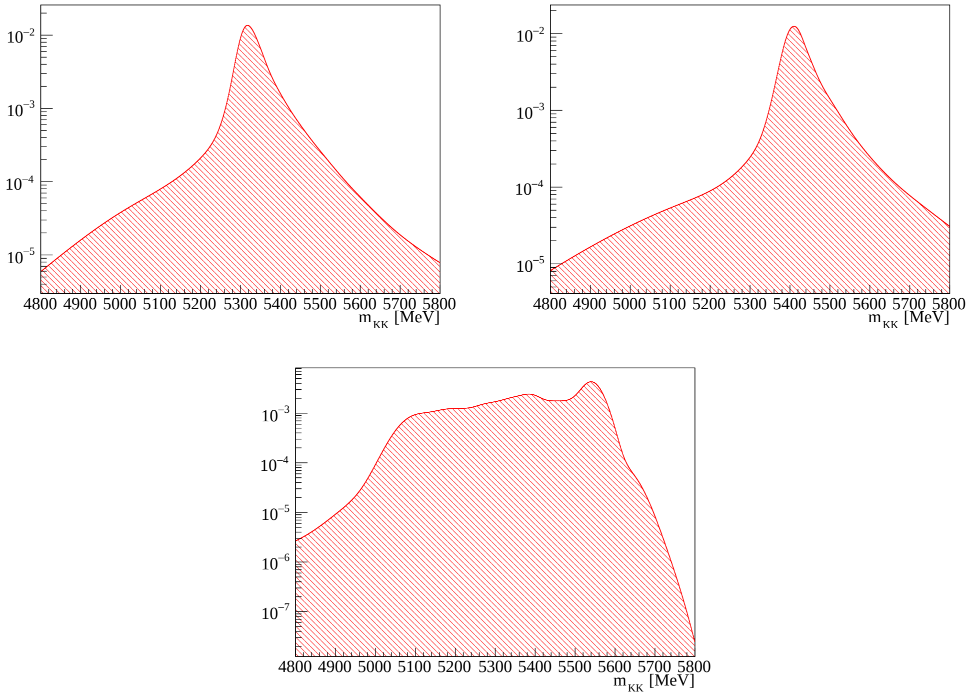

FIGURE 8.19: Kernelised histograms produced from PID weighted MC samples determined from the $B_s^0 \to K^+K^-$ decay channel used in the Run II analysis. Top Left - The $B^0 \to K^+\pi^-$ contamination. Top Right - The $B_s^0 \to \pi^+K^-$ contamination. Bottom - The $\Lambda_b^0 \to pK^-$ contamination.

that passed this selection were then reweighted using PIDCalib with an event-by-event efficiency calculated at the PID cuts imposed on the true data sample. The kernelised histograms produced by this method for the $B_s^0 \to K^+K^-$ event selection are given in Figure 8.19 and those produced for the $B^0 \to \pi^+\pi^-$ event selection are given in Figure 8.20. All rejected events for $\Lambda_b^0 \to pK^-$ decays in the $B_s^0 \to K^+K^-$ selection were found to come from the trigger, stripping, substitute particle identification and BDT requirements, thus no extra events would have been removed from the PID cut requirements.

8.3.2.2 Partially-reconstructed Background

The partially-reconstructed background comes from decays of particles to a final state with more than two daughters. Due to the missing daughters the reconstructed four-momentum is lower than the true four-momentum, and hence these decays lie towards lower invariant mass regions. Due to a lack of MC available with Run II conditions to model this effect, the shape of this background was taken from Run I knowledge. The partially reconstructed background events in

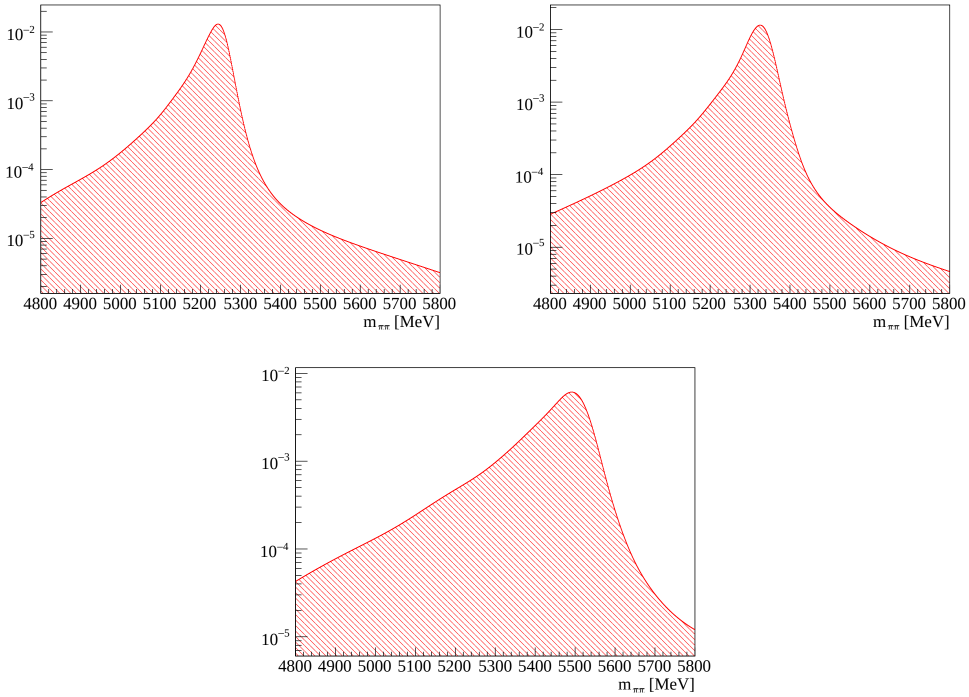

FIGURE 8.20: Kernelised histograms produced from PID weighted MC samples determined from the $B^0 \to \pi^+\pi^-$ decay channel used in the Run II analysis. Top Left - The $B^0 \to K^+\pi^-$ contamination. Top Right - The $B^0_s \to \pi^+K^-$ contamination. Bottom - The $\Lambda^0_b \to p\pi^-$ contamination.

both channels were modelled as an exponentially modified Gaussian, which takes the form

$$f(x;\mu,\sigma,\lambda) = \frac{\lambda}{2} e^{\frac{\lambda}{2}(2\mu+\lambda\sigma^2 - 2x)} \mathrm{erfc}\left(\frac{\mu+\lambda\sigma^2 - x}{\sqrt{2}\sigma}\right) \tag{8.2}$$

where μ is the mean of the Gaussian, σ is the Gaussian width, λ is the decay constant of the exponential and erfc(z) is the complementary error function[13]. All three parameters were left floating, however μ was required to be less than the mean of the mother particle of interest.

8.3.3 Fit Results

The invariant mass of both spectra was fitted using the parametrisation of the MC previously discussed between 5000 and 5800 MeV/c^2 to allow for proper modelling of the combinatorial and partially-reconstructed backgrounds from the upper and lower mass sidebands respectively. This modelling is particularly important to

---

[13] See Section 8.7.1 for more information.

discern combinatorial background events from signal ones as the mean decay time of these events was found to be strongly correlated to the MVA cut.

The data sets were split by the predicted flavour of the mother particle (flavour tag) and a simultaneous fit was performed on each subsample to measure the flavour-specific decay probabilities of each component of the fit. These probabilities are expected to change for each component due to direct CP asymmetries apparent in certain decays (the $\mathrm{B}^0 \to \mathrm{K}^+\pi^-$ and $\mathrm{B}^0_\mathrm{s} \to \pi^+\mathrm{K}^-$ decays), different interaction cross sections for particles and their CP conjugates (K^+ particles have a higher interaction cross section in matter than K^- particles), track reconstruction efficiencies and particle identification asymmetries.

The fit to the $\mathrm{K}^+\mathrm{K}^-$ invariant mass is given in Figure 8.21 with the results listed in Table 8.12. This fit uses the full 2015 and 2016 data collected by LHCb. After the final selection, 143671 candidates were found in the mass window. This results in 53719 ± 460 $\mathrm{B}^0_\mathrm{s} \to \mathrm{K}^+\mathrm{K}^-$ signal candidates and 2859 ± 891 $\mathrm{B}^0 \to \mathrm{K}^+\mathrm{K}^-$ signal candidates. As the $\mathrm{B}^0 \to \mathrm{K}^+\mathrm{K}^-$ yield resulted in a low signal to background ratio with respect to the combinatorial background and $\mathrm{B}^0 \to \mathrm{K}^+\pi^-$ misidentified background it was necessary to fix the mean and width of that signal to what had been measured in MC.

Similarly, the fit to the $\pi^+\pi^-$ invariant mass is given in Figure 8.22 with the results listed in Table 8.13. This fit uses the full 2015 and 2016 data collected by LHCb. After the final selection, 156254 candidates were found in the mass window. This results in 40954 ± 406 $\mathrm{B}^0 \to \pi^+\pi^-$ signal candidates and 1578 ± 125 $\mathrm{B}^0_\mathrm{s} \to \pi^+\pi^-$ signal candidates. In the region of the $\mathrm{B}^0_\mathrm{s} \to \pi^+\pi^-$ signal there was no misidentified background so it was possible to fit for the mass and width of the B^0_s in this channel.

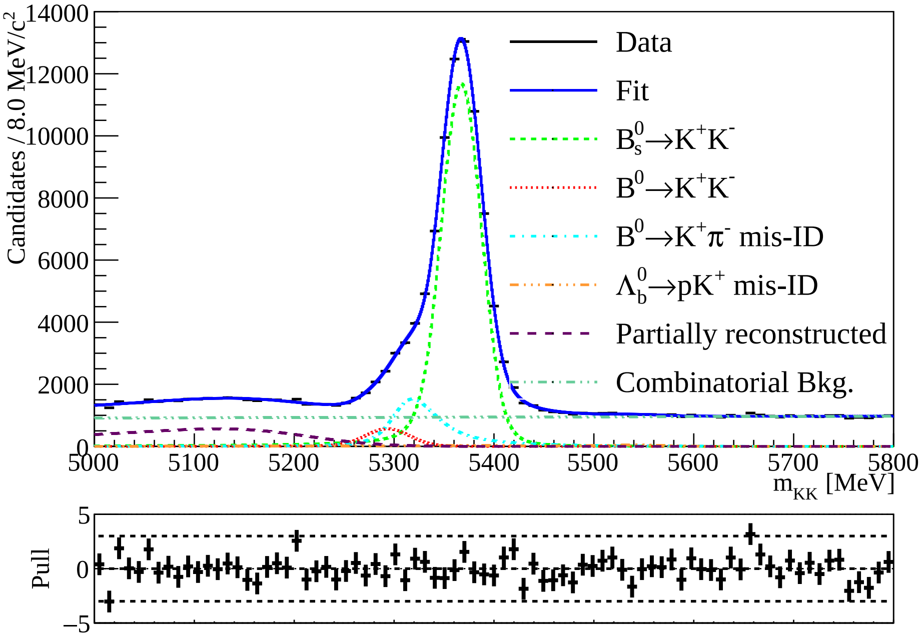

FIGURE 8.21: The fit to the K^+K^- invariant mass fit using the full 2015 and 2016 data after the selection was applied.

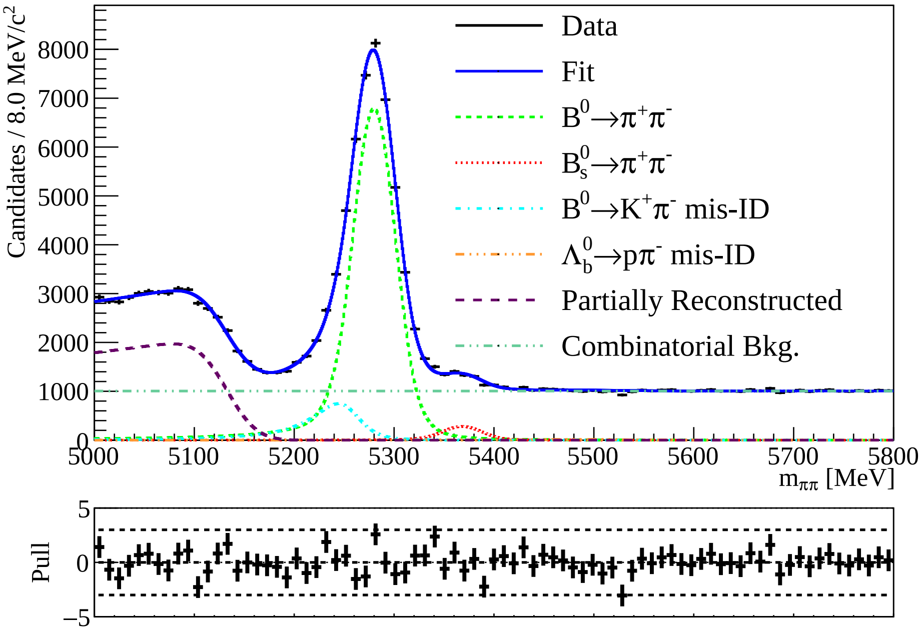

FIGURE 8.22: The fit to the $\pi^+\pi^-$ invariant mass fit using the full 2015 and 2016 data after the selection was applied.

Parameter	Value
$f(\mathrm{B_s^0}\rightarrow \mathrm{K^+K^-})$	0.3612 ± 0.0020
$f(\mathrm{B^0}\rightarrow \mathrm{K^+K^-})$	$(1.17 \pm 0.62)\times 10^{-2}$
$f(\mathrm{B^0}\rightarrow \mathrm{K^\pm\pi^\mp})$	$(7.41 \pm 0.92)\times 10^{-2}$
$f(\Lambda_b^0 \rightarrow \overset{(-)}{\mathrm{p}}\mathrm{K^\mp})$	$(6.38 \pm 2.12)\times 10^{-3}$
$f(\mathrm{PRB})$	$(4.42 \pm 0.70)\times 10^{-2}$
$\mu(\mathrm{B_s^0}\rightarrow \mathrm{K^+K^-})$	$5367.31 \pm 0.16\,\mathrm{MeV}/c^2$
$\sigma(\mathrm{B_s^0}\rightarrow \mathrm{K^+K^-})$	$20.84 \pm 0.16\,\mathrm{MeV}/c^2$
$\mu(\mathrm{B^0}\rightarrow \mathrm{K^+K^-})$	$5281.46 \pm 0.32\,\mathrm{MeV}/c^2$
$\sigma(\mathrm{B^0}\rightarrow \mathrm{K^+K^-})$	$18.58 \pm 0.19\,\mathrm{MeV}/c^2$
$\mu(\mathrm{PRB})$	$5183 \pm 7\,\mathrm{MeV}/c^2$
$\sigma(\mathrm{PRB})$	$57 \pm 11\,\mathrm{MeV}/c^2$
$\lambda(\mathrm{PRB})$	$(8.8 \pm 2.0)\times 10^{-3}(\,\mathrm{MeV}/c^2)^{-1}$
$\nabla(\mathrm{Comb})$	$(\text{-}4.78 \pm 0.49)\times 10^{-7}(\,\mathrm{MeV}/c^2)^{-1}$
Mis-ID Translation	$0.543\,\mathrm{MeV}$
$P(-1\vert\mathrm{B_s^0}\rightarrow \mathrm{K^+K^-})$	0.345 ± 0.005
$P(+1\vert\mathrm{B_s^0}\rightarrow \mathrm{K^+K^-})$	0.343 ± 0.005
$P(-1\vert\mathrm{B^0}\rightarrow \mathrm{K^+K^-})$	0.338 ± 0.068
$P(+1\vert\mathrm{B^0}\rightarrow \mathrm{K^+K^-})$	0.323 ± 0.065
$P(-1\vert\mathrm{B^0}\rightarrow \mathrm{K^\pm\pi^\mp})$	0.347 ± 0.026
$P(+1\vert\mathrm{B^0}\rightarrow \mathrm{K^\pm\pi^\mp})$	0.373 ± 0.028
$P(-1\vert\Lambda_{\mathrm{b}}^0 \rightarrow \overset{(-)}{\mathrm{p}}\mathrm{K^\mp})$	0.070 ± 0.070
$P(+1\vert\Lambda_{\mathrm{b}}^0 \rightarrow \overset{(-)}{\mathrm{p}}\mathrm{K^\mp})$	0.070 ± 0.070
$P(-1\vert\mathrm{PRB})$	0.331 ± 0.019
$P(+1\vert\mathrm{PRB})$	0.345 ± 0.019
$P(-1\vert\mathrm{Comb})$	0.373 ± 0.008
$P(+1\vert\mathrm{Comb})$	0.374 ± 0.008

TABLE 8.12: The result of the fit to the $\mathrm{K^+K^-}$ invariant mass for the Run II analysis. $f(\mathrm{B}\rightarrow h^+h'^-)$ refers to the fraction of the sample measured to originate from that decay chain, μ and σ are the mean and width of the shapes used to describe the sample component, mis-ID translation is the shift of the two-body backgrounds applied with respect to the position of the kernelised histograms, ∇ is the gradient of the linear function used to describe the combinatorial background and $P(\pm 1|\mathrm{B}\rightarrow h^+h'^-)$ is the probability that, if the candidate comes from the decay $\mathrm{B}\rightarrow h^+h'^-$, it is tagged as ± 1.

Parameter	Value
$f(\mathrm{B}^0\to \pi^+\pi^-)$	0.2621 ± 0.0026
$f(\mathrm{B}^0_\mathrm{s}\to \pi^+\pi^-)$	$(1.01\pm0.08)\times10^{-2}$
$f(\mathrm{B}^0\to \mathrm{K}^\pm\pi^\mp)$	$(3.65\pm0.29)\times10^{-2}$
$f(\Lambda^0_b\to \overset{(-)}{\mathrm{p}}\pi^\mp)$	$(1.31\pm0.24)\times10^{-3}$
$f(\mathrm{PRB})$	0.1674 ± 0.0014
$\mu(\mathrm{B}^0\to \pi^+\pi^-)$	$5279.92\pm0.25\,\mathrm{MeV}/c^2$
$\sigma(\mathrm{B}^0\to \pi^+\pi^-)$	$21.61\pm0.21\,\mathrm{MeV}/c^2$
$\mu(\mathrm{B}^0_\mathrm{s}\to \pi^+\pi^-)$	$5368.11\pm0.05\,\mathrm{MeV}/c^2$
$\sigma(\mathrm{B}^0_\mathrm{s}\to \pi^+\pi^-)$	$19.87\pm0.01\,\mathrm{MeV}/c^2$
$\mu(\mathrm{PRB})$	$5132\pm1\,\mathrm{MeV}/c^2$
$\sigma(\mathrm{PRB})$	$24\pm1\,\mathrm{MeV}/c^2$
$\lambda(\mathrm{PRB})$	$(1.39\pm0.40)\times10^{-3}(\,\mathrm{MeV}/c^2)^{-1}$
$\nabla(\mathrm{Comb})$	$(0\pm2.64)\times10^{-8}(\,\mathrm{MeV}/c^2)^{-1}$
Mis-ID Translation	$0.335\,\mathrm{MeV}$
$P(-1\|\mathrm{B}^0\to \pi^+\pi^-)$	0.421 ± 0.010
$P(+1\|\mathrm{B}^0\to \pi^+\pi^-)$	0.457 ± 0.011
$P(-1\|\mathrm{B}^0_\mathrm{s}\to \pi^+\pi^-)$	0.403 ± 0.004
$P(+1\|\mathrm{B}^0_\mathrm{s}\to \pi^+\pi^-)$	0.410 ± 0.095
$P(-1\|\mathrm{B}^0\to \mathrm{K}^\pm\pi^\mp)$	0.421 ± 0.058
$P(+1\|\mathrm{B}^0\to \mathrm{K}^\pm\pi^\mp)$	0.425 ± 0.058
$P(-1\|\Lambda^0_b\to \overset{(-)}{\mathrm{p}}\pi^\mp)$	0.146 ± 0.146
$P(+1\|\Lambda^0_b\to \overset{(-)}{\mathrm{p}}\pi^\mp)$	0.162 ± 0.162
$P(-1\|\mathrm{PRB})$	0.440 ± 0.014
$P(+1\|\mathrm{PRB})$	0.428 ± 0.013
$P(-1\|\mathrm{Comb})$	0.422 ± 0.008
$P(+1\|\mathrm{Comb})$	0.412 ± 0.008

TABLE 8.13: The result of the fit to the $\pi^+\pi^-$ invariant mass for the Run II analysis. $f(\mathrm{B}\to h^+h'^-)$ refers to the fraction of the sample measured to originate from that decay chain, μ and σ are the mean and width of the shapes used to describe the sample component, mis-ID translation is the shift of the two-body backgrounds applied with respect to the position of the kernelised histograms, ∇ is the gradient of the linear function used to describe the combinatorial background and $P(\pm1|\mathrm{B}\to h^+h'^-)$ is the probability that, if the candidate comes from the decay $\mathrm{B}\to h^+h'^-$, it is tagged as ±1.

8.4 Acceptance Corrections

The decay time acceptance was corrected by using the swimming method as for the Run I analysis. Due to the significant resources and time required to swim a sample, approximately one minute per-event, and the online/offline equivalence in Run II, it was felt that it would be possible to perform the swimming directly to the offline data sample rather than re-evaluating the event online within the full LHCb framework. This in practice means that an analyst would be able to make a local file with all the required variables and apply the acceptance correction within a stand-alone program rather than apply the correction using the raw event file within the full online LHCb framework.

While this new method would involve some significant initial effort the final swimming would be vastly quicker than performing the corrections within the full framework. This is partly due to a large number of variables within the selection that do not change when the PV is moved (and hence do not have to be re-evaluated) and partly by running one single program locally rather than running several programs sequentially using the Worldwide LHC Computing Grid. Examples of such variables that do not need to be re-evaluated are the particle's transverse momentum and the distance of closest approach between the two daughter candidate tracks.

Within the event selection, the only variables that change when the PV is moved are the flight distance χ^2 (FD χ^2), the cosine of the angle between the mothers momentum and flight displacement (DIRA) and the daughter's IP χ^2. As the MVAs used in the selection have a dependence on some parameters that change with the PV, their response must also be re-evaluated. Finally, a radial flight distance cut was implemented to reject B-meson candidates that would have traversed VELO material and thus would be poorly reconstructed. This requirement exists within the swimming framework that was used for the Run I analysis. An exaggerated depiction of the variables that need to be recalculated is shown in Figure 8.23. As it is not possible to visually describe a χ^2 requirement on a figure such as this, the flight distance and the impact parameter of a daughter are shown instead. The flight distance χ^2 and impact parameter χ^2 are proportional to the flight distance and the impact parameter respectively while also accounting for the uncertainties on their measurements. θ is the angle between the momentum and flight displacement and hence its cosine is the DIRA.

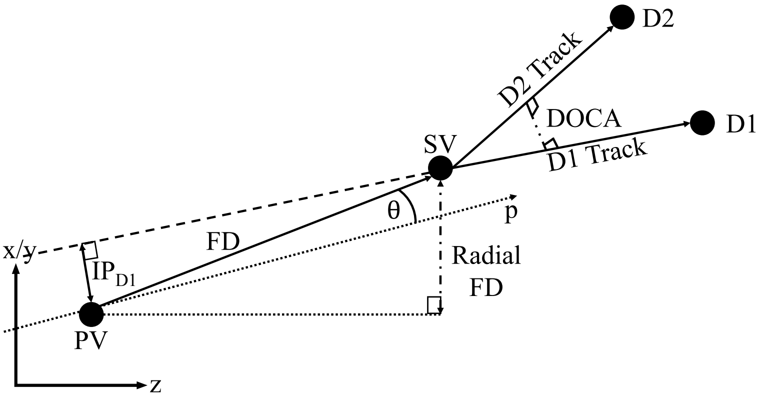

Figure 8.23: Exaggerated explanation of the source of the variables requiring re-evaluation in the swimming. The LHC beamline is defined to be along the z-axis within the LHCb framework.

As the recalculation of the selection variables is not a standard task for an LHCb analysis, several parameters are required to be written to the offline file to allow for an accurate correction. To perform the acceptance corrections detailed here the analysts requires access to the full seven element particle vector (a particles x-, y-, z- position and 4-momentum) and its associated 7×7 covariance matrix, the position and covariance matrix for *every* PV in the event and the position and covariance matrix of the SV. Detailed explanations of how different parameters are recalculated are given below.

8.4.1 Impact Parameter χ^2

The impact parameter of a particle is given as the distance of closest approach of a track to a primary vertex and can be calculated for both mothers and daughters. At LHCb, a particle's track is uniquely defined by a reference point, $\overrightarrow{X}$, and its slope, $\overrightarrow{S}$, where the slope is given by the particles momentum component with respect to the z-momentum (i.e. $\overrightarrow{S}(D_1) = (p_x/p_z, p_y/p_z, 1)$). The IP is then given by

$$\mathrm{IP} = \left| \overrightarrow{X} - \overrightarrow{\mathrm{PV}} - \frac{\overrightarrow{S} \cdot (\overrightarrow{X} - \overrightarrow{\mathrm{PV}})}{\overrightarrow{S} \cdot \overrightarrow{S}} \overrightarrow{S} \right|. \tag{8.3}$$

The accuracy of this calculation was confirmed by measuring the IP of the mother particle in a sample of $\mathrm{B}^0_\mathrm{s} \to \mathrm{K}^+\mathrm{K}^-$ decays and comparing it to the measurement from the full LHCb framework. The mean fractional difference between the two calculations was $7.8{\times}10^{-16}$ with an RMS of $1.0{\times}10^{-14}$ and is shown in Figure 8.24.

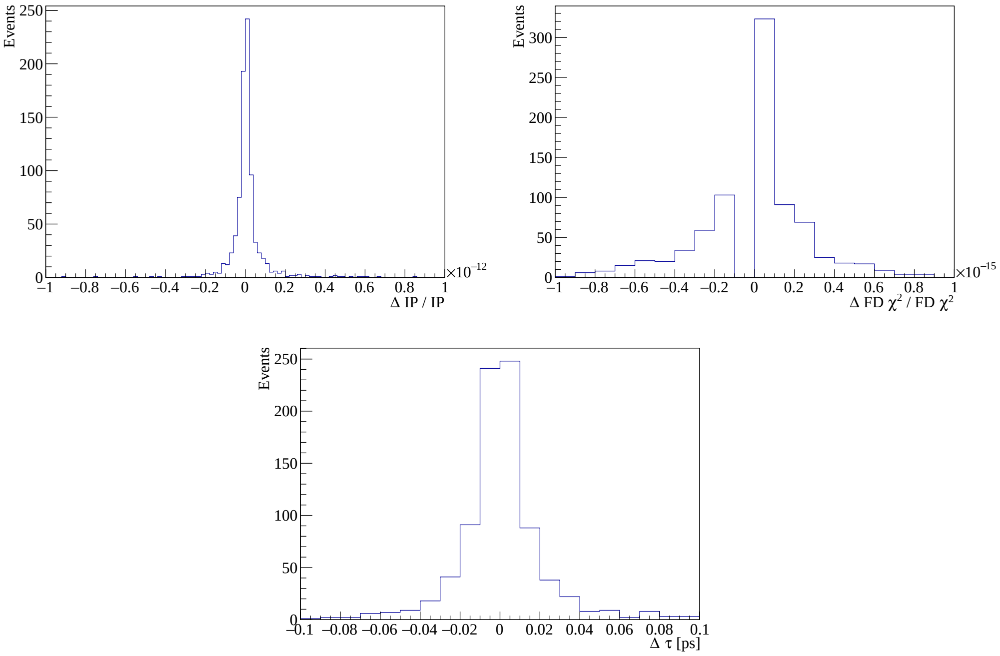

FIGURE 8.24: Comparison of several recalculated variables used in the new Swimming method for a sample of $\mathrm{B_s^0} \rightarrow \mathrm{K^+K^-}$ decays. Top Left - The difference between the recalculated IP and the true IP with respect to the true IP. The IP was calculated using Equation 8.3. Top Right - The difference between the recalculated FD χ^2 and the true FD χ^2 with respect to the true FD χ^2. The FD χ^2 was calculated using Equation 8.6. Bottom - The difference between the first estimate of the recalculated decay time and the true decay time. The decay time was calculated using Equation 8.10.

χ^2 tests can be used as an example of the goodness-of-fit of a variable [169] and can be given as

$$\chi^2 = \sum_{\mathrm{i}} \frac{(x_i \ - \ \mu)^2}{\sigma_i^2} \tag{8.4}$$

where x_i is the value of the measured parameter, μ is the mean and σ_i is the variance. At LHCb, the IP χ^2 is defined as the difference in the χ^2 of the PV fit with and without the track under investigation. This is approximately

$$\mathrm{IP}\chi^2 = \left(\frac{\mathrm{IP}}{\sigma_{\mathrm{IP}}}\right)^2 \tag{8.5}$$

and is what is used in calculating the IP χ^2 in the swimming.

As the slope is defined by the track's momentum and the swimming involves moving the PV in the direction of the momentum, the IP of the mother particle is constant and thus the mother IP χ^2 does not change when swimming within this analysis. However, the daughter IP χ^2 does change when moving the PV.

As there can be multiple primary vertices in an event, the IP χ^2 of each daughter must be calculated for each of these vertices with the minimum IP χ^2 of each track required to be larger than the selection requirements.

As the requirement for the `Hlt1TrackMVADecision_TOS` trigger line is for at least one track to pass the requirements then at least one of the daughters are required to pass the functional dependence of the IP χ^2. If this requirement is satisfied by one track but not the other then the latter track must have an IP $\chi^2 > 16$ to satisfy the HLT2 and stripping requirements. The IP χ^2 of the mother and the daughters are used in both the stripping and the offline MVA and thus must be passed to the respective BDTs to re-evaluate their response during the swimming.

Events with a smaller IP will lie closer to the PV and hence are associated with shorter mother lifetimes so the IP χ^2 is proportional to the square of the lifetime. This results in the IP χ^2 requirement of the daughters being a source of lower decay time acceptance.

8.4.2 Flight Distance χ^2

The flight distance (FD) of a particle is defined as the magnitude difference between the primary and secondary vertex and is proportional to the lifetime. The FD χ^2 is given by

$$\mathrm{FD}\chi^2 = \overrightarrow{\mathrm{FD}}\,\mathcal{C}^{-1}\,\overrightarrow{\mathrm{FD}}^{\mathrm{T}} \tag{8.6}$$

where $\mathcal{C}$ is the sum of the covariance matrices of the primary and secondary vertices [170]. The difference between the FD χ^2 calculated using Equation 8.6 and the true FD χ^2 calculated using the LHCb framework with respect to the true FD χ^2 was found to be -1.8×10^{-17} with an RMS of 2.8×10^{-16} and is shown in Figure 8.24.

The FD χ^2 is required to be larger than 100 as defined in both the HLT2 and stripping requirements. As the FD χ^2 is also proportional to the square of the lifetime, then the FD χ^2 will be another source of lower decay time acceptance.

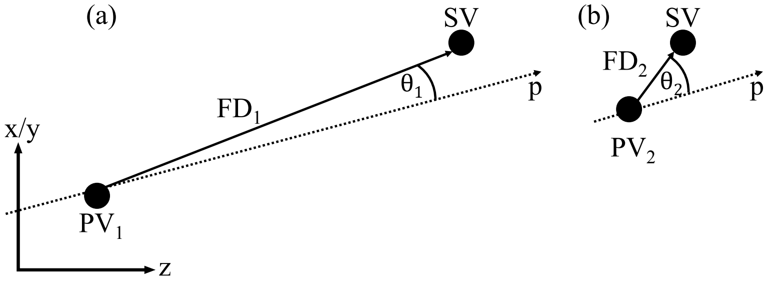

FIGURE 8.25: Exaggerated explanation of the source of the lower decay time acceptance from the DIRA. As the PV's move towards the SV, the flight distance decreases and thus the hypothetical decay time decreases in proportion. The angle between the momentum and the flight distance will increase which in turn decreases the DIRA, eventually to a value smaller than the acceptance requirement.

8.4.3 DIRA

The cosine of the angle between the flight distance vector and the momentum is described by the dot product of their unit vectors,

$$\cos\theta = \frac{\overrightarrow{p}\cdot\overrightarrow{\mathrm{FD}}}{|\overrightarrow{p}||\overrightarrow{\mathrm{FD}}|} \tag{8.7}$$

and tends to one rapidly as the PV is moved away from the SV. The DIRA is required to be greater than 0.99 and thus events will be rejected when the PV moves near the SV. Also, events will be rejected when the PV passes the SV due to the helicity flip of the mother. This shows that the DIRA will also be a source of lower decay time acceptance.

Figure 8.25 explains the source of the lower decay time acceptance. As the PV's are moved from point *a* to *b* the flight distance changes from FD_1 to FD_2. The decay time of a particle is proportional to the flight distance, thus the hypothetical decay time decreases between *a* and *b*. As the hypothetical decay time decreases, the angle between the flight distance and the momentum increases and hence it's cosine will decrease, eventually to a value smaller than the acceptance requirement. The DIRA requirement will also ensure that the decay cannot occur backwards. As the PV passes the SV the angle between the flight distance and the momentum will exceed $\pi/2$ and the DIRA will become negative which will be rejected by the acceptance requirements.

8.4.4 Distance of Closest Approach

The distance of closest approach (DOCA) is taken from the tracks of the two daughters. As these tracks do not move when swimming, this variable does not change when moving the PV. However, the DOCA is not a standard output of the LHCb framework but is used to evaluate the stripping BDT response and thus must be recalculated for each event before it is swum. The DOCA is given by

$$\mathrm{DOCA} = \left|(\overrightarrow{X}_1 - \overrightarrow{X}_2)\cdot\frac{\overrightarrow{S}_1\times\overrightarrow{S}_2}{|\overrightarrow{S}_1\times\overrightarrow{S}_2|}\right| \tag{8.8}$$

8.4.5 Radial Flight Distance

As previously stated, the radial flight distance cut is applied to remove candidates that interact with the VELO material and thus have poor reconstruction. It is simply defined as

$$r = \sqrt{(\mathrm{SV}_x - \mathrm{PV}_x)^2 + (\mathrm{SV}_y - \mathrm{PV}_y)^2} \tag{8.9}$$

and is required to be less than 4 mm thus it is a source of upper decay time acceptance. This value was chosen from a studied performed in a previous LHCb analysis on the effective decay time of $\mathrm{B}\rightarrow h^+h'^-$ decays [146] when the swimming method was used to correct for the decay time acceptance. The VELO track reconstruction efficiency has a dependence on the angle of the track with respect to the beam line of the LHC [90, 171] as the reconstruction algorithms match r and ϕ segments. The algorithms have a preference for decays occurring close to the beam-axis and, hence, have a lower efficiency for long lived candidates. A radial flight distance cut at 4 mm was chosen as this was the minimum distance where the fit to the effective decay time of the data was found to be unbiased.

8.4.6 Decay Time

The decay time, t, of a particle is measured as

$$t = \frac{|\overrightarrow{\mathrm{FD}}|m}{|\overrightarrow{p}|c} \tag{8.10}$$

where m is the reconstructed mass of the particle, $|\overrightarrow{p}|$ is its momentum, and c is the speed of light in a vacuum [90]. This function gives a reasonable estimate of the decay time but it must be further refined using a minimisation technique. The difference between the first estimation of the decay time using Equation 8.10 and the reconstructed decay time is given in Figure 8.24 where the mean difference in the decay times was 6.9×10^{-4} ps with an RMS of 0.02 ps.

8.4.7 Verification of the Method

To ensure that the method returned the correct value of the observables, a MC sample of $\mathrm{B}^0 \to \pi^+\pi^-$ decays was swum and the decay time was measured using the fitter used in the final analysis which had previously been shown to be unbiased[14]. As the generated decay time of this decay is known to be 1.519 ps then recovering this value would give confidence to the applicability of the previously described method. The result of a fit to 147248 events gave a decay time of 1.525 ± 0.004 ps and can be seen in Figure 8.26 along with the resulting acceptance distribution from these events. The method was further confirmed by measuring the CP observables, $C_{\pi\pi}$ and $S_{\pi\pi}$, with perfectly tagged candidates. This was achieved by using the generated flavour of the signal candidate as the tagging decision. The generated values were $C_{\pi\pi} = -0.27$ and $S_{\pi\pi} = -0.68$, the fitted values were $C_{\pi\pi} = -0.278 \pm 0.005$ and $S_{\pi\pi} = -0.672 \pm 0.005$

The swimming was performed by moving the PV in steps of 50 µm until the radial flight distance requirement was exceeded. When the acceptance requirement changed, the PV was moved back by 50 µm then reswum in steps of 0.5 µm to refine the turning point location. The new swimming method was found to take approximately 200 ms to swim an event compared to the previous 1 minute per-event.

---

[14] See Figure 8.40

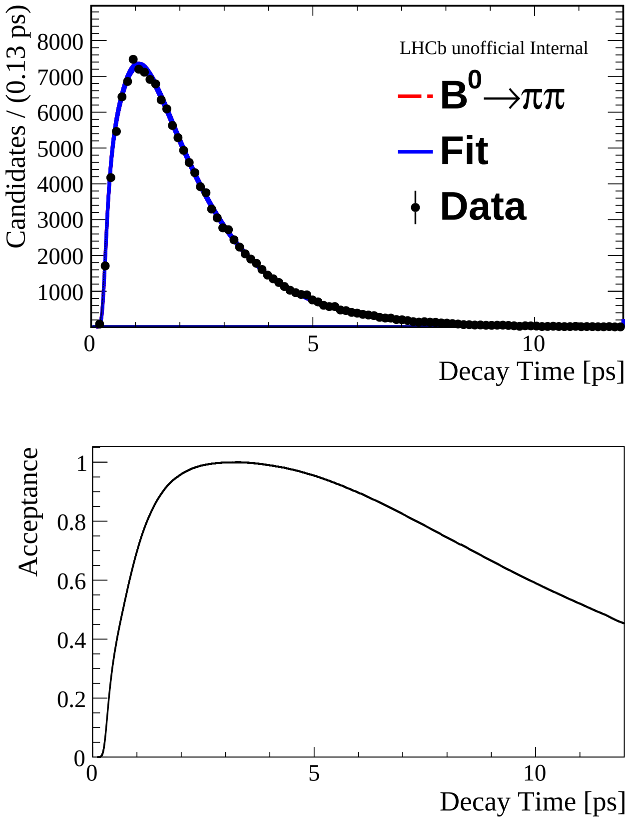

FIGURE 8.26: The results of the fit of the decay time distribution for a MC sample of $\mathrm{B}^0 \to \pi^+\pi^-$ decays produced with the Run II event selection and swum using the new method for correcting for the acceptance. The fitted decay time was 1.525 ± 0.004 ps compared to the generated decay time of 1.519 ps. Top - The decay time distribution and the resulting fit. Bottom - The associated acceptance distribution determined using the new method.

8.5 Decay Time Resolution

8.5.1 Decay Time Resolution from Simulated $\mathrm{B}^0_\mathrm{s} \to \mathrm{K}^+\mathrm{K}^-$

As the oscillation period of the B^0_s meson has been measured to be 353.6 ± 0.5 (syst.) $\pm\, 0.1$ (stat.) fs [56], it is important to have a good understanding of the decay time resolution of the detector. This can be achieved by taking the difference between the true decay time and the reconstructed decay time of a particle from MC. We used simulated $\mathrm{B}^0_\mathrm{s} \to \mathrm{K}^+\mathrm{K}^-$ events, generated under 2016 conditions and modelled the resolution using a triple Gaussian. The triple Gaussian was translated into an effective Gaussian by taking the weighted mean of the contributions given from the statistical dilution originating from the decay time resolution, $\mathcal{D}_t$.

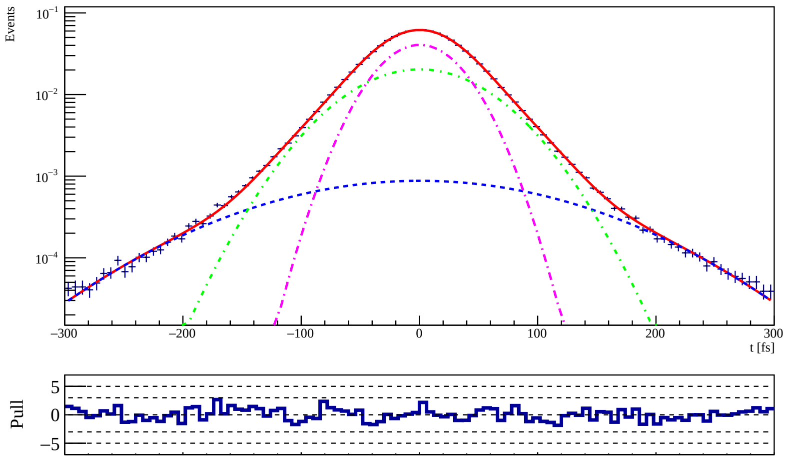

FIGURE 8.27: Results of the fit to the difference of true decay time and reconstructed decay time for $B_s^0 \to K^+K^-$ 2016 MC events. The fit is performed using a triple Gaussian which gives an effective resolution of 39.20 ± 0.47 fs.

Parameter	Value
f_1	$1.42 \pm 0.13\%$
f_2	$32.87 \pm 1.58\%$
μ	$0.21 \pm 0.05\,\text{fs}$
σ_1	$114.31 \pm 2.55\,\text{fs}$
σ_2	$51.68 \pm 0.71\,\text{fs}$
σ_3	$30.54 \pm 0.31\,\text{fs}$
σ_{eff}	$39.20 \pm 0.47\,\text{fs}$

TABLE 8.14: Fit results to the decay time resolution of $B_s^0 \to K^+K^-$ 2016 MC events.

The dilution is given by

$$\mathcal{D}_t = \sum_{\text{i}} f_i \exp(-\Delta m_{\text{s}}^2 \sigma_i^2/2) \tag{8.11}$$

where f_i is the fraction of the i^{th} Gaussian in the fit, Δm_{s} is the B_s^0 oscillation frequency and σ_{i} is the fitted width of the i^{th} Gaussian. After calculating the dilution, Equation 8.11 can be rearranged to give an expression for an effective single Gaussian

$$\sigma_{\text{eff}} = \frac{\sqrt{-2\ln \mathcal{D}_t}}{\Delta m_{\text{s}}} \tag{8.12}$$

The results of the fit to the MC sample can be seen in Figure 8.27 and in Table 8.14.

The individual event resolution is highly correlated with the decay time error

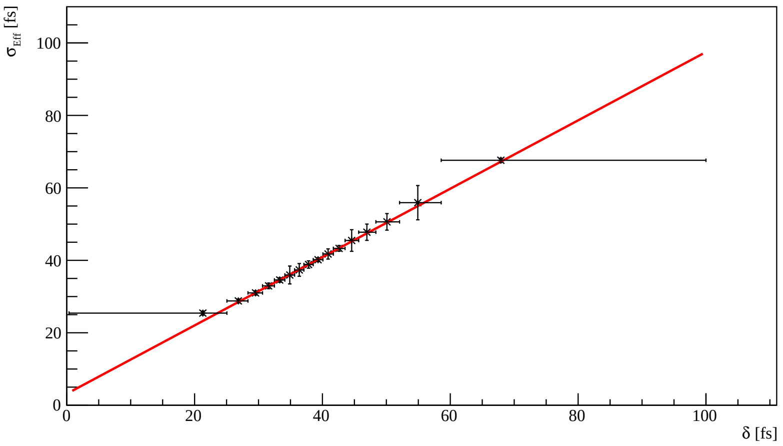

FIGURE 8.28: Results of the fit to the per-event decay time resolution for $B_s^0 \to K^+K^-$ 2016 MC.

Parameter	Value
q_0	2.65 ± 1.35 fs
q_1	0.96 ± 0.04

TABLE 8.15: Fit results to the per-event decay time resolution of $B_s^0 \to K^+K^-$ 2016 MC events.

estimated from the decay time fit in the reconstruction thus the sample was divided into bins of decay time error, δ_t, with each bin containing the same number of events to avoid biasing the fit. The decay time resolution can thus be described as a function of the decay time error

$$\sigma_{\text{eff}} = q_0 + q_1\delta_t. \tag{8.13}$$

Linear fits were performed over a range of bin numbers to investigate any dependence of the binning scheme used, with a negligible dependence observed. The results of the per-event decay time resolution using 16 bins can be seen in Figure 8.28 while the gradient and intercept of the fits as a function of the number of bins can be seen in Figure 8.29. The gradient of the fit to the intercepts as a function of the number of bins was $(1.8 \pm 4.1) \times 10^{-2}$ while the gradient to the fit of the gradients was $(-0.45 \pm 1.16) \times 10^{-3}$. The typical result of the per-event decay time resolution can be seen in Table 8.15.

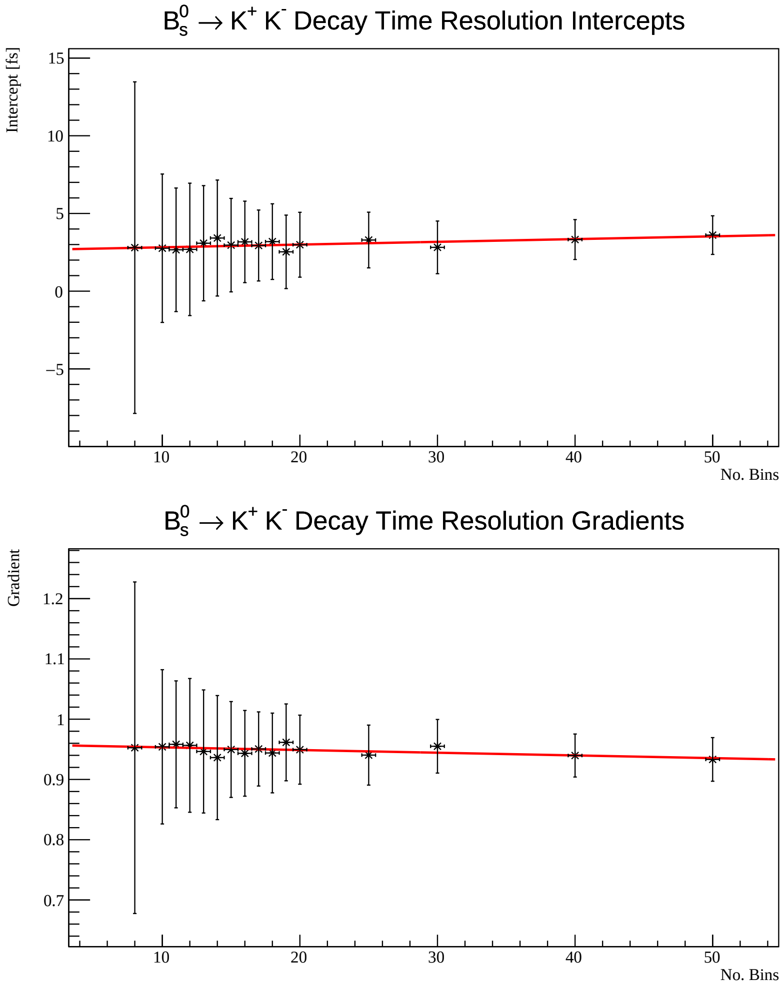

FIGURE 8.29: Results for the intercept (top) and gradient (bottom) of the per-event decay time resolution as a function of the number of bins of decay time error.

8.5.2 Decay Time Resolution from Prompt $J/\psi \rightarrow \mu^+\mu^-$

Prompt $J/\psi \rightarrow \mu^+\mu^-$ candidates were used to make a data-driven calibration of the decay time resolution and per-event decay time resolution. As these decays are prompt, any structure in their decay time will be due to the resolution of the detector. The samples were taken directly from the PROMPTJPSI2MUMUCONTROLLINE stripping line with the additional requirement that the invariant mass of the two muons is within the range $3000 < m_{\mu\mu}[\text{MeV}] < 3200$ to reduce the data size. The invariant mass was fitted with a double Crystal Ball for the signal and an exponential function for the combinatorial fraction. The sample included 7.5×10^6 events with a fit fraction of $83.83 \pm 0.04\%$ which gives $(6.284 \pm 0.003) \times 10^6$ signal candidates. The mass was measured to be 3096.84 ± 0.01 MeV and the fit can be seen in Figure 8.30.

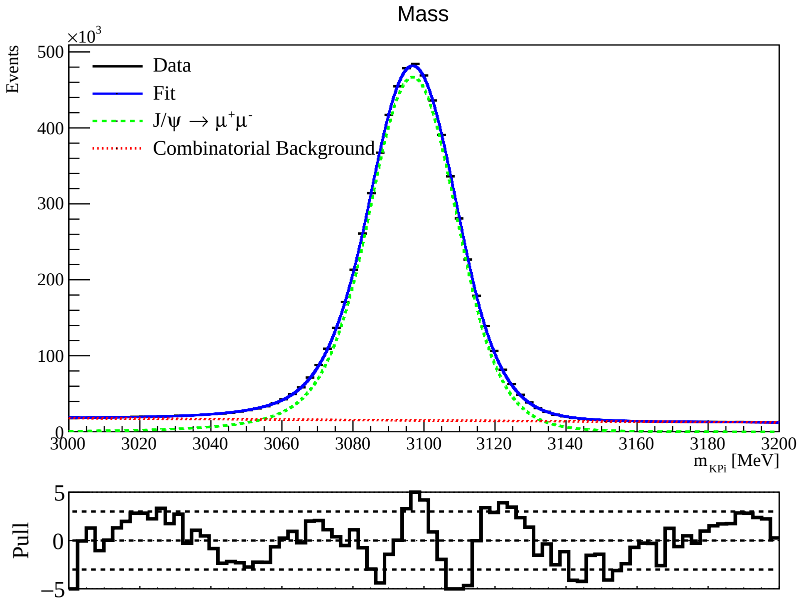

FIGURE 8.30: Fit to the $\mu\mu$ invariant mass between $3000 < m_{\mu\mu}[\text{MeV}] < 3200$. The signal is fit using a double Crystal Ball while the background is modelled with an exponential function. The yield of the sample is $(6.284 \pm 0.003) \times 10^6$ J/ψ→ $\mu^+\mu^-$ candidates.

Parameter	Value
f_1	$3.22 \pm 0.29\%$
f_2	$53.73 \pm 0.70\%$
μ	-6.30 ± 0.76 fs
σ_1	77.08 ± 0.86 fs
σ_2	50.02 ± 0.28 fs
σ_3	30.37 ± 0.22 fs
σ_{eff}	43.02 ± 0.27 fs

TABLE 8.16: Fit reuslts to the decay time resolution of J/ψ → $\mu^+\mu^-$ 2016 data events.

sWeights were used to extract the signal from the background events before fitting to the reconstructed lifetime. The decay time was fit using a triple Gaussian as before but a bifurcated Gaussian[15] was used to model a secondaries component arising from B-decays with a J/ψ daughter. The result of the decay time fit can be seen in Figure 8.31 with the results of the fit in Table 8.16. The decay time resolution for prompt J/ψ→ $\mu^+\mu^-$ was measured to be 43.0 ± 0.27 fs.

As for the $B_s^0 \to K^+K^-$ analysis, linear fits were performed over a range of bin

---

[15] A bifurcated Gaussian is one in which the Gaussian width is different on each side of the mean value.

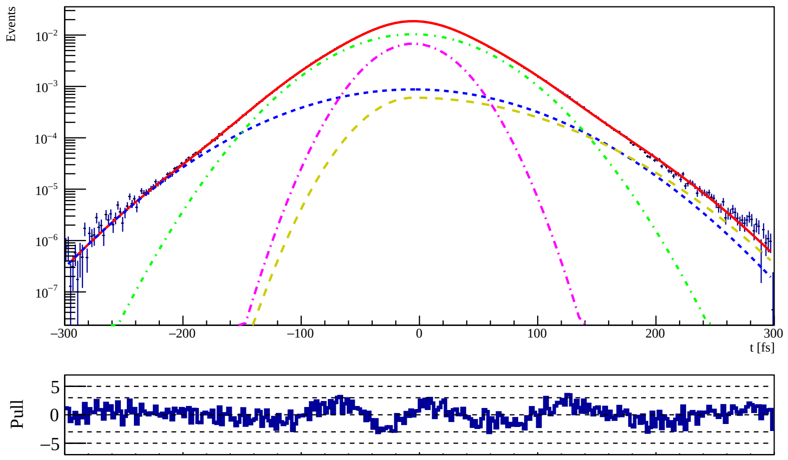

FIGURE 8.31: Results of the reconstructed decay time for J/ψ→ μ^{+}μ^{-} 2016 data events. The fit is performed using a triple Gaussian for the prompt signal and a bifurcated Gaussian for the secondary background arising from B-decays with a J/ψ daughter. The effective resolution was measured to be 43.0 ± 0.27 fs.

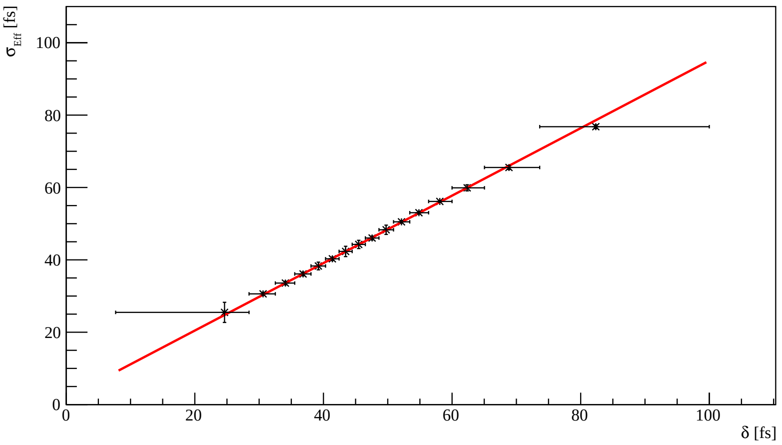

FIGURE 8.32: Results of the fit to the per-event decay time resolution for J/ψ→ μ^{+}μ^{-} 2016 Data.

numbers to investigate any dependence of the binning scheme used, with a negligible dependence observed. The results of the per-event using 16 bins can be seen in Figure 8.32 while the gradient and intercept of the fits as a function of the number of bins can be seen in Figure 8.33. The gradient of the fit to the intercepts as a function of the number of bins was $(0.68 \pm 2.99) \times 10^{-2}$ while the gradient to the fit of the gradients was $(-1.72 \pm 6.45) \times 10^{-4}$. The typical result of the per-event decay time resolution can be seen in Table 8.17.

The results of the calibration of the decay time resolution from $\mathrm{B}^{0}_{\mathrm{s}} \rightarrow \mathrm{K}^{+}\mathrm{K}^{-}$

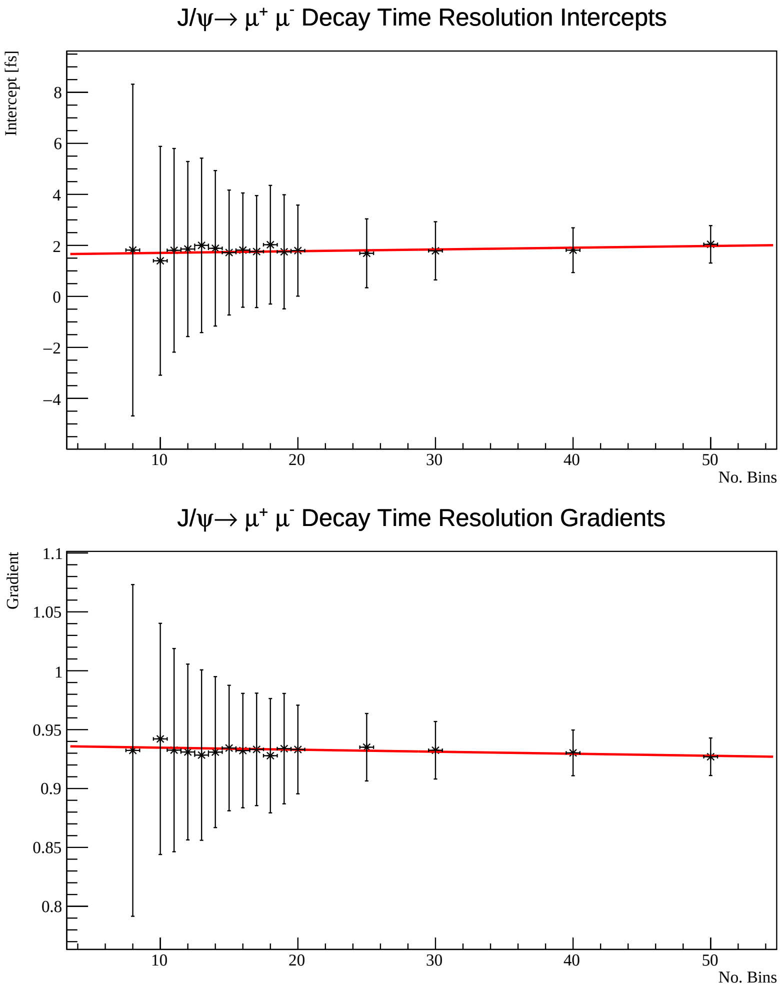

FIGURE 8.33: Results for the intercept (top) and gradient (bottom) of the per-event decay time resolution as a function of the number of bins of decay time error.

Parameter	Value
q_0	$1.64 \pm 1.09\,\mathrm{fs}$
q_1	0.94 ± 0.02

TABLE 8.17: Fit results to the per-event decay time resolution of $J/\psi \to \mu^+\mu^-$ 2016 data events.

MC was compared to the results from $\mathrm{J}/\psi \rightarrow \mu^+\mu^-$ data and were found to be consistent with each other. As the calibration on the $\mathrm{J}/\psi \rightarrow \mu^+\mu^-$ sample used true data, these calibration parameters were used in the final fit to the $\mathrm{B}^0_s \rightarrow \mathrm{K}^+\mathrm{K}^-$ data.

8.6 Flavour Tagging

8.6.1 The Theory of Flavour Tagging

It was shown previously that a CP asymmetry will arise if there is a difference between the decay rates for a particle and its CP conjugate. This is given quantitatively in Equation 2.43. As neutral mesons will mix between their two CP states a practical way to obtain the flavour of the meson at production must be devised. This is known as *Flavour Tagging* and presents a great challenge for physicists, especially at the LHC due to the nature of proton-proton collisions unlike at the B-factories where it was possible to produce B-mesons in correlated pairs with a well-defined total momentum. However by exploiting the $q\bar{q}$ pair production, excellent vertex resolution and particle identification it is possible to discern the flavour of particles at production within LHCb.

There are two main methods used to obtain the production flavour; this first technique is known as *opposite-side tagging* while the second is known as *same-side tagging*. Opposite-side tagging exploits $b\bar{b}$ pair production and looks at the decay structure of the other b-quark produced with the one of interest. If the other hadron produced in the production does not undergo mixing (such as a Λ^0_b which contains a b-quark) or has a charge specific decay (such as a B^+ which contains a $\bar{b}$-quark) then it is possible through charge conservation to discern the flavour of the other b-quark at production [172]. Same-side tagging works in a similar principle as opposite-side tagging, however the pair production of the other quark in the B-meson system is discerned to obtain the flavour of the B-meson at production. For example, if the B^0 meson is produced in association with a π^+ (a $u\bar{d}$ system) then the B^0 was a $\bar{b}d$ system at production [173]. The two methods of tagging B-mesons are described pictorially in Figure 8.34. To ensure good tagging performance, the candidates are required to have high momentum and transverse momentum with good impact parameter separation and harsh PID cuts. This however reduces the available statistics to perform measurements of CP violation.

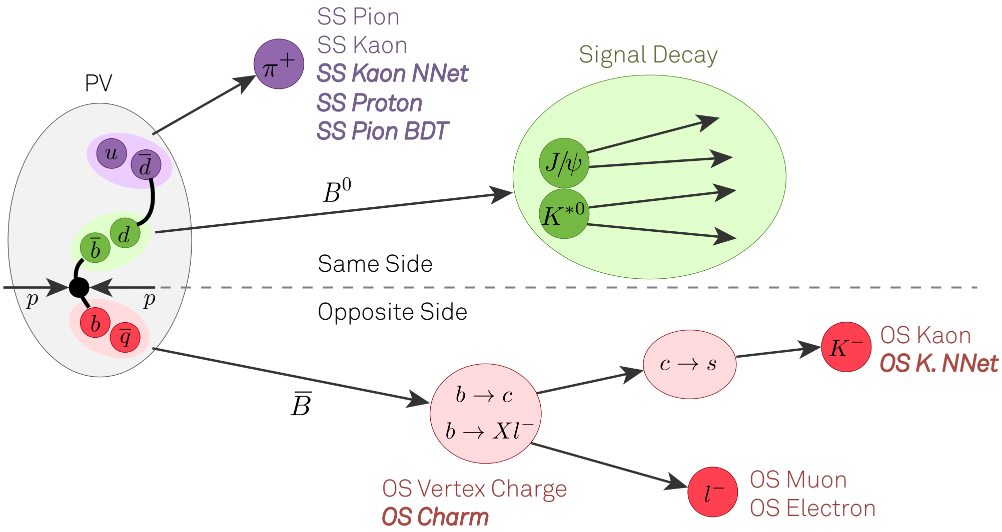

FIGURE 8.34: The two methods employed at LHCb to discern the flavour of a B-meson at production. The proton-proton collision occurs at the far left where a $b\bar{b}$ pair is produced. Opposite-side tagging discerns the flavour of the other b-quark at production to state the flavour of the B-meson of interest at production while same-side tagging discerns the flavour of the other quark produced in association with the B-meson of interest. Credit to Ulrich Eitschberger.

The flavour taggers assign a value of +1 to an event which was predicted to have been produced as a B at production while a value of −1 is assigned to events predicted to have been produced as a $\bar{B}$ at production. If the taggers have been unable to decide a flavour at production then a value of 0 is given and the event is described as *untagged*. It is also possible that the taggers have made an incorrect prediction for the flavour of the B-meson. The tagging efficiency, ε_{tag}, is then given as

$$\varepsilon_{\text{tag}} = \frac{R + W}{R + W + U} \tag{8.14}$$

where R is the fraction of correctly tagged events, W is the fraction of incorrectly tagged events and U is the fraction of untagged events. This is thus a measure of the total fraction of events in the sample that have an associated tag, regardless of whether the decision is correct or not. To account for an incorrect decision, each event is associated a measure of the probability that the tag decision is incorrect, known as the mistag probability, η. This value is determined via a neural net trained on MC samples, accounting for both the properties of the tagger and the event and can take a value between $0 \leq \eta < 0.5$[16]. The mistag in effect dilutes the amplitude of the oscillations, hence getting the wrong value of the mistag for an event will lead to incorrect values of the CP violating parameters.

---

[16] A mistag probability of 0.5 is given to untagged events where the flavour cannot be discerned while a value of $\eta > 0.5$ would change the value of the tag decision

As the value of η is calculated from a neural network which was trained on simulated events it must be recalibrated on real data to ensure the correct value of mistag is applied to the data. This recalibrated value of the mistag, ω, is evaluated on an event-by-event basis using a flavour-specific calibration sample where the final state of a decay (and its CP conjugate) is well defined, and the kinematics of the decay are consistent with that of the channel of interest. For $\mathrm{B}^0 \to \pi^+\pi^-$ decays this calibration was achieved using $\mathrm{B}^0 \to \mathrm{K}^+\pi^-$ decays, while for $\mathrm{B}_s^0 \to \mathrm{K}^+\mathrm{K}^-$ decays this was achieved via $\mathrm{B}_s^0 \to \mathrm{D}_s^-\pi^+$ decays. As the final state of the two calibration channels ensures that the flavour of the B-meson is well known at decay, the calculated value of ω for these decays is assumed to be correct. Hence, a polynomial fit to ω as a function of η is performed then this calibration is applied to the channels of interest. The polynomial fit is normally of degree one and is given by

$$\omega = p_0 + p_1(\eta - \hat{\eta}) \tag{8.15}$$

where $\hat{\eta}$ is the mean value of the predicted mistag. The tagging calibration is not assumed to be the same for particles tagged as B or $\bar{\mathrm{B}}$ so extra fit parameters, Δp_0 and Δp_1 , are introduced to reduce correlations between the two tagged states.

With this it is possible to define a PDF to describe the fraction of right, wrong and untagged events

$$F(\mathrm{dec}) = \begin{cases} \varepsilon_{\mathrm{tag}}(1 - \omega) & \mathrm{dec} = \text{“right tag”} \\ \varepsilon_{\mathrm{tag}}\omega & \mathrm{dec} = \text{“wrong tag”} \\ 1 - \varepsilon_{\mathrm{tag}} & \mathrm{dec} = \text{“untagged tag”} \end{cases} \tag{8.16}$$

and an effective tagging power, $\varepsilon_{\mathrm{eff}}$, as

$$\varepsilon_{\mathrm{eff}} = \varepsilon_{\mathrm{tag}}(1 - 2\omega)^2. \tag{8.17}$$

The effective tagging power is hence a measure of the effective statistical size of the sample.

Each tagger has its own associated tagging efficiency and predicted mistag, however it is possible to combine individual taggers into a single tagger using weighted decisions from all *sensible* taggers. It is important to note that the mention of *sensible* taggers is required. While all opposite-side taggers can be used to make a final decision, as their decision does not matter on the quark composition of the mother B-meson of interest, the use of same-side taggers does require knowledge of the quark composition to make sense. For example, a same-side kaon tagger can be used to calibrate decays of $\mathrm{B_s^0}$ mesons due to the $s\bar{s}$ pair production, however a same-side pion or proton tagger cannot be used for these decays as they require $s\bar{d}$ production and vice-versa for $\mathrm{B^0}$ decays.

The combined mistag probability that a B-meson contained a $[\bar{b}/b]$-quark is given by

$$\eta(\varepsilon_{\text{tag}} = +1) = 1 \ - \ P(\bar{b}) \qquad \eta(\varepsilon_{\text{tag}} = -1) = 1 \ - \ P(b) \tag{8.18}$$

where $P(x)$ is the combined probability of the meson containing an x-quark and

$$P(\bar{b}) = \frac{p(\bar{b})}{p(b) + p(\bar{b})} \qquad P(b) = \frac{p(b)}{p(b) + p(\bar{b})} \tag{8.19}$$

and

$$p(\bar{b}) = \prod_{\mathrm{i}} \Big(\frac{1-\varepsilon_i}{2} - \varepsilon_i(1 \ - \ \eta_i) \Big) \qquad p(b) = \prod_{\mathrm{i}} \Big(\frac{1+\varepsilon_i}{2} + \varepsilon_i(1 \ - \ \eta_i) \Big) \tag{8.20}$$

where ε_i and η_i are the tag decision and predicted mistag probability of the i-th tagger respectively. It is then possible to apply the calibrated values of these taggers to the sample of interest.

8.6.2 Calibrating the $\mathbf{B^0} \to \pi^+\pi^-$ Sample using $\mathbf{B^0} \to \mathbf{K}^+\pi^-$

As previously mentioned, the measured mistag for the $\mathrm{B^0} \to \pi^+\pi^-$ sample was calibrated using $\mathrm{B^0} \to \mathrm{K}^+\pi^-$ decays. The $\mathrm{B^0} \to \mathrm{K}^+\pi^-$ events were selected by keeping the event selection as similar to the $\mathrm{B^0} \to \pi^+\pi^-$ selection as possible. The same trigger and stripping requirements were imposed and a BDT was used to reduce the combinatorial background contamination. The BDT was trained using the same variables as the $\pi^+\pi^-$ sample but with a $\mathrm{B^0} \to \mathrm{K}^+\pi^-$ signal MC sample and events from the upper mass sideband of the $\mathrm{K}^+\pi^-$ invariant mass distribution. As there is less combinatorial background present in this sample with respect to the $\pi^+\pi^-$ sample a looser BDT cut could be used. This cut required that the BDT response was greater than 0.02 which was chosen to be at the maximum predicted significance. This changes from the optimisation procedure for the $\mathrm{B^0} \to \pi^+\pi^-$ selection as $\mathrm{B^0} \to \mathrm{K}^+\pi^-$ decays show direct CP violation thus maximising the signal yield would minimise the uncertainties on the CP

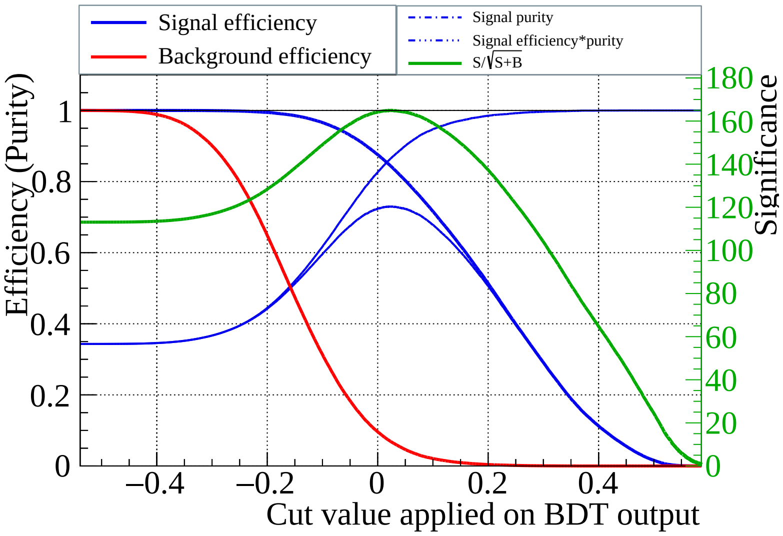

FIGURE 8.35: Green - The predicted significance (right axis) as a function of BDT cut for $B^0 \to K^+\pi^-$ decays assuming the measured signal to background ratio between $5200 \leq m_{K\pi} \leq 5330\,\text{MeV}$. The maximum significance was predicted to occur at a response of 0.02. Red - The predicted signal acceptance efficiency. Thick blue - The predicted combinatorial background acceptance efficiency.

parameters. The signal and background yields before the BDT cut was applied were measured in the range $5200 \leq m_{K\pi} \leq 5330\,\text{MeV}$ where the upper limit was chosen to avoid contamination from $B_s^0 \to \pi^+K^-$ decays. A comparison of the signal acceptance efficiency, combinatorial background acceptance efficiency and predicted significance as a function of BDT response is shown in Figure 8.35.

The PID selection was also changed to account for the kaon daughter and loosened slightly to improve the signal yield. The cuts imposed on the daughters are given in Table 8.18. The misidentified backgrounds were again produced with the same trigger, stripping and BDT selection and then reweighted using PIDCalib to give an event-by-event efficiency while the signals were modelled as double Crystal Ball functions. The partially reconstructed background was modelled as an exponentially modified Gaussian. The same selection was applied to the charge conjugate decay which was then added to the $B^0 \to K^+\pi^-$ events. The resulting fit to the $K^\pm\pi^\mp$ invariant mass is given in Figure 8.36 with the measured parameters given in Table 8.19. There were 361956 events after applying the selection which results in 162084 ± 615 $B^0 \to K^\pm\pi^\mp$ candidates and 10678 ± 398 $B_s^0 \to \pi^\pm K^\mp$ candidates.

The sample was *sWeighted* using the results of the mass fit to extract the signal candidates. The charges of the daughter kaons and pions were used to tag the

Track	Cuts
Kaon	$\Delta\log(\mathcal{L}_{\mathrm{K}\pi}) > 3.0$
	$\Delta\log(\mathcal{L}_{\mathrm{Kp}}) >$ -2.0
Pion	$\Delta\log(\mathcal{L}_{\mathrm{K}\pi}) <$ -2.0
	$\Delta\log(\mathcal{L}_{\mathrm{p}\pi}) < 3.0$

TABLE 8.18: The $\Delta\log(\mathcal{L})$ cuts for the 2015 and 2016 data sample as applied to the $\mathrm{K}^+\pi^-$ sample. The cuts are initially taken against the pion hypothesis, for example $\Delta\log(\mathcal{L}_{\mathrm{Kp}}) = \log\mathcal{L}_{\mathrm{K}} - \log\mathcal{L}_{\pi} - (\log\mathcal{L}_{\mathrm{p}} - \log\mathcal{L}_{\pi})$

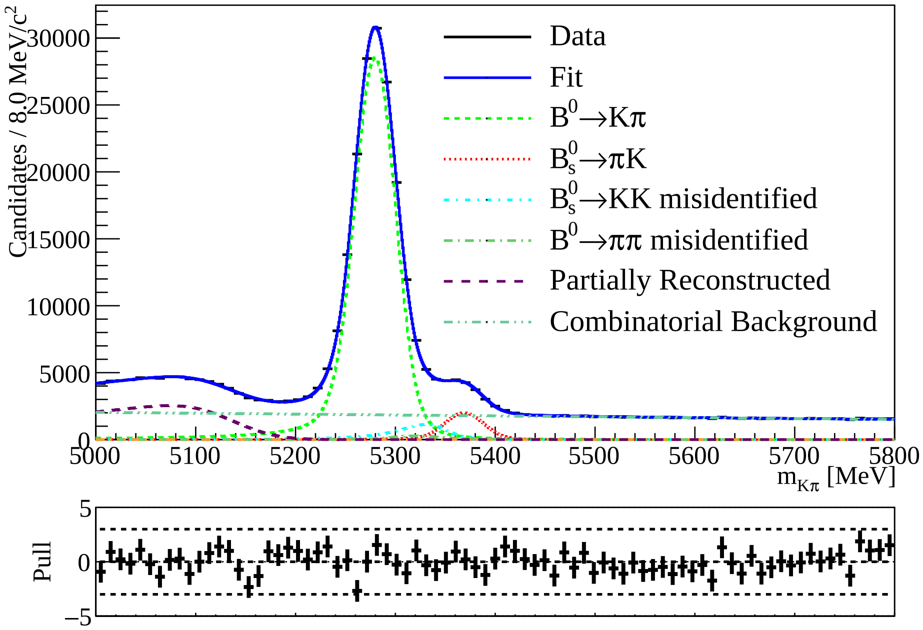

FIGURE 8.36: The fit to the $\mathrm{K}^{\pm}\pi^{\mp}$ invariant mass fit using the full 2015 and 2016 data after the selection was applied.

predicted flavour of the mother at decay. The flavour tagging calibration was then performed using ESPRESSO PERFORMANCE MONITOR which is a package developed by LHCb to perform flavour tagging studies. This was used to combine the following taggers available from the sample using the method detailed in Equations 8.18 to 8.20

- Opposite-side Muon
- Opposite-side Electron
- Opposite-side Kaon
- Opposite-side Charm

Parameter	Value
$f(\mathrm{B}^0 \to \mathrm{K}^+\pi^-)$	0.4478 ± 0.0017
$f(\mathrm{B}^0_\mathrm{s} \to \pi^+\mathrm{K}^-)$	$(2.95 \pm 0.11) \times 10^{-2}$
$f(\mathrm{B}^0_\mathrm{s} \to \mathrm{K}^+\mathrm{K}^-)$	$(2.38 \pm 0.47) \times 10^{-2}$
$f(\mathrm{B}^0 \to \pi^+\pi^-)$	$(5.86542 \pm 4.38) \times 10^{-3}$
$f(\mathrm{PRB})$	$(9.71 \pm 0.20) \times 10^{-2}$
$\mu(\mathrm{B}^0 \to \mathrm{K}^+\pi^-)$	$5279.58 \pm 0.00\,\mathrm{MeV}/c^2$
$\sigma(\mathrm{B}^0 \to \mathrm{K}^+\pi^-)$	$20.67 \pm 0.08\,\mathrm{MeV}/c^2$
$\mu(\mathrm{B}^0_\mathrm{s} \to \pi^+\mathrm{K}^-)$	$5368.79 \pm 0.83\,\mathrm{MeV}/c^2$
$\sigma(\mathrm{B}^0_\mathrm{s} \to \pi^+\mathrm{K}^-)$	$19.45 \pm 0.68\,\mathrm{MeV}/c^2$
$\mu(\mathrm{PRB})$	$5133.67 \pm 2.21\,\mathrm{MeV}/c^2$
$\sigma(\mathrm{PRB})$	$35.70 \pm 2.12\,\mathrm{MeV}/c^2$
$\lambda(\mathrm{PRB})$	$(3.58 \pm 0.65) \times 10^{-3}(\,\mathrm{MeV}/c^2)^{-1}$
$\nabla(\mathrm{Comb})$	$(-4.70 \pm 0.37) \times 10^{-7}(\,\mathrm{MeV}/c^2)^{-1}$
Mis-ID Translation	$0.003\,\mathrm{MeV}$

TABLE 8.19: The result of the fit to the $\mathrm{K}^\pm\pi^\mp$ invariant mass for the Run II analysis.

- Opposite-side Vertex Charge
- Same-side Pion
- Same-side Proton

Measurements of the CP observables were performed on MC samples of $\mathrm{B}^0 \to \pi^+\pi^-$ and $\mathrm{B}^0_\mathrm{s} \to \mathrm{K}^+\mathrm{K}^-$ to ensure that the generated values of each observable could be recovered. It was found that the opposite-side electron tagger introduced a significant bias to both $S_{\pi\pi}$ and S_{KK} which resulted in this tagger being removed from the final calibration. The observable $S_{\pi\pi}$ was generated with a value of -0.27 while the MC fit returned a fit value of 0.30 ± 0.33 and S_{KK} was generated with a value of 0.22 while the MC fit returned a value of 0.02 ± 0.15. The tagging power of the opposite-side electron tagger was measured to be 0.18 ± 0.04 % and 0.30 ± 0.07 % for the $\mathrm{B}^0 \to \pi^+\pi^-$ and $\mathrm{B}^0_\mathrm{s} \to \mathrm{K}^+\mathrm{K}^-$ samples respectively, hence this tagger can be removed with a minimal impact on the overall tagging power of the samples. The results of the calibration from $B^0 \to K^\pm\pi^\mp$ decays are shown in Figure 8.37 and Table 8.20. The calibration parameters from Table 8.20 were then applied to the full $\pi^+\pi^-$ sample.

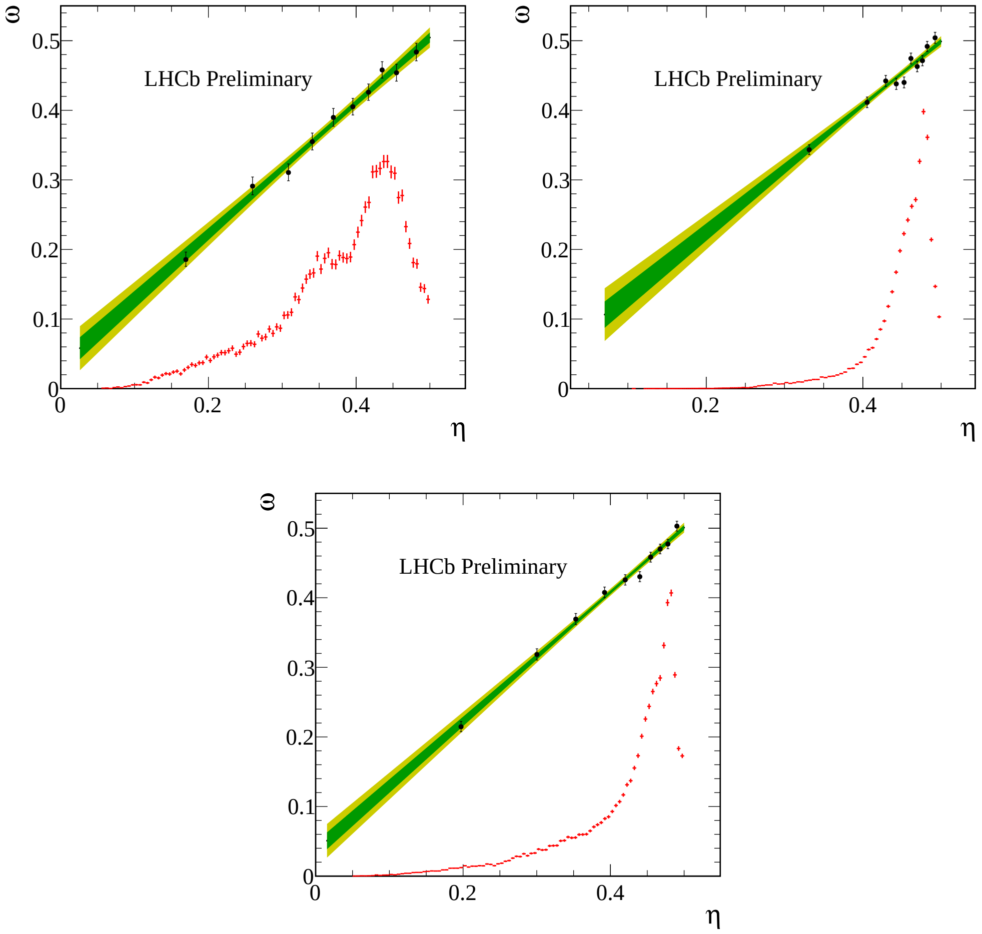

FIGURE 8.37: The measured mistag calibrations from $B^0 \to K^{\pm}\pi^{\mp}$ signal candidates with one and two sigma confidence limits in green and yellow respectively. The distribution of the predicted mistag, η, of each tagger is shown in red. Top Left - The combined opposite-side taggers. Top Right - The combined same-side taggers. Bottom - The combined opposite- and same-side taggers.

Parameter	Opposite-Side	Same-Side	Combination	Source
$p_0 - \hat{\eta}$	$(1.2 \pm 0.4)\times10^{-2}$	$(3.6 \pm 2.5)\times10^{-3}$	$(7.1 \pm 2.5)\times10^{-3}$	$\mathrm{B}^0 \to \mathrm{K}^{\pm}\pi^{\mp}$
Δp_0	$(1.2 \pm 0.5)\times10^{-2}$	$(2.9 \pm 3.3)\times10^{-3}$	$(6.6 \pm 3.2)\times10^{-3}$	$\mathrm{B}^0 \to \mathrm{K}^{\pm}\pi^{\mp}$
p_1	0.942 ± 0.045	0.914 ± 0.050	0.929 ± 0.030	$\mathrm{B}^0 \to \mathrm{K}^{\pm}\pi^{\mp}$
Δp_1	$(-1.4 \pm 5.8)\times10^{-2}$	$(4.9 \pm 7.0)\times10^{-2}$	$(-1.8 \pm 3.9)\times10^{-2}$	$\mathrm{B}^0 \to \mathrm{K}^{\pm}\pi^{\mp}$
$\hat{\eta}$(cal.)	35.14 ± 0.42 %	43.23 ± 0.24 %	38.77 ± 0.25 %	$\mathrm{B}^0 \to \mathrm{K}^{\pm}\pi^{\mp}$
$\hat{\eta}$(sig.)	32.83 ± 0.50 %	43.69 ± 0.23 %	38.81 ± 0.26 %	$\mathrm{B}^0 \to \pi^+\pi^-$
p_0(cal.)	0.363 ± 0.006	0.436 ± 0.002	0.395 ± 0.004	$\mathrm{B}^0 \to \mathrm{K}^{\pm}\pi^{\mp}$
p_0(sig.)	0.375 ± 0.006	0.441 ± 0.002	0.402 ± 0.004	$\mathrm{B}^0 \to \pi^+\pi^-$
$\varepsilon_{\mathrm{tag}}$	33.98 ± 0.35 %	82.85 ± 0.28 %	88.09 ± 0.24 %	$\mathrm{B}^0 \to \pi^+\pi^-$
$\varepsilon_{\mathrm{eff}}$	4.01 ± 0.24 %	1.32 ± 0.10 %	4.41 ± 0.20 %	$\mathrm{B}^0 \to \pi^+\pi^-$

TABLE 8.20: The flavour tagging calibration parameters measured using ESPRESSO PERFORMANCE MONITOR to calibrate the $\mathrm{B}^0 \to \pi^+\pi^-$ signal. The calibration was performed using $\mathrm{B}^0 \to \mathrm{K}^{\pm}\pi^{\mp}$ events.

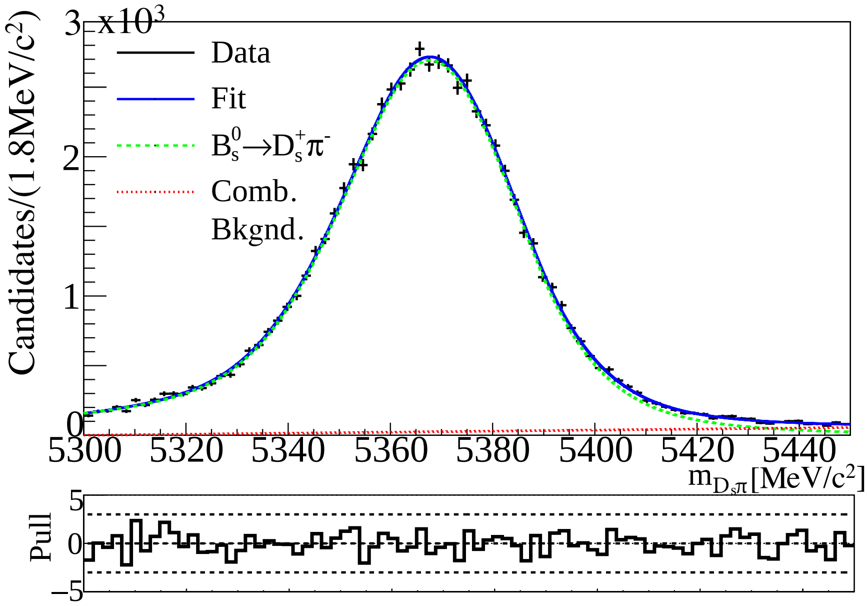

FIGURE 8.38: Fit to the invariant mass distribution for $\mathrm{B_s^0} \to \mathrm{D_s^-}\pi^+$

8.6.3 Calibrating the $\mathbf{B_s^0} \to \mathbf{K^+K^-}$ Sample using $\mathbf{B_s^0} \to \mathbf{D_s^+}\,\pi^-$

A sample of $\mathrm{B_s^0} \to \mathrm{D_s^-}\pi^+$ events were used to calibrate the same-side and combined flavour taggers for $\mathrm{B_s^0} \to \mathrm{K^+K^-}$ while opposite-side taggers were calibrated using the results from the $\mathrm{B^0} \to \mathrm{K^+}\pi^-$ calibration. These samples were produced as a general LHCb sample for use in flavour tagging analyses from data collected during 2016. The $\mathrm{D_s^-}\pi^+$ invariant mass distribution is given in Figure 8.38.

Due to the rapid oscillation of the $\mathrm{B_s^0}$ meson, the decay time resolution had to be accounted for in the tagging calibration. A per-event decay time resolution was used with linear calibration parameters taken from the study on $\mathrm{J}/\psi \to \mu^+\mu^-$ decays as discussed in Section 8.5.2. The Espresso Performance Monitor was again used to the compute the calibration using the following taggers

- Opposite-side Combination
- Same-side Kaon

As the response of opposite-side taggers are independent of the species of the mother particle, these taggers were calibrated using the results of the $\mathrm{B^0} \to \mathrm{K^+}\pi^-$ calibration. The results of the calibration from $\mathrm{B_s^0} \to \mathrm{D_s^-}\pi^+$ decays is shown in Figure 8.39 and Table 8.21. The opposite-side calibration parameters from Table 8.20 and same-side kaon and combination calibration parameters from Table 8.21 were

Parameter	Same-Side Kaon	Combination	Source
$p_0-\hat{\eta}$	$(2.6\pm0.5)\times10^{-2}$	$(-1.2\pm4.0)\times10^{-3}$	$\mathrm{B_s^0}\to\mathrm{D_s^-}\pi^+$
Δp_0	$(-9.7\pm4.7)\times10^{-3}$	$(-1.0\pm4.5)\times10^{-3}$	$\mathrm{B_s^0}\to\mathrm{D_s^-}\pi^+$
p_1	0.790 ± 0.057	0.997 ± 0.047	$\mathrm{B_s^0}\to\mathrm{D_s^-}\pi^+$
Δp_1	$(0.05\pm6.5)\times10^{-2}$	$(-5.0\pm5.2)\times10^{-2}$	$\mathrm{B_s^0}\to\mathrm{D_s^-}\pi^+$
$\hat{\eta}$(cal.)	41.89 ± 0.43 %	37.53 ± 0.40 %	$\mathrm{B_s^0}\to\mathrm{D_s^-}\pi^+$
$\hat{\eta}$(sig.)	41.87 ± 0.43 %	36.18 ± 0.43 %	$\mathrm{B_s^0}\to\mathrm{K^+K^-}$
p_0(cal.)	0.445 ± 0.004	0.374 ± 0.004	$\mathrm{B_s^0}\to\mathrm{D_s^-}\pi^+$
p_0(sig.)	0.445 ± 0.004	0.361 ± 0.006	$\mathrm{B_s^0}\to\mathrm{K^+K^-}$
$\varepsilon_{\mathrm{tag}}$	52.57 ± 0.26 %	68.80 ± 0.24 %	$\mathrm{B_s^0}\to\mathrm{K^+K^-}$
$\varepsilon_{\mathrm{eff}}$	1.40 ± 0.37 %	5.25 ± 0.33 %	$\mathrm{B_s^0}\to\mathrm{K^+K^-}$

TABLE 8.21: The flavour tagging calibration parameters measured using ESPRESSO PERFORMANCE MONITOR to calibrate the $\mathrm{B_s^0}\to\mathrm{K^+K^-}$ signal. The calibration was performed using $\mathrm{B_s^0}\to\mathrm{D_s^-}\pi^+$ events.

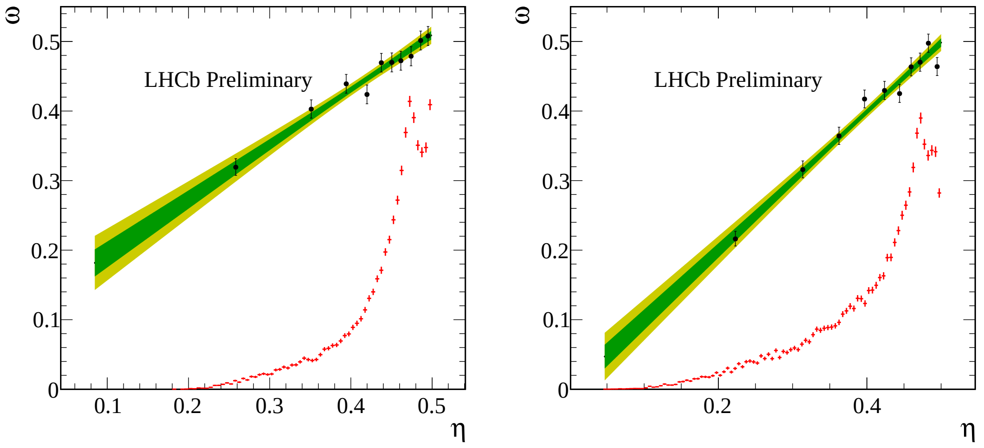

FIGURE 8.39: The measured mistag calibrations from $\mathrm{B_s^0}\to\mathrm{D_s^-}\pi^+$ signal candidates with one and two sigma confidence limits in green and yellow respectively. The distribution of the predicted mistag, η, of each tagger is shown in red. Left - The same-side kaon tagger. Right - The combined opposite- and same-side kaon taggers.

then applied to the full $\mathrm{K^+K^-}$ sample. The opposite tagging efficiency of the $\mathrm{B_s^0}\to\mathrm{K^+K^-}$ sample was measured to be $\varepsilon_{\mathrm{tag}}=35.06\pm0.25\,\%$ while the tagging power was measured to be $\varepsilon_{\mathrm{eff}}=4.58\pm0.27\,\%$.

8.7 CP Observables Results

8.7.1 The Fit Model

It has previously been shown that neutral mesons evolve according to Equations 2.37 and 2.38. To properly model decays within LHCb, these equations must be modified by detector effects such as the decay time resolution, $G(t;\sigma_{\text{eff}})$, the decay time acceptance, $\mathcal{A}$, the mistag probability, ω, and meson production asymmetries, A_{Prod}. The decay time acceptance is measured on an event-by-event basis using the previously described swimming method and thus is not required in the fit-model description.

The decay time resolution in effect smears the decay rate and in 8.5 it was shown that this smearing can be approximated by an effective Gaussian. The expression for the modification can be found by the convolution of Equations 2.37 and 2.38 with a Gaussian with a mean of 0 s and width of σ_{eff}.

$$\begin{aligned}\Gamma_{\text{eff}}(t;q) &= e^{-\Gamma t}\left[\cosh\left(\frac{\Delta\Gamma}{2}t\right) + \mathcal{A}_f^{\Delta\Gamma}\sinh\left(\frac{\Delta\Gamma}{2}t\right)\right. \\ &\quad \left. +q\times\left(C_f\cos(\Delta m t) \;-\; S_f\sin(\Delta m t)\right)\right]\otimes G(t;\sigma_{\text{eff}}), \qquad (8.21)\end{aligned}$$

where q is the tag of the particle and takes the value of $+1$ for mesons and -1 for antimesons.

An analytic form of the convolution was not found in the literature and so was developed by the candidate. The full proof of this solution is given in Appendix E. The general solution is stated here, however it is recommended to read the appendix to understand how to apply it to trigonometric functions. The solution is made possible as hyberbolic and trigonometric functions can be rewritten in terms of exponential functions. If we have a generic exponential, e^{kx}, we can convolve it with a Gaussian as follows

$$H(t;k) = e^{kx}\otimes\frac{1}{\sqrt{2\pi}\sigma}e^{\frac{x^2}{2\sigma^2}} = \frac{1}{\sqrt{2\pi}\sigma}\int_{-\infty}^{\infty}e^{kx}e^{\frac{-(t-x)^2}{2\sigma^2}}dx \qquad (8.22)$$

where k is some generic constant with respect to x and σ is the width of the Gaussian. This can be used to form the general expression for an exponential function convolved with a Gaussian

$$H(t;k) = \frac{1}{2}e^{\frac{(\sigma k)^2}{2}}e^{kt}\left(\text{erf}\left[\frac{t+\sigma^2 k}{\sqrt{2}\sigma}\right]+1\right) \tag{8.23}$$

To allow for a fast normalization of the PDF, the indefinite integral of $H(t;k)$ is

$$\int H(t;k)dt = \frac{1}{k}\left[H(t;k) - \frac{1}{2}\text{erf}\left(\frac{t}{\sqrt{2}\sigma}\right)\right] \tag{8.24}$$

It should be noted that there are no magnitudes within this solution thus it is equally applicable to complex exponentials.

As well as the decay time resolution, there are also dilution effects introduced by the measured mistag, ω, of the signal candidate described by the difference between the "right" and "wrong" tag given in Equation 8.16. This dilution can be described for each tagged state by the function Ω [61],

$$\overset{(-)}{\Omega} = \varepsilon_{\text{tag}}(1 - \overset{(-)}{\omega}(\eta)) - \varepsilon_{\text{tag}}\overset{(-)}{\omega}(\eta) \tag{8.25}$$

where the bar indicates the calibration is applied to a candidate with a tag of -1 while the unbarred state indicates the calibration is applied to a candidate with a tag of $+1$. ω is described by Equation 8.15, however to reduce biases introduced by the two tagged states, a mistag asymmetry is introduced. The mistag asymmetry is described by

$$p_0 = \hat{p}_0(1 + \Delta p_0), \tag{8.26}$$

$$\bar{p}_0 = \hat{p}_0(1 - \Delta p_0), \tag{8.27}$$

$$p_1 = \hat{p}_1(1 + \Delta p_1), \tag{8.28}$$

$$\bar{p}_1 = \hat{p}_1(1 - \Delta p_1). \tag{8.29}$$

The mistag asymmetry parameters are given in Tables 8.20 and 8.21.

There is also an associated asymmetry with the tagging efficiency, $\Delta\varepsilon_{\text{tag}}$, when the candidates are split by their tagging decision. This is described by

$$\varepsilon_{\text{tag}} = \frac{1 + \Delta\varepsilon_{\text{tag}}}{2}\hat{\varepsilon}_{\text{tag}}, \tag{8.30}$$

$$\bar{\varepsilon}_{\text{tag}} = \frac{1 - \Delta\varepsilon_{\text{tag}}}{2}\hat{\varepsilon}_{\text{tag}}. \tag{8.31}$$

As the LHC is a proton-proton collider, there is an associated production asymmetry, A_{Prod}, for B^0 and B^0_s mesons which must be accounted for. If the production asymmetry is non-zero then the trigonometric terms in Equations 2.37 and 2.38 do not cancel when they are summed as is the case for untagged candidates. This can introduce a small oscillation effect for these candidates. The full function describing the decays will then be given by

$$\begin{aligned} f(t; q, \hat{\varepsilon}_{\mathrm{tag}}, \Delta\varepsilon_{\mathrm{tag}}, A_{\mathrm{Prod}}, \eta, \sigma_{\mathrm{eff}}) &= \frac{1+qA_{\mathrm{Prod}}}{2}\frac{1+q\Delta\varepsilon_{\mathrm{tag}}}{2}\hat{\varepsilon}_{\mathrm{tag}}\left(1-2\overset{(-)}{\omega}(\eta;q)\right) \\ &\quad \times \Gamma(t;q)\otimes G(t;\sigma_{\mathrm{eff}}) \end{aligned} \tag{8.32}$$

The solutions to the PDF were validated using toy Monte Carlo events generated using Equations 2.37 and 2.38. The fit results and pulls from 300 pseudo-experiments generated with as realistic a configuration as possible for the two decay channels is shown in Figure 8.40. The toys were produced using the CP observables for $\mathrm{B}^0\rightarrow \pi^+\pi^-$ and $\mathrm{B}^0_\mathrm{s}\rightarrow \mathrm{K}^+\mathrm{K}^-$ decays from [166] and include known background contributions, a per-event decay time resolution and a per-event mistag. These fits use the analytic form of the normalization which improves the fit time by a factor of approximately 20. The mean and width of the pull for $S_{\pi\pi}$ were found to be -0.045 ± 0.057 and 0.98 ± 0.04 respectively. The mean and width of the pull for $C_{\pi\pi}$ were found to be 0.027 ± 0.05 and 0.93 ± 0.04 respectively. The mean and width of the pull for S_{KK} were found to be -0.065 ± 0.056 and 0.96 ± 0.04 respectively. The mean and width of the pull for C_{KK} were found to be 0.039 ± 0.064 and 1.10 ± 0.05 respectively. The mean and width of the pull for $\mathcal{A}^{\Delta\Gamma}_{\mathrm{KK}}$ were found to be -0.070 ± 0.060 and 1.04 ± 0.04 respectively.

8.7.2 Results of CP Violation in $\mathrm{B}^0\rightarrow\pi^+\pi^-$ and $\mathrm{B}^0_\mathrm{s}\rightarrow \mathrm{K}^+\mathrm{K}^-$

The fits to the three tagged states were performed simultaneously for each final state using an *sFit*[161] which is an extension of the *sWeights* discussed in Section 7.4. The *sFit* uses the *sWeights* measured from the invariant mass distributions to effectively remove the background contributions by applying their weights to the proper time distribution assuming that the weights were correctly calculated. This is advantageous as it removes the need to model these distributions in decay time.

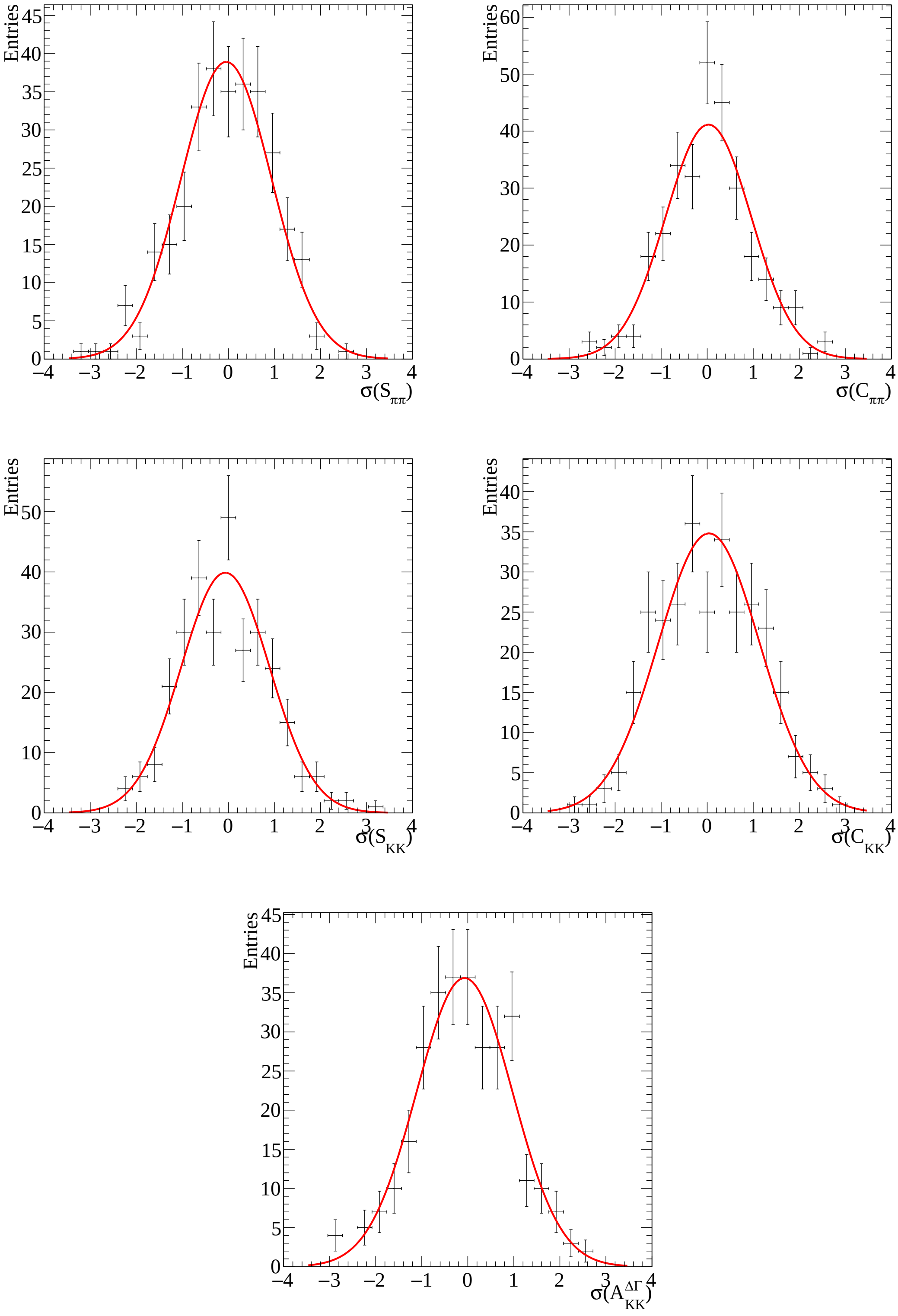

FIGURE 8.40: Pulls from toy studies of 300 simulations of $\mathrm{B}^0 \to \pi^+\pi^-$ and $\mathrm{B}^0_\mathrm{s} \to \mathrm{K}^+\mathrm{K}^-$ decays using the results found in [166]. These studies were performed under as realistic a situation as was possible and includes background events, a per-event decay time resolution and a per-event mistag. Top Left - Pull of $S_{\pi\pi}$. Top Right - Pull of $C_{\pi\pi}$. contaminations dle Left - Pull of S_{KK}. contaminations dle Right - Pull of C_{KK}. Bottom - Pull of $\mathcal{A}^{\Delta\Gamma}_{\mathrm{KK}}$.

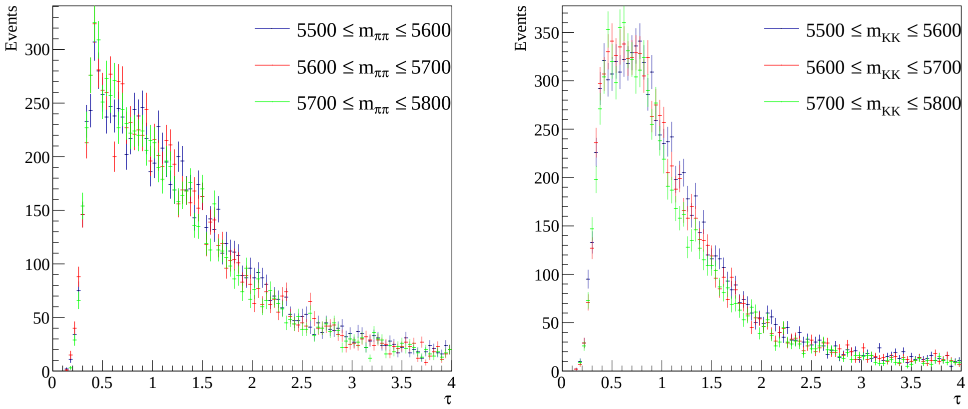

FIGURE 8.41: Comparison of the decay time distribution for combinatorial background candidates in bins of invariant mass. Left - The distribution in the $\mathrm{K^+K^-}$ spectrum. Right - The distribution in the $\pi^+\pi^-$ spectrum.

As previously mentioned, the *sWeight* technique requires that the variable used to calculate the event weights are uncorrelated with the variable you wish to measure. To ensure that this was the case, the upper mass sideband of the invariant mass distribution was split into bins and the decay time distribution of each bin was compared. The data was split into three bins, each with a width of 100 MeV, in the range $5500 \leq m_{\mathrm{d_1d_2}}\,[\mathrm{MeV}] \leq 5800$ with the results of the comparison shown in Figure 8.41. The comparison shows no variation of the combinatorial background distribution with respect to the mass. There is known to be a contribution of less than one percent from decays of Λ_b^0 in the second bin (in the range $5600 \leq m_{\mathrm{d_1d_2}}\,[\mathrm{MeV}] \leq 5700$). To ensure that this did not introduce a bias, the comparison was rerun increasing the kaon-proton separation to above 10 for the $\mathrm{K^+K^-}$ sample and decreasing the proton-pion separation to below -10 for the $\pi^+\pi^-$ sample. No significant difference was observed between the two comparisons.

The *sFit* method is advantageous to this analysis as the proper time distribution is a function of four variables; the lifetime, flavour tag, mistag and decay time error. These variables increase the time required to fit the data with respect to the Run I analysis. If the fit was performed with all the background events then it would take over 24 hours to converge whereas it takes approximately 40 minutes to converge using the *sFit* method.

The fit was performed leaving the CP observables floating for each final state to avoid constraining any of the parameters by their unitary condition. The calibration parameters for the flavour tagging for the $\mathrm{B}^0 \to \pi^+\pi^-$ decay were taken

Parameter	$\mathrm{B}^0 \to \pi^+\pi^-$	$\mathrm{B}^0_\mathrm{s} \to \mathrm{K}^+\mathrm{K}^-$
τ	$1.520 \pm 0.004\,\mathrm{ps}$	$1.509 \pm 0.004\,\mathrm{ps}$ [36]
Δm_q	$0.5064 \pm 0.0019\,\mathrm{ps}^{-1}$	$17.757 \pm 0.021\,\mathrm{ps}^{-1}$ [36]
$\Delta\Gamma$	$0\,\mathrm{ps}^{-1}$	$0.088 \pm 0.006\,\mathrm{ps}^{-1}$ [36]
A_Prod	-0.0140 ± 0.0055 ± 0.0010	0.0198 ± 0.0190 ± 0.0059 [174]

TABLE 8.22: The fixed parameters used in the fit to the proper lifetime distribution taken from [36]. The parameters used for the per-event decay time resolution in the $\mathrm{B}^0_\mathrm{s} \to \mathrm{K}^+\mathrm{K}^-$ were previously given in Table 8.16 while the flavour tagging calibration parameters for the $\mathrm{B}^0 \to \pi^+\pi^-$ and $\mathrm{B}^0_\mathrm{s} \to \mathrm{K}^+\mathrm{K}^-$ decays were previously given in Tables 8.20 and 8.21 respectively.

from Table 8.20 while for the $\mathrm{B}^0_\mathrm{s} \to \mathrm{K}^+\mathrm{K}^-$ decay were taken from Table 8.21. The per-event decay time resolution calibration for the $\mathrm{B}^0_\mathrm{s} \to \mathrm{K}^+\mathrm{K}^-$ decays was taken from Table 8.16. The rest of the parameters fixed in the fit were taken from the Particle Data Group [36] and the LHCb paper on production asymmetries[174]. The values are given in Table 8.22.

The fit to the $\pi^+\pi^-$ distribution found $S_{\pi\pi} = -0.653 \pm 0.043$ (stat.) $\pm\, 0.016$ and $C_{\pi\pi} = -0.237 \pm 0.036$ (stat.) $\pm\, 0.018$ (syst.). The result of $S_{\pi\pi}$ is compatible with previous measurements while $C_{\pi\pi}$ is compatible with measurements from BaBar [163] and a previous measurement from LHCb [166] the result is not compatible with the latest LHCb result [61]. The fit to the $\mathrm{K}^+\mathrm{K}^-$ distribution found S_KK $= 0.138 \pm 0.041$ (stat.) $\pm\, 0.012$ and $C_\mathrm{KK} = 0.121 \pm 0.040$ (stat.) $\pm\, 0.021$ (syst.). These results are compatible with previous measurements by LHCb [61, 165]. $\mathcal{A}^{\Delta\Gamma}_\mathrm{KK}$ was measured to be -0.183 ± 0.084 (stat.) $\pm\, 0.067$ (syst.). This result is significantly different from previous measurements by LHCb [61, 146] and is discussed in Section 8.9.

The results are summarised in Table 8.23 with the time-dependent CP asymmetries shown in Figures 8.42 and 8.43. To ensure the stability of the results, the fit was performed with the data split by year and magnet polarity. The comparison of the fit results for the observables are given in Figures 8.45 and 8.44. For $\mathrm{B}^0 \to \pi^+\pi^-$, the correlation between $S_{\pi\pi}$ and $C_{\pi\pi}$ was measured to be -0.15. For $\mathrm{B}^0_\mathrm{s} \to \mathrm{K}^+\mathrm{K}^-$, the correlation between S_KK and C_KK was measured to be -0.012, the correlation between S_KK and $\mathcal{A}^{\Delta\Gamma}_\mathrm{KK}$ was measured to be 0.027 and the correlation between C_KK and $\mathcal{A}^{\Delta\Gamma}_\mathrm{KK}$ was measured to be 0.026.

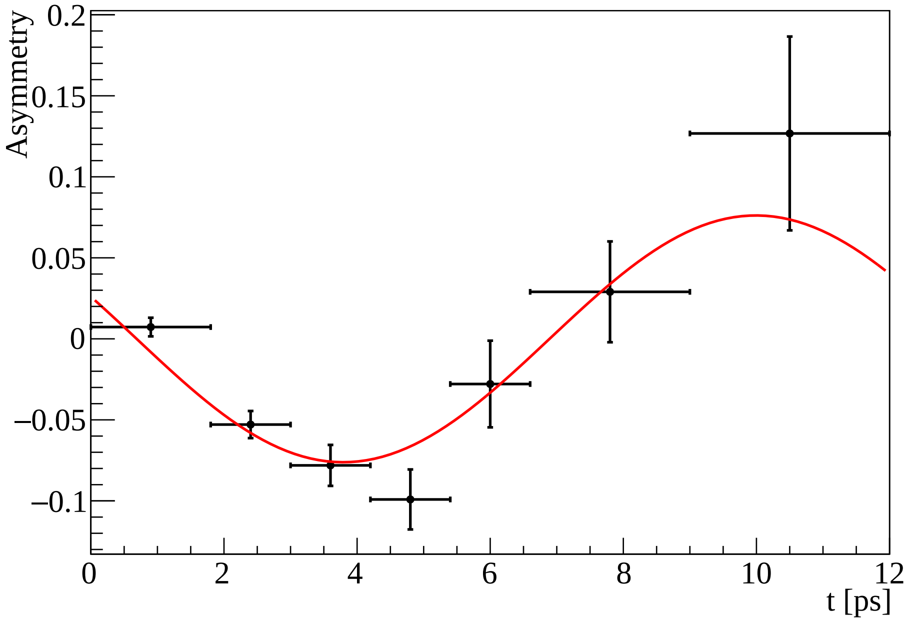

FIGURE 8.42: The observed time-dependent asymmetry from $B^0 \to \pi^+\pi^-$ signal candidates. The fit is given by Equation 2.43 with the input values taken from Table 8.22.

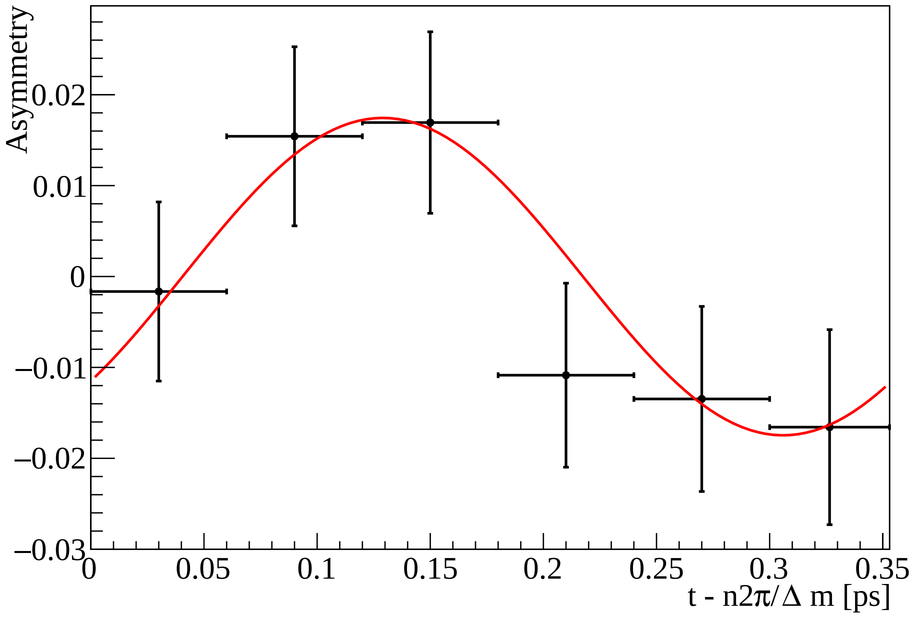

FIGURE 8.43: The observed time-dependent asymmetry from $B_s^0 \to K^+K^-$ signal candidates. The fit is given by Equation 2.43 with the input values taken from Table 8.22.

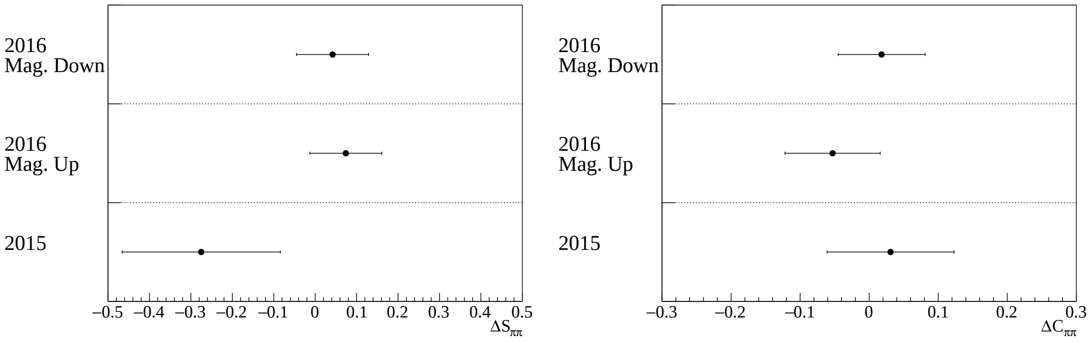

FIGURE 8.44: The measured difference between the CP observables in the full data sample and in the data samples split by run year and magnet polarity for $\mathrm{B}^0 \to \pi^+\pi^-$ signal candidates. Left - The difference in $S_{\pi\pi}$. Right - The difference in $C_{\pi\pi}$. The errors given here are statistical only.

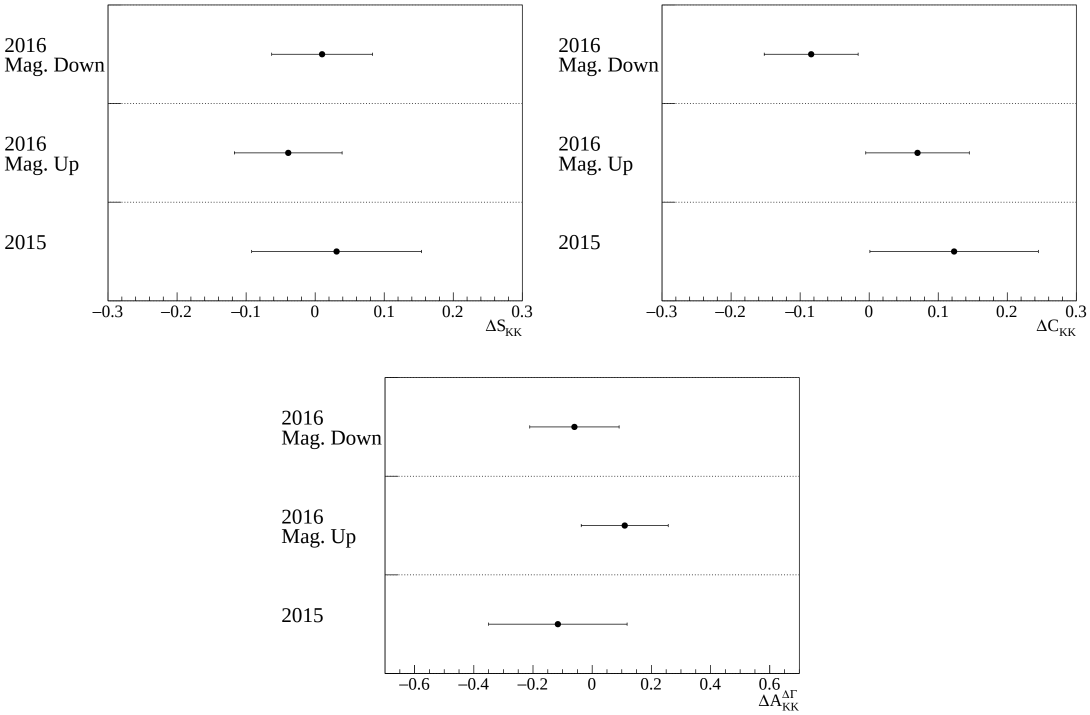

FIGURE 8.45: The measured difference between the CP observables in the full data sample and in the data samples split by run year and magnet polarity for $\mathrm{B}^0_s \to \mathrm{K}^+\mathrm{K}^-$ signal candidates. Top Left - The difference in S_{KK}. Top Right - The difference in C_{KK}. Bottom - The difference in $\mathcal{A}^{\Delta\Gamma}_{\mathrm{KK}}$. The errors given here are statistical only.

Parameter	Value
$C_{\pi\pi}$	-0.237 ± 0.036 (stat.) ± 0.018 (syst.)
$S_{\pi\pi}$	-0.653 ± 0.043 (stat.) ± 0.016 (syst.)
C_{KK}	0.121 ± 0.042 (stat.) ± 0.021 (syst.)
S_{KK}	0.138 ± 0.041 (stat.) ± 0.012 (syst.)
$\mathcal{A}^{\Delta\Gamma}_{\mathrm{KK}}$	-0.183 ± 0.084 (stat.) ± 0.067 (syst.)

TABLE 8.23: The final results from the Run II analysis of time-dependent CP violation.

8.8 Systematic Uncertainties

To investigate the contribution of any systematic biases to the final measurements of the CP observables a comprehensive list of parameters involved in the measurements was compiled and their effect on the results was quantified. The sources studied were taken from previous measurements of CP violation in $\mathrm{B}^0 \to \pi^+\pi^-$ and $\mathrm{B}_s^0 \to \mathrm{K}^+\mathrm{K}^-$ decays [61] and a previous study of the effective decay time of $\mathrm{B} \to h^+h'^-$ decays when the Swimming method was used to correct for the decay time acceptance [146].

8.8.1 Signal Mass Model

The invariant mass distribution is used to *sWeight* the candidates by their predicted source. Thus, improper modelling of this distribution will result a bias in the decay time distribution. To investigate the bias resulting from the modelling of the signal, the fixed tail parameters of the double Crystal Ball function were allowed to vary within 1σ of the uncertainty determined from the MC fits given in Tables 8.10 and 8.11 with the difference between the results with and without the variation taken as the systematic uncertainty.

8.8.2 Two-body Mass Model

Due to detector effects, the reconstructed mean mass of a particle may not be consistent with the literature mass of the particle which is in turn used to define the mean mass of the MC simulation. This requires that the position of the two-body background shapes are offset by the difference between the measured and literature mean mass. As with the signal mass model, the value of this offset will affect the weight of the candidate. To account for this effect, 300 pseudo-experiments were produced for the two data sets where the value of the offset of the background shapes were allowed to vary within the statistical uncertainty of the measured mean mass of the signal.

The contribution of the two-body backgrounds were Gaussian constrained to their predicted values from PidCalib and thus are accounted for in the statistical uncertainty on the parameters.

8.8.3 Partially Reconstructed Mass Model

The partially reconstructed background candidates constitute a sizeable contribution to the overall decay samples but are located in a lower invariant mass region than the signal candidates, thus their associated biases are predicted to be small. To investigate their contribution to the measurements, the parameters of the exponentially modified Gaussian describing their shape were varied within 1σ of the uncertainty determined from the fit to the data with the resulting difference between the results taken as the systematic uncertainty.

8.8.4 Combinatorial Mass Model

The combinatorial background candidates are described by a linear function for both of the data sets. This model was changed to an exponential function and the CP observables recalculated with the resulting difference between the measurements taken as the systematic uncertainty.

8.8.5 $\mathrm{B_c^+}$ Contamination

A known source of $\mathrm{B_s^0}$ mesons is from the decay $\mathrm{B_c^+} \to \mathrm{B_s^0}\pi^+$ [175] with an upper limit on this contribution of 1 %. As the decay time of the $\mathrm{B_c^+}$ has been measured as $0.507 \pm 0.009\,\mathrm{ps}$, this will introduce an increase in the measured decay time of $\mathrm{B_s^0}$ decays by introducing an extra exponential decay term to the decay time distribution.

To account for this contamination, 300 pseudo-experiments of the $\mathrm{B_s^0} \to \mathrm{K^+K^-}$ decay were produced with a 1% contribution from $\mathrm{B_c^+} \to \mathrm{B_s^0}\pi^+$ decays with the candidates being evenly distributed between the three tagged states.

8.8.6 Tracking Efficiency Acceptance

The VELO track reconstruction efficiency has a dependence on the angle of the track with respect to the beam line of the LHC [90, 171] as the reconstruction algorithms match r- and ϕ-segments. The algorithms have a preference for decays occurring close to the beam-axis and, hence, have a lower efficiency for long lived candidates. This effect has been shown to be well parametrised from a quadratic dependence on the distance of closest approach of a track to the beam line (DOCAZ) [146, 147, 176], given by

$$\varepsilon(\mathrm{DOCAZ}) = \alpha + \beta \times \mathrm{DOCAZ} \tag{8.33}$$

where α and β are constants derived from data and DOCAZ is described by Equation 8.8. The fit parameters were taken from a previous LHCb study on decays of B-hadrons [177]. To account for the bias resulting from this acceptance effect, the modelling was removed from the fit and the difference between measurements taken as the systematic uncertainty.

8.8.7 Production Asymmetry

The production asymmetry (A_{Prod}) for B^0 and B^0_s mesons at the LHC has been measured by the LHCb collaboration [174] with the results assigned as a fixed value in the fit. A_{Prod} was varied within 1σ of the measured uncertainty with the difference between measurements taken as the systematic uncertainty.

8.8.8 Decay Time Acceptance

The description of the method for correcting for the decay time acceptance was outlined in Section 8.4. This method involves moving the primary vertex of the mother and re-evaluating the selection then assigning a “turning point” for each hypothetical decay time where the selection acceptance changes. As this method uses a finite step size of 0.5 µm then it is possible to overstep the true turning point. The typical time difference for each step is approximately 0.02 fs, however the time difference is highly dependant on the momentum of the particle as described in Equation 8.10. To account for this, each turning point was varied by 1 % with the difference between measurements taken as the systematic uncertainty.

8.8.9 Decay Time Resolution Model

Due to the rapid oscillation of the B^0_s, the measured CP observables in the $\mathrm{B}^0_\mathrm{s} \to \mathrm{K}^+\mathrm{K}^-$ channel are sensitive to the detector resolution. To correct for this, the

Parameter	Value
q_0	$1.29 \pm 0.97\,\mathrm{fs}$
q_1	0.94 ± 0.02

TABLE 8.24: Fit results to the per-event decay time resolution of $\mathrm{J}/\psi \to \mu^+\mu^-$ 2016 data events using a double Gaussian as a decay time model.

decay time resolution must be accounted for on an event-by-event basis. The decay time resolution was modelled from prompt $\mathrm{J}/\psi \to \mu^+\mu^-$ decays as a triple Gaussian as described in Section 8.5.2. To investigate the dependence on the decay time model used, the triple Gaussian was replaced by a double Gaussian. The new calibration parameters are given in Table 8.24 where it can be seen that they are consistent with using a triple Gaussian to model the resolution, thus no systematic is assigned.

8.8.10 Decay Time Resolution Calibration

To account for the decay time resolution calibration, the fit parameters were varied by 1σ of the measured uncertainty given in Table 8.17 with the resulting difference between measurements taken as the systematic uncertainty. As the intercept and gradient of the per-event resolution are precisely anti-correlated with each other this must be accounted for in the calculation by decreasing the value of the intercept while increasing the value of the gradient and vice-versa.

8.8.11 Flavour Tagging Model

The measurement of the CP observables depends strongly on the calibration of the flavour taggers as the mistag has the effect of diluting the amplitudes of the oscillation. The calibration method was described in Section 8.6 where a linear calibration of predicted mistag, η was performed. To account for small variations in η, the calibration model was altered to a second order polynomial where the new calibration parameters are given in Table 8.25 and the calibrated mistag distributions are given in Figure 8.46.

Parameter	B^0 Calibration	B_s^0 Calibration
$p_0 - \hat{\eta}$	$(7.1 \pm 2.5) \times 10^{-3}$	$(2.5 \pm 0.4) \times 10^{-2}$
Δp_0	$(-6.6 \pm 3.2) \times 10^{-3}$	$(0.4 \pm 4.3) \times 10^{-3}$
p_1	0.932 ± 0.030	0.892 ± 0.045
Δp_1	$(-1.7 \pm 3.9) \times 10^{-2}$	$(-1.5 \pm 4.5) \times 10^{-2}$
p_2	0.14 ± 0.26	-0.98 $\pm$ 0.36
Δp_2	(0.06 ± 0.35)	(1.2 ± 0.4)
$\hat{\eta}$(cal.)	38.68 ± 0.25 %	38.12 ± 0.37 %
$\hat{\eta}$(sig.)	38.60 ± 0.26 %	37.20 ± 0.39 %
p_0(cal.)	0.394 ± 0.004	0.406 ± 0.005
p_0(sig.)	0.386 ± 0.004	0.397 ± 0.006
ε_{tag}	85.23 ± 0.26 %	72.80 ± 0.23 %
ε_{eff}	4.43 ± 0.20 %	4.77 ± 0.23 %

TABLE 8.25: The flavour tagging calibration parameters measured using ESPRESSO PERFORMANCE MONITOR to calibrate the $\mathrm{B}^0 \to \pi^+\pi^-$ and $\mathrm{B}_s^0 \to \mathrm{K}^+\mathrm{K}^-$ signals when a quadratic model was used to define the relationship between η and ω.

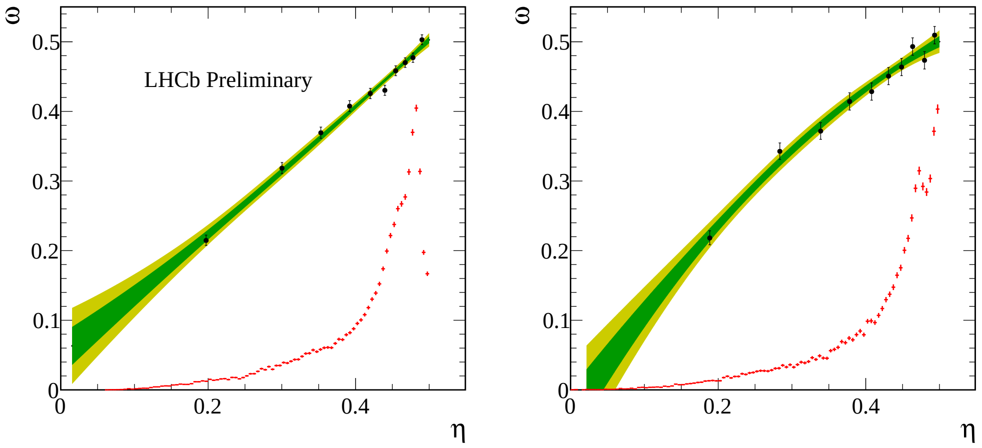

FIGURE 8.46: The measured mistag calibrations when using a polynomial model with one and two sigma confidence limits in green and yellow respectively. The distribution of the predicted mistag, η, of each tagger is shown in red. Left - The combined mistag calibration from B^0 decays. Right - The combined mistag calibration from B_s^0 decays.

Systematic	$C_{\pi\pi}$	$S_{\pi\pi}$	C_{KK}	S_{KK}	$\mathcal{A}^{\Delta\Gamma}_{\mathrm{KK}}$
Signal Mass Model	6.3×10^{-3}	0.75×10^{-3}	0.27×10^{-3}	0.13×10^{-3}	0.29×10^{-2}
Two-body Mass Model	2.0×10^{-3}	9.9×10^{-3}	6.0×10^{-3}	4.8×10^{-3}	1.5×10^{-2}
P.R.B. Mass Model	0.06×10^{-3}	0.15×10^{-3}	0.17×10^{-3}	0.35×10^{-3}	0.69×10^{-2}
Combinatorial Mass Model	5.9×10^{-3}	0.09×10^{-3}	0.11×10^{-3}	0.10×10^{-3}	0.27×10^{-2}
$\mathrm{B}_{\mathrm{c}}^{+}$ Contamination	-	-	5.4×10^{-3}	2.8×10^{-3}	2.4×10^{-2}
Production Asymmetry	1.7×10^{-3}	5.6×10^{-3}	0.02×10^{-3}	0.03×10^{-3}	0.04×10^{-2}
Tracking Efficiency Acceptance	12×10^{-3}	2.5×10^{-3}	0.93×10^{-3}	0.43×10^{-3}	2.5×10^{-2}
Decay Time Acceptance	6.3×10^{-3}	9.6×10^{-3}	1.5×10^{-3}	0.62×10^{-3}	3.3×10^{-2}
Decay Time Resolution Calibration	-	-	0.34×10^{-3}	0.58×10^{-3}	0.00×10^{-2}
Flavour Tagging Model	2.8×10^{-3}	2.8×10^{-3}	14×10^{-3}	7.8×10^{-3}	0.69×10^{-2}
Flavour Tagging Calibration	2.7×10^{-3}	1.6×10^{-3}	10×10^{-3}	5.8×10^{-3}	0.06×10^{-2}
Input Parameters	6.7×10^{-3}	1.6×10^{-3}	6.9×10^{-3}	5.1×10^{-3}	4.2×10^{-2}
Total	0.018	0.016	0.021	0.012	0.067

Table 8.26: The sources of systematic errors on the CP observables that were studied and their contribution to the total systematic error.

8.8.12 Flavour Tagging Calibration

To account for the flavour tagging calibration, the fit parameters are varied by 1σ of the measured uncertainties given in Tables 8.20 and 8.21 with the resulting difference between measurements taken as the systematic uncertainty.

8.8.13 Input Parameters

In the fit, the lifetime, oscillation period and decay width difference were kept as fixed parameters. To study their impact on the measured values of the CP observables, they were allowed to vary by 1σ of their quoted uncertainties given in Table 8.22 with the resulting differences between measurements taken as the systematic uncertainty.

8.8.14 Summary

The various systematics studied and their associated contributions are summarised in Table 8.26. The contributions were summed in quadrature to give the final systematic error for each measured parameter.

8.9 Discussion of $\mathcal{A}^{\Delta\Gamma}_{\mathrm{KK}}$

The measured value of $\mathcal{A}^{\Delta\Gamma}_{\mathrm{KK}}$ was found to be $-0.183 \pm 0.084\,(\mathrm{stat.}) \pm 0.067\,(\mathrm{syst.})$ which is significantly different from the previous measurements of this parameter from both an effective lifetime measurement ($-0.975 \pm 0.092\,(\mathrm{stat.}) \pm 0.113\,(\mathrm{syst.}) \pm 0.082\,(\mathrm{ext.})$) and from the CP observables ($-0.79 \pm 0.07\,(\mathrm{stat.}) \pm 0.10\,(\mathrm{syst.})$). The combined results from the $\mathrm{B}^0_\mathrm{s} \to \mathrm{K}^+\mathrm{K}^-$ analysis are also incompatible with the unitarity condition of the CP observables stated in Equation 2.44. The measured value of $\mathcal{A}^{\Delta\Gamma}_{\mathrm{KK}}$ warrants further investigation to uncover any sources of bias in the analysis.

The full fitting method was tested using MC samples which passed the same selection and calibration as the data samples and these MC samples were found to return the generated values of the observables. Hence the source of the discrepancy is believed to have arisen from a difference between data and simulation.

The fitter used in the analysis was previously used to measure the effective lifetimes detailed in Chapter 7, which is compatible with previous results: the effective decay time fitter hence appears to be free from bias. As a cross-check, the effective decay time of the $\mathrm{B}^0_\mathrm{s} \to \mathrm{K}^+\mathrm{K}^-$ sample was measured to be $1.505 \pm 0.008\,\mathrm{ps}$ where the error is statistical only. This was compared to the predicted decay time of approximately $1.504\,\mathrm{ps}$ obtained using Equation 7.14 and the measured value of $\mathcal{A}^{\Delta\Gamma}_{\mathrm{KK}}$ in this analysis. This prediction is compatible with the measured effective decay time and so the fitter is not believed to be the source of the discrepancy. The PDF used to measure the observables was developed for this analysis and was shown to be unbiased when using the results previously reported by LHCb [166] and with the calibration parameters discussed in this chapter, therefore it is also not believed to be a source of the discrepancy.

A difference between the fit to the collected data and MC samples is in the lack of background contaminations within the MC. The background was subtracted from the data sample using *sWeights*, which rely on the variables used to calculate the event weights (in this case the invariant mass) being uncorrelated with the variables to be measured (the decay time). The lack of correlation was verified by studying the decay time distribution in bins of invariant mass as shown in Figure 8.41. However, it is possible that a correlation is present between the *sWeights* themselves and the decay time distribution. To investigate this, the signal

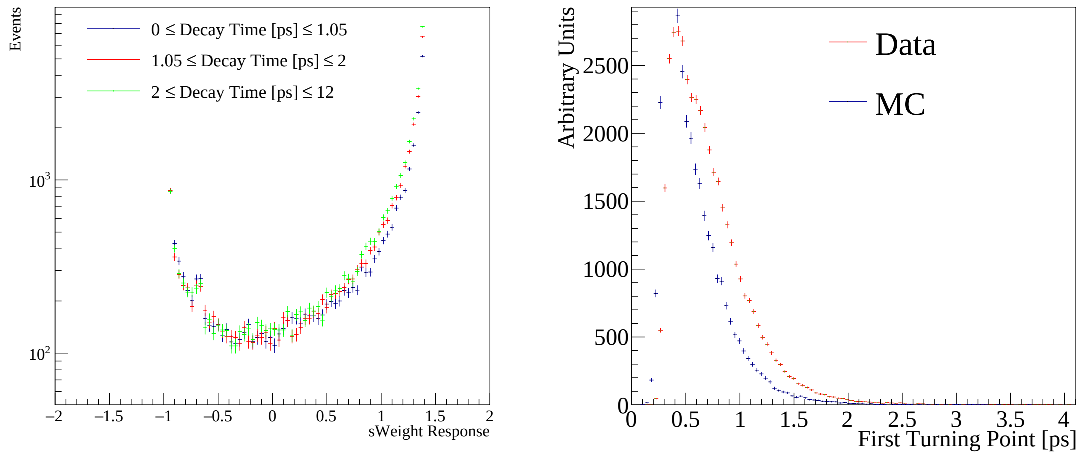

FIGURE 8.47: Left - The $\mathrm{B}_s^0 \to \mathrm{K}^+\mathrm{K}^-$ *sWeights* response within $3\,\sigma$ of the signal mass peak. The data has been split into three bins of equal statistics to ensure there is no variation in the *sWeights* as a function of decay time. Right - A comparison between the first turning point in data in red and a MC sample in blue.

sWeights were divided into bins of decay time then compared for both the full data sample and a subset within $3\,\sigma$ of the signal mass peak. The observed distribution of signal *sWeights* within the signal region as a function of decay time bins is given in Figure 8.47, where no significant differences were found.

By elimination, this indicates that there is an issue with the acceptance correction as applied to data. To investigate the acceptance, the fit range was altered, which was found to affect the value of $\mathcal{A}_{\mathrm{KK}}^{\Delta\Gamma}$, while the values of S_{KK} and C_{KK} were found to vary within their statistical uncertainty and hence, these two variables are unaffected by the fit range used.

The same correction was applied to both the data and to the MC samples but upon inspection of the first turning point a difference has been observed in the distributions. At this stage, the reader should be reminded that the turning points are defined as the region where the acceptance decision of an event changes, thus the first turning point is the location at which an event is first accepted by the selection. It can be seen in the right hand side of Figure 8.47 that the data distribution is different from the MC distribution with a large number of events turning on at a later period than seen for MC events.

It is felt that the discrepancy is due to variations between the acceptance corrections for data and MC. The decay time acceptance is known to be well modelled in simulations, hence this indicates that the acceptance correction as applied to

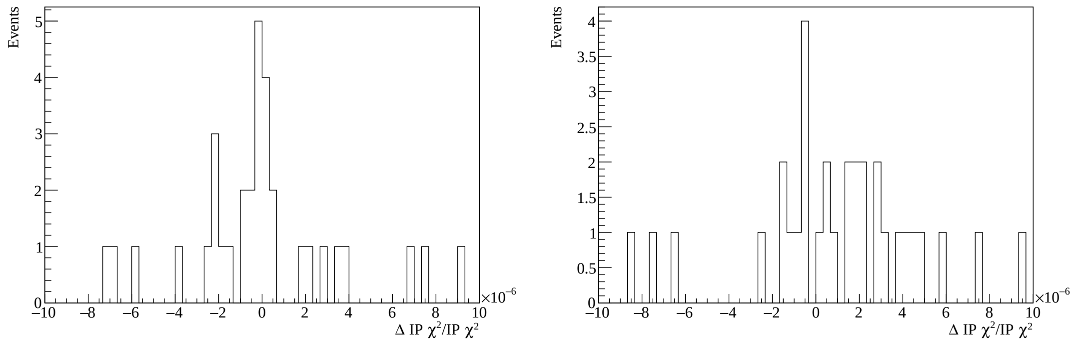

FIGURE 8.48: The difference between the recalculated and the true IPχ^2 with respect to the true IPχ^2 using a subset of the $B_s^0 \to K^+K^-$ final data sample and calculated within the full LHCb framework. Left - The distribution of the difference using K^+ tracks. Right - The distribution of the difference using K^- tracks.

data is incorrect and it is currently under investigation as to the precise source for this effect.

In the new swimming method, two approximations for recalculating parameters were made; the calculations of the hypothetical decay time and the IPχ^2. Cross-checks of the new method as applied to MC samples revealed that the fitter was able to recover the generated values and hence the method was felt to be applicable to the final data set. To avoid these approximations, the swimming method was altered to use the true lifetime and IPχ^2 calculations from the LHCb framework. It was found that using the LHCb framework changed the difference between the recalculated decay time and the true decay time with respect to the true decay time from 6.9×10^{-4} ps with an RMS of 0.02 ps to 1.6×10^{-6} ps with an RMS of 1.2×10^{-6} ps when applied to a subset of the final data. The recalculation of the IPχ^2 was performed separately on the two daughter tracks. It was found that the difference between the recalculated IPχ^2 and the true IPχ^2 with respect to the true IPχ^2 on the K^+ tracks was -5.1×10^{-9} with an RMS of 3.5×10^{-6} while for the K^- tracks was 9.4×10^{-7} with an RMS of 3.8×10^{-6}. The results of the IPχ^2 test can be seen in Figure 8.48. As the accuracy of the IPχ^2 calculation will define which swimming steps the acceptance condition will change and the lifetime calculation will determine the translation of the swimming step to the hypothetical decay time recorded for the turning point, these alterations to the method are expected to improve the determination of $\mathcal{A}_{KK}^{\Delta\Gamma}$; however, at the time of writing, the effect of the alterations on $\mathcal{A}_{KK}^{\Delta\Gamma}$ has not been determined.

8.10 Conclusions

This chapter has presented a study of CP violation in $\mathrm{B^0_s} \to \mathrm{K^+K^-}$ and $\mathrm{B^0} \to \pi^+\pi^-$ decays using $2\,\mathrm{fb^{-1}}$ of data collected at $\sqrt{s} = 13\,\mathrm{TeV}$ at LHCb. These decays are of particular importance as they can probe the effects of physics beyond the Standard Model due to loop decays contributing in equal magnitude to tree decays, allowing for new physics contributions to enter within the loop components. To improve of the methodology of the previous analysis [61], new MC samples were produced with a larger number of events than was previously available to aid in reducing the systematic uncertainties on the CP observables of interest. A new technique to optimise the selection of data was performed to minimise the errors on the CP observables rather than to maximise the signal significance. A different technique to correct for the detector acceptance, swimming, was used with respect to the previous analysis to investigate how this affected the final error determination on the parameters. Data-driven methods to calibrate the flavour tagging algorithms and measure the decay time acceptance of the decays were performed to account for dilution effects introduced to the proper time distribution by these effects. Fits to the invariant mass distribution were performed to discriminate signal from background events and event weights were applied to assign events to the relevant decay classes. These weights were then used to subtract the background events from the proper time distribution before the CP observables were measured.

The final results were measured to be

$$\begin{aligned}
C_{\pi\pi} &= -0.237 \pm 0.036(\mathrm{stat.}) \pm 0.018(\mathrm{syst.}) \\
S_{\pi\pi} &= -0.653 \pm 0.043(\mathrm{stat.}) \pm 0.016(\mathrm{syst.}) \\
C_{\mathrm{KK}} &= 0.121 \pm 0.042(\mathrm{stat.}) \pm 0.021(\mathrm{syst.}) \\
S_{\mathrm{KK}} &= 0.138 \pm 0.041(\mathrm{stat.}) \pm 0.012(\mathrm{syst.}) \\
\mathcal{A}^{\Delta\Gamma}_{\mathrm{KK}} &= -0.183 \pm 0.084(\mathrm{stat.}) \pm 0.067(\mathrm{syst.})
\end{aligned}$$

The results presented here are the most precise measurements of these parameters by a single experiment to date.

Part IV

Conclusions

Chapter 9

Conclusion

The undertaking of a Ph.D. is not an easy task. I recall sitting in the waiting room of one interview day being told about the work of the group and the speaker remarked that “if anyone is looking for lots of money, the banks are around the corner”. While everyone laughed it does highlight a good point about what drives scientists. A physics graduate can do a lot of good work in the financial sector but it requires a certain love for knowledge and discovery that takes precedence over all other needs to complete a Ph.D. The work presented in the preceding chapters would not have been seen to completion without that drive.

The LHCb collaboration has performed phenomenally throughout its history. The detector has operated beyond its design expectations, and the teamwork shown by the various members of the large collaboration has allowed for some truly remarkable results to be published. The first subdetector traversed by the products of the proton-proton collisions is the VELO. At the end of Long Shutdown I, the VELO group began recommissioning the detector. It was important to ensure the optimal performance of the high voltage system to allow the silicon sensors to be fully depleted. To this end, this system was extensively studied before the 2015, 2016 and 2017 data taking periods to guarantee the optimal performance of the VELO. Several tests were devised to qualify the high voltage system and it has always shown itself capable of operating reliably until the end of Run II. Further to this, monitoring software was developed to allow on-call experts to observe the behaviour of this system during operations which is now seeing extensive use.

Run II of the LHC comes to an end in December 2018. At this point the detector will undergo a full upgrade to improve the physics capabilities of the experiment.

One of the major projects is the upgrade of the VELO detector, moving from a silicon strip detector with a readout of 1 MHz to a pixel detector with a readout of 40 MHz. This requires a significant research investment to ensure the project can deliver its goals. To achieve this a new data readout system was devised with high speed flex cables to transfer signals to and from the detector modules and opto-power boards to properly control these signals and convert them to/from optical from/to electrical.

Several prototypes of these components were constructed to design a system that would meet the requirements needed of it. The signal transmission parameters, impedance, bit-error rate and jitter of the prototypes were measured and used to refine the designs of the components along with the effects of repeated bending on the high-speed flex cables. The production of these components should allow for the detector to be delivered well within in time for the restart of the LHC in 2021. The first physics results to come from the new LHCb detector will be very interesting to read.

The physics goals of the experiment are wide reaching in a very challenging environment to conduct precision physics in. One such area of research is the study of $\mathrm{B} \to h^+ h'^-$ decays such as $\mathrm{B}^0 \to \mathrm{K}^+\pi^-$ and $\mathrm{B}^0_\mathrm{s} \to \pi^+\mathrm{K}^-$ which constitute part of the "$\mathrm{B} \to K\pi$" puzzle [145]. Also, measurements of CP violation in the decays $\mathrm{B}^0_\mathrm{s} \to \mathrm{K}^+\mathrm{K}^-$ and $\mathrm{B}^0 \to \pi^+\pi^-$ can be used to probe for physics beyond the Standard Model. The LHCb collaboration previously measured the lifetimes of $\mathrm{B}^0_\mathrm{s} \to \mathrm{K}^+\mathrm{K}^-$, $\mathrm{B}^0 \to \mathrm{K}^+\pi^-$ and $\mathrm{B}^0_\mathrm{s} \to \pi^+\mathrm{K}^-$ decays at 7 TeV [146] from data recorded in 2011. With the full Run I data set it was possible to remeasure these parameters with an improved precision as the available statistics had more than doubled in 2012 compared to 2011. With the increased statistics it was also possible to measure the effective lifetimes in $\mathrm{B}^0 \to \pi^+\pi^-$, $\Lambda^0_\mathrm{b} \to \mathrm{p}\pi^-$ and $\Lambda^0_\mathrm{b} \to \mathrm{pK}^-$ decays. The measurement of the effective lifetimes of these decays formed the main topic of the thesis of Sarah Karodia [147] with the candidate selection and initial modelling of the Λ^0_b decays conducted by the candidate. The final results of these measurements are given in Table 9.1 for completeness.

The LHCb collaboration has also previously reported on CP violation in the decays $\mathrm{B}^0_\mathrm{s} \to \mathrm{K}^+\mathrm{K}^-$ and $\mathrm{B}^0 \to \pi^+\pi^-$ using Run I data [61]. Several new techniques were implemented in the analysis using Run II data with respect to the one conducted with Run I data to reduce both the systematic and statistical errors associated with the previous measurements. The final results of these measurements are given

Parameter	Value
$\tau_{\mathrm{B_s^0\to K^+K^-}}$	1.410 ± 0.009 (stat.) ± 0.011 (syst.)
$\tau_{\mathrm{B^0\to \pi^+\pi^-}}$	1.495 ± 0.012 (stat.) ± 0.007 (syst.)
$\tau_{\mathrm{B^0\to K^+\pi^-}}$	1.504 ± 0.006 (stat.) ± 0.023 (syst.)
$\tau_{\mathrm{B_s^0\to \pi^+K^-}}$	1.548 ± 0.028 (stat.) ± 0.023 (syst.)
$\tau_{\mathrm{\Lambda_b^0\to pK^-}}$	1.477 ± 0.022 (stat.) ± 0.022 (syst.)
$\tau_{\mathrm{\Lambda_b^0\to p\pi^-}}$	1.511 ± 0.028 (stat.) ± 0.012 (syst.)
$\mathcal{A}^{\Delta\Gamma}_{\mathrm{KK}}$	-0.975 ± 0.092 (stat.) ± 0.113 (syst.) ± 0.082 (ext.)

TABLE 9.1: The final results from the Run I lifetime analysis.

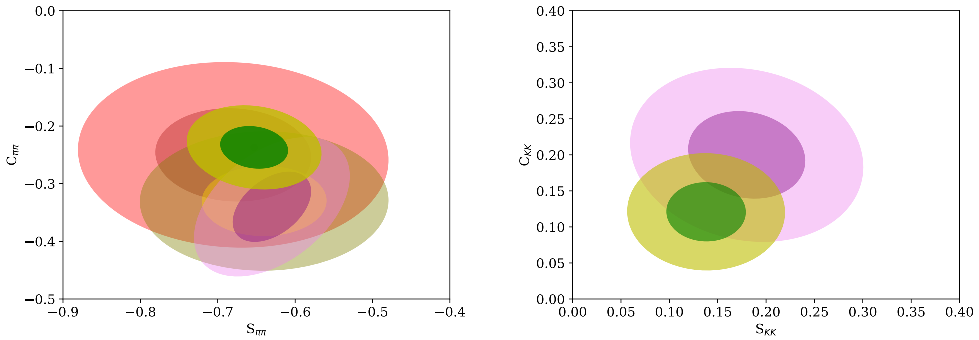

FIGURE 9.1: The measured CP observables presented in this thesis with 1- and 2-σ confidence levels given in green and yellow respectively. The previous LHCb measurements are shown in purple [61], the BaBar results are shown in red [163] and the Belle results are shown in gold [164]. Left - The results of the $\mathrm{B^0 \to \pi^+\pi^-}$ fit. Right - The results of the $\mathrm{B_s^0 \to K^+K^-}$ fit.

Parameter	Value
$C_{\pi\pi}$	-0.237 ± 0.036 (stat.) ± 0.018 (syst.)
$S_{\pi\pi}$	-0.653 ± 0.043 (stat.) ± 0.016 (syst.)
C_{KK}	0.121 ± 0.042 (stat.) ± 0.021 (syst.)
S_{KK}	0.138 ± 0.041 (stat.) ± 0.012 (syst.)

TABLE 9.2: The final results from the Run II analysis of time-dependent CP violation.

in Table 9.2 with a comparison of the results and previous measurements of these observables shown in Figure 9.1. For $\mathrm{B^0 \to \pi^+\pi^-}$, the correlation between $S_{\pi\pi}$ and $C_{\pi\pi}$ was measured to be -0.15 while, for $\mathrm{B_s^0 \to K^+K^-}$, the correlation between S_{KK} and C_{KK} was measured to be -0.012.

Overall, the work conducted throughout the Ph.D. has contributed to both the operation of the current detector, ensuring the stable operation of the VELO throughout data taking, and to the production of the upgraded detector. Without the excellent performance of LHCb in its current state, none of the physics results presented here would be possible and the contributions made to the upgrade project will ensure that the data can be read out effectively at 40 MHz trigger rate.

The measurements of CP violation in the decays, $\mathrm{B}^0 \to \pi^+\pi^-$ and $\mathrm{B}^0_\mathrm{s} \to \mathrm{K}^+\mathrm{K}^-$, are sensitive to physics beyond the Standard Model as they have equal contributions from tree and loop decays. These decays can be used to measure the CKM angles γ and β_s, hence comparisons of these angles can be made with global measurements. The discrepancy shown by $\mathcal{A}^{\Delta\Gamma}_{\mathrm{KK}}$ compared to previous measurements is under investigation and will be addressed before publication. The source of the bias is believed to be caused by the acceptance corrections, which have been shown to have a negligible affect on C_{KK} and S_{KK}. The results presented here are the most precise measurements of these observables to date.

Appendices

Appendix A

The Dirac Equation

The use of the Dirac equation was previously outlined in Section 2.1. The purpose of this section is to give a more complete description of the equation and how it describes fermions with their associated properties.

The motivation for the Dirac equation arose from the need for a relativistic description of quantum mechanics. The Schrödinger equation is limited to the non-relativistic regime as it is first order in time but second order in space making it intrinsically Lorentz invariance violating. The Klein-Gordon equation came from applying quantum mechanical operators to the relativistic energy equation ($E^2 = p^2 + m^2$) but this equation is only valid for spin-0 particles. Dirac then proposed an equation that was first-order in space and time. The initial form that will be looked at is

$$(-i\alpha_k\partial_k + \beta m)\psi = i\partial_0\psi, \tag{A.1}$$

where α_k and β are constants, ∂_k is the spatial derivative (it should be noted that $-i\partial_k$ is the momentum operator in natural units)and ∂_0 is the time derivative ($i\partial_0$ is the energy operator). The index k runs from 1 to 3 and Equation A.1 has an implicit summation. We now wish to introduce the gamma matrices $\gamma^\mu = \{\gamma^0, \gamma^1, \gamma^2, \gamma^3\}$ by multiplying Equation A.1 left and right by β then defining the matrices as

$$\gamma^0 = \beta \qquad \gamma^k = \beta\alpha^k.$$

This allows us to arrive at the common form of the Dirac equation,

$$(i\gamma^\mu\partial_\mu \ - \ m)\psi = 0, \tag{A.2}$$

if $\beta^2 = I$ where I is the identity matrix. The gamma matrices satisfy the anticommutation relation

$$\{\gamma^\mu, \gamma^\nu\} = 2g^{\mu\nu}$$

where $g^{\mu\nu}$ is the space-like Minkowski metric and immediately gives the properties of the gamma matrices

$$(\gamma^0)^2 = I \qquad (\gamma^k)^2 = -I \qquad \gamma^\mu\gamma^\nu = -\gamma^\nu\gamma^\mu. \tag{A.3}$$

A sensible decision for solutions to the gamma matrices would be to use the Pauli matrices. To satisfy the anticommutation relation in Minkowski space, the minimal dimension must be four. By also satisfying the properties of the gamma matrices, we arrive at their usual form of

$$\gamma^0 = \begin{pmatrix} I & 0 \\ 0 & -I \end{pmatrix} \qquad \gamma^k = \begin{pmatrix} 0 & \sigma_k \\ -\sigma_k & 0 \end{pmatrix}, \tag{A.4}$$

where σ_k are the three Pauli matrices

$$\sigma_1 = \begin{pmatrix} 0 & 1 \\ 1 & 0 \end{pmatrix} \qquad \sigma_2 = \begin{pmatrix} 0 & -i \\ i & 0 \end{pmatrix} \qquad \sigma_3 = \begin{pmatrix} 1 & 0 \\ 0 & -1 \end{pmatrix}. \tag{A.5}$$

A.1 Momentum Conservation in the Dirac Equation

For the Dirac equation to be valid we want to know that it is Lorentz Invariant. From Noether's theorem [178], a Lorentz invariant quantity will commute with momentum. If we assume a typical Cartesian coordinate system with a particle moving in the $x_1 - x_2$ plane (thus angular momentum, $\hat{L}$, is on the x_3-axis) and use the Dirac Hamiltonian from Equation A.1 then the commutation relation is

$$[\hat{\boldsymbol{H}}_{\boldsymbol{D}}, \hat{\boldsymbol{L}}] = [\boldsymbol{\alpha} \cdot \hat{\boldsymbol{p}} + \beta\hat{\boldsymbol{m}}, \hat{\boldsymbol{L}}] = [\boldsymbol{\alpha} \cdot \hat{\boldsymbol{p}}, \hat{\boldsymbol{L}}], \tag{A.6}$$

as m is a constant and thus always commutes. As $p_3 = 0$ then the previous equation becomes (operators are implied throughout)

$$[H_D, L] = [\alpha^1 p_1 + \alpha^2 p_2, x^1 p_2 \; - \; x^2 p_1]. \tag{A.7}$$

We can then expand this to be

$$\begin{aligned}[H_D, L] &= (\alpha^1 p_1 + \alpha^2 p_2)(x^1 p_2 - x^2 p_1) - (x^1 p_2 - x^2 p_1)(\alpha^1 p_1 + \alpha^2 p_2) \quad (A.8)\\ &= \alpha^1 p_1(x^1 p_2) - \alpha^1 p_1(x^2 p_1) + \alpha^2 p_2(x^1 p_2) - \alpha^2 p_2(x^2 p_1)\\ &\quad - x^1 p_2(\alpha^1 p_1) - x^1 p_2(\alpha^2 p_2) + x^2 p_1(\alpha^1 p_1) + x^2 p_1(\alpha^2 p_2). \quad (A.9)\end{aligned}$$

In natural units, the momentum operator is $p_k = -i\partial_k$ and can be used to simplify Equation A.9 to

$$\begin{aligned}[H_D, L] = \; & -i\alpha^1 p_2 + \alpha^1 x^1 (p_1 p_2) - \alpha^1 x^2 (p_1)^2 + \alpha^2 x^1 (p_2)^2 - \alpha^2 x^2 (p_2 p_1)\\ & +i\alpha^2 p_1 - \alpha^1 x^1 (p_2 p_1) - \alpha^2 x^1 (p_2)^2 + \alpha^1 x^2 (p_1)^2 + \alpha^2 x^2 (p_1 p_2) \quad (A.10)\end{aligned}$$

Equation A.10 can be reduced using the commutation relation for momentum, $p_i p_j = p_j p_i$ to give

$$[H_D, L] = -i(\alpha^1 p_2 - \alpha^2 p_1) = -i(\boldsymbol{\alpha} \times \boldsymbol{p})_3. \quad (A.11)$$

Therefore, angular momentum is not conserved in the Dirac equation. To remedy this issue we add an extra term to the momentum, spin. We define spin in terms of the Pauli matrices from Equation A.5 in a 4×4 matrix in natural units as

$$S = \frac{1}{2}\Sigma = \frac{1}{2}\begin{pmatrix} \sigma_k & 0 \\ 0 & \sigma_k \end{pmatrix}. \quad (A.12)$$

We can now check the commutation of the spin operator with the Dirac Hamiltonian

$$\begin{aligned}[H_D, S] &= [\alpha \cdot \mathbf{p}, S], \quad (A.13)\\ &= \frac{1}{2}[\alpha^1 p_1 + \alpha^2 p_2, \Sigma_3], \quad (A.14)\\ &= \frac{1}{2}[\alpha^1 p_1 \Sigma_3 + \alpha^2 p_2 \Sigma_3 - \Sigma_3 \alpha^1 p_1 - \Sigma_3 \alpha^2 p_2]. \quad (A.15)\end{aligned}$$

It can be noted that $p_i \Sigma_3$ leaves p_i unchanged so $p_i \Sigma_3 = \Sigma_3 p_i$, which helps simplify the commutation relation to

$$\begin{aligned}[H_D, S] &= \frac{1}{2}[p_1(\alpha_1 \Sigma_3 - \Sigma_3 \alpha_1) + p_2(\alpha_2 \Sigma_3 - \Sigma_3 \alpha_2)] \quad (A.16)\\ &= \frac{1}{2}(p_1[\alpha_1, \Sigma_3] + p_2[\alpha_2, \Sigma_3]). \quad (A.17)\end{aligned}$$

α is known to be

$$\alpha_k = \begin{pmatrix} 0 & \sigma_k \\ \sigma_k & 0 \end{pmatrix}. \tag{A.18}$$

This allows us to solve Equation A.17

$$\begin{aligned}
[\alpha_1, \Sigma_3] &= \begin{pmatrix} 0 & \sigma_1 \\ \sigma_1 & 0 \end{pmatrix} \begin{pmatrix} \sigma_3 & 0 \\ 0 & \sigma_3 \end{pmatrix} - \begin{pmatrix} \sigma_3 & 0 \\ 0 & \sigma_3 \end{pmatrix} \begin{pmatrix} 0 & \sigma_1 \\ \sigma_1 & 0 \end{pmatrix}, \\
&= \begin{pmatrix} 0 & 0 & 0 & 1 \\ 0 & 0 & 1 & 0 \\ 0 & 1 & 0 & 0 \\ 1 & 0 & 0 & 0 \end{pmatrix} \begin{pmatrix} 1 & 0 & 0 & 0 \\ 0 & -1 & 0 & 0 \\ 0 & 0 & 1 & 0 \\ 0 & 0 & 0 & -1 \end{pmatrix} - \begin{pmatrix} 1 & 0 & 0 & 0 \\ 0 & -1 & 0 & 0 \\ 0 & 0 & 1 & 0 \\ 0 & 0 & 0 & -1 \end{pmatrix} \begin{pmatrix} 0 & 0 & 0 & 1 \\ 0 & 0 & 1 & 0 \\ 0 & 1 & 0 & 0 \\ 1 & 0 & 0 & 0 \end{pmatrix}, \\
&= \begin{pmatrix} 0 & 0 & 0 & -1 \\ 0 & 0 & 1 & 0 \\ 0 & -1 & 0 & 0 \\ 1 & 0 & 0 & 0 \end{pmatrix} - \begin{pmatrix} 0 & 0 & 0 & 1 \\ 0 & 0 & -1 & 0 \\ 0 & 1 & 0 & 0 \\ -1 & 0 & 0 & 0 \end{pmatrix}, \\
&= \frac{2}{i} \begin{pmatrix} 0 & \sigma_2 \\ \sigma_2 & 0 \end{pmatrix} = -2i\alpha_2,
\end{aligned} \tag{A.19}$$

and, similarly

$$[\alpha_2, \Sigma_3] = 2i\alpha_1. \tag{A.20}$$

Therefore, the commutation relation between the Dirac Hamiltonian and spin is

$$[H_D, S] \;=\; i[-p_1\alpha_2 + p_2\alpha_1] = i(\alpha \times \mathbf{p})_3. \tag{A.21}$$

It can be seen that this also does not commute with the Dirac Hamiltonian but the sum of Equations A.11 and A.21, $J = L + S$, does. We are now interested in the expectation value of the spin operator and thus what class of particles it describes.

$$S \cdot S \;=\; \frac{1}{4}(\Sigma_1^2 + \Sigma_2^2 + \Sigma_3^2), \tag{A.22}$$

$$\;=\; \frac{1}{4}(I + I + I), \tag{A.23}$$

$$\;=\; \frac{3}{4}I, \tag{A.24}$$

which we now act of state $|\psi\rangle$ to give

$$S^2|\psi\rangle = s(s+1)|\psi\rangle = \frac{3}{4}|\psi\rangle, \tag{A.25}$$

$$s = \frac{1}{2}. \tag{A.26}$$

Thus, the Dirac equation is the Lorentz invariant equation of motion for spin-1/2 particles.

A.2 Solutions to the Dirac Equation

We can look for solutions to the Dirac equation for a relativistic particle in motion, ψ, by solving Equation A.2. If we assume that the solutions come from typical plane waves such that

$$\psi = A(p^\mu)e^{ip^\mu x_\mu} = A(E,p)e^{i(p\cdot x\ -\ Et)}. \tag{A.27}$$

As the gamma matrices are 4×4 matrices, we should expect four solutions for Equation A.2.

$$\left\{E\begin{pmatrix} I & 0 \\ 0 & -I\end{pmatrix} - \begin{pmatrix} 0 & \sigma\cdot p \\ -\sigma\cdot p & 0\end{pmatrix} - m\begin{pmatrix} I & 0 \\ 0 & I\end{pmatrix}\right\}\psi = 0, \tag{A.28}$$

$$\left\{\begin{pmatrix} (E\ -\ m)I & \sigma\cdot p \\ -\sigma\cdot p & -(E+m)I\end{pmatrix}\right\}\psi = 0. \tag{A.29}$$

If we assume that ψ takes the form

$$\boldsymbol{\psi} = \begin{pmatrix} \boldsymbol{u} \\ \boldsymbol{v}\end{pmatrix}. \tag{A.30}$$

Then we can write $\mathbf{u}$ in terms of $\mathbf{v}$ (and vice-versa) using Equation A.29 as

$$\mathbf{u} = \frac{\sigma\cdot p}{E-m}\mathbf{v} \qquad \mathbf{v} = \frac{\sigma\cdot p}{E+m}\mathbf{u}. \tag{A.31}$$

The simplest form of $\mathbf{u}$ or $\mathbf{v}$ is

$$\mathbf{u} = \begin{pmatrix} 1 \\ 0\end{pmatrix}, \begin{pmatrix} 0 \\ 1\end{pmatrix} \qquad \mathbf{v} = \begin{pmatrix} 1 \\ 0\end{pmatrix}, \begin{pmatrix} 0 \\ 1\end{pmatrix} \tag{A.32}$$

and $\sigma \cdot p$ is

$$\sigma \cdot p = \begin{pmatrix} p_3 & p_1 - ip_2 \\ p_1 + ip_2 & -p_3 \end{pmatrix}. \tag{A.33}$$

If we solve for $\mathbf{u} = (1\ 0)\mathbf{v}$ then we find

$$\mathbf{v} = \begin{pmatrix} \frac{p_3}{E+m} & \frac{p_1 - ip_2}{E+m} \\ \frac{p_1+ip_2}{E+m} & \frac{-p_3}{E+m} \end{pmatrix} \begin{pmatrix} 1 \\ 0 \end{pmatrix}, \tag{A.34}$$

$$= \begin{pmatrix} \frac{p_3}{E+m} \\ \frac{p_1+ip_2}{E+m} \end{pmatrix}. \tag{A.35}$$

If we repeat this for all states then this leads us to the four solutions for the Dirac Equation

$$u_1 = N_u \begin{pmatrix} 1 \\ 0 \\ \frac{p_3}{E+m} \\ \frac{p_1+ip_2}{E+m} \end{pmatrix}, \tag{A.36}$$

$$u_2 = N_u \begin{pmatrix} 0 \\ 1 \\ \frac{p_1 - ip_2}{E+m} \\ \frac{p_3}{E+m} \end{pmatrix}, \tag{A.37}$$

$$v_1 = N_v \begin{pmatrix} \frac{p_3}{E - m} \\ \frac{p_1+ip_2}{E - m} \\ 1 \\ 0 \end{pmatrix}, \tag{A.38}$$

$$v_2 = N_v \begin{pmatrix} \frac{p_1 - ip_2}{E - m} \\ \frac{-p_3}{E - m} \\ 0 \\ 1 \end{pmatrix}, \tag{A.39}$$

where $N_{u/v}$ are appropriate normalisations, which can be obtained from the probability density, $\rho = \psi^\dagger\psi$, as $N_u = \sqrt{E+m}$ and $N_v = \sqrt{E - m}$. It can be seen that v_1 and v_2 have negative energy solutions, using the Feynman-Stückelberg interpretation [179] these negative energy solutions represent particles moving backwards in time *or* positive energy antiparticles moving forward in time (from the plane wave equation the negative energy and time cancel and thus are equivalent to positive energy and time). Equations 2.3 to 2.4 refer to four particles states with u_1 representing spin-up particles, u_2 representing spin-down particles, v_1 representing spin-down antiparticles and v_2 representing spin-up antiparticles.

A.3 CP and the Dirac Equation

A useful form of the Dirac equation is to have it in the Lagrangian formalism, where it takes the form

$$\mathcal{L} = i\bar{\psi}\not{\partial}\psi \; - \; m\bar{\psi}\psi, \tag{A.40}$$

where $\bar{\psi}$ is the adjoint spinor defined as $\bar{\psi} = \psi^{\dagger}\gamma^0$ and $\not{\partial} = \gamma^0\partial_\mu$. As the Dirac equation has been shown to be Lorentz invariant, it is sensible to discuss what happens to quantities under gauge transformations. The gauge transformation is given by

$$\partial_\mu \rightarrow \partial_\mu \; - \; iqA_\mu, \tag{A.41}$$

where q is the electric charge and A_μ is the electromagnetic four-potential. We can then add the transformation to Equation A.2 to obtain

$$[i\gamma^\mu(\partial_\mu \; - \; iqA_\mu) \; - \; m]\psi = 0. \tag{A.42}$$

A.3.1 Charge Conjugation

Using the complex conjugate of the particle spinor defined in Equation 2.3, and by multiplying by $i\gamma^2$, we find

$$i\gamma^2 = \begin{pmatrix} 0 & 0 & 0 & 1 \\ 0 & 0 & -1 & 0 \\ 0 & -1 & 0 & 0 \\ 1 & 0 & 0 & 0 \end{pmatrix}, \tag{A.43}$$

$$i\gamma^2\psi^\star = \begin{pmatrix} \frac{p_1 \; - \; ip_2}{E+m} \\ \frac{-p_3}{E+m} \\ 0 \\ 1 \end{pmatrix} \tag{A.44}$$

and we have transformed from a particle to an antiparticle (the values of the denominator in Equation A.44 can be found from other solutions to the Dirac equation that were not mentioned here). We can take the complex conjugate of Equation A.42 then multiply through by $i\gamma^2$ to find the equation of motion for an antiparticle

$$i\gamma^2[-i(\gamma^\mu)^\star(\partial_\mu + iqA_\mu) \ - \ m]\psi^\star = 0. \tag{A.45}$$

From the form of the gamma matrices defined in Equations A.4 and A.5 it should be noted that

$$(\gamma^{0,1,3})^\star = \gamma^{0,1,3} \qquad \text{and} \qquad (\gamma^2)^\star = -\gamma^2$$

and also using the properties of the gamma matrices we find that the equation of motion becomes

$$[i\gamma^\mu(\partial_\mu + iqA_\mu) \ - \ m]i\gamma^2\psi^\star = 0. \tag{A.46}$$

Noting what was shown in Equation A.44, then the Equation A.46 shows the equation of motion for an antiparticle is the same as for a particle but with the opposite charge. Thus we define $i\gamma^2\psi^\star$ as the Charge Conjugation operator

$$\mathrm{C}\psi = \mathrm{i}\gamma^2\psi^\star. \tag{A.47}$$

We now observe how the Charge Conjugation operator affects the Dirac Lagrangian

$$\mathrm{C}^{-1}\mathcal{L}\mathrm{C} = i\mathrm{C}^{-1}\bar{\psi}\partial\!\!\!/\psi\mathrm{C} \ - \ m\mathrm{C}^{-1}\bar{\psi}\psi\mathrm{C}. \tag{A.48}$$

As the double operation of the Charge Conjugation operator is required to return the original particle then $\mathrm{C}^2 = 1$ and thus $\mathrm{C} = \mathrm{C}^{-1}$. This helps us to look at the components of the equation individually,

$$\begin{aligned} \mathrm{C}^{-1}\bar{\psi}\psi\mathrm{C} &= i\gamma^2\psi^T\gamma^0 i\gamma^2\psi^\star, & \text{(A.49)} \\ &= -\psi^T\gamma^0\psi^\star. & \text{(A.50)} \end{aligned}$$

The Dirac Spinors satisfy the anticommutation relation [180], this leads us to

$$-\,\psi^T\gamma^0\psi^\star = (\psi^T)^\star\gamma^0\psi = \bar{\psi}\psi \tag{A.51}$$

and doing the same for the first term in the Lagrangian finds

$$\mathrm{C}^{-1}\bar{\psi}\partial\!\!\!/\psi\mathrm{C} = \bar{\psi}\partial\!\!\!/\psi, \tag{A.52}$$

so

$$\mathrm{C}^{-1}\mathcal{L}\mathrm{C} = \mathcal{L}. \tag{A.53}$$

This means the action is unchanged by the Charge Conjugation operator and thus, by Noethers law, we have a charge symmetry.

A.3.2 Parity and the Dirac Equation

We are now interested in studying the effect of parity on the Dirac equation. The Parity operator will satisfy the relations

$$P\psi(r) = \psi(-r) = \psi\prime, \tag{A.54}$$

$$P^2 = I. \tag{A.55}$$

If we multiply the Dirac equation by γ^0 we find

$$(i\gamma^0\gamma^\mu\partial_m u \ - \ \gamma^0 m)\psi = (i\partial_0 + i\gamma^0\gamma^k\partial_k \ - \ \gamma^0 m)\psi = 0. \tag{A.56}$$

We can then use the gamma matrix relationships to get

$$(i\gamma^0 i\gamma^0\gamma^\mu\partial_m u \ - \ i\gamma^k\gamma^0\partial_k \ - \ \gamma^0 m)\psi = (i\partial_0 - \gamma^k\partial_k \ - \ m)\gamma^0\psi = 0. \tag{A.57}$$

If we change the reference frame so that $r \to -r$ and $\psi(r) \to \psi\prime$, we introduce a negative sign to the spatial derivatives

$$(i\gamma^\mu\partial_\mu \ - \ m)\gamma^0\psi\prime = 0 \tag{A.58}$$

and we can identify the parity operator as

$$P = \gamma^0. \tag{A.59}$$

If we apply the Parity operator to the Dirac Lagrangian like was done for the Charge Conjugation operator we see

$$P\bar{\psi}\psi P^{-1} = \gamma^0\psi^\dagger\gamma^0\psi\gamma^0 = \psi^\dagger\gamma^0\gamma^0\gamma^0\psi \tag{A.60}$$

and using the gamma matrix relations shows us that the Parity operator leaves $\bar{\psi}\psi$ unchanged. The same procedure can be used for the other term in the Lagrangian to show that it is invariant under parity and thus we have P symmetry.

A.3.3 Conclusions

It has been shown in the last two sections that the Dirac Lagrangian is invariant under C and P thus it is trivial to show that it is also invariant under CP. This leads us to CP conservation and symmetry. These proofs were given for scalar particles but the method can be extended to any type of particle but it is more in depth so it is not presented here. There were also assumptions made about applying this to the electromagnetic force which is thought to be CP conserving along with the strong force. It is reasonable to assume that this methodology could be applied to the weak force but Appendix B will outline violations of the work presented in this section.

One final part of this appendix, for completeness, is to show the effect of the CP operator on a Dirac spinor. This can be applied to any spinor with the same outcome. We show the CP operator to be

$$\mathrm{CP}\psi = i\gamma^2\gamma^0\psi^\star \tag{A.61}$$

and apply it to the spin-up particle from Equation 2.3 (neglecting the normalisation)

$$\begin{aligned}
\mathrm{CP}u_1 &= i\begin{pmatrix} 0 & 0 & 0 & -i \\ 0 & 0 & i & 0 \\ 0 & -i & 0 & 0 \\ i & 0 & 0 & 0 \end{pmatrix}\begin{pmatrix} 1 & 0 & 0 & 0 \\ 0 & 1 & 0 & 0 \\ 0 & 0 & -1 & 0 \\ 0 & 0 & 0 & -1 \end{pmatrix}\begin{pmatrix} 1 \\ 0 \\ \frac{p_3}{E+m} \\ \frac{p_1+ip_2}{E+m} \end{pmatrix} e^{i(p^\mu x_\mu)}, && \text{(A.62)} \\
\mathrm{CP}u_1 &= \begin{pmatrix} \frac{-(p_1\ -\ ip_2)}{E\ -\ m} \\ \frac{p_3}{E\ -\ m} \\ 0 \\ 1 \end{pmatrix} e^{-i(p^\mu x_\mu)}, && \text{(A.63)} \\
\mathrm{CP}u_1 &= -v_2. && \text{(A.64)}
\end{aligned}$$

It can be seen that the CP operator changes a spin-[up/down] particle to a spin-[down/up] antiparticle and vice-versa. It is hoped that this appendix explains the need for CP violation to explain the matter-antimatter asymmetry.

Appendix B

The Physics of Neutral Mesons

B.1 Neutral Meson Mixing

The Hamiltonian, $\mathcal{H}$, of a system can be expressed as

$$\mathcal{H} = \begin{pmatrix} m_{11} - \frac{i}{2}\Gamma_{11} & m_{12} - \frac{i}{2}\Gamma_{12} \\ m_{21} - \frac{i}{2}\Gamma_{21} & m_{22} - \frac{i}{2}\Gamma_{22} \end{pmatrix}. \tag{B.1}$$

If the off-diagonal elements are non-zero then a neutral meson can undergo oscillations whereby it can change between particle and antiparticle via charged current interactions. The mass eigenstate of the system will evolve according to the Schrödinger equation,

$$\mathcal{H} \begin{pmatrix} |P_1(t)\rangle \\ |P_2(t)\rangle \end{pmatrix} = i\frac{\partial}{\partial t} \begin{pmatrix} |P_1(t)\rangle \\ |P_2(t)\rangle \end{pmatrix}. \tag{B.2}$$

The state can be split into time and space components so that equation B.2 becomes

$$\mathcal{H} \begin{pmatrix} a(t)|P_1\rangle \\ b(t)|P_2\rangle \end{pmatrix} = i\frac{\partial}{\partial t} \begin{pmatrix} a(t)|P_1\rangle \\ b(t)|P_2\rangle \end{pmatrix}, \tag{B.3}$$

where a(t) and b(t) tell us the amplitude of $|P_1(t)\rangle$ and $|P_2(t)\rangle$ at time t respectively. This results in two equations of motion,

$$(m_1 - \frac{i}{2}\Gamma_1)a(t)|P_1\rangle = i\frac{d}{dt}a(t)|P_1\rangle, \tag{B.4}$$

$$(m_2 - \frac{i}{2}\Gamma_2)b(t)|P_2\rangle = i\frac{d}{dt}b(t)|P_2\rangle, \tag{B.5}$$

where m_1 and m_2 are found from solving the eigenvalue equation of Equation B.1. These result in

$$\frac{da(t)}{dt} = -i(m_1 - \frac{i}{2}\Gamma_1)a(t), \tag{B.6}$$

$$\frac{db(t)}{dt} = -i(m_2 - \frac{i}{2}\Gamma_2)b(t). \tag{B.7}$$

If we then solve these via separation of variables from the point of particle creation to a time t we have

$$\int\limits_{a(0)}^{a(t)} \frac{da(t')}{a(t')} = -i\int\limits_{0}^{t}(m_1 - \frac{i}{2}\Gamma_1)dt', \tag{B.8}$$

$$\int\limits_{b(0)}^{b(t)} \frac{db(t')}{b(t')} = -i\int\limits_{0}^{t}(m_2 - \frac{i}{2}\Gamma_2)dt' \tag{B.9}$$

which results in

$$a(t) = a(0)e^{-i(m_1 - \frac{i}{2}\Gamma_1)t} = e^{-i(m_1 - \frac{i}{2}\Gamma_1)t}, \tag{B.10}$$

$$b(t) = b(0)e^{-i(m_2 - \frac{i}{2}\Gamma_2)t} = e^{-i(m_2 - \frac{i}{2}\Gamma_2)t}. \tag{B.11}$$

If the mass eigenstates, $|P_{1,2}\rangle$, exist as a linear superposition of the weak eigenstates, $|P^0\rangle$ and $|\bar{P}^0\rangle$, such that

$$|P_1\rangle = p|P^0\rangle + q|\bar{P}^0\rangle \tag{B.12}$$

and

$$|P_2\rangle = p|P^0\rangle - q|\bar{P}^0\rangle, \tag{B.13}$$

where p is the weak amplitude of particle $|P^0\rangle$ and q is the weak amplitude of antiparticle $|\bar{P}^0\rangle$ which satisfy $|p|^2 + |q|^2 = 1$. The time evolution of the neutral meson is thus

$$|P^0(t)\rangle = \frac{1}{2p}\left(|P_1(t)\rangle + |P_2(t)\rangle\right), \tag{B.14}$$

$$|\bar{P}^0(t)\rangle = \frac{1}{2q}\left(|P_1(t)\rangle - |P_2(t)\rangle\right). \tag{B.15}$$

Substituting Equation B.10 and B.11 gives

$$|P^0(t)\rangle = \frac{1}{2p}\left(e^{-i(m_1\ -\ \frac{i}{2}\Gamma_1)t}|P_1\rangle + e^{-i(m_2\ -\ \frac{i}{2}\Gamma_2)t}|P_2\rangle\right), \tag{B.16}$$

$$|\bar{P}^0(t)\rangle = \frac{1}{2q}\left(e^{-i(m_1\ -\ \frac{i}{2}\Gamma_1)t}|P_1(t)\rangle\ -\ e^{-i(m_2\ -\ \frac{i}{2}\Gamma_2)t}|P_2(t)\rangle\right). \tag{B.17}$$

If we substitute equations B.12 and B.13 into equations B.16 and B.17 respectively, we find

$$|P^0(t)\rangle = \frac{1}{2p}\left(e^{-i(m_1\ -\ \frac{i}{2}\Gamma_1)t}(p|P^0\rangle + q|\bar{P}^0\rangle) + e^{-i(m_2\ -\ \frac{i}{2}\Gamma_2)t}(p|P^0\rangle\ -\ q|\bar{P}^0\rangle)\right) \tag{B.18}$$

$$|\bar{P}^0(t)\rangle = \frac{1}{2q}\left(e^{-i(m_1\ -\ \frac{i}{2}\Gamma_1)t}(p|P^0\rangle + q|\bar{P}^0\rangle)\ -\ e^{-i(m_2\ -\ \frac{i}{2}\Gamma_2)t}(p|P^0\rangle\ -\ q|\bar{P}^0\rangle)\right). \tag{B.19}$$

If we define

$$f_{\pm}(t) = \frac{1}{2}\left(e^{-i(m_1\ -\ \frac{i}{2}\Gamma_1)t} \pm e^{-i(m_2\ -\ \frac{i}{2}\Gamma_2)t}\right), \tag{B.20}$$

then we can simplify equations B.18 and B.19 to

$$|P^0(t)\rangle = f_+(t)|P^0\rangle + \frac{q}{p}f_-(t)|\bar{P}^0\rangle \tag{B.21}$$

$$|\bar{P}^0(t)\rangle = \frac{p}{q}f_-(t)|P^0\rangle + f_+(t)|\bar{P}^0\rangle. \tag{B.22}$$

B.2 The Decays of Neutral Mesons

The decay rate, Γ_f, to a final state, $\langle f|$, given an initial state, $|P^0(t)\rangle$, is

$$\Gamma_f = |\langle f|\mathcal{H}|P^0(t)\rangle|^2, \tag{B.23}$$

with a corresponding decay rate, $\bar{\Gamma}_f$, from the state , $|\bar{P}^0(t)\rangle$

$$\bar{\Gamma}_f = |\langle f|\mathcal{H}|\bar{P}^0(t)\rangle|^2. \tag{B.24}$$

We can solve the inner product, $\langle f|\mathcal{H}|P^0(t)\rangle$, using the relationships found above so that

$$\langle f|\mathcal{H}|P^0(t)\rangle = f_+(t)\langle f|\mathcal{H}|P^0\rangle + \frac{q}{p}f_-(t)\langle f|\mathcal{H}|\bar{P}^0\rangle. \tag{B.25}$$

If we define the decay amplitudes, A_f and $\bar{A}_f$, and the eigenvalue, λ, as

$$A_f = \langle f|\mathcal{H}|P^0\rangle, \tag{B.26}$$

$$\bar{A}_f = \langle f|\mathcal{H}|\bar{P}^0\rangle \tag{B.27}$$

and

$$\lambda = \frac{q}{p}\frac{\bar{A}_f}{A_f} = \left|\frac{q}{p}\right|\left|\frac{\bar{A}_f}{A_f}\right| e^{i(\phi_{\frac{q}{p}}+\phi_{\bar{A}_f}\ -\ \phi_{A_f})}, \tag{B.28}$$

where ϕ_x is the phase of quantity x then

$$\langle f|\mathcal{H}|P^0(t)\rangle = f_+(t)A_f + \frac{q}{p}f_-(t)\bar{A}_f = A_f(f_+(t) + \lambda f_-(t)). \tag{B.29}$$

The decay rate then becomes

$$\Gamma_f = |A_f|^2||f_+(t) + \lambda f_-(t)|^2 = |A_f|^2|(|f_+(t)|^2 + |f_-(t)|^2 + 2f_+(t)f_-(t)). \tag{B.30}$$

We can find $|f_\pm(t)|^2$ by

$$|f_\pm(t)|^2 = \frac{1}{4}\left|e^{-i(m_1\ -\ \frac{i}{2}\Gamma_1)t} \pm e^{-i(m_2\ -\ \frac{i}{2}\Gamma_2)t}\right|^2, \tag{B.31}$$

$$|f_\pm(t)|^2 = \frac{1}{4}\left(e^{-\Gamma_1 t} + e^{-\Gamma_2 t} \pm e^{-i(m_1-m_2)t}e^{-\frac{1}{2}(\Gamma_1+\Gamma_2)t} \pm e^{i(m_1-m_2)t}e^{-\frac{1}{2}(\Gamma_1+\Gamma_2)t}\right)^2. \tag{B.32}$$

If we define $\Delta m = m_1 - m_2, \bar{\Gamma} = \frac{1}{2}(\Gamma_1 + \Gamma_2)$ and use Euler's formula:

$$|f_\pm(t)|^2 = \frac{1}{4}\left(e^{-\Gamma_1 t} + e^{-\Gamma_2 t} \pm 2\cos(\Delta m t)e^{-\bar{\Gamma}t}\right). \tag{B.33}$$

Using the same method for $f_+(t)f_-(t)$ we find that

$$f_+(t)f_-(t) = \frac{1}{4}\left(e^{-\Gamma_1 t}\ -\ e^{-\Gamma_2 t}\ -\ 2i\sin(\Delta m t)e^{-\bar{\Gamma}t}\right). \tag{B.34}$$

We can now substitute equations B.33 and B.34 into equation B.30 to see

$$\begin{aligned}\Gamma_f \quad = \quad & \frac{|A_f|^2}{4}\left[\left(e^{-\Gamma_1 t} + e^{-\Gamma_2 t}\right)\left(1 + |\lambda|^2\right) + 2\cos(\Delta m t)e^{-\bar{\Gamma}t}\left(1 - |\lambda|^2\right)\right. \\ & \left. +2\lambda\left(e^{-\Gamma_1 t} - e^{-\Gamma_2 t} - 2i\sin(\Delta m t)e^{-\bar{\Gamma}t}\right)\right], \end{aligned} \tag{B.35}$$

$$\begin{aligned}\Gamma_f &= \frac{|A_f|^2}{2}\left(1+|\lambda|^2\right)\left[\frac{1}{2}\left(e^{-\Gamma_1 t}+e^{-\Gamma_2 t}\right)+\frac{1-|\lambda|^2}{1+|\lambda|^2}\cos(\Delta m t)e^{-\bar{\Gamma}t}\right.\\ &\left.+\frac{\lambda}{1+|\lambda|^2}\left(e^{-\Gamma_1 t}-e^{-\Gamma_2 t}-2i\sin(\Delta m t)e^{-\bar{\Gamma}t}\right)\right]. \qquad \text{(B.36)}\end{aligned}$$

If we define $\Delta\Gamma = \Gamma_2 - \Gamma_1$ and note that

$$e^{-\Gamma_1 t+\bar{\Gamma}t} = e^{-\Gamma_1 t+\frac{1}{2}\Gamma_1 t+\frac{1}{2}\Gamma_2 t} = e^{-\frac{\Delta\Gamma t}{2}} \qquad \text{(B.37)}$$

and

$$e^{-\Gamma_2 t+\bar{\Gamma}t} = e^{-\Gamma_2 t+\frac{1}{2}\Gamma_1 t+\frac{1}{2}\Gamma_2 t} = e^{\frac{\Delta\Gamma t}{2}} \qquad \text{(B.38)}$$

then we can simplify equation B.36 to

$$\begin{aligned}\Gamma_f &= \frac{|A_f|^2}{2}\left(1+|\lambda|^2\right)e^{-\bar{\Gamma}t}\left[\cosh(\frac{\Delta\Gamma t}{2})+\frac{1-|\lambda|^2}{1+|\lambda|^2}\cos(\Delta m t)\right.\\ &\left.+\frac{\lambda}{1+|\lambda|^2}\left(2\sinh(\frac{\Delta\Gamma t}{2})-2i\sin(\Delta m t)\right)\right]. \qquad \text{(B.39)}\end{aligned}$$

If we define

$$I(t) = \frac{1-|\lambda|^2}{1+|\lambda|^2}\cos(\Delta m t) - \frac{2Im(\lambda)}{1+|\lambda|^2}\sin(\Delta m t) \qquad \text{(B.40)}$$

and

$$H(t) = \cosh(\frac{\Delta\Gamma t}{2}) + \frac{2Re(\lambda)}{1+|\lambda|^2}\sinh(\frac{\Delta\Gamma t}{2}) \qquad \text{(B.41)}$$

then

$$\Gamma_f = \frac{|A_f|^2}{2}\left(1+|\lambda|^2\right)e^{-\bar{\Gamma}t}\left[H(t)+I(t)\right]. \qquad \text{(B.42)}$$

Repeating this method for $\bar{\Gamma}_f$ yields

$$\bar{\Gamma}_f = \frac{|\bar{A}_f|^2}{2}\frac{1+|\lambda|^2}{|\lambda|^2}e^{-\bar{\Gamma}t}\left[H(t) - I(t)\right]. \qquad \text{(B.43)}$$

We can now see that the meson will oscillate from particle to antiparticle with a frequency given by Δm

B.3 CP Asymmetries

If we now define the CP asymmetry, A^{CP}, as:

$$A^{\mathrm{CP}} = \frac{\Gamma_f - \bar{\Gamma}_f}{\Gamma_f + \bar{\Gamma}_f} \qquad \text{(B.44)}$$

and use equations B.42 and B.43 we can find a quantitative answer for A^{CP}

$$A^{\mathrm{CP}} = \frac{|A_f|^2[H(t)+I(t)] \; - \; \frac{|\bar{A}_f|^2}{|\lambda|^2}[H(t) \; - \; I(t)]}{|A_f|^2[H(t)+I(t)] + \frac{|\bar{A}_f|^2}{|\lambda|^2}[H(t) \; - \; I(t)]} \tag{B.45}$$

$$A^{\mathrm{CP}} = \frac{(|A_f|^2 - \frac{|\bar{A}_f|^2}{|\lambda|^2})H(t) + (|A_f|^2 + \frac{|\bar{A}_f|^2}{|\lambda|^2})I(t)]}{(|A_f|^2 + \frac{|\bar{A}_f|^2}{|\lambda|^2})H(t) + (|A_f|^2 - \frac{|\bar{A}_f|^2}{|\lambda|^2})I(t)]} \tag{B.46}$$

$$A^{\mathrm{CP}} = \frac{I(t) + \frac{|A_f|^2 - \frac{|\bar{A}_f|^2}{|\lambda|^2}}{|A_f|^2 + \frac{|\bar{A}_f|^2}{|\lambda|^2}} H(t)}{H(t) + \frac{|A_f|^2 - \frac{|\bar{A}_f|^2}{|\lambda|^2}}{|A_f|^2 + \frac{|\bar{A}_f|^2}{|\lambda|^2}} I(t)}. \tag{B.47}$$

If we use equation B.28 to simplify, then

$$A^{\mathrm{CP}} = \frac{I(t) + \frac{|\frac{q}{p}|^2 \; - \; 1}{|\frac{q}{p}|^2 + 1} H(t)}{H(t) + \frac{|\frac{q}{p}|^2 \; - \; 1}{|\frac{q}{p}|^2 + 1} I(t)}. \tag{B.48}$$

Although $|p|^2 \neq |q|^2, |q|^2/|p|^2 \approx 1$ so that equation B.48 becomes

$$A^{\mathrm{CP}} = \frac{I(t)}{H(t)} \tag{B.49}$$

or

$$A^{\mathrm{CP}}(t) = \frac{S_f \sin(\Delta m t) \; - \; C_f \cos(\Delta m t)}{\cosh\left(\frac{\Delta\Gamma}{2}t\right) + \mathcal{A}_f^{\Delta\Gamma} \sinh\left(\frac{\Delta\Gamma}{2}t\right)} \tag{B.50}$$

where the observables C_f, S_f and $\mathcal{A}_f^{\Delta\Gamma}$ are

$$C_f = \frac{1 - |\lambda|^2}{(1 + |\lambda|^2)} = \frac{1 - \left(\left|\frac{q}{p}\right| \left|\frac{\bar{A}_f}{A_f}\right|\right)^2}{1 + \left(\left|\frac{q}{p}\right| \left|\frac{\bar{A}_f}{A_f}\right|\right)^2}, \tag{B.51}$$

$$S_f = \frac{2Im(\lambda)}{(1 + |\lambda|^2)} = \frac{2\left|\frac{q}{p}\right| \left|\frac{\bar{A}_f}{A_f}\right| \sin(\phi_{\frac{q}{p}} + \phi_{\bar{A}_f} \; - \; \phi_{A_f})}{1 + \left(\left|\frac{q}{p}\right| \left|\frac{\bar{A}_f}{A_f}\right|\right)^2}, \tag{B.52}$$

$$\mathcal{A}_f^{\Delta\Gamma} = \frac{-2Re(\lambda)}{(1 + |\lambda|^2)} = \frac{-2\left|\frac{q}{p}\right| \left|\frac{\bar{A}_f}{A_f}\right| \cos(\phi_{\frac{q}{p}} + \phi_{\bar{A}_f} \; - \; \phi_{A_f})}{1 + \left(\left|\frac{q}{p}\right| \left|\frac{\bar{A}_f}{A_f}\right|\right)^2}. \tag{B.53}$$

It can be seen that these oscillations can result in an excess of one final state over another. Using the definition of the observables, we can rewrite Equations B.42

and B.43 as

$$\Gamma_f = e^{-\Gamma t}\left[\cosh\left(\frac{\Delta\Gamma}{2}t\right) + \mathcal{A}_f^{\Delta\Gamma}\sinh\left(\frac{\Delta\Gamma}{2}t\right) + C_f\cos(\Delta m t) \;-\; S_f\sin(\Delta m t)\right] \tag{B.54}$$

$$\bar{\Gamma}_f = e^{-\Gamma t}\left[\cosh\left(\frac{\Delta\Gamma}{2}t\right) + \mathcal{A}_f^{\Delta\Gamma}\sinh\left(\frac{\Delta\Gamma}{2}t\right) \;-\; C_f\cos(\Delta m t) + S_f\sin(\Delta m t)\right]. \tag{B.55}$$

B.4 CP Observables in the Standard Model

In the Standard Model, it is trivial to show that the sum of the square of the CP observables should be one. Using Equations B.51 to B.53, this means that

$$(C_f)^2 + (S_f)^2 + (\mathcal{A}_f^{\Delta\Gamma})^2 = 1 \tag{B.56}$$

$$\begin{aligned}
1 &= \frac{\left[1-\left(\left|\frac{q}{p}\right|\left|\frac{\bar{A}_f}{A_f}\right|\right)^2\right]^2 + 4\left(\left|\frac{q}{p}\right|\left|\frac{\bar{A}_f}{A_f}\right|\right)^2\left(\sin^2\phi+\cos^2\phi\right)}{\left[1+\left(\left|\frac{q}{p}\right|\left|\frac{\bar{A}_f}{A_f}\right|\right)^2\right]^2} && \text{(B.57)}\\
&= \frac{1+2\left(\left|\frac{q}{p}\right|\left|\frac{\bar{A}_f}{A_f}\right|\right)^2 + \left(\left|\frac{q}{p}\right|\left|\frac{\bar{A}_f}{A_f}\right|\right)^4}{\left[1+\left(\left|\frac{q}{p}\right|\left|\frac{\bar{A}_f}{A_f}\right|\right)^2\right]^2} && \text{(B.58)}\\
&= \frac{\left[1+\left(\left|\frac{q}{p}\right|\left|\frac{\bar{A}_f}{A_f}\right|\right)^2\right]^2}{\left[1+\left(\left|\frac{q}{p}\right|\left|\frac{\bar{A}_f}{A_f}\right|\right)^2\right]^2}. && \text{(B.59)}
\end{aligned}$$

Appendix C

Background Contaminations in $B \rightarrow h^+ h'^-$ Decays

As particle identifications are based on likelihood distributions then it is possible to misidentify one or both daughters in the selection of the candidates. In the two analyses discussed in the thesis the dominant source of these decays is believed to be due to other $B \rightarrow h^+ h'^-$ channels (excluding $B^0 \rightarrow p\bar{p}$ decays which have a branching fraction of $(1.25 \pm 0.32) \times 10^{-8}$ compared to the branching fractions of the other $B \rightarrow h^+ h'^-$ decays which are of order $\mathcal{O}(10^{-6})$ to $\mathcal{O}(10^{-5})$ [149]). An event-by-event mistag efficiency was calculated using the same method to estimate the signal efficiencies detailed in Section 7.1.2 using dedicated samples of the background decays. The relative contamination, k^{mid}_{chann}, of these backgrounds in each final state was quantified for each cut combination, where *chann* is the channel being probed and *mid* is the mis-identified channel contaminating the signal. The generic form of the equation for obtaining the contamination fraction is

$$k^{mid}_{chann} = \frac{f_{mid}}{f_{chann}} \frac{\mathcal{B}_{mid}}{\mathcal{B}_{chann}} \frac{\omega_{mid}}{\varepsilon_{chann}} \tag{C.1}$$

where f_P is the hadronization fraction of the mother particle, $\mathcal{B}_P$ is the branching fraction of the decay, ω_{mid} is the MID efficiency and ε_{chann} is the signal efficiency. The MID is calculated by passing MC samples of other similar decays through the same selection requirements as the signal class. The measured contamination of these backgrounds with respect to the signal channels investigated are given in Figures C.1 to C.7.

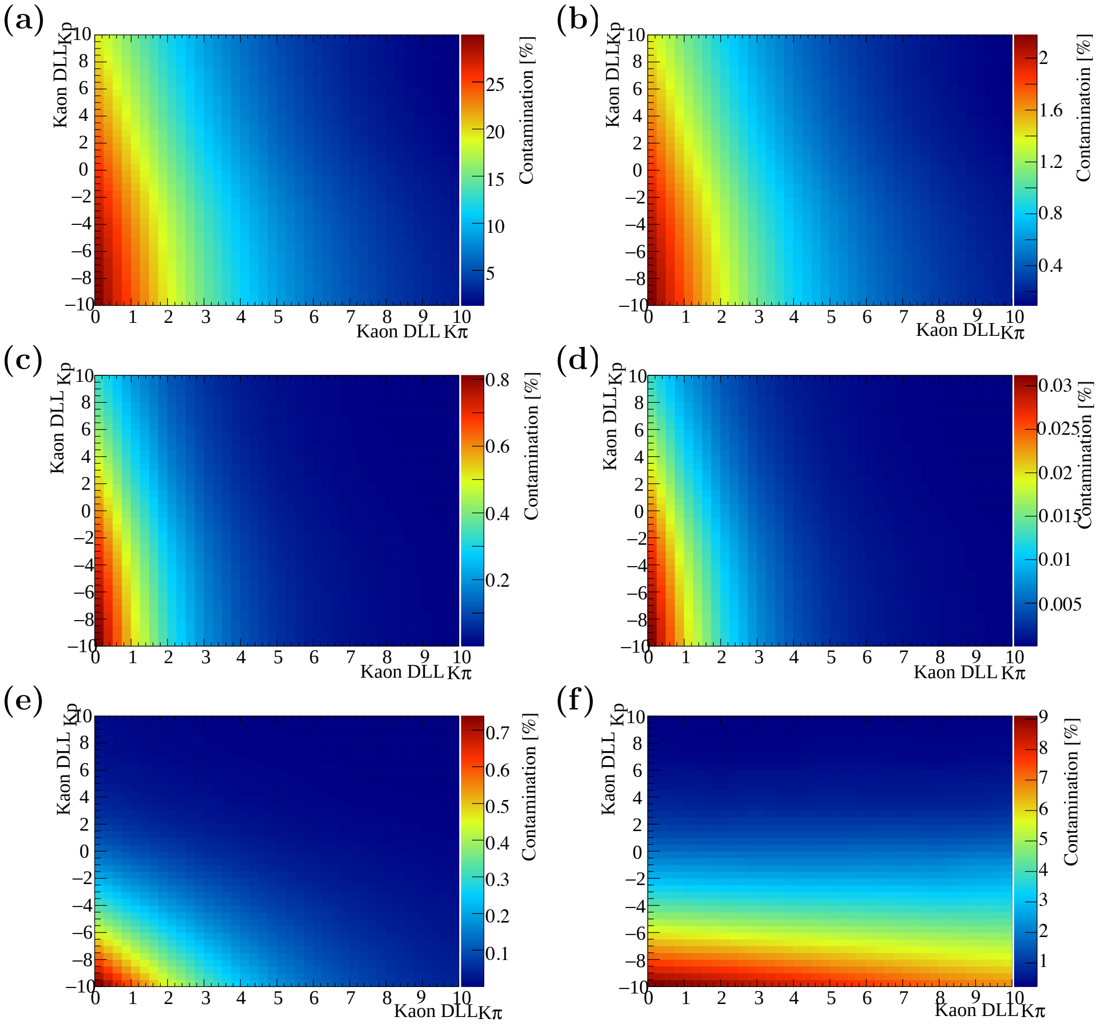

FIGURE C.1: 2D phase space distributions of background contaminations with respect to the $B_s^0 \to K^+K^-$ signal using 2012 MC. (a) $B^0 \to K^+\pi^-$ contamination. (b) $B_s^0 \to \pi^+K^-$ contamination. (c) $B^0 \to \pi^+\pi^-$ contamination. (d) $B_s^0 \to \pi^+\pi^-$ contamination. (e) $\Lambda_b^0 \to p\pi^-$ contamination. (f) $\Lambda_b^0 \to pK^-$ contamination.

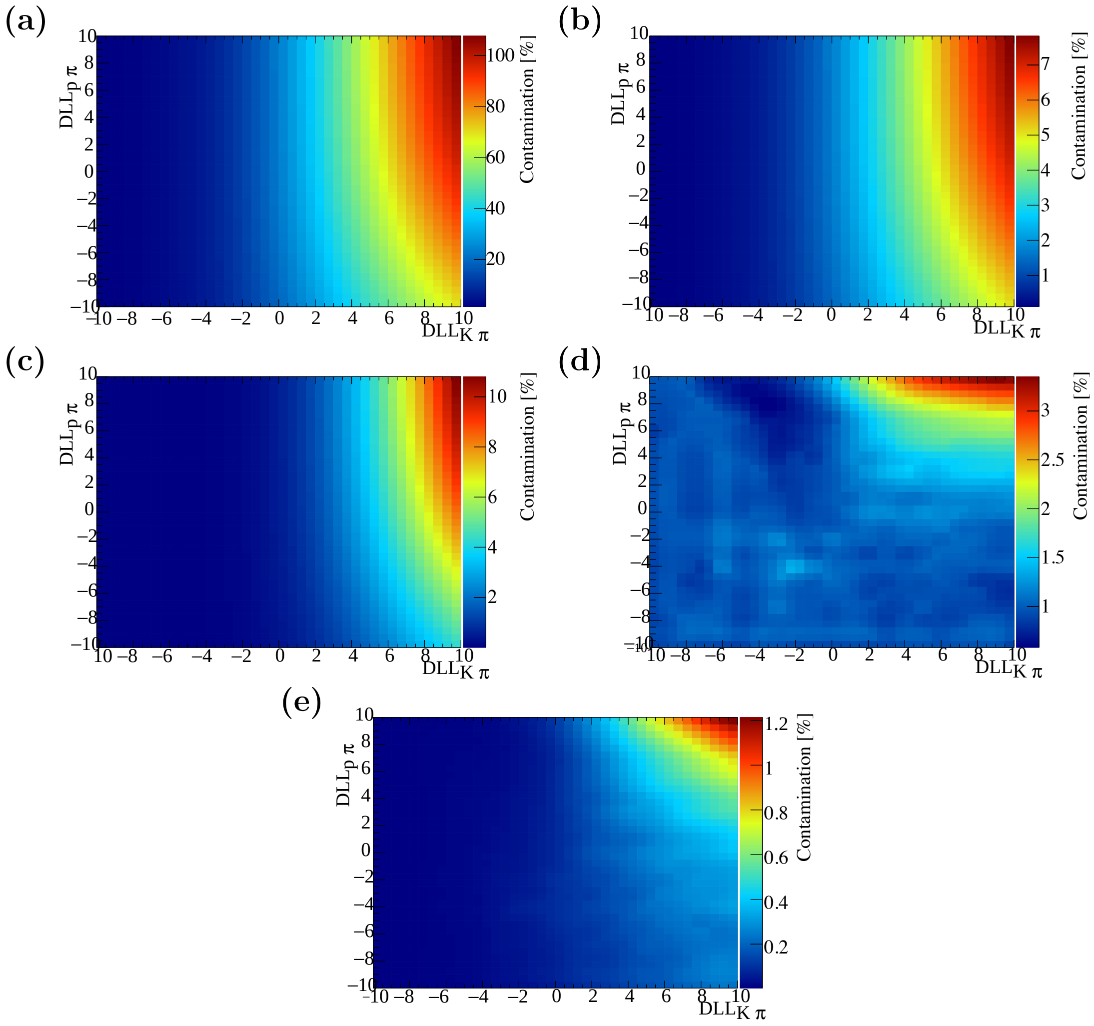

FIGURE C.2: 2D phase space distributions of background contaminations with respect to the $B^0 \rightarrow \pi^+\pi^-$ signal using 2012 MC. (a) $B^0 \rightarrow K^+\pi^-$ contamination. (b) $B^0_s \rightarrow \pi^+K^-$ contamination. (c) $B^0 \rightarrow K^+K^-$ contamination. (d) $\Lambda^0_b \rightarrow p\pi^-$ contamination. (e) $\Lambda^0_b \rightarrow pK^-$ contamination.

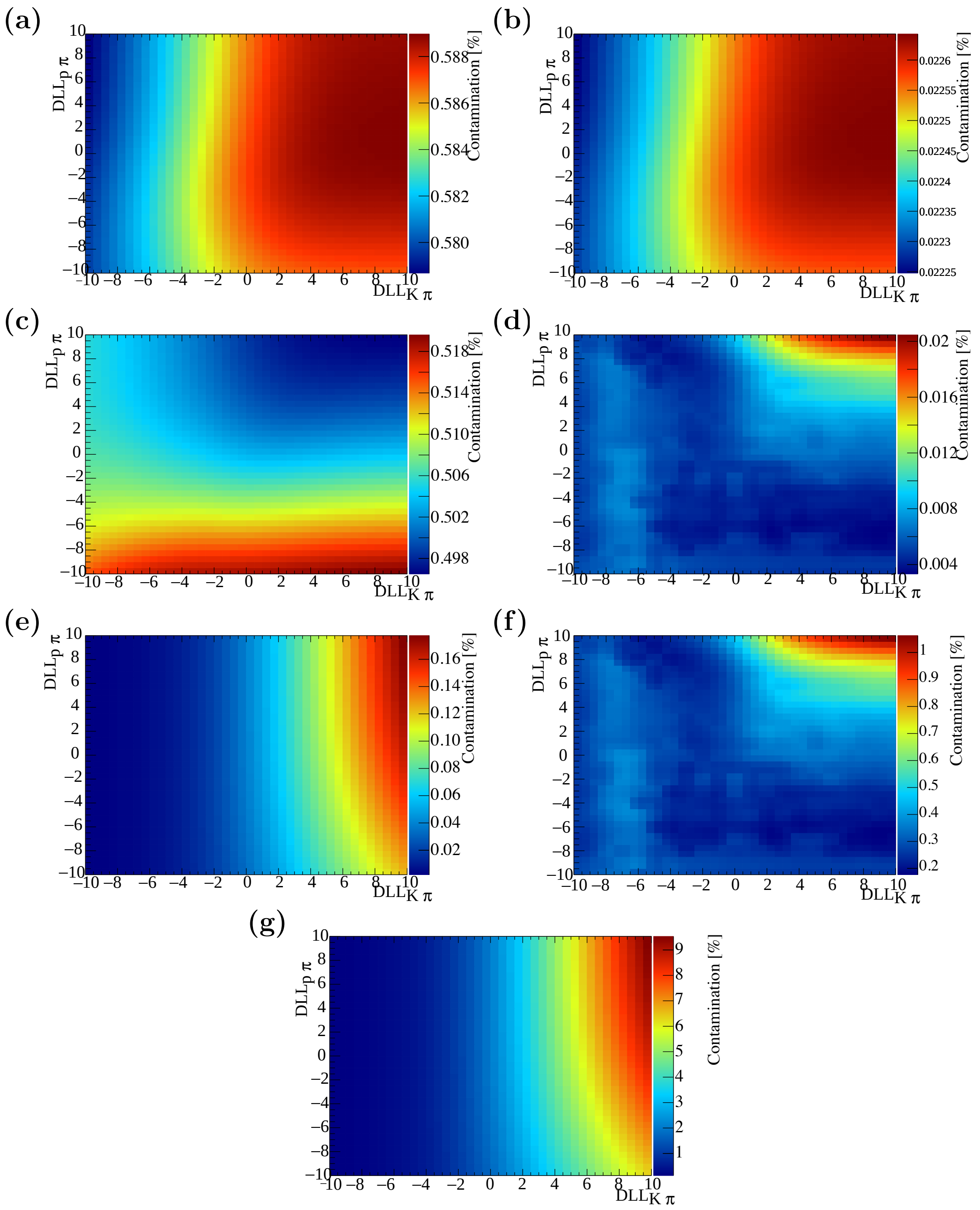

FIGURE C.3: 2D phase space distributions of background contaminations with respect to the $\mathrm{B}^0\to \mathrm{K}^+\pi^-$ signal using 2012 MC. (a) $\mathrm{B}^0\to\pi^+\pi^-$ contamination. (b) $\mathrm{B}^0_{\mathrm{s}}\to\pi^+\pi^-$ contamination. (c) $\Lambda^0_{\mathrm{b}}\to \mathrm{p}\pi^-$ contamination. (d) $\bar{\Lambda}^0_b\to\bar{p}\pi^+$ contamination. (e) $\Lambda^0_{\mathrm{b}}\to \mathrm{pK}^-$ contamination. (f) $\bar{\Lambda}^0_b\to\bar{p}K^+$ contamination. (g) $\mathrm{B}^0_{\mathrm{s}}\to \mathrm{K}^+\mathrm{K}^-$ contamination.

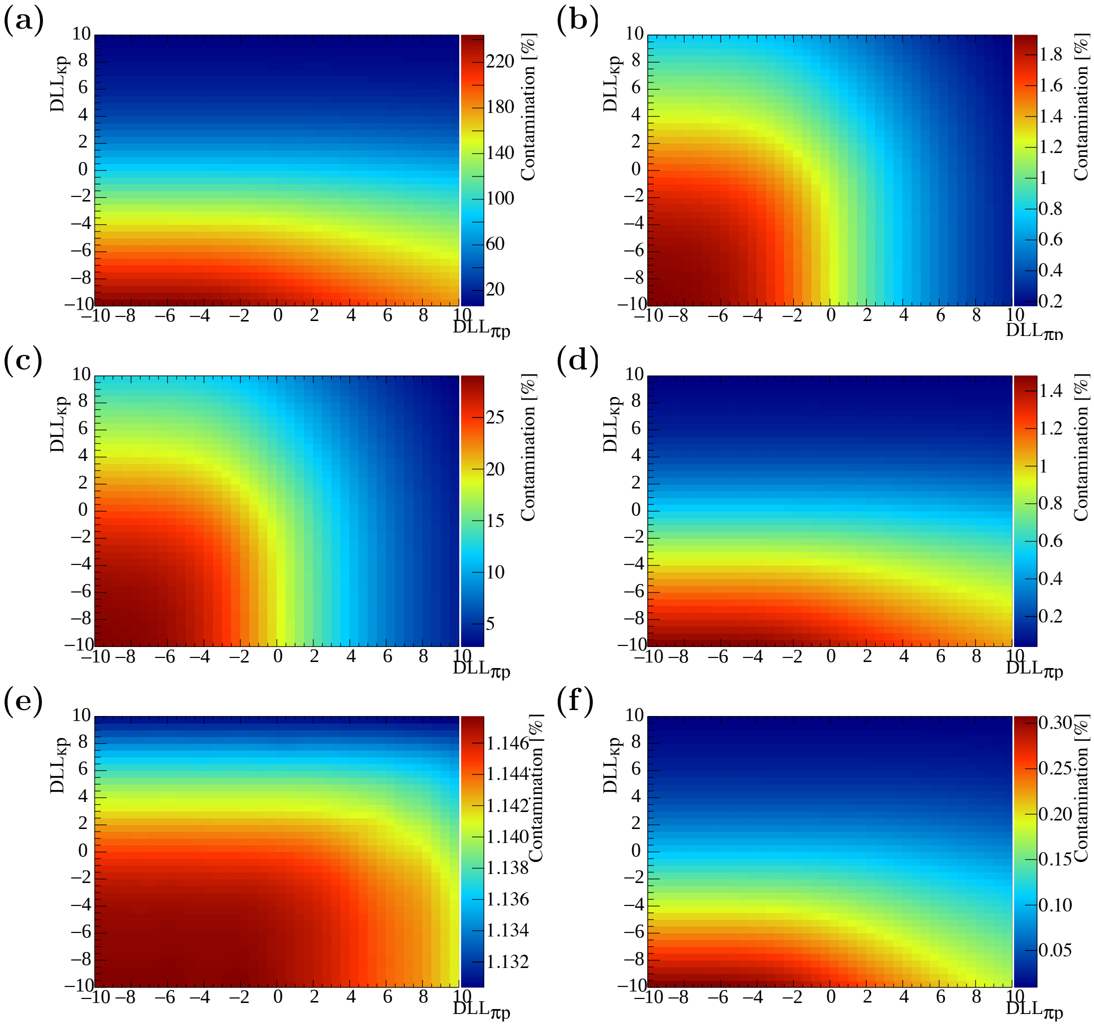

FIGURE C.4: 2D phase space distributions of background contaminations with respect to the $\Lambda_b^0 \to p\pi^-$ signal using 2012 MC. (a) $B^0 \to K^+\pi^-$ contamination. (b) $\bar{B}^0 \to K^-\pi^+$ contamination. (c) $B^0 \to \pi^+\pi^-$ contamination. (d) $B_s^0 \to K^+K^-$ contamination. (e) $\Lambda_b^0 \to pK^-$ contamination. (f) $\bar{\Lambda}_b^0 \to \bar{p}K^+$ contamination.

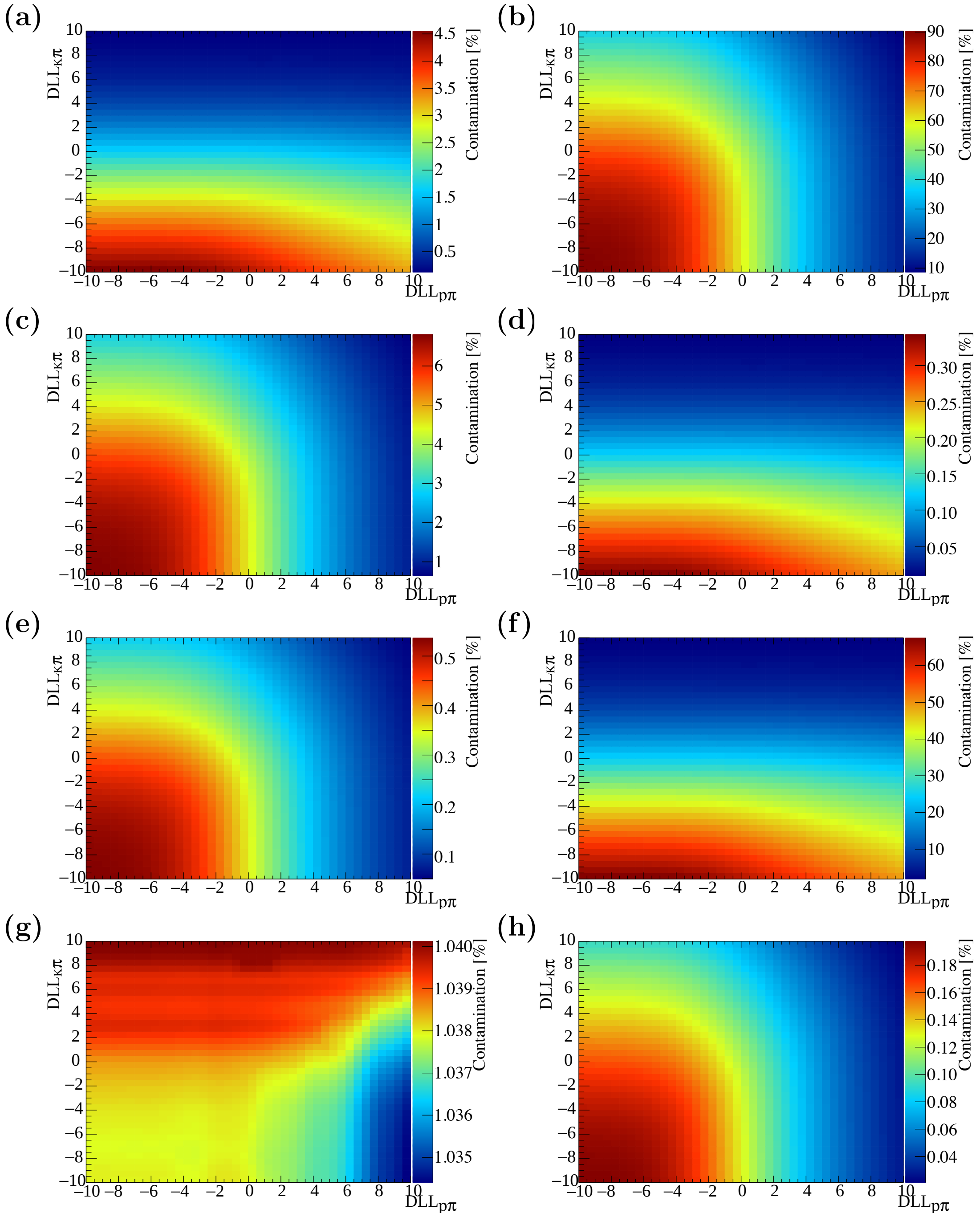

FIGURE C.5: 2D phase space distributions of background contaminations with respect to the $\Lambda_b^0 \to pK^-$ signal using 2012 MC. (a) $B^0 \to K^+\pi^-$ contamination. (b) $\bar{B}^0 \to K^-\pi^+$ contamination. (c) $B_s^0 \to \pi^+K^-$ contamination. (d) $\bar{B}_s^0 \to \pi^-Ki^+$ contamination. (e) $B^0 \to \pi^+\pi^-$ contamination. (f) $B_s^0 \to K^+K^-$ contamination. (g) $\Lambda_b^0 \to p\pi^-$ contamination. (h) $\bar{\Lambda}_b^0 \to \bar{p}\pi^+$ contamination.

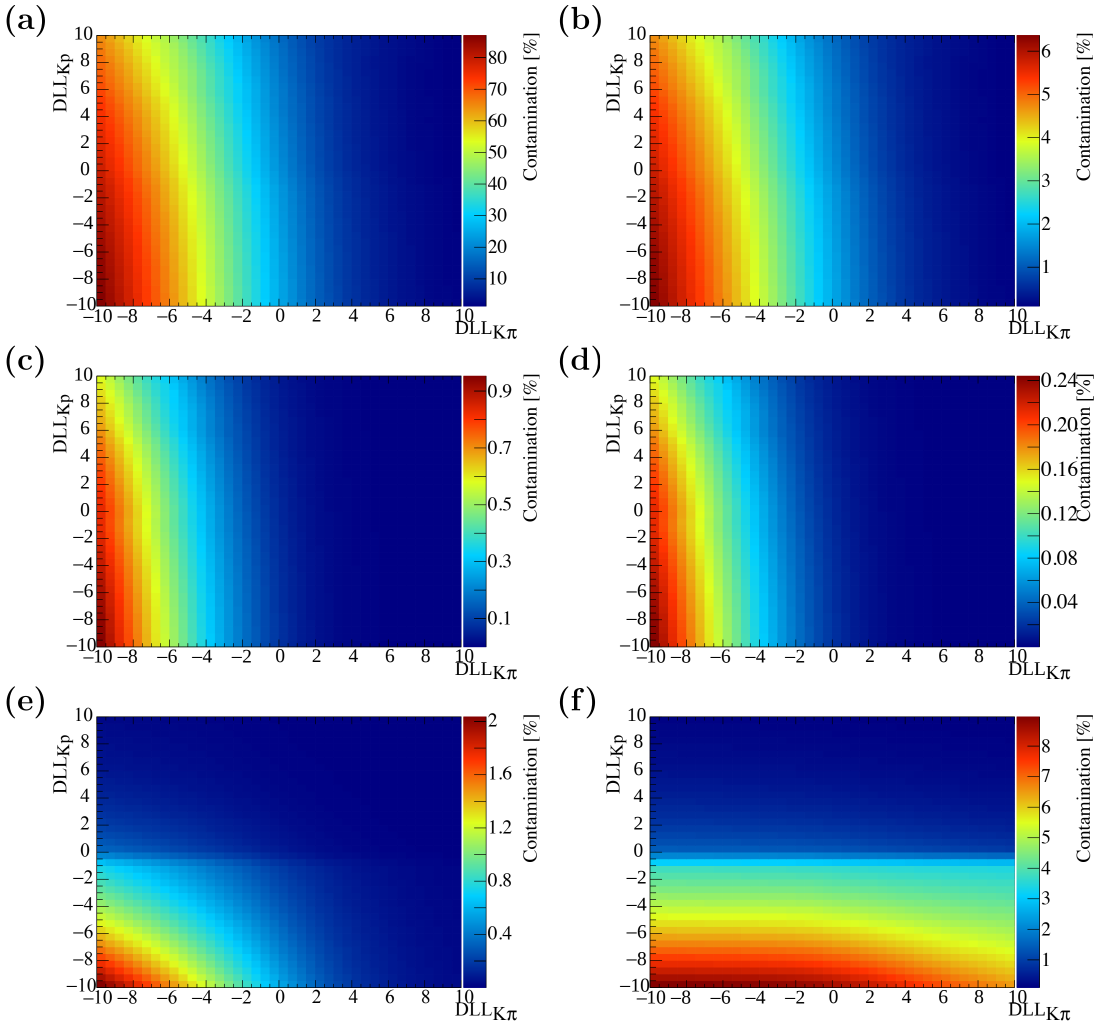

FIGURE C.6: 2D phase space distributions of background contaminations with respect to the $B_s^0 \rightarrow K^+K^-$ signal using 2016 MC. (a) $B^0 \rightarrow K^+\pi^-$ contamination. (b) $B_s^0 \rightarrow \pi^+K^-$ contamination. (c) $B^0 \rightarrow \pi^+\pi^-$ contamination. (d) $B_s^0 \rightarrow \pi^+\pi^-$ contamination. (e) $\Lambda_b^0 \rightarrow p\pi^-$ contamination. (f) $\Lambda_b^0 \rightarrow pK^-$ contamination.

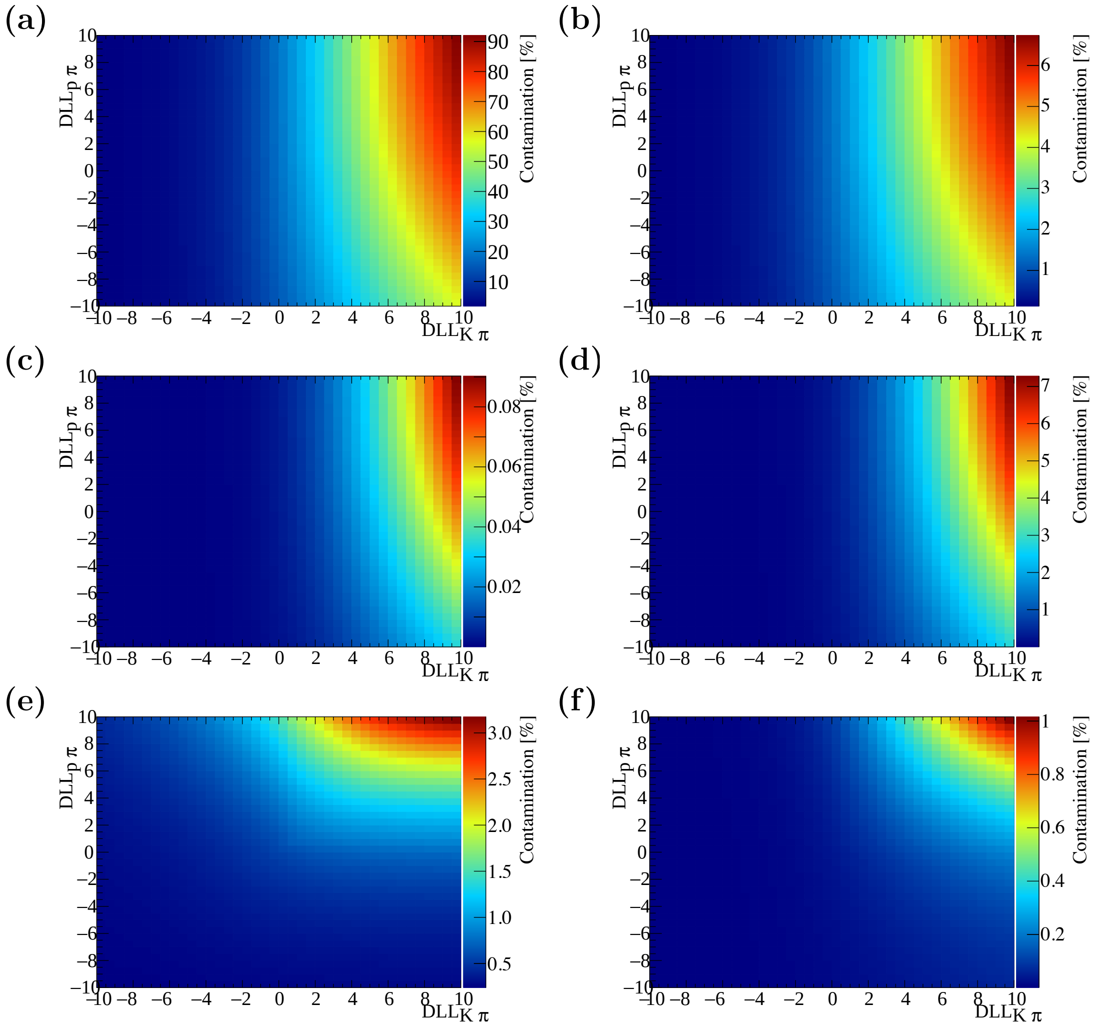

FIGURE C.7: 2D phase space distributions of background contaminations with respect to the $B^0 \to \pi^+\pi^-$ signal using 2016 MC. (a) $B^0 \to K^+\pi^-$ contamination. (b) $B^0_s \to \pi^+K^-$ contamination. (c) $B^0 \to K^+K^-$ contamination. (d) $B^0_s \to K^+K^-$ contamination. (e) $\Lambda^0_b \to p\pi^-$ contamination. (f) $\Lambda^0_b \to pK^-$ contamination.

Appendix D

Variable Studies For Selection Optimisation

To ensure the best possible sensitivity on the CP observables $S_{\pi\pi}$, $C_{\pi\pi}$, S_{KK}, C_{KK} and $\mathcal{A}^{\Delta\Gamma}_{\mathrm{KK}}$, the final candidate selection was determined through a simultaneous optimisation of the BDT used to reject combinatorial events and the $\Delta\log(\mathcal{L}_{K\pi})$ (PID) value used to reject kaon candidates in the $\pi^+\pi^-$ spectrum and pions in the $\mathrm{K}^+\mathrm{K}^-$ spectrum. Several parameters involved in the fit were studied at the four corners of the BDT and PID cut space to observe their variation. The cuts studied were

- The decay time distribution of the combinatorial background
- The decay time distribution of the partially reconstructed background
- The decay time error of the signal
- The decay time error of the combinatorial background
- The predicted mistag distribution of the signal
- The predicted mistag distribution of the combinatorial background

The results of this study are presented in Figures D.1 to D.5 for the $\mathrm{B}^0_\mathrm{s} \to \mathrm{K}^+\mathrm{K}^-$ optimisation [1].

---

[1] Due to kinematic similarities between the decays, the $\mathrm{B}^0 \to \pi^+\pi^-$ variables were assumed to show the same behaviour.

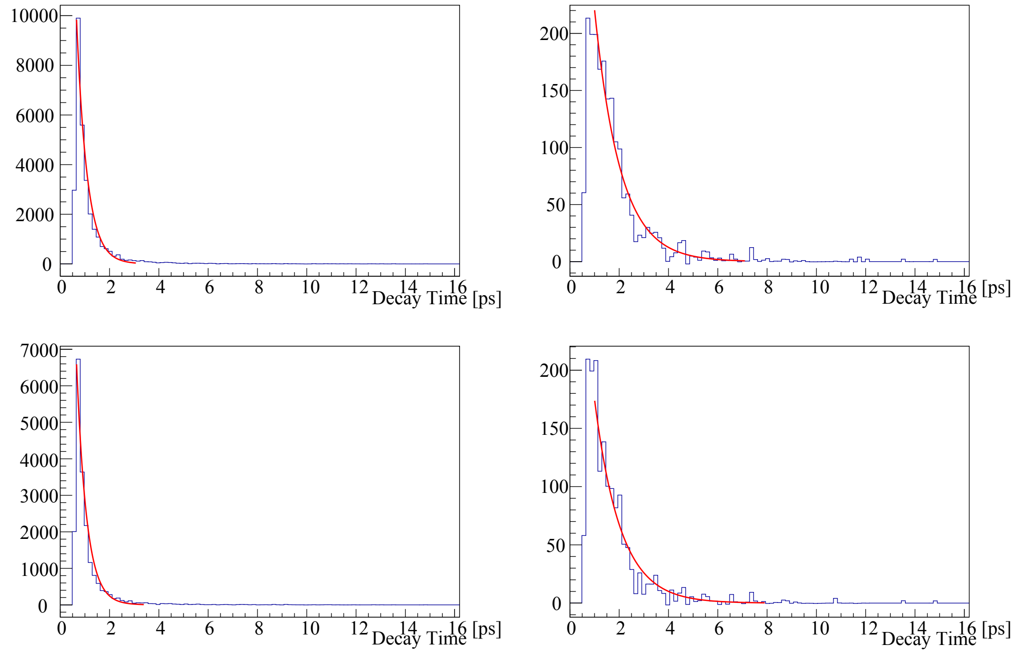

FIGURE D.1: The fit to the decay time distribution of the combinatorial background at the four corners of the kinematic variables for the selection optimisation study. Top Left - Fit for the loosest PID and BDT cut. Top Right - Fit for the loosest PID and tightest BDT cut. Bottom Left - Fit for the tightest PID and loosest BDT cut. Bottom Right - Fit for the tightest PID and BDT cut.

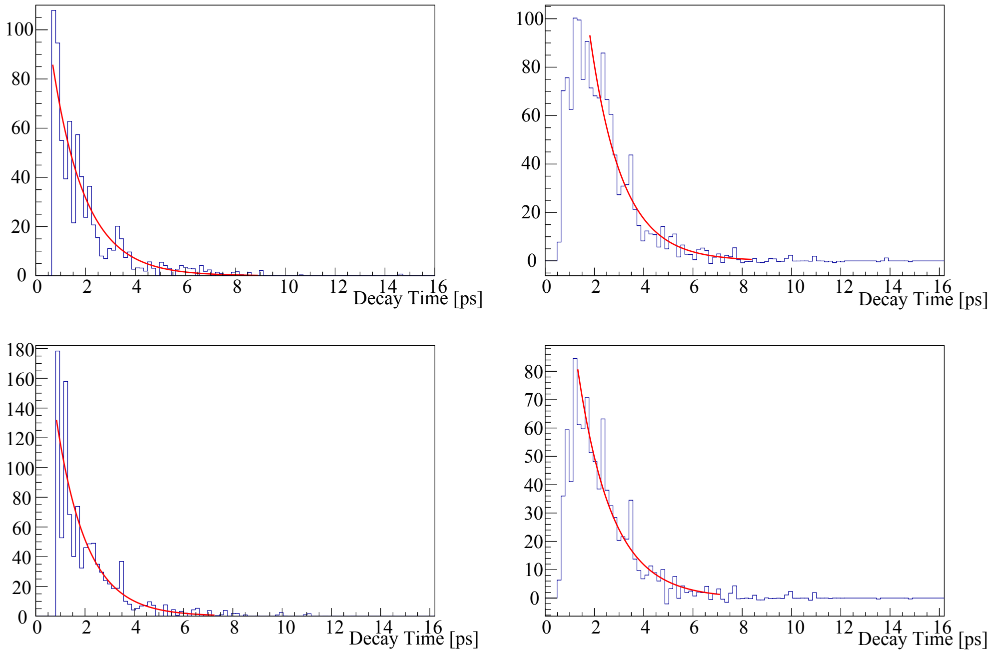

Figure D.2: The fit to the decay time distribution of the partially reconstructed background at the four corners of the kinematic variables for the selection optimisation study. Top Left - Fit for the loosest PID and BDT cut. Top Right - Fit for the loosest PID and tightest BDT cut. Bottom Left - Fit for the tightest PID and loosest BDT cut. Bottom Right - Fit for the tightest PID and BDT cut.

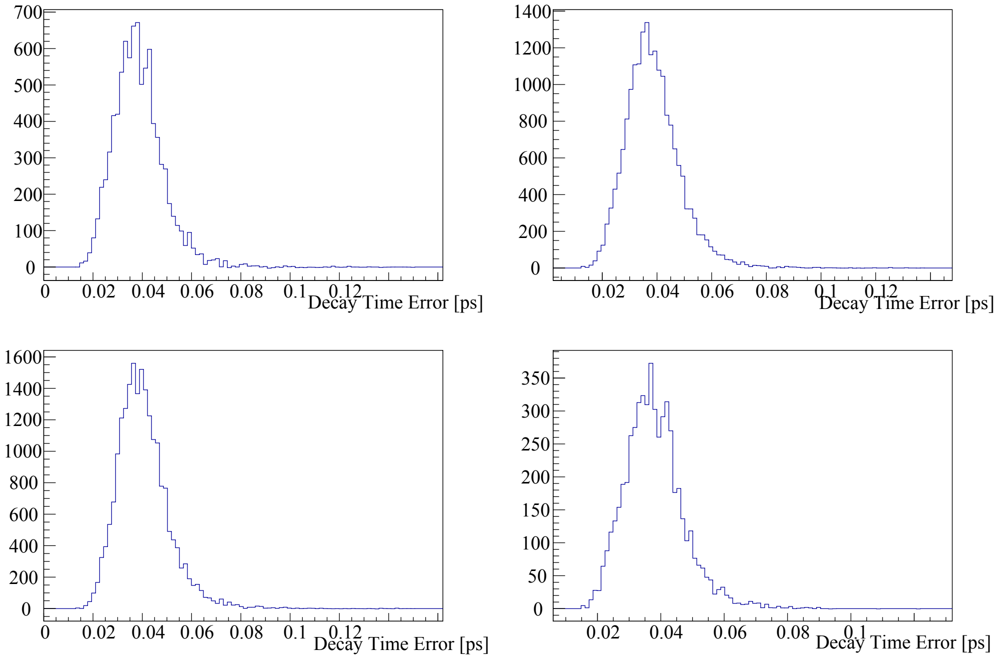

FIGURE D.3: The distribution of the decay time error of the signal at the four corners of the kinematic variables for the selection optimisation study. Top Left - Distribution for the loosest PID and BDT cut. Top Right - Distribution for the loosest PID and tightest BDT cut. Bottom Left - Distribution for the tightest PID and loosest BDT cut. Bottom Right - Distribution for the tightest PID and BDT cut.

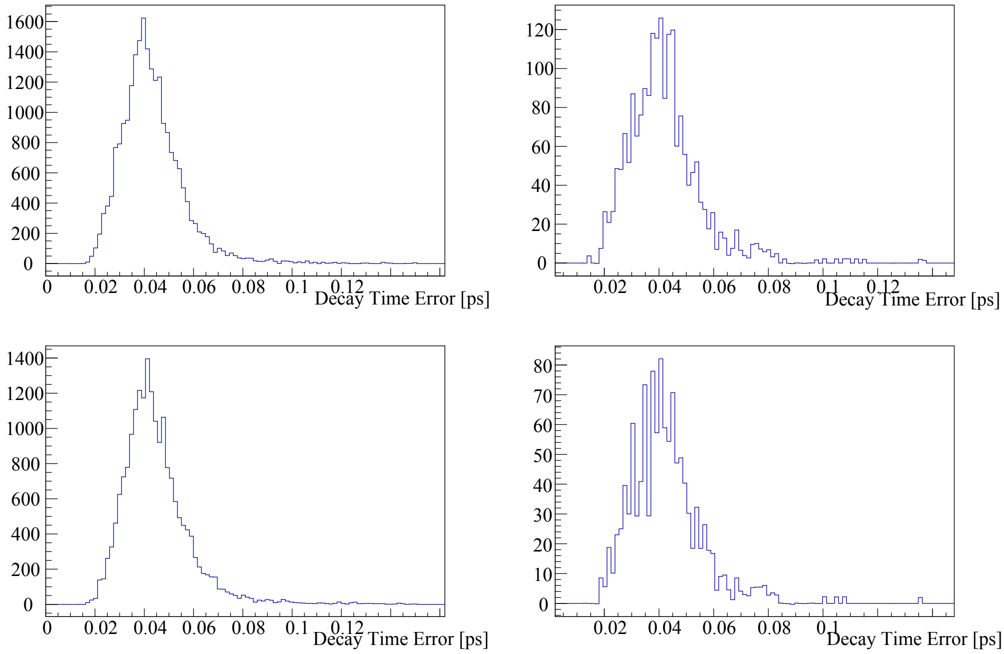

Figure D.4: The distribution of the decay time error of the combinatorial background at the four corners of the kinematic variables for the selection optimisation study. Top Left - Distribution for the loosest PID and BDT cut. Top Right - Distribution for the loosest PID and tightest BDT cut. Bottom Left - Distribution for the tightest PID and loosest BDT cut. Bottom Right - Distribution for the tightest PID and BDT cut.

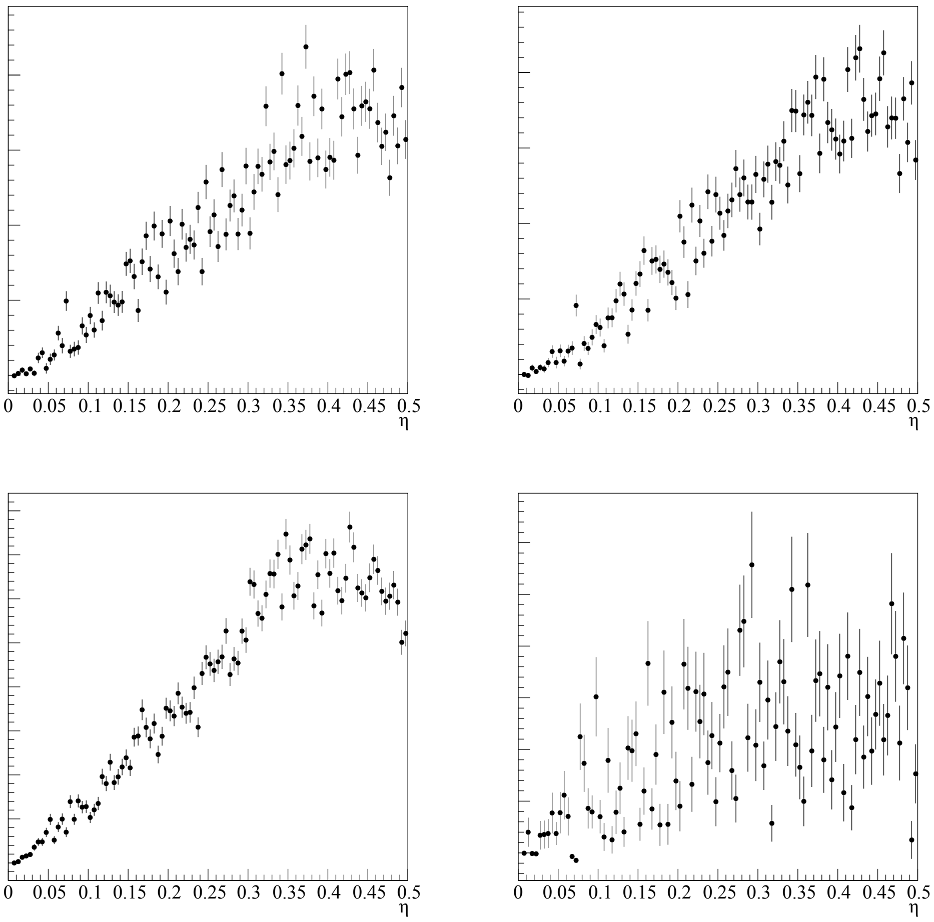

Figure D.5: The distribution of the predicted mistag for signal and combinatorial background at the loosest and tightest corners of the kinematic variables for the selection optimisation study. This is the distribution of the predicted mistag, η, for the combined OS and SS taggers using a Run I optimisation. Top Left - Distribution for the loosest PID and BDT cut for signal events. Top Right - Distribution for the tightest PID and BDT cut for signal events. Bottom Left - Distribution for the loosest PID and BDT cut for combinatorial background events. Bottom Right - Distribution for the tightest PID and BDT cut for combinatorial background events.

Appendix E

Analytic Solutions to Resolution-Corrected Decay Rates

The theory behind the decay rate of particles is well understood and was developed in Appendix B. However, in a realistic scenario the finite resolution of a particle detector requires corrections to be made to Equations B.54 and B.55. As the decay time resolution is normally distributed this can be achieved by convolving these functions with a Gaussian with a mean of 0 s and width of σ_{eff}.

$$\begin{aligned}\Gamma_{\text{eff}}(t;q) \quad = \quad & e^{-\Gamma t}\left[\cosh\left(\frac{\Delta\Gamma}{2}t\right)+\mathcal{A}_f^{\Delta\Gamma}\sinh\left(\frac{\Delta\Gamma}{2}t\right)\right. \\ & \left.+q\times\left(C_f\cos(\Delta m t)\;-\;S_f\sin(\Delta m t)\right)\right]\otimes G(t;\sigma_{\text{eff}}) \qquad \text{(E.1)}\end{aligned}$$

where q is the tag of the particle and takes the value of $+1$ for mesons and -1 for antimesons.

Hyberbolic and trigonometric functions can be rewritten in terms of exponential functions which makes it possible to find analytic solutions to the convolution. If we have a generic exponential, e^{kx}, we can convolve it with a Gaussian as follows

$$H(t;k)=e^{kx}\otimes\frac{1}{\sqrt{2\pi}\sigma}e^{\frac{x^2}{2\sigma^2}}=\frac{1}{\sqrt{2\pi}\sigma}\int_{-\infty}^{\infty}e^{kx}e^{\frac{-(t-x)^2}{2\sigma^2}}dx \qquad \text{(E.2)}$$

As the decay rate is both real and positive, then values less than 0 s are zero which simplifies the integral to

$$H(t;k) = \frac{1}{\sqrt{2\pi}\sigma}\int_0^{\infty} e^{-\frac{(-2\sigma^2 kx + x^2 + t^2 \; - \; 2tx)}{2\sigma^2}} dx \tag{E.3}$$

The integral can be solved with an appropriate u-substitution

$$u = \frac{x \; - \; t \; - \; \sigma^2 k}{\sqrt{2}\sigma} \tag{E.4}$$

which has the properties that when $x = \infty$ then $u = \infty$, when $x = 0$ then $u = -(t + \sigma^2 k)/(\sqrt{2}\sigma)$ and $dx = \sqrt{2}\sigma du$. It is also trivially shown that

$$u^2 - kt \; - \; \frac{(\sigma k)^2}{2} = \frac{-2\sigma^2 kx + x^2 + t^2 \; - \; 2tx}{2\sigma^2} \tag{E.5}$$

This substitution leads to

$$H(t;k) = \frac{1}{\sqrt{\pi}} e^{\frac{(\sigma k)^2}{2}} e^{kt} \int_{-(t+\sigma^2 k)/(\sqrt{2}\sigma)}^{\infty} e^{-u^2} du \tag{E.6}$$

The error function, erf(x), is an odd function that is bounded between -1 and 1. It takes the form

$$\mathrm{erf}(x) = \frac{2}{\sqrt{\pi}} \int_0^x e^{-t^2} dt \tag{E.7}$$

and as it has a maximum value of +1 we can define the complementary error function, erfc(x), as

$$\mathrm{erfc}(x) = 1 \; - \; \mathrm{erf}(x) = 1 + \mathrm{erf}(-x) = \frac{2}{\sqrt{\pi}} \int_x^{\infty} e^{-t^2} dt \tag{E.8}$$

which can be used to form the general expression for an exponential function convolved with a Gaussian

$$H(t;k) = \frac{1}{2} e^{\frac{(\sigma k)^2}{2}} e^{kt} (\mathrm{erf}\left[\frac{t + \sigma^2 k}{\sqrt{2}\sigma}\right] + 1) \tag{E.9}$$

To allow for a fast normalization of the PDF, the indefinite integral of $H(t;k)$ is

$$\int H(t;k) dt = \frac{1}{k}\left[H(t;k) \; - \; \frac{1}{2}\mathrm{erf}\left(\frac{t}{\sqrt{2}\sigma}\right)\right] \tag{E.10}$$

It should be noted that there are no magnitudes within this solution thus it is equally applicable to complex exponentials. The product of an exponential decay with lifetime τ and a hyperbolic function with a factor $\Delta\Gamma/2$ convolved with a Gaussian, $G(t)$, can be solved by noting

$$e^{\frac{-t}{\tau}} \cosh\left(\frac{\Delta\Gamma}{2}t\right) = \frac{1}{2}\left(e^{\left(\frac{\Delta\Gamma}{2} - \frac{1}{\tau}\right)t} + e^{\left(\frac{-\Delta\Gamma}{2} - \frac{1}{\tau}\right)t}\right) \tag{E.11}$$

$$e^{\frac{-t}{\tau}} \sinh\left(\frac{\Delta\Gamma}{2}t\right) = \frac{1}{2}\left(e^{\left(\frac{\Delta\Gamma}{2} - \frac{1}{\tau}\right)t} - e^{\left(\frac{-\Delta\Gamma}{2} - \frac{1}{\tau}\right)t}\right) \tag{E.12}$$

Therefore

$$e^{\left(\frac{\pm\Delta\Gamma}{2} - \frac{1}{\tau}\right)t} \otimes G(t) = \frac{1}{2} e^{\frac{\sigma^2}{2}\left(\frac{\pm\Delta\Gamma}{2} - \frac{1}{\tau}\right)^2} e^{\left(\frac{\pm\Delta\Gamma}{2} - \frac{1}{\tau}\right)t} \left(\mathrm{erf}\left[\frac{1}{\sqrt{2}}\left(\frac{t}{\sigma} - \frac{\sigma}{\tau} \pm \frac{\Delta\Gamma\sigma}{2}\right)\right] + 1\right) \tag{E.13}$$

The trigonometric parts can be solved using Euler's formula

$$e^{\left(\pm i\Delta m - \frac{1}{\tau}\right)t} \otimes G(t) = \frac{1}{2} e^{\frac{1}{2}\left(-(\Delta m\sigma)^2 + \left(\frac{\sigma}{\tau}\right)^2\right)} e^{\frac{-t}{\tau}} e^{\pm i\left(\Delta m t - \frac{\Delta m \sigma^2}{\tau}\right)} \left(\mathrm{erf}\left[\frac{1}{\sqrt{2}}\left(\frac{t}{\sigma} - \frac{\sigma}{\tau} \pm i\Delta m\sigma\right)\right] + 1\right. \tag{E.14}$$

It can be seen at this stage that the convolution of a complex exponential has led to a complex error function which is unrealistic in the context of a real decay. Some substitutions can be made to make the equation more palatable.

$$D(t) = e^{\frac{1}{2}\left(-(\Delta m\sigma)^2 + \left(\frac{\sigma}{\tau}\right)^2\right)} e^{\frac{-t}{\tau}} \tag{E.15}$$

$$x = \frac{1}{\sqrt{2}}\left(\frac{t}{\sigma} - \frac{\sigma}{\tau}\right) \tag{E.16}$$

$$y = \frac{\Delta m}{\sqrt{2}} \tag{E.17}$$

$$z = x + iy \tag{E.18}$$

which simplifies equation E.14 to

$$h^{(*)}(x, y) = \frac{D(t)}{2} e^{\pm 2i(xy)} (\mathrm{erf}(z^{(*)} + 1) \tag{E.19}$$

Noting the forms of sine and cosine using Euler's formula, we find

$$e^{-\frac{t}{\tau}} \cos(\Delta m t) \otimes G(t) = \frac{D(t)}{4}\big(\cos(2xy)\,(\mathrm{erf}(z) + \mathrm{erf}(z^*) + 2) + i\sin(2xy)\,(\mathrm{erf}(z) - \mathrm{erf}(z^*))\big) \tag{E.20}$$

$$e^{-\frac{t}{\tau}} \sin(\Delta m t) \otimes G(t) = \frac{D(t)}{4i}\big(i\sin(2xy)\,(\mathrm{erf}(z) + \mathrm{erf}(z^*) + 2) + \cos(2xy)\,(\mathrm{erf}(z) - \mathrm{erf}(z^*))\big) \tag{E.21}$$

A complex error function can be approximated as an infinite series [181] where

$$\begin{aligned}\mathrm{erf}(x+iy) &= \mathrm{erf}(x)+\frac{e^{-x^2}}{2\pi x}[1 - \cos(2xy)+i\sin(2xy)] \\ &\quad +\frac{2}{\pi}\sum_{n=1}^{\infty}\frac{e^{\frac{-n^2}{4}}}{n^2+4x^2}[f_n(x,y)+ig_n(x,y)]+\varepsilon(x,y)\end{aligned} \tag{E.22}$$

$$f_n(x,y) = 2x\,(1 - \cosh(ny)\cos(2xy)) + n\sinh(ny)\sin(2xy) \tag{E.23}$$

$$g_n(x,y) = 2x\cosh(ny)\sin(2xy) + n\sinh(ny)\cos(2xy) \tag{E.24}$$

$$\varepsilon(x,y) \approx 10^{-16}\mathrm{erf}(x+iy) \tag{E.25}$$

where $f_n(x,y)$ is an even function and $g_n(x,y)$ is an odd function. Thus the sum of a complex error function and its complex conjugate is

$$\mathrm{erf}(z)+\mathrm{erf}(z^*) = 2\mathrm{erf}(x)+\frac{e^{-x^2}}{\pi x}[1 - \cos(2xy)]+\frac{4}{\pi}\sum_{n=1}^{\infty}\frac{e^{\frac{-n^2}{4}}f_n(x,y)}{n^2+4x^2} \tag{E.26}$$

while the difference of a complex error function and its complex conjugate is

$$\mathrm{erf}(z) - \mathrm{erf}(z^*) = i\Big(\frac{e^{-x^2}}{\pi x}\sin(2xy)+\frac{4}{\pi}\sum_{n=1}^{\infty}\frac{e^{\frac{-n^2}{4}}g_n(x,y)}{n^2+4x^2}\Big) \tag{E.27}$$

Thus when equations E.26 and E.27 are substituted back into equations E.20 and E.21, real functions for the convolution are obtained. This method can be applied to obtaining the normalization for the trigonometric terms but care must be taken of the complex fraction in front of the normalization.

$$\frac{1}{\pm i\Delta m - \frac{1}{\tau}} = -\frac{1}{\tau(\Delta m^2+\frac{1}{\tau^2})} \mp i\frac{\Delta m}{\Delta m^2+\frac{1}{\tau^2}} \tag{E.28}$$

which results in real values for the normalization. The validity of the PDF presented here has been tested by itself with no extra assumptions about the decay (such as acceptance of mistag dilution effects) and returned unbiased values for the CP observables S_f, C_f and $\mathcal{A}_f^{\Delta\Gamma}$ with a series expansion up to order 4 in both $f_n(x,y)$ and $g_n(x,y)$. It was further validated when the effects of the detector acceptance and the mistag dilution were taken into account. At this level, the series expansions were required to be taken to order 7 before the PDFs were found to be unbiased.

Bibliography

[1] K. Popper. The Logic of Scientific Discovery. Routledge, 2005.

[2] T. S. Kuhn. The Structure of Scientific Revolutions. University of Chicago press, Third Edition, 1996.

[3] J. J. Thomson. XL. Cathode Rays. *The London, Edinburgh, and Dublin Philosophical Magazine and Journal of Science*, 44(269):293–316, 1897.

[4] J. J. Aubert et al. Experimental Observation of a Heavy Particle *J. Phys. Rev. Lett.*, 33:1404–1406, Dec 1974.

[5] J. E. Augustin et al. Discovery of a Narrow Resonance in e^+e^- Annihilation. *Phys. Rev. Lett.*, 33:1406–1408, Dec 1974.

[6] The ATLAS Collaboration. Observation of a New Particle in the Search for the Standard Model Higgs Boson with the ATLAS Detector at the LHC. *Physics Letters B*, 716(1):1 – 29, 2012.

[7] The CMS Collaboration. Observation of a New Boson at a Mass of 125 GeV with the CMS Experiment at the LHC. *Physics Letters B*, 716(1):30–61, 2012.

[8] F. Zwicky. On the Masses of Nebulae and of Clusters of Nebulae. *The Astrophysical Journal*, 86:217, 1937.

[9] F. Capozzi, E. Lisi, A. Marrone, D. Montanino, and A. Palazzo. Neutrino Masses and Mixings: Status of Known and Unknown 3ν Parameters. *Nuclear Physics B*, 908:218–234, 2016.

[10] E. W. Kolb, D. S. Salopek, and M. S. Turner. Origin of Density Fluctuations in Extended Inflation. *Physical Review D*, 42(12):3925, 1990.

[11] A. A. Penzias and R. W. Wilson. A Measurement of Excess Antenna Temperature at 4080 Mc/s. *The Astrophysical Journal*, 142:419–421, 1965.

[12] R. A. Alpher and R. Herman. Evolution of the Universe. *Nature*, 162: 774–775, 1948.

[13] A. D. Sakharov. Violation of CP Invariance, C Asymmetry, and Baryon Asymmetry of the Universe. *JETP Lett.(USSR)(Engl. Transl.), 5: 24-7 (Jan. 1, 1967).*, 1967.

[14] A. G. Cohen, D. B. Kaplan, and A. E Nelson. Progress in Electroweak Baryogenesis. *Annual Review of Nuclear and Particle Science*, 43(1):27–70, 1993.

[15] J.H. Chistenson, J. Cronin, V. Fitch, and R. Turlay. Evidence for the 2π Decay of the K^0. *Phys. Rev. Lett*, 13:138, 1964.

[16] B. Aubert et al. Measurement of CP-Violating Asymmetries in B^0 Decays to CP Eigenstates. *Phys. Rev. Lett.*, 86:2515–2522, Mar 2001.

[17] A. Abashian et al. Measurement of the CP Violation Parameter $\sin2\varphi_1$ in B^0 Meson Decays. *Phys. Rev. Lett.*, 86:2509–2514, Mar 2001.

[18] The LHCb Collaboration. First Observation of CP Violation in the Decays of B_s^0 Mesons. *Phys. Rev. Lett.*, 110:221601, May 2013.

[19] CL Bennett et al. Nine-year Wilkinson Microwave Anisotropy Probe (WMAP) Observations: Final Maps and Results. *The Astrophysical Journal Supplement Series*, 208(2):20, 2013.

[20] M. B. Gavela, M. Lozano, J. Orloff, and O. Pene. Standard Model CP-Violation and Baryon Asymmetry. *Nuclear Physics B*, 430(2):345–381, 1994.

[21] The LHCb Collaboration. LHCb Reoptimized Detector Design and Performance: Technical Design Report. Technical Report, Geneva, 2003.

[22] C. Dean. The LHCb VELO for Phase 1 Upgrade. In *The 25th International Workshop on Vertex Detectors*, Volume 287, page 071. SISSA Medialab, 2017.

[23] Y. Fukuda et al. Evidence for Oscillation of Atmospheric Neutrinos. *Phys. Rev. Lett.*, 81:1562–1567, Aug 1998.

[24] Q. R. Ahmad et al. Measurement of the Rate of $\nu_e + d \to p^+p^+e^-$ Interactions Produced by ^8B Solar Neutrinos at the Sudbury Neutrino Observatory. *Phys. Rev. Lett.*, 87:071301, Jul 2001.

[25] H. Fritzsch, M. Gell-Mann, and H. Leutwyler. Advantages of the Color Octet Gluon Picture. *Physics Letters B*, 47(4):365 – 368, 1973.

[26] M. Gell-Mann. A Schematic Model of Baryons and Mesons. *Physics Letters*, 8(3):214 – 215, 1964.

[27] G Zweig. An SU_3 Model for Strong Interaction Symmetry and its Breaking. (CERN-TH-401), Jan 1964.

[28] I. Adachi et al. Study of $e^+ \; e^- \to \pi^+ \; \pi^-$ J/ψ and Observation of a Charged Charmoniumlike State Belle. *Phys. Rev. Lett.*, 110:252002, Jun 2013.

[29] M. Ablikim et al. Observation of a Charged Charmoniumlike Structure in $e^+ \; e^- \to \pi^+ \; \pi^-$ J/ψ at $\sqrt{s}$= 4.26 GeV. *Phys. Rev. Lett.*, 110:252001, Jun 2013.

[30] The LHCb Collaboration. Observation of J/ψ p Resonances Consistent with Pentaquark States in $\Lambda_b^0 \to$ J/ψK$^-$p Decays. *Phys. Rev. Lett.*, 115(7): 072001, 2015.

[31] A. Esposito, A. Pilloni, and A.D. Polosa. Multiquark Resonances. *Physics Reports*, 668:1 – 97, 2017.

[32] C.-W. Shen, F.-K. Guo, J.-J. Xie, and B.-S. Zou. Disentangling the Hadronic Molecule Nature of the $\mathrm{P_c}$(4380) Pentaquark-like Structure. *Nuclear Physics A*, 954:393 – 405, 2016.

[33] C. Wang, L.-L. Liu, X.-W. Kang, X.-H. Guo, and R.-W. Wang. Possible Open-charmed Pentaquark Molecule Ω_c (3188) - the DΞ bound state -in the Bethe-Salpeter Formalism. *The European Physical Journal C*, 78(5):407, 2018.

[34] K. Azizi, Y. Sarac, and H. Sundu. Possible Molecular Pentaquark States with Different Spin and Quark Configurations. *Phys. Rev. D*, 98:054002, Sep 2018.

[35] A. Ali, J. S. Lange, and S. Stone. Exotics: Heavy Pentaquarks and Tetraquarks. *Progress in Particle and Nuclear Physics*, 97:123–198, 2017.

[36] The Particle Data Group. Review of Particle Physics. *Chinese Physics C*, 40(10):100001, 2016.

[37] M. Thomson. Modern Particle Physics. Cambridge, First Edition, 2013.

[38] B. P. Abbott, B. L. Pearlstone, et al. Observation of Gravitational Waves from a Binary Black Hole Merger. *Phys. Rev. Lett.*, 116:061102, Feb 2016.

[39] The UA1 Collaboration. Experimental Observation of Isolated Large Transverse Energy Electrons with Associated Missing Energy at $\sqrt{s}$=540 GeV. *Physics Letters B*, 122(1):103 – 116, 1983.

[40] The UA2 Collaboration. Observation of Single Isolated Electrons of High Transverse Momentum in Events with Missing Transverse Energy at the CERN pp Collider. *Physics Letters B*, 122(5):476 – 485, 1983.

[41] The UA1 Collaboration. Experimental Observation of Lepton Pairs of Invariant Mass around 95 GeV/c^2 at the CERN SPS Collider. *Physics Letters B*, 126(5):398 – 410, 1983.

[42] The UA2 Collaboration. Evidence for Z^0 at the CERN pp Collider. *Physics Letters B*, 129(1):130 – 140, 1983.

[43] D. Griffiths. Introduction to Elementary Particles. Wiley, Second, Revised Edition, 2008.

[44] CKMfitter. CKM Fitter. https://ckmfitter.in2p3.fr.

[45] R. Eisberg and R. Resnick. Quantum Physics of Atoms, Molecules, Solids, Nuclei, and Particles. Wiley, First Edition, 1974.

[46] P. F. Harrison et al. The BaBar Physics Book: Physics at an Asymmetric B factory. Technical Report, 1998.

[47] B. Pontecorvo. Inverse β Processes and Non-Conservation of Lepton Charge. *Zhur. Eksptl. i Teoret. Fiz.*, 34, 1958.

[48] Z. Maki, M. Nakagawa, and S. Sakata. Remarks on the Unified Model of Elementary Particles. *Progress of Theoretical Physics*, 28(5):870–880, 1962.

[49] L. L. Chau and W. Y. Keung. Comments on the Parametrization of the Kobayashi-Maskawa Matrix. *Phys. Rev. Lett.*, 53:1802–1805, Nov 1984.

[50] L. Wolfenstein. Parametrization of the Kobayashi-Maskawa Matrix. *Phys. Rev. Lett.*, 51:1945–1947, Nov 1983.

[51] K. Lande, E. T. Booth, J. Impeduglia, L. M. Lederman, and W. Chinowsky. Observation of Long-Lived Neutral V Particles. *Phys. Rev.*, 103:1901–1904, Sep 1956.

[52] The ARGUS Collaboration. Observation of $\mathrm{B}^0 - \bar{\mathrm{B}}^0$ Mixing. *Physics Letters B*, 192(1-2):245–252, 1987.

[53] The CDF Collaboration. Observation of $\mathrm{B}_s^0 - \overline{\mathrm{B}}_s^0$ Oscillations. *Phys. Rev. Lett.*, 97:242003, Dec 2006.

[54] The LHCb Collaboration. Observation of $\mathrm{D}^0{-}\overline{\mathrm{D}}^0$ Oscillations. *Phys. Rev. Lett.*, 110:101802, Mar 2013.

[55] The LHCb Collaboration. A Precise Measurement of the B^0 Meson Oscillation Frequency. *The European Physical Journal C*, 76(7):412, 2016.

[56] The LHCb Collaboration. Precision Measurement of the B_s^0–$\overline{\mathrm{B}}_\mathrm{s}^0$ Oscillation Frequency with the Decay $\mathrm{B}_\mathrm{s}^0 \to \mathrm{D}_\mathrm{s}^-\pi^+$. *New Journal of Physics*, 15(5): 053021, 2013.

[57] R. Fleischer. New Strategies to Extract β and γ from $\mathrm{B}_d \to \pi^+\pi^-$ and $\mathrm{B}_s^0 \to \mathrm{K}^+\mathrm{K}^-$. *Physics Letters B*, 459(1-3):306–320, 1999.

[58] H. J. Lipkin. Penguins, Trees and Final State Interactions in B Decays in Broken SU3. *Physics Letters B*, 415(2):186 – 192, 1997.

[59] M. Gronau. U-spin Symmetry in Charmless B Decays. *Physics Letters B*, 492(3):297 – 302, 2000.

[60] The LHCb Collaboration. Determination of γ and $-2\beta_s$ from Charmless Two-body Decays of Beauty Mesons. *Physics Letters B*, 741:1 – 11, 2015. ISSN 0370-2693.

[61] The LHCb Collaboration. Measurement of CP Asymmetries in Two-body $B_{(s)}^0$-Meson Decays to Charged Pions and Kaons. *Phys. Rev. D*, 98:032004, Aug 2018.

[62] CERN. Convention for the Establishment of a European Organization for Nuclear Research, . http://cds.cern.ch/record/480837/files/cm-p00047703.pdf.

[63] CERN. The Birth of the Web, . https://home.cern/topics/birth-web.

[64] CERN. The First Capacitative Touch Screens at CERN, . http://cerncourier.com/cws/article/cern/42092.

[65] F. J. Hasert et al. Observation of Neutrino-like Interactions without Muon or Electron in the Gargamelle Neutrino Experiment. *Physics letters B*, 46 (1):138–140, 1973.

[66] The ISOLDE Collaboration. ISOLDE, . https://home.cern/about/experiments/isolde.

[67] F. Mingrone, O. Aberle, J. Andrzejewski, and L. Audouin. The CERN nTOF Facility: A Unique Tool for Nuclear Data Measurement. *EPJ Web of Conferences*, 122:05001, 2016.

[68] The CLOUD Collaboration. CLOUD Experiment - How It Works, . https://cds.cern.ch/record/2154271.

[69] M. H. Holzscheiter. ACE: The Relative Biological Efficiency (RBE) of Antiprotons. Combined Data Analysis for the 2008 –2012 Runs. Technical Report CERN-SPSC-2016-004. SPSC-SR-176, CERN, Jan 2016.

[70] CERN. The CERN Accelerator Complex, . https://cds.cern.ch/record/2197559?ln=en.

[71] L. Arnaudon et al. Linac4 Technical Design Report. Technical Report CERN-AB-2006-084 ; CARE-Note-2006-022-HIPPI, 2006.

[72] L. Evans and P. Bryant. LHC Machine. *JINST*, 3(08):S08001, 2008.

[73] The ALICE Collaboration. The ALICE Experiment at the CERN Large Hadron Collider. *JINST*, 3:S08002, 2008.

[74] The ATLAS Collaboration. The ATLAS Experiment at the CERN Large Hadron Collider. *JINST*, 3:S08003, 2008.

[75] The CMS Collaboration. The CMS Experiment at the CERN Large Hadron Collider. *JINST*, 3:S08004, 2008.

[76] The LHCb Collaboration. The LHCb Experiment at the CERN Large Hadron Collider. *JINST*, 3(08):S08005, 2008.

[77] The LHCf Collaboration. The LHCf Experiment at the CERN Large Hadron Collider. *JINST*, 3:S08006, 2008.

[78] The TOTEM Collaboration. The TOTEM Experiment at the CERN Large Hadron Collider. *JINST*, 3:S08007, 2008.

[79] The MoEDAL Collaboration. The Physics Programme of the MoEDAL Experiment at the LHC. *International Journal of Modern Physics A*, 29 (23):1430050, 2014.

[80] C. Wyss. LHC Arc Dipole Status Report. Technical Report LHC-Project-Report-288. CERN-LHC-Project-Report-288, 1999.

[81] O. Bruning et al. Electron Cloud and Beam Scrubbing in the LHC. Volume 4, pages 2629–2631, 1999.

[82] R. Valizadeh et al. Low Secondary Electron Yield Engineered Surface for Electron Cloud Mitigation. *Applied Physics Letters*, 105(23):231605, 2014.

[83] The LHCb Collaboration. LHCb Detector Performance. *International Journal of Modern Physics A*, 30(07):1530022, 2015.

[84] The LHCb Collaboration. Measurement of the b-Quark Production Cross Section in 7 and 13 TeV pp Collisions. *Phys. Rev. Lett.*, 118(5):052002, 2017.

[85] The LHCb Collaboration. The LHCb Detector. Sep 1998.

[86] The LHCb Collaboration. Angular Distribution of b-quarks, . http://www.mpi-hd.mpg.de/lhcb/index.php?id=detector.

[87] R Alemany-Fernandez, R Jacobsson, and F Follin. The LHCb Online Luminosity Control and Monitoring. *IPAC2013: Proceedings of the 4th International Particle Accelerator Conference*, 2013.

[88] The LHCb Collaboration. LHCb Operation Plots Webpage, . https://lbgroups.cern.ch/online/OperationsPlots/index.htm.

[89] M. Adinolfi et al. LHCb VELO (VErtex LOcator): Technical Design Report. Technical Report CERN-LHCC-2001-011 ; LHCb-TDR-5, Geneva, 2001.

[90] R. Aaij et al. Performance of the LHCb Vertex Locator. *JINST*, 9(09): P09007, 2014.

[91] The LHCb Collaboration. The LHCb Detector and Triggers. *Nuclear Physics B-Proceedings Supplements*, 167:229–232, 2007.

[92] The LHCb Collaboration. Three Modules of the LHCb Vertex Locator in the H8 Test Beam in the North Area, . http://cds.cern.ch/record/1118792?ln=zh_CN.

[93] M. Agari, N. van Bakel, and C. Bauer. Beetle - A Radiation Hard Readout Chip for the LHCb Experiment. *Nuclear Instruments and Methods in Physics Research A*, 518(1):468 – 469, 2004.

[94] R. Brenner, J. Kaplon, H. von der Lippe, E. Nygård, S. Roe, P. Weilhammer, and K. Yoshioka. Performance of a LHC Front-end Running at 67 MHz. *Nuclear Instruments and Methods in Physics Research A*, 339(3):477 – 484, 1994.

[95] N. Van Bakel et al. The Beetle Reference Manual. Technical Report, CERN-LHCb-2001-046, 2001.

[96] J. Hahn, A. Zidon, C. Gillman, and A. Atzmon. The Design of Derandomizing Buffer Stores for High Data Rates. *IEEE Transactions on Nuclear Science*, 16(1):154–161, 1969.

[97] G. Haefeli et al. The LHCb DAQ Interface Board TELL1. *Nuclear Instruments and Methods in Physics Research A*, 560(2):494 – 502, 2006.

[98] The LHCb Collaboration. LHCb VELO Upgrade Technical Design Report. Technical Report CERN-LHCC-2013-021. LHCB-TDR-013, CERN, Geneva, Nov 2013.

[99] The LHCb Collaboration. LHCb Inner Tracker Technical Design Report. Technical Report CERN-LHCC-2002-029. LHCB-TDR-008, CERN, Geneva, Nov 2002.

[100] R. Arink et al. Performance of the LHCb Outer Tracker. *JINST*, 9:P01002, 2014.

[101] S Amato et al. LHCb RICH: Technical Design Report. Technical Report CERN-LHCC-2000-037 ; LHCb-TDR-3, Geneva, 2000.

[102] S. Amato et al. LHCb Calorimeters: Technical Design Report. Technical Report CERN-LHCC-2000-036 ; LHCb-TDR-2, Geneva, 2000.

[103] M. Adinolfi et al. LHCb Muon System: Technical Design Report. Technical Report CERN-LHCC-2001-010 ; LHCb-TDR-4, Geneva, 2001.

[104] V. L. Ginzburg. Transition Radiation and Transition Scattering. *Physica Scripta*, 1982(T2A):182, 1982.

[105] D. H. Perkins. Introduction to High Energy Physics. Addison Wesley, Second Edition, 1982.

[106] A. Papanestis et al. Performance of the LHCb RICH Detectors During the LHC Run II. *Nuclear Instruments and Methods in Physics Research A*, 2017.

[107] S. Eisenhardt. Hybrid Photon Detectors for the LHCb RICH. *Nuclear Instruments and Methods in Physics Research A*, 565(1):234 – 240, 2006.

[108] S. Eisenhardt. Hybrid Photon Detectors and Ion Feedback. *Nuclear Instruments and Methods in Physics Research A*, 617(1):391 – 392, 2010.

[109] M. Adinolfi et al. Performance of the LHCb RICH Detector at LHC. *Eur. Phys. J. C*, 73(arXiv:1211.6759. CERN-LHCb-DP-2012-003. LHCb-DP-2012-003):2431. 25 p, Nov 2012.

[110] A. A. Alves Jr. et al. Performance of the LHCb Muon System. *JINST*, 8 (02):P02022, 2013.

[111] K. Akiba et al. The HeRSCheL Detector: High-rapidity Shower Counters for LHCb. *JINST*, 13(04):P04017, 2018.

[112] S. Amato et al. LHCb Magnet: Technical Design Report. Technical Report CERN-LHCC-2000-007 ; LHCb-TDR-1, Geneva, 2000.

[113] R. Antunes-Nobrega et al. LHCb Trigger System: Technical Design Report. Technical Report CERN-LHCC-2003-031 ; LHCb-TDR-10, Geneva, 2003.

[114] B. Sciascia. LHCb Run 2 Trigger Performance. (LHCb-PROC-2016-020), May 2016.

[115] M. Kenzie and V. Gligorov. Lifetime Unbiased Beauty and Charm Triggers at LHCb. Technical Report LHCb-PUB-2015-026. CERN-LHCb-PUB-2015-026, CERN, Geneva, Oct 2016.

[116] R. Aaij et al. The LHCb Trigger and its Performance in 2011. *JINST*, 8 (04):P04022, 2013.

[117] V. Dubinko. New Principles of Radiation Damage and Recovery Based on the Radiation Induced Emission of Schottky Defects. *arXiv preprint cond-mat/0212154*, 2002.

[118] B. Rakotomiaramanana. The Design and Production of the LHCb VELO High Voltage System and Analysis of the $B^0 \to K^{*}\mu^{+}\mu^{-}$ Rare Decay, Ph.D. Thesis, University of Glasgow, 2010.

[119] J. Libby. VELO: The LHCb Vertex Detector. *Nuclear Instruments and Methods in Physics Research A*, 494(1):113 – 119, 2002.

[120] L. Eklund. VELO HV Verification Procedure. https://edms.cern.ch/edmsui/#!master/navigator/document?D:1447591477:1447591477:subDocs.

[121] M. Moll et al. Leakage Current of Hadron Irradiated Silicon Detectors - Material Dependence. *Nuclear Instruments and Methods in Physics Research A*, 426(1):87–93, 1999.

[122] K. Akiba et al. Use of IT (Current vs Temperature) Scans to Study Radiation Damage in the LHCb VELO. Technical Report LHCb-PUB-2011-021 ; CERN-LHCb-PUB-2011-021, 2011.

[123] CERN. The LHC Racks Up Records, . http://home.cern/about/updates/2017/06/lhc-racks-records.

[124] G Apollinari, I Béjar Alonso, O Brüning, M Lamont, and L Rossi. High-Luminosity Large Hadron Collider (HL-LHC): Preliminary Design Report. Technical Report, Geneva, 2015.

[125] The LHCb Collaboration. Framework TDR for the LHCb Upgrade. Technical Report CERN-LHCC-2012-007 ; LHCb-TDR-12, CERN, 07 2012.

[126] The LHCb Collaboration. Observation of the Doubly Charmed Baryon Ξ_{cc}^{++}. *Phys. Rev. Lett.*, 119(11):112001, 2017.

[127] The LHCb Collaboration. LHCb PID Upgrade Technical Design Report. Technical Report CERN-LHCC-2013-022. LHCB-TDR-014, Nov 2013.

[128] C. Joram, G. Haefeli, and B. Leverington. Scintillating Fibre Tracking at High Luminosity Colliders. *JINST*, 10(08):C08005, 2015.

[129] T. Poikela. VeloPix: the Pixel ASIC for the LHCb Upgrade. *JINST*, 10(01):C01057, 2015.

[130] O. A. De Aguiar Francisco, J. Buytaert, P. Collins, R. Dumps, M. John, A. Mapelli, and G. Romagnoli. Evaporative CO2 Microchannel Cooling for the LHCb VELO Pixel Upgrade. *JINST*, 10(05):C05014, 2015.

[131] M. van Beuzekom et al. Timepix3: a 65K Channel Hybrid Pixel Readout Chip with Simultaneous ToA/ToT and Sparse Readout. *JINST*, 9(05): C05013, 2014.

[132] T. Poikela et al. The VeloPix ASIC. *JINST*, 12(01):C01070, 2017.

[133] L. Eklund and S. Naik. Description of the VELO Upgrade Opto and Power Board. Technical Report.

[134] F. L. Luo et al. Digital Power Electronics and Applications. Academic Press, 2005.

[135] C. Soos et al. The Versatile Transceiver: Towards Production Readiness. *JINST*, 8(03):C03004, 2013.

[136] W. T. Beyene. The Design of Continuous-Time Linear Equalizers Using Model Order Reduction Techniques. In *Electrical Performance of Electronic Packaging, 2008 IEEE-EPEP*, pages 187–190. IEEE, 2008.

[137] W. J. Dally and J. W. Poulton. Digital Systems Engineering. Cambridge University Press, 2008.

[138] P. R. Gray, P. Hurst, R. G. Meyer, and S. Lewis. Analysis and Design of Analog Integrated Circuits. Wiley, 2001.

[139] E. W. Matthews. The Use of Scattering Matrices in Microwave Circuits. *IRE Transactions on Microwave Theory and Techniques*, 3(3):21–26, April 1955.

[140] V. Belevitch. Summary of the History of Circuit Theory. *Proceedings of the IRE*, 50(5):848–855, 1962.

[141] D. M. Pozar. Microwave Engineering. Wiley, Fourth Edition, 2012.

[142] W. Che et al. Formulas of Dielectric and Total Attenuations of a Microstrip Line. *Radio Science*, 45:RS5006, 2010.

[143] M. Mechaik. Signal Attenuation in Transmission Lines. *Proceedings of the IEEE 2001. 2nd International Symposium on Quality Electronic Design*, page 191, 2001.

[144] L. Pal, P. Kroó, P. Pellionisz, F. Szlavik, and I. Vizi. Correlation-type Time-of-flight Spectrometer with Magnetically Chopped Polarized Neutron Beam. *Neutron Inelastic Scattering Vol. II. Proceedings of a Symposium on Neutron Inelastic Scattering*, 1968.

[145] N. B. Beaudry, A. Datta, D. London, A. Rashed, and J.-S. Roux. The $B \to \mathrm{K}\pi$ Puzzle Revisited. *Journal of High Energy Physics*, 2018(1):74, 2018.

[146] The LHCb Collaboration. Effective Lifetime Measurements in the $\mathrm{B}_\mathrm{s}^0 \to \mathrm{K}^+\mathrm{K}^-, \mathrm{B}^0 \to \mathrm{K}^+\pi^-$ and $\mathrm{B}_\mathrm{s}^0 \to \pi^+\mathrm{K}^-$ Decays. *Physics Letters B*, 736:446–454, 2014.

[147] S. Karodia. CP Violation and Lifetime Measurements of Two-body Charmless Decays of B Hadrons at LHCb, Ph.D. Thesis, University of Glasgow, 2018.

[148] L. Anderlini, S. Ogilvy, et al. The PIDCalib Package. Technical Report LHCb-PUB-2016-021 ; CERN-LHCb-PUB-2016-021, 2016.

[149] The LHCb Collaboration. First Observation of the Rare Purely Baryonic Decay $\mathrm{B}^0 \to \mathrm{p}\bar{\mathrm{p}}$. *Phys. Rev. Lett.*, 119:232001, Dec 2017.

[150] The LHCb Collaboration. Measurement of b Hadron Production Fractions in 7 TeV pp Collisions. *Physical Review D*, 85(3):032008, 2012.

[151] Heavy Flavor Averaging Group. Averages of b-hadron, c-hadron, and τ-lepton Properties as of Summer 2016. *Eur. Phys. J. C*, 77(12):895, 2017.

[152] B. P. Roe et al. Boosted Decision Trees as an Alternative to Artificial Neural Networks for Particle Identification. *Nuclear Instruments and Methods in Physics Research A*, 543(2-3):577–584, 2005.

[153] A. Hoecker et al. TMVA-Toolkit for Multivariate Data Analysis. *arXiv preprint physics/0703039*, 2007.

[154] J. Gaiser. Charmonium Spectroscopy From Radiative Decays of the J/ψ and ψ', Ph.D. Thesis, SLAC, 1982.

[155] K. Cranmer. Kernel Estimation in High-Energy Physics. *Computer Physics Communications*, 136(3):198–207, 2001.

[156] B Knuteson and H Miettinen. Mass Analysis and Parameter Estimation with PDE. Technical Report D0-3396, 1997.

[157] I. S. Abramson. On Bandwidth Variation in Kernel Estimates - A Square Root Law. *The Annals of Statistics*, pages 1217–1223, 1982.

[158] F. Andrianala, T. Bird, and R. W. Lambert. Proper Time for Semileptonics, Acceptance Functions, Resolution Functions, and k-factors. (LHCb-INT-2011-020).

[159] R. Bailey et al. Measurement of the Lifetime of Charged and Neutral D Mesons with High Resolution Silicon Strip Detectors. *Zeitschrift für Physik C Particles and Fields*, 28(3):357–363, 1985.

[160] V. Gligorov et al. Swimming: A Data Driven Acceptance Correction Algorithm. *Journal of Physics: Conference Series*, 396(2):022016, 2012.

[161] M. Pivk and F.R. Le Diberder. sPlot: A Statistical Tool to Unfold Data Distributions. *Nuclear Instruments and Methods in Physics Research A*, 555 (1):356 – 369, 2005.

[162] R. Fleischer and R. Knegjens. In Pursuit of New Physics with $B_s^0 \to K^+K^-$. *The European Physical Journal C*, 71(1):1532, 2011.

[163] The BaBar Collaboration. Measurement of CP Asymmetries and Branching Fractions in Charmless Two-Body B-Meson Decays to Pions and Kaons. *Phys. Rev.*, D87(5):052009, 2013.

[164] The Belle Collaboration. Measurement of the CP Violation Parameters in $B^0 \to \pi^+\pi^-$ Decays. *Phys. Rev.*, D88(9):092003, 2013.

[165] The LHCb Collaboration. First Measurement of Time-dependent CP Violation in $B_s^0 \to K^+K^-$ Decays. *JHEP*, 10:183, 2013.

[166] The LHCb Collaboration. Measurement of Time-Dependent CP-violating Asymmetries in $B^0 \to \pi^+\pi^-$ and $B_s^0 \to K^+K^-$ Decays at LHCb. *LHCb-CONF-2016-018*, .

[167] D. J. Lange. The EvtGen Particle Decay Simulation Package. *Nuclear Instruments and Methods in Physics Research A*, 462(1):152 – 155, 2001.

[168] T. Sjöstrand, S. Mrenna, and P. Skands. A Brief Introduction to PYTHIA 8.1. *Computer Physics Communications*, 178(11):852–867, 2008.

[169] G. Cowan. Statistical Data Analysis. Oxford University Press, 1998.

[170] L. Demortier. Equivalence of the Best-fit and Covariance Matrix Methods for Comparing Binned Data with a Model in the Presence of Correlated Systematic Uncertainties. Technical Report CDF/MEMO/STATISTICS/PUBLIC/8661, CDF Note 8661, 1999.

[171] LHCb Collaboration. Measurement of the Track Reconstruction Efficiency at LHCb. *JINST*, 10(02):P02007, 2015.

[172] The LHCb Collaboration. Opposite-side Flavour Tagging of B Mesons at the LHCb Experiment. *Eur. Phys. J. C*, 72(6), 2012.

[173] The LHCb Collaboration. Optimization and Calibration of the Same-side Kaon Tagging Algorithm using Hadronic B_s^0 Decays in 2011 Data. *LHCb-CONF-2012-033*, .

[174] The LHCb Collaboration. Measurement of B^0, B_s^0, B^+, and Λ_b^0 Production Asymmetries in 7 and 8 TeV Proton–Proton Collisions. *Physics Letters B*, 774:139–158, 2017.

[175] The LHCb Collaboration. Observation of the Decay $\mathrm{B}_\mathrm{c}^+ \to \mathrm{B}_\mathrm{s}^0\pi^+$. *Phys. Rev. Lett.*, 111(18):181801, 2013.

[176] The LHCb Collaboration. Measurements of Indirect CP Asymmetries in $\mathrm{D}^0 \to \mathrm{K}^+\mathrm{K}^-$ and $\mathrm{D}^0 \to \pi^+\pi^-$ Decays. *Phys. Rev. Lett.*, 112:041801, Jan 2014.

[177] F. Dordei. Lifetime Measurements of Beauty Hadrons at the LHCb Experiment, Ph.D. Thesis, University of Heidelberg, 2015.

[178] E. Noether. Invariant Variation Problems. *Transport Theory and Statistical Physics*, 1(3):186–207, 1918.

[179] R. P. Feynman. The Theory of Positrons. *Phys. Rev.*, 76:749–759, Sep 1949.

[180] M. E. Peskin and D. V. Schroeder. An Introduction to Quantum Field Theory. Levant, First Indian Edition, 2005.

[181] M. Abramowitz and I. A. Stegun. Handbook of Mathematical Functions: with Formulas, Graphs, and Mathematical Tables, Volume 55. Courier Corporation, 1965.